

A Thesis Submitted for the Degree of PhD at the University of Warwick

Permanent WRAP URL:

<http://wrap.warwick.ac.uk/162704>

Copyright and reuse:

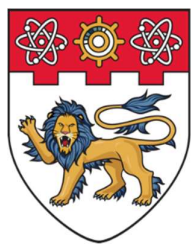
This thesis is made available online and is protected by original copyright.

Please scroll down to view the document itself.

Please refer to the repository record for this item for information to help you to cite it.

Our policy information is available from the repository home page.

For more information, please contact the WRAP Team at: wrap@warwick.ac.uk



**NANYANG
TECHNOLOGICAL
UNIVERSITY**
SINGAPORE



**LOCALIZED STRUCTURAL AND BULK EFFECTS IN
HYBRID ORGANIC-INORGANIC PEROVSKITES**

WALTER WONG PEI DE

**SCHOOL OF MATERIALS SCIENCE AND ENGINEERING,
NANYANG TECHNOLOGICAL UNIVERSITY**

DEPARTMENT OF PHYSICS, UNIVERSITY OF WARWICK

2020

LOCALIZED STRUCTURAL AND BULK EFFECTS IN HYBRID ORGANIC-INORGANIC PEROVSKITES

WALTER WONG PEI DE

SCHOOL OF MATERIALS SCIENCE AND ENGINEERING, NANYANG
TECHNOLOGICAL UNIVERSITY

DEPARTMENT OF PHYSICS, UNIVERSITY OF WARWICK

A thesis submitted to the Nanyang Technological
University and the University of Warwick in partial
fulfilment of the requirement for the degree of Doctor of
Philosophy under the NTU/Warwick Joint PhD
Programme

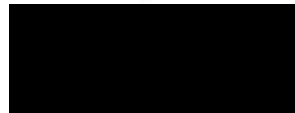
2020

Statement of Originality

I hereby certify that the work embodied in this thesis is the result of original research, is free of plagiarized materials, and has not been submitted for a higher degree to any other University or Institution.

18th May 2021

.....
Date



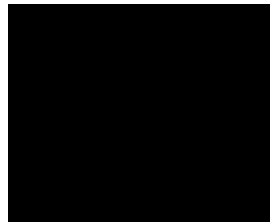
.....
Walter Wong Pei De

Supervisor Declaration Statement

We have reviewed the content and presentation style of this thesis and declare it is free of plagiarism and of sufficient grammatical clarity to be examined. To the best of our knowledge, the research and writing are those of the candidate except as acknowledged in the Author Attribution Statement. We confirm that the investigations were conducted in accord with the ethics policies and integrity standards of Nanyang Technological University and the University of Warwick, and that the research data are presented honestly and without prejudice.

18th May 2021

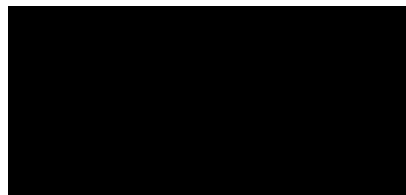
.....
Date



.....
Assoc Prof Andrew C. Grimsdale

18th May 2021

.....
Date



Prof John V. Hanna

Authorship Attribution Statement

This thesis contains material from 2 papers published in the following peer-reviewed journals where I was the first author.

Chapter 4 is published as Walter P. D. Wong, Jun Yin, Bhumika Chaudhary, Xin Yu Chin, Daniele Cortecchia, Shu-Zee A. Lo, Andrew C. Grimsdale, Omar F. Mohammed, Guglielmo Lanzani, and Cesare Soci. Large Polaron Self-Trapped States in Three-Dimensional Metal-Halide Perovskites. *ACS Materials Lett.* 2, 1, 20-27 (2020). DOI: 10.1021/acsmaterialslett.9b00276. This paper is co-first authored by Walter P.D. Wong and Jun Yin.

The contributions of the co-authors are as follows:

- A/Prof C. Soci and A/Prof A. Grimsdale provided the initial project direction and edited the manuscript drafts.
- I prepared the manuscript drafts. The manuscript was revised by Prof. Lanzani
- I co-designed the study with A/Prof C. Soci and performed all the laboratory work at the School of Physical and Mathematical Science and Centre for Disruptive Photonics Technology, Nanyang Technological University.
- All steady state PIA measurements were carried out by me and assisted by Dr X.Y. Chin in the Centre for Disruptive Photonics Technology, Nanyang Technological University.
- Steady state PIA spectral interpretation was conducted by me and assisted by Prof Lanzani
- Dr J. Yin and A/Prof O.F Mohammed performed all DFT theoretical analysis at King Abdullah University of Science and Technology (KAUST)
- Dr S-Z A. Lo assisted in the collection of femtosecond transient absorption spectroscopic results and I carried out the spectral interpretation
- B. Chaudhary collected the transient photocurrent results and I carried out the spectral interpretation

Chapter 5 and 6 is currently being prepared as a manuscript: Walter P.D. Wong, Adam J. Carver, Nicole L. Kelly, Sam J. Page, David Walker, Guy Clarkson, Albert Bartok-Partay, Andrew C. Grimsdale, John V. Hanna. A section of Chapter 6 is published as Walter P. D. Wong, John V. Hanna, and Andrew C. Grimsdale. The Classification of 1D ‘Perovskites’. *Acta Cryst. B* 77, 408-415 (2021). DOI: 10.1107/S2052520621004376. This paper is first authored by Walter P.D. Wong.

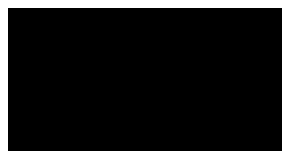
The contributions of the co-authors are as follows:

- I conceived the project idea with guidance from A/Prof A. C. Grimsdale and Prof J. V. Hanna
- I carried out the synthesis work with guidance from A/Prof A. C. Grimsdale at Nanyang Technological University, and with Dr G. Clarkson at the University of Warwick
- XRD experiments and analysis are done with guidance from Dr D. Walker and Dr G. Clarkson at the University of Warwick
- SSNMR results were collected with the collaboration and assistance from A. J. Carver, N. L. Kelly, Dr S. J. Page at the University of Warwick
- I carried out all steady state optical and photoluminescence experiments and analysis at The Research Technology Platform and Warwick Centre for Ultrafast Spectroscopy (WCUS) at the University of Warwick
- Dr A. Bartok-Partay performed all DFT theoretical work and A. J. Carver assisted with the analysis at the University of Warwick
- I prepared the manuscript drafts. The drafts were revised together with A/Prof A. C. Grimsdale and Prof J. V. Hanna

18th May 2020

.....

Date



.....

Walter Wong Pei De

Abstract

This thesis is a study on hybrid organic inorganic perovskites (HOIP) and systematically studies the effect of localized structural distortion and disorder in perovskites, which is indirectly observed in the 3-dimensional (3D) methylammonium lead iodide (MAPbI_3), and directly observed in the reduced dimensional perovskites. The study then further aims to establish a structure-property relationship in the hybrid perovskites.

Chapter 1 and 2 outlines the early developments in the field of hybrid perovskite up until recent times. These chapters lay the background for the work done prior to this thesis and shows how there are knowledge gap in the field, particularly in the understanding of the structural – property relationship. Additionally, a better understanding of the material's structure – property relationship would be valuable to the respective material's application, like photovoltaics or efficient lighting application which are of increasing importance towards sustainability efforts. This would then allow scientists to design various aspects of the structure to exploit the respective desired material property.

Chapter 3 summarizes the various background and theoretical aspects of the experimental techniques used in this thesis, namely X-ray diffraction, solid state nuclear magnetic resonance, steady-state and transient optoelectronic characterization techniques. X-ray diffraction and solid state nuclear magnetic resonance would probe the structural configuration while the suite of optoelectronic characterization techniques would investigate the optical and electronic properties of the material at various timescale.

In Chapter 4, the study focuses on using first principles Density Functional Theory (DFT) simulations and spectroscopic methods to investigate the well-studied prototypical MAPbI_3 . DFT simulations provided an indication that charge carriers in MAPbI_3 exists as localized polarons, thus, the experimental studies seek spectroscopic evidence for the existence for these self-trapped polaronic states. Through a

combination of steady state photoinduced absorption, transient absorption and transient photocurrent measurements, this chapter has confirmed the existence of theoretically predicted polaronic states in MAPbI₃ which finds its origins in the ‘soft’ lead – iodide bond.

Chapter 5 primarily revolves around the 2-dimensional (2D) layered <110> cut of perovskite where this class of hybrid perovskites are known for several remarkable properties, such as white light emission or sometimes also called broadband emission. This work starts off re-examining a previously studied N-(3-aminopropyl)imidazole lead bromide (APIPbBr₄), which was reported to exist in the 2-dimensional layered <110> cut of perovskite. However, detailed X-ray Diffraction (XRD) structural analysis of the obtained compound was shown to exist as a polymorphic API₂Pb₃Br₁₀, which shows no resemblance to the <110> cut of perovskite. Hence, another compound, 2-(1H-Imidazol-1-yl)ethan ammonium lead bromide (IEAPbBr₄) was synthesized and was shown to exist in the <110> cut of perovskite. Detailed cation dynamics of API and IEA was further studied through Solid State Nuclear Magnetic Resonance (SSNMR) and it was shown to be considerably different. Given the huge difference between the API₂Pb₃Br₁₀ and IEAPbBr₄, it is therefore unsurprising that the bulk measured photophysical properties and characteristic are also different.

Chapter 6 then ensued to study the significance of the perovskite A-site cation through using an imidazolium cation. It was shown to crystallize into three different polymorphs, IMIPbBr₃, IMI₂PbBr₄ and IMI₃PbBr₅ (IMI = imidazolium), by varying the ratio of imidazole to lead concentrations through the precursors. The structures were thoroughly characterized by XRD and the cation dynamics probed through SSNMR. One of the polymorphs, IMIPbBr₃, undergoes an unusual phase transition while the remaining two do not show any phase transition. Remarkably, all three polymorphs show distinct cationic dynamics, even though IMI₂PbBr₄ and IMI₃PbBr₅ are structurally very similar. Furthermore, photophysical measurements of each polymorph showed different characteristics which indicates the significance of cationic disorder in determining the bulk properties of HOIP.

Lay Summary

Hybrid Organic Inorganic Perovskites (HOIPs) are a new branch of exciting materials which contain an organic molecule, and several other inorganic elements, typically consisting of lead or tin cations and halide anions. The inorganic elements form the framework, with the organic molecule sitting in the empty spaces of the framework. By analogy with the relationship of a cage and a ball, the inorganic framework acts as the cage while the organic molecule is like a rattling ball inside the cage. The prototypical methylammonium lead iodide is a very strong contender as the active material for the next generation of solar cells. This material has seen a very rapid growth rate in its efficiency values and has recently attained above 25% energy conversion efficiency after less than 5 years of active research; an achievement which has taken silicon based solar cells more than two decades to achieve. However, much of the underlying reasons behind the various unusual properties which makes the material such a good candidate for photovoltaic applications remain a mystery. As such, this thesis utilizes several techniques to study these HOIPs in greater depth. The main objective would be to establish the correlation between the structure of HOIP and some of the remarkable properties observed.

In this thesis, strong evidence is presented to show that the charge carriers exist as a ‘polaron’. A polaron can be imagined as a ball sitting in the mattress, and when the ball is at rest, it would sit in its localized bump. Similarly, that charge carrier would interact with the local environment to form such a localized ‘low energy’ state. When the mattress is tilted in a direction, the ball starts to roll very slowly as compared to a ball rolling on a hard surface with the same degree of tilt. If the contributions from the localized environmental are not recognized, then judging by the speed of the rolling ball and assuming that the surface is a hard surface, it would be inevitable to reach an erroneous interpretation that the ball is massive. This thesis first utilizes theoretical predictions, which are then validated through experimental results to show that the charge transport carriers indeed exists as a ‘polaron’. An accurate understanding of the material’s charge transport property would further help the optimization of the material and hopefully, better device efficiencies.

Branching out from this class of hybrid perovskite, the structural flexibility of the hybrid perovskite is also demonstrated in this work. Again, using the analogy of a ball in a cage, one can also choose to use a ball with a small tail protruding from it, like a lollipop. This way, the tail would protrude out from cage while the spherical part would still be enclosed within the cage. Consequently, the cages would not be able to stack nicely above and below current cage due to the protruding tail and would only be able to form a continuous layer of cages instead. In the same way, by changing the organic cations, the same inorganic framework would also be obtained, thus forming layers of inorganic framework. These structures are therefore also called 2 – Dimensional (2D) layered hybrid perovskite structures. By the same logic, when using an appropriate organic cation, it is also possible to obtain a continuous 1 – Dimensional chain of hybrid perovskite. An earlier reported 2D layered hybrid perovskite compound is revisited in this work and is found to take on a different structure. This phenomenon is known as polymorphism. Studies were also extended to the 1D perovskite and it was shown that the organic cations are highly dynamic and moving around in the crystal. From several structures studied in this work, a trend was observed and the microscopic differences are then established to influence different macroscopic observed properties, such as the optical properties.

Acknowledgements

First and foremost, I would like to extend my thanks to my supervisors, A/Prof Andrew, A/P Cesare and Prof John, who have given me the opportunity and freedom to pursue the direction which I wanted to for my PhD with a chemist's perspective of things.

A big shoutout to the OSON Group and CDPT staff like Dr X. Y. Chin and Dr K. Harish who have been great mentors guiding me through the world of optical spectroscopy, and in general through the start of my PhD. Without their help I would probably had been a hazard in the lab.

I am grateful to the Warwick NMR group for being so hospitable to me and my 1 year stay at Warwick University. Lunch was always exciting with you guys, Adam, Ben, Sam, Nicole, Sarah, Trent, Angelo. Special mention to the cake king, Ben! Even though my time there was cut short because of COVID and I had to leave in such a rush, it was nevertheless a memorable time.

Special thanks to the XRD crew at NTU MSE FACTS lab, Dr Weiling, Dr Pio and Dr Teddy who have provided inputs towards the direction of my research and all the bragging sessions we shared together. A special thank you to Dr Sam Morris, who has been a wonderful mentor and for introducing me to the wonderful world of crystallography, and to the British Crystallographic Association. Without whom, I would not have even done crystallography, let alone participate in the 17th BCA/CCG Intensive Teaching School in X-Ray Structure Analysis at the Trevelyan College, Durham University, UK.

Last, but not least, I would like to thank my family, especially to my lovely wife, Carine, for supporting me throughout the trying years this journey has brought.

“I found my ~~face~~ phase!” – Walter's punchline at 17th BCA/CCG presentation night, referencing to the phase problem in X-ray crystallography.

Table of Contents

Abstract	i
Lay Summary	iii
Acknowledgements	v
Table of Contents	vii
Table Captions	xiii
Figure Captions	xv
Abbreviations	xxv
Chapter 1 Introduction.....	1
1.1 Background and Motivation	2
1.2 Problem Statement.....	4
1.3 Objective and Scope	4
1.4 Dissertation Overview	5
1.5 Findings and Outcomes.....	7
References.....	8
Chapter 2 Literature Review	11
2.1 Introduction.....	12
2.2 3-Dimensional Hybrid Organic-Inorganic Perovskites	14
2.3 Structural characterization and cation dynamics of 3D hybrid perovskite	17
2.4 Lower dimensional perovskites: layered 2-Dimensional perovskites	20

2.5	Lower dimensional perovskites: 1D and other novel perovskite-like structures .	29
	References.....	32
Chapter 3	Experimental Methodology	53
3.1	Synthesis	54
3.1.1	Crystallization from hydrohalic acid	54
3.1.2	Preparation of thin films	55
3.2	Materials Characterization	56
3.2.1	X-ray Diffraction: Single Crystal Diffraction (scXRD)	56
3.2.1.1	The Phase Problem.....	58
3.2.1.2	Twinning	60
3.2.1.3	Least Squares Refinement	62
3.2.1.4	Reporting and Validation	64
3.2.1.5	Software and Hardware utilized	64
3.2.2	Powder X-ray diffraction (pXRD)	64
3.2.2.1	Bragg-Brentatano and Transmission geometry	65
3.2.2.2	Rietveld Refinement.....	66
3.3	Nuclear Magnetic Resonance (NMR).....	68
3.3.1	Solid State Nuclear Magnetic Resonance (SSNMR).....	68
3.3.2	Solution Nuclear Magnetic Resonance.....	73
3.3.4	1D NMR pulse sequences: One pulse, CPMAS, Hahn Echo, Saturation Recovery, $T_{1\rho}$	74
3.3.5	2D Pulse Sequences	76
3.3.5.1	2D Homonuclear experiment: NOESY and BABA	77
3.3.5.2	2D HETCOR: hCH and FSLG	78

3.4	Optoelectronic Characterization	79
3.4.1	Fundamentals of Fourier Transform Infrared (FTIR) Spectroscopy ...	79
3.4.2	Ultrafast spectroscopy: Transient absorption	82
3.4.3	Linear Absorption and Photoluminescence	84
3.4.4	Basic Concepts of Photoconductivity	87
	References.....	91
Chapter 4	Large polaron self-trapped states in 3D MAPbI₃	95
4.1	Introduction.....	96
4.2	Experimental Methods	97
4.2.1	Computational methods: polaronic and free carrier mobility	97
4.2.2	Fourier Transform Infrared Spectroscopy and Continuous-Wave Photoinduced Absorption Spectroscopy	100
4.2.3	Ultrafast Transient Absorption Spectroscopy	100
4.2.4	Transient and Steady State Photocurrent Spectroscopy.....	101
4.3	Results.....	102
4.3.1	Computational Results	102
4.3.2	Comparison of DFT results against steady-state UV-Vis and photocurrent	105
4.3.3	Continuous Wave Photoinduced Absorption Spectroscopy	106
4.3.4	Transient dynamics	111
4.4	Conclusions.....	115
	References.....	116
Chapter 5	Localized effects in polymorphic <110> oriented 2-D layered perovskites	125
5.1	Introduction.....	126
5.2	Experimental Methods	128

5.2.1	X-ray diffraction	128
5.2.2	Nuclear Magnetic Resonance.....	129
5.2.3	Calorimetric characterization.....	129
5.2.4	Steady-state absorption and photoluminescence	130
5.2.5	Theoretical analysis using Density Functional Theory.....	130
5.3	Results and Discussion	131
5.3.1	X-ray Structural characterization.....	131
5.3.2	NMR characterization.....	137
5.3.3	Analysis of API cation across the phase transition by XRD and NMR	144
5.3.4	Band structure predicted by Density Functional Theory and validated experimentally through steady-state absorption and photoluminescence	148
5.4	Conclusion	153
	References.....	154
 Chapter 6 Imidazolium lead bromide polymorphs: from 3D polytype to 1D perovskite..... 161		
6.1	Introduction.....	162
6.2	Experimental Methods	162
5.2.1	X-ray Structural characterization.....	162
5.2.2	NMR characterization	163
5.2.3	Calorimetric characterization.....	163
5.2.4	Steady-state absorption and photoluminescence	163
5.2.5	Theoretical analysis through Density Functional Theory.....	164
6.3	Results and Discussion	164
6.3.1	New proposed notation for haloplumbate structures or ‘perovskitoids’	164

6.3.2	X-ray Sturctural Characterization of imidazolium lead bromide.....	169
6.3.3	Nuclear Magnetic Resonance Characterization	178
6.3.4	Band structure predicted by Density Functional Theory and validated experimentally through steady-state absorption and photoluminescence	187
6.4	Conclusions.....	193
	References.....	194
Chapter 7	Conclusions and Recommendations	197
7.1	Summary of Thesis	198
7.2	Contributions and Implications.....	198
7.3	Future work and direction.....	199
	References.....	201
	Appendix.....	205

Table Captions

Table 3.1 definition of the various parameters utilized in single crystal XRD

Table 3.2 definition of the various parameters utilized in pRXD refinements

Table 3.3 definition of the various parameters utilized in Rietveld refinements

Table 4.1. The parameters for calculating free carrier mobility. Band (m_b^*), conductivity (m_l^*) and density of state (m^*) effective mass, hole/electron-phonon coupling (Ξ), bulk modulus (B), and free hole/electron mobility (μ_{carrier}) for tetragonal and orthorhombic phase MAPbI₃.

Table 4.2. The parameters for calculating polaron mobility. Optical and static dielectric constants (ϵ_∞ and ϵ_s), angular frequencies of a characteristic LO phonon mode (ω), average hole/electron effective masses of bare electron bands (m^*), electron-phonon coupling constant (α), phono occupation factor (β), positive/negative polaron mass (m_{polaron}^*) and positive/negative polaron mobility (μ_{polaron}) for tetragonal- and orthorhombic-phase MAPbI₃.

Table 4.3. Calculated effective mass ($m^*, \times m_0$) and mobility ($\text{cm}^2/\text{V}\cdot\text{s}$, average of different crystallographic directions) of free charges and polarons in tetragonal and orthorhombic phase MAPbI₃ (spin-orbit coupling effects included)

Table 5.1 Selected parameters to the solution and refinement of scXRD results

Table 5.2 Distortion parameter in corrugated $\langle 110 \rangle$ oriented 2D layered perovskites

Table 5.2 Distortion parameter in corrugated $\langle 110 \rangle$ oriented 2D layered perovskites

Table 5.3 ^1H chemical shifts of API₂Pb₃Br₁₀, APIPbBr₄ and IEAPbBr₄ as determined experimentally and predicted through DFT simulation

Table 5.4 ^{13}C chemical shifts of $\text{API}_2\text{Pb}_3\text{Br}_{10}$, APIPbBr_4 and IEAPbBr_4 as determined experimentally and predicted through DFT simulations

Table 5.5 T_1 and $T_{1\rho}$ of $\text{API}_2\text{Pb}_3\text{Br}_{10}$ and IEAPbBr_4 at different magnetic field strength

Table 5.6 Band gaps obtained from DFT simulations. The inclusion of SOC effects gives a better estimate of the band gap. Corner shared octahedra, as in APIPbBr_4 and IEAPbBr_4 , shows a consistently smaller band gap than the face and edge shared $\text{API}_2\text{Pb}_3\text{Br}_{10}$ perovskitoid.

Table 5.7 Table of key optical properties extracted from photoluminescence results

Table 6.1: Selected parameters to the solution and refinement of scXRD results

Table 6.2 Table showing experimental and theoretically predicted values of the ^1H and ^{13}C chemical shifts based on XRD results, the relative intensities of each ^1H peak and the $T_{1\rho}$ results of each identity peak. Since ^{13}C CPMAS is carried out, the ^{13}C spectra do not provide any quantitation. The experimental deconvolution for ^1H is seen in Figure 6.6.

Table 6.3 Comparison of variable field T_1 for IMIPbBr_3 , $\text{IMI}_2\text{PbBr}_4$ and $\text{IMI}_3\text{PbBr}_5$. The decreasing T_1 with decreasing magnetic field follows a well-established trend observed by Bloembergen et al.

Table 6.4 Band gaps of the three phases of IMIPbBr_3 , $\text{IMI}_2\text{PbBr}_4$ and $\text{IMI}_3\text{PbBr}_5$ obtained from DFT simulations. The inclusion of SOC effects gives a better estimate of the band gap.

Table 6.5 Table of key optical properties extracted from photoluminescence results

Figure Captions

Figure 2.1 Chart detailing the growth of solar cell efficiencies. [Taken from NREL, 2020]

Figure 2.2 Illustration showing the Goldschmidt tolerance factor of the various hybrid perovskite that are well studied in the literature¹

Figure 2.3 the plot of T_1 relaxation time against the correlation time of the process. The molecular correlation time is the time the average molecule completes one radian of rotation. In the very short correlation time, it is suitable for small molecules. At the moderate to long correlation time regime, it is suitable for large molecules like polymers or proteins, or to the extreme limit of solids.²

Figure 2.4 Schematic comparison of (a) Ruddlesden – Popper (RP), (b) Dion – Jacobson (DJ) in oxide perovskite against layered hybrid perovskites, and (c) the new alternating cation (ACI) structure unique to hybrid perovskite system. Notably, in RP perovskites, there is an offset of ($\frac{1}{2}$, $\frac{1}{2}$), while in DJ and ACI, there is no offset of the layers^{3, 4} (d) Oxide perovskite specific Aurivillius phase, with $n = 3$, $\text{Bi}_4\text{Ti}_3\text{O}_{12}$ and $\text{Bi}_2\text{Sr}_2\text{NbMnO}_{12-8}$. In Aurivillius phase, the spacer group is strictly Bi_2O_2 .⁵

Figure 2.5 One scheme of reduced dimensional perovskite in the form of nanostructured (a) $\text{MAPbBr}_3 - (\text{OA})_2\text{PbBr}_4$ core-shell structure to exploit absorption upconversion effects⁶ (b) CsPbBr_3 in nanocube structure in LED device⁷ (c) MAPbI_3 in nanowires for lasing applications and (d) colloidal MAPbBr_3 nanocrystal in LED devices⁸

Figure 2.6 (a) schematic diagram showing the relation between 3D perovskites ($n = \infty$) and the $\langle 100 \rangle$ oriented 2D halide layers are indicated by n^9 (b) $\langle 100 \rangle$ oriented layered hybrid perovskites $(\text{BA})_2\text{PbBr}_4$ ¹⁰ (c) schematic showing the layered $\langle 110 \rangle$ oriented perovskite (d) $\langle 110 \rangle$ oriented hybrid perovskite APIPbBr_4 ¹¹ (e) schematic showing the layered $\langle 111 \rangle$ oriented perovskite structure (f) $\langle 111 \rangle$ oriented metal

halide perovskite $\text{Cs}_4\text{CuSb}_2\text{Cl}_{12}$ perovskite¹²

Figure 2.7 (a) photoluminescence of 2 -, 3 -, 4 - MOP at room temperature (b) octahdra tilting of 2 -, 3 -, 4 - MOP samples measured through the dihedral angles¹³ (c) absorption and emission spectra of $(\text{BA})_2\text{PbI}_4$ and $(\text{EDBE})\text{PbI}_4$ ¹⁴ (d) structural distortion of $(\text{BA})_2\text{PbBr}_4$ and $(\text{HIS})\text{PbBr}_4$ and the corresponding variable temperature photoluminescence emission profile¹⁵

Figure 2.8 Various reported 1D and novel type perovskite or perovskitoid structures (a) one dimensional lead halide perovskite $(\text{DMEDA})\text{PbBr}_4$ ¹⁶ (b) 1D bromoplumbate 1-(Ethyl)pyridin-1-ium lead bromide¹⁷ (c) one dimensional zigzag edge-sharing perovskite $(\text{AMP})\text{PbBr}_4$ ¹⁸ (d) one dimensional ImPbI_3 ¹⁹ and (e) one dimensional nanotube $(\text{HMTA})_3\text{Pb}_2\text{Br}_7$ ²⁰. [DMEDA = N,N'-dimethylethylenediamine, AMP = 4-(aminomethyl)pyridinium, Im = imidazolium, HMTA = hexamethylenetetramine]

Figure 2.9 Reported photoluminescence spectra of (a) $(\text{DMEDA})\text{PbBr}_4$ ¹⁶ (b) $(\text{AMP})\text{PbBr}_4$ ¹⁸ (c) ImPbI_3 ¹⁹ and (d) $(\text{HMTA})_3\text{Pb}_2\text{Br}_7$ ²⁰. All the variants of 1D perovskite exhibits varying degree of broadband emission.

Figure 3.1 schematic showing the principles behind XRD, and Bragg's law

Figure 3.2 a schematic of the general flow of work for single crystal XRD studies

Figure 3.3 schematic of a diffractometer in the Bragg-Brentano geometry

Figure 3.4 schematic of a diffractometer in the transmission geometry

Figure 3.5 schematic of energy level. Energy splitting increases with increasing B_0

Figure 3.6 schematic of magnetization vectors (a) at equilibrium when placed in a magnetic field B_0 , (b) when the system is perturbed by the application of B_1 , the magnetization vector is rotated onto the x-y plane, which can then be detected.

Figure 3.7 (a) peak splitting due to spin-spin coupling in 1,1,2-trichloroethane. H_{a1}

and H_{a2} are chemically equivalent hydrogen and does not split each other. H_b would be split into a triplet due to the presence of two H_a . (b) H_a in ethyl acetate is not affected by coupling more than three bonds away, and hence is a singlet. H_b and H_c , are triplets and quartets respectively.

Figure 3.8 (a) schematic of the pulse sequence in a one pulse and (b) saturation recovery experiment to measure the T_1

Figure 3.9 (a) schematic of the pulse sequence in $T_{1\rho}$ measurements. (b) illustration showing the various regimes of motion which correlates to the various relaxation mechanisms and the type of experiments²¹

Figure 3.10 (a) schematic of the pulse sequence in CPMAS and (b) a spin echo experiment

Figure 3.11 (a) schematic of the pulse sequence in a 2D NOESY (b) 2D BABA experiment

Figure 3.12 (a) schematic of the pulse sequence in a 2D hCH HETCOR and (b) 2D FSLG HETCOR experiment

Figure 3.13 schematic of a Michelson interferometer, which is the basis of an FTIR. R1 and R2 are collimating mirrors and M1 and M2 are flat mirrors.

Figure 3.14 schematic of the Bruker V80v FTIR, with laser add-on for cw-PIA measurement

Figure 3.15 schematic of band diagram and the formation of absorption band due to photoexcitation

Figure 3.16 schematic of the experimental setup for ultrafast transient absorption spectroscopy

Figure 3.17 schematic of the band diagram from a nearly-free electron model. The

photoexcitation would create electron-hole pairs which relaxes to the bottom of the conduction band and top of the valence band. There, it can recombine radiatively to emit a photon, which is observed as photoluminescence.

Figure 3.18 schematic of the various quantities which determines the photoconductivity process in based on Drude model. I_0 is the illumination intensity, F is the applied electric field, J is the current density and v_d is the charge carrier drift velocity.

Figure 3.18 schematic of the various quantities which determines the photoconductivity process in based on Drude model. I_0 is the illumination intensity, F is the applied electric field, J is the current density and v_d is the charge carrier drift velocity.

Figure 3.19 schematic of the transient photocurrent setup. The photoelectrons are generated with an optical excitation source of 400 nm pulsed laser with a beam diameter of 0.2mm, and is collected by applying a bias across the gold channel and recorded with an 100 GHz oscilloscope

Figure 4.1. Electronic and optical properties of MAPbI₃. (a, b) calculated electronic band structures, (c, d) real part (in red) and imaginary part (in blue) of dielectric function, and (e, f) far-infrared vibrational modes and intensity for tetragonal-phase (up) and orthorhombic-phase (down) MAPbI₃.

Figure 4.2. Far-infrared optical response of MAPbI₃. Calculated real part (in red), imaginary part (in blue) of dielectric function, and imaginary part of the inverse dielectric function (in black) for (a) tetragonal-phase and (b) orthorhombic-phase MAPbI₃.

Figure 4.3 (a) Experimental steady state absorption and (b) steady state photocurrent results showing good agreement with the ab initio band structure without SOC effects, (Fig 4.1a, pink line). Schematic of (c) positive and (d) negative polaron charge density from DFT simulations

Figure 4.4 (a) Full PIA spectra at 78 K showing key photoabsorption feature and are sub divided into regions I, II, IV and III (b) full PIA spectrum at 298 K showing the concurrent disappearance of these key photoabsorption features (c) schematic energy level diagram of the photoexcited states. P0 would correspond to the trap states, P₁ and P₂ corresponding to a high-low energy photoabsorption pair, which is a signature of polarons. P_n is assigned to the higher-level energy transitions of the photoinduced states.

Figure 4.5 Experimental and simulated infrared active vibrational (IRAV) and Raman modes. (a) PIA spectrum ($T = 78$ K) fitted to two Gaussian peaks centred at 1650 cm^{-1} and 516 cm^{-1} (red dashed lines), (b) FTIR spectrum ($T = 78$ K), and (c) Raman spectrum ($\lambda_{\text{exc}} = 1024\text{ nm}$, $T = 300$ K), where green asterisks denote peaks from the CaF_2 substrate. (d) Simulated photoinduced absorption modes are obtained as $-(\Delta T/T) = -(\text{IR}_{\text{neut}} - \text{IR}_{\text{exc}})/\text{IR}_{\text{neut}}$, where IR_{exc} and IR_{neut} are the IR mode intensities of excited and ground states, respectively. (e, f) Calculated IR and Raman mode intensity spectra of orthorhombic MAPbI_3 . The main vibrational modes are indicated by black vertical lines, showing the correspondence between IRAV modes and Raman modes, which become IR-active under photoexcitation.

Figure 4.6 The Infrared active modulation (IRAM) of C – H and N – H stretching mode. (a) the FTIR absorbance spectrum of MAPbI_3 , $f(\bar{\nu})$, (b) the fitted results (red line) against experimental results (black open circles) with only the 0th order derivative, $f(\bar{\nu}) = -0.0015 f(\bar{\nu})$, (c) only the 1st order derivative, $f(\bar{\nu}) = -0.02 f'(\bar{\nu})$, (d) only the 2nd order derivative, $f(\bar{\nu}) = 0.11 f''(\bar{\nu})$ (d) best fit of this region with a combination of 1st and 2nd order derivative $f(\bar{\nu}) = -0.0075 f'(\bar{\nu}) + 0.1 f''(\bar{\nu})$. (e) the representative IR vibrational frequencies and displacement vectors obtained from phonon calculations, and corresponding blue-shift of IR-active-mode frequencies in the charged state.

Figure 4.7 (a) Steady state PIA compared against (b) transient PA. (c) ultrafast transient absorption map of MAPbI_3 (d) shows the slice at 1.64 eV, which is the band gap and subsequent global fitting shows three distinct lifetimes. Detailed discussion are in the text. (e) transient photocurrent and insert shows the linear dependence of peak photocurrent against the applied bias. Note the change in timescale from linear to

logarithmic in (d) and (e) marked by breaks.

Figure 5.1 (a) $\text{API}_2\text{Pb}_3\text{Br}_{10}$ in the high temperature $I2$ phase, (b) $\text{API}_2\text{Pb}_3\text{Br}_{10}$ in the low temperature $P\bar{1}$ phase (standard unit cell), (c) an overlay of the high (in pink) and low temperature (in grey) viewed down the b-axis and (d) down the a-axis of the monoclinic cell. (e) API cation in the low temperature $P\bar{1}$ phase and (f) high temperature $I2$ phase. (g) projection of IEAPbBr_4 which is in a $\langle 110 \rangle$ oriented 2D layered perovskite structure.

Figure 5.2 Powder XRD Rietveld refinement of (a) $\text{API}_2\text{Pb}_3\text{Br}_{10}$ in the room temperature $I2$ phase, and (b) $\text{API}_2\text{Pb}_3\text{Br}_{10}$ in the low temperature $P\bar{1}$ phase. (c) The plot of R_{wp} and unit cell volume of the $I2$ phase. A dip in R_{wp} can be observed at 273 K and 290 K. This is attributed to the phase transition where both $I2$ and $P\bar{1}$ phases are observed to be in considerable amounts of each other. (d) Rietveld refinement of IEAPbBr_4 with an X-ray radiation of 0.825°\AA .

Figure 5.3 ^1H (left) and ^{13}C (right) SSNMR spectra of (a) $\text{API}_2\text{Pb}_3\text{Br}_{10}$ in the high temperature $I2$ phase, (b) $\text{API}_2\text{Pb}_3\text{Br}_{10}$ in the low temperature $P\bar{1}$ phase (c) IEAPbBr_4 assigned to the individual atoms.

Figure 5.4 Variable temperature sweep of $\text{API}_2\text{Pb}_3\text{Br}_{10}$ and ^1H , ^{13}C and ^{207}Pb showing a clear correlation with XRD results. ^1H T_1 shows three distinct regions, below 20°C , the intermediate $20^\circ\text{C} - 40^\circ\text{C}$, and after 45°C . Phase transition confirmed through XRD, NMR and calorimetric methods.

Figure 5.5 2D NMR spectra of $\text{API}_2\text{Pb}_3\text{Br}_{10}$ in the low (left) and high temperature (right) phase. (a,b) homonuclear NOESY (c, d) BABA and (e, f) heteronuclear hCH experiment

Figure 5.6 ORTEP diagram of the 1-(3-aminopropyl)imidazolium (API) cation in the low temperature ($P\bar{1}$) phase viewed (a) down the imidazolium plane, (b) almost parallel to the imidazolium plane, and high temperature $I2$ phase viewed (c) down the imidazolium plane, (d) almost parallel to the imidazolium plane. The orange and blue

arrows show the two correlation, which was observed in the $^1\text{H} - ^1\text{H}$ BABA homonuclear NMR correlation experiment at the low temperature phase but absent in the high temperature phase.

Figure 5.7 2D NMR spectra of IEAPbBr₄ in the low (left) and high temperature (right) phase. (a) homonuclear NOESY with contact time 10 ms, (b) NOESY with contact time 200 ms (c) homonuclear BABA and (d) heteronuclear hCH experiment.

Figure 5.8 The density of states (left) and joint density of states (right) of API₂Pb₃Br₁₀, APIPbBr₄, and IEAPbBr₄ as calculated by Density Functional Theory (DFT) using the Perdew–Burke–Ernzerhof (PBE) with Spin Orbit Coupling (SOC) functional.

Figure 5.9 Absorption and photoluminescence results. Asterisk marks the spectral artefact arising from the second order effects arising from the monochromator while using the source radiation (290 nm), which has not filtered out by long pass filter (Schott 320).

Figure 6.1 Crystal structure of (a) API₂Pb₃Br₁₀ which can be seen to be in the 1-3EFF configuration, (b) IMI₂PbBr₄ which can be seen to be in the 2EE-1(CC) configuration, (c) catena-(2-methylimidazo[1,5-a]pyridin-2-ium tris(μ -bromo)-lead²² which can be seen to be in the 1-2FF configuration, (d) IMI₃PbBr₅ which can be seen to be in the 1-1C configuration, (e-f) the configuration of 1D tubular structure of (HMTA)PbBr₄²⁰. In this case the notation breaks down into an awkward form and this proposed notation should not be used.

Figure 6.2 Crystal structure of the three imidazole lead bromide polymorphs, (a) IMIPbBr₃ in the room temperature *Cmcm* phase (b) IMI₂PbBr₄ in $\bar{1}$, and (c) IMI₃PbBr₅ in $P\bar{1}$

Figure 6.3 Rietveld refinements of the samples (a) IMIPbBr₃ fitted to the *Cmcm* space group, (b) IMIPbBr₃ fitted to the *P6₃/mmc* space group. The difference in the R_{wp} and overall fitting, particularly between 13° and 20° showed that IMIPbBr₃ would take

on the orthorhombic *Cmcm* space group. The presence of contaminant IMIPbBr₄ phase is shown in the green curve (c) Rietveld refinement of 98% IMI₂PbBr₄ with 2% of IMIPbBr₃ contaminant, and (d) Rietveld refinement of the bulk synthesized IMI₃PbBr₅. Refinement results showed the bulk sample consist of approximately 0.2% of IMIPbBr₃, 37% IMI₂PbBr₄, and 63% IMI₃PbBr₅.

Figure 6.4 Comparison of IMIPbBr₃ phases, with the organic imidazole cation hidden for clarity. (a) shows the intermediate *P2₁2₁2₁* superstructure through the doubling of the c-axis. A slight modulation of the octahedra connectivity can be seen, as highlighted by the red and green dotted circles. Such behaviour is neither seen in (b) the higher temperature *Cmcm* phase nor in (c) the lower temperature *Pnma* phase. Note the change in axis orientation to match crystallographic convention.

Figure 6.5 Simulated precession image of IMIPbBr₃ in the *P2₁2₁2₁* phase showing (a) reflections from *0kl*. Weak satellite peaks can be observed in several (*0 2 l*) planes (b) reflections of *hk0* showing no satellite peaks (c) reflections on the *h0l* showing a threefold twinning and satellite peak on several reflection such as (*2 0 12*) (d) projection of the superstructure IMIPbBr₃ down the a-axis.

Figure 6.6 (a) powder XRD pattern of IMIPbBr₃ from 300 K to 100 K, in steps of 10 K for clarity. The pattern shows a clear transition at around 220 K. (b) powder XRD pattern from 100 K to 300 K, in steps of 10 K for clarity, but the diffractogram shows that IMIPbBr₃ does not undergo any phase transition (c) the theoretical XRD pattern of the various phases of IMIPbBr₃ as predicted from the single crystal XRD results. The inclusion of the contaminant IMI₂PbBr₄ shows the presence of a peak at 7.18° and is observed in the experimental XRD plots (d) the plot of refinement *R_{wp}* against temperature showing the stability of the sequential refinements. The plot of IMIPbBr₃ *P2₁2₁2₁* unit cell volume against temperature with increasing temperature shows that logical validity of the refinement (e) differential scanning calorimetric study of IMIPbBr₃, showing a first phase transition between 236 K and 244 K and a second phase transition between 193 K and 225 K (f) Group subgroup relation, from *Cmcm* to *P2₁2₁2₁* with index 4. Since *P2₁2₁2₁* is a superstructure, it would have twice as large a *Z* value than the *Cmcm* phase. *D_{2h}*(mmm) would have order 8 while *D₂*(222) would have order 4.

Figure 6.7 Multinuclear Solid State Nuclear Magnetic Resonance (SSNMR) studies of (a) IMIPbBr₃ (b) IMI₂PbBr₄ and (c) IMI₃PbBr₅, where ¹H spectra is shown on the left and ¹³C spectra on the right. In the ¹H spectra, the experimental spectra are fitted to the deconvolution of peaks, and the details are shown in Table 6.2. In the ¹³C spectra, the insert shows the zoomed in section of each peak, which is split for IMIPbBr₃ and IMI₂PbBr₄. The ²⁰⁷Pb Hahn Echo spectra are seen for (d) IMIPbBr₃, (e) IMI₂PbBr₄ and (f) IMI₃PbBr₅. ¹H and ¹³C are referenced to alanine and ²⁰⁷Pb referenced to PbNO₃.

Figure 6.8 2D NMR correlation of IMIPbBr₃ (a) ¹H-¹H homonuclear NOESY, with a relatively short contact time of 500 ms, (b) NOESY with a relatively long contact time of 2000 ms. The NOESY results provide evidence for the presence of two peaks, ¹H-7 and ¹H-8, between 11 ppm and 12 ppm, while the peak, ¹H-3, is a split peak. (c) ¹H-¹H BABA homonuclear correlation boosts the confidence in peak assignment (d) The heteronuclear FSLG correlation shows a clear correlation for ¹H-1,2 with ¹³C-1,2 and ¹H-3 with ¹³C-3 and provides further evidence to support the assignments.

Figure 6.9 2D NMR correlation of IMI₂PbBr₄ (a) ¹H-¹H homonuclear NOESY, with a relatively short contact time of 100 ms, (b) NOESY with a relatively long contact time of 500 ms. The NOESY results provide evidence for the presence of two peaks, ¹H-7 and ¹H-8, between 11 ppm and 12 ppm, while the peak, ¹H-3, is a split peak. (c) ¹H-¹H BABA homonuclear correlation boosts the confidence in peak assignment (d) The heteronuclear FSLG correlation shows a clear correlation for ¹H-1 with ¹³C-1, ¹H-2 with ¹³C-2 and ¹H-3 with ¹³C-3. The correlation for ¹H-7 with ¹³C-3 and ¹H-8 with ¹³C-3 is not unexpected because of the close proximity of the atoms.

Figure 6.10 2D NMR correlation of a 63% IMI₃PbBr₅ – 37% IMI₂PbBr₄ mixture (a) ¹H-¹H homonuclear NOESY, with a relatively short contact time of 100 ms, (b) NOESY with a relatively long contact time of 500 ms. (c) ¹H-¹H BABA homonuclear correlation boosts the confidence in peak assignment (d) The heteronuclear FSLG correlation shows a clear correlation for ¹H-1 with ¹³C-1, ¹H-2 with ¹³C-2 and ¹H-3 with ¹³C-3. The correlation for ¹H-7 with ¹³C-3 and ¹H-8 with ¹³C-3 is not unexpected because of the proximity of the atoms.

Figure 6.11 ^1H and ^{13}C spectra compared against variable field strength. Since both ^1H and ^{13}C peaks become narrower with increasing field strength, CSA is the dominant process in the NMR spectra.

Figure 6.12 The density of states (left) and joint density of states (right) of the three phases of IMIPbBr_3 , $\text{IMI}_2\text{PbBr}_4$ and $\text{IMI}_3\text{PbBr}_5$ as calculated by Density Functional Theory (DFT) using the Perdew–Burke–Ernzerhof (PBE) with Spin Orbit Coupling (SOC) functional.

Figure 6.13 Steady state absorption of (a) IMIPbBr_3 , (c) $\text{IMI}_2\text{PbBr}_4$, and (d) a physical mixture of 63% $\text{IMI}_3\text{PbBr}_5$ – 37% $\text{IMI}_2\text{PbBr}_4$ and photoluminescence of (b) IMIPbBr_3 , (d) $\text{IMI}_2\text{PbBr}_4$, and (f) a physical mixture of 63% $\text{IMI}_3\text{PbBr}_5$ – 37% $\text{IMI}_2\text{PbBr}_4$. The insert on the absorption plot (a, c, d) shows the extracted band gap values taken from the Tauc plot of the absorption spectra at different temperatures. Due to experimental limitations in photoluminescence measurement, the peak at 290 nm arising from the second order effects of the monochromator cannot be completely filtered and is marked with an asterisk.

Abbreviations

API	N-(3-aminopropyl)imidazolium cation
BA	butylammonium cation
CIF	Crystallographic Information File
cw-PIA	continuous wave photoinduced absorption
DFT	Density Functional Theory
DMF	N-N-Dimethylformamide
DMSO	Dimethyl sulfoxide
EQE	External Quantum Efficiency
FID	Free Induction Decay
FTIR	Fourier Transform Infrared Spectroscopy
GoF	Goodness of Fit
HOIP	Hybrid Organic-Inorganic Perovskite
HOMO	Highest Occupied Molecular Orbital
I	Nuclear Spin
IEA	2-(1H-Imidazol-1-yl)ethan ammonium cation
IPA	Isopropyl Alcohol
IUCr	International Union of Crystallography
LED	Light Emitting Diode
LUMO	Lowest Unoccupied Molecular Orbital
MAPI	Methylammonium Lead Iodide
MAS	Magic Angle Spinning
n	Number of perovskite layers
NOE	Nuclear Overhauser Effect
NQR	Nuclear Quadrupole Resonance
OLED	Organic Light Emitting Diodes
ORTEP	Oak Ridge Thermal Ellipsoid Plot
PEA	phenylethylammonium cation
PIA	Photoinduced Adsorption
PL	Photoluminescence
pXRD	Powder X-ray Diffraction

R_{obs}	R-factor
SCLC	Space Charge Limited Current
scXRD	Single Crystal X-ray Diffraction
SSNMR	Solid State Nuclear Magnetic Resonance
STE	Self-trapped exciton
T_1	Spin-lattice relaxation time
$T_{1\rho}$	Spin-lattice relaxation time in the rotating frame
TA	Transient Adsorption
TPC	Transient Photocurrent
wR	Generalized R factor
XRD	X-ray Diffraction

Chapter 1

Introduction

A brief history and overview of the field of hybrid organic-inorganic hybrid perovskites is presented. The aim of this project is to study the correlation between the structural properties and observed optoelectronic properties of mixed-dimension hybrid organic-inorganic perovskites containing the lead bromide inorganic framework. Expected outcomes and potential challenges of this project are also highlighted.

Introduction

1.1 Background and Motivation

The term Perovskite originally referred to CaTiO_3 which was discovered in the Ural Mountains of Russia by Gustav Rose in 1839 and named after Russian mineralogist Lev Perovski¹. Perovskite was later generalized to include materials which have similar crystal structures with the general formula of ABO_3 . These compounds exist naturally and abundantly in the Earth's crusts and include MgSiO_3 (Enstatite) and FeSiO_3 (Iron (II) silicate). Early applications of perovskites were of BaTiO_3 involving exploiting its ferroelectric, piezoelectric and photorefractive effects in applications such as capacitors, precision positioners, and nonlinear optics.

The discovery of the halide perovskites dates to the 1890s and the first few reported halide perovskites were based on cesium² and methylammonium³ lead halide. Distinct from the inorganic oxide perovskites, the hybrid organic-inorganic perovskites (HOIP) got their name from the combination of organic and inorganic moieties. In HOIP, typically, the A-site is an organic ammonium cation (e.g. methylammonium, phenylethylammonium), the B-site is a divalent metal cation (e.g. Pb^{2+} , Sn^{2+} , Ni^{2+}) and X will be a halide (e.g. Cl^- , Br^- , I^-). Earlier works regarding hybrid perovskites available in literature date as far back at 1980⁴⁻⁶ but interest in this material remained relatively dormant for a long period of time.

From the spring of 2009, HOIP have gathered significant attention because great interest was generated by the prototypical 3-dimensional (3D) methylammonium lead iodide perovskite, MAPbI_3 , becoming a leading contender in developing the next generation of photovoltaic devices. This came against a backdrop of seeking fossil fuel alternatives and the efficiencies of MAPbI_3 based solar cells have been growing rapidly with current photovoltaic (PV) efficiencies comparable with silicon-based PV. While the PV device operation has improved significantly, there are key missing areas in our understanding of the charge transport properties of such materials. Hence, this thesis aims to take a step back from device operations and examine the structural-property relationships.

Scientific interest in the lower dimensional perovskites, such as the 2D layered perovskites and 1D chain perovskite and ‘perovskitoids’ have also gained attention for a variety of reasons. The layered 2D perovskites are thought to be in a natural quantum well structure⁷ because the organic layers are typically insulating while the inorganic lead halide octahedra cages are the charge transport channels. Similarly, the 1D chained perovskites are also seen as natural nanowires because the lead halide octahedra connectivity resembles that of a 1D nanowire and hence electron transport is confined to only one dimension.

Owing to the flexibility of the HOIP structures, the corresponding structural-property relation is not well established where one likely consequence is charge localization effects, which remains largely underexplored. Furthermore, the role of lead halide octahedra connectivity and cation dynamics are also underexplored. A shift away from the purely corner shared lead halide octahedra, as in MAPbI₃, to edge or face sharing octahedra should also follow a slight change in the nomenclature, such as perovskite polytypes and ‘perovskitoids’, which will be discussed in the subsequent chapter. Although there has been some correlation between octahedral tilting and the resultant bulk properties (e.g. photoluminescence) in layered 2D perovskites⁸, the underlying microscopic origins of the mechanism are not well understood. The area of 1D perovskites remains highly fragmented partly because there have not been many systems reported and hence, no design rationale has been laid out. Consequently, much is still unknown concerning this group of 1D perovskites.

The understanding of the process and consequences of charge localization in the field of hybrid perovskites is still limited, although there is a consensus that the ‘soft bonds’ in hybrid perovskites can be easily deformed^{9, 10}. Through variable temperature charge transport measurements¹¹ and terahertz spectroscopy measurements^{12, 13}, these indirect studies hints at the likelihood of charge carriers (i.e. electron and holes) becoming localized to within several unit cells in 3D hybrid perovskites instead of behaving like a free charge carrier. However, there is no direct evidence for the effects of such charge localization to form a polaron. The effects of polaronic charge transport would alter our understanding of this class of material, and ultimately how affects the principles of device operation. At the same time, in the area of 2D layered Ruddlesden-Popper perovskites, there is a general consensus that the broadband emission properties are

linked to the octahedral tilting⁸ but there is a lack of understanding of the role of octahedral structural connectivity and charge localization effects. Similarly, in the 1D perovskites and ‘perovskitoids’ such understanding is still highly fragmentary and there is no common consensus on the relationship between structural properties and experimentally observed optical properties.

1.2 Problem Statement

While an extensive effort has been directed towards the study of hybrid perovskite-based devices unravelling the stability mechanism, there has been, to a lesser extent, focus on the fundamental properties of the material. With the reports of anomalous charge transport characteristics¹⁴⁻¹⁶, the analysis has typically been assuming that the charge carriers behave similar to traditional semiconductors, an effort to look at the localized effects is still lacking. Similarly, in the layered 2D perovskite and 1D perovskite and ‘perovskitoids’, such materials have not been receiving much attention. Hence, even less attention is given to the localized effects such as the organic cation motion and how such localized effects are correlated with the bulk material properties.

1.3 Objective and Scope

Based on the motivation and the problem statement presented thus far, this thesis aims to look at the localized effects in hybrid perovskites and its correlation with the observed bulk properties.

The scope of this thesis is to:

1. Use first principles DFT simulations and both steady state and transient fast spectroscopic evidence to prove the existence of charge localization in 3D MAPbI₃. The implications of charge localization can then be studied by DFT simulations and compared with experimental charge mobilities to validate both theoretical and experimental work
2. Probe the structural correlation of perovskite polytype, reduced dimensional

perovskites and “perovskitoid” structures with the observed bulk properties. The localized dynamics, particularly those originating from the organic cation, are then studied in detail and the results compared against theoretical DFT simulations. The structural properties of each compound are then studied alongside the observed bulk optical properties and attempts to elucidate the role of cationic motional dynamics.

The material of interest in 3D perovskite is the prototypical methylammonium lead iodide due to the widespread interest in this material, and a wide amount of knowledge which has been, and still is, being acquired by the scientific community. The direct experimental evidence relies on optical spectroscopic techniques while charge transport properties are measured through the photocurrent spectroscopy. While exploring the reduced dimensional perovskites, a variety of organic cations are utilized, specifically aminoalkyl substituted imidazolium and imidazolium cations, and the structures obtained showed considerable differences. This would provide a basis for the cross comparison structural properties like the lead halide octahedra connection or cation dynamics with experimentally observable effects of charge localization, such as broadband photoluminescence emission.

It is hoped that from this work, there would be an enhanced understanding of the role of charge localization and how this would be considered during device operations and optimization work. The work on the reduced dimensional perovskites would also hope to provide some clarity and classification to the types of reduced dimensional perovskites and the charge localization effects.

1.4 Dissertation Overview

This thesis is structured where each chapter is dedicated to the topics outlined below:

Chapter 1 starts off by giving a brief overview of the field of hybrid perovskite and highlighted out specific gaps in the understanding of hybrid perovskites and areas which this thesis would address.

Chapter 2 gives an outline on the growth of the interest in hybrid perovskite and moves on to review relevant literature and the current state of understanding of self-trapping in hybrid perovskites and structural dynamics of the organic cation. Moving beyond the 3D perovskite, the chapter also carries out a review of the layered 2D, 1D, and exotic perovskites and perovskitoids.

Chapter 3 covers the experimental theory and procedures on the synthesis and the suite of characterization techniques utilized to thoroughly characterize the materials, namely X-ray diffraction, solid state nuclear magnetic resonance, steady state optical characterization, and transient absorption and photocurrent techniques.

Chapter 4 studies formation of polarons in the prototypical 3D MAPbI₃ from first principles DFT simulations and the predictions are followed up by optical spectroscopic techniques to experimentally prove the existence of the formation of large polarons. The formation dynamics are studied through transient optical absorption spectroscopy and charge carrier properties are elucidated through photocurrent measurements. The implications of charge localization through the formation of polarons are further discussed within the chapter.

Chapter 5 moves away from the well-established 3D MAPbI₃ and into the corrugated <110> oriented 2D layered perovskites. In the process of doing so, a new polymorph of a previously reported APbBr₄ is discovered and helped to establish that the substituted alkyl chain length is crucial to the formation of the corrugated perovskite, IEAPbBr₄. Both systems exhibit broadband photoluminescence emission, which is an evidence for the presence of self-trapped states, although IEAPbBr₄ shows a distinct excitonic emission peak even up to room temperatures.

Chapter 6 examines a more exotic subbranch of perovskites, studying the perovskite polytype structures and a new branch of 1D perovskite and perovskitoid. The importance of the A-site cation chemical activity is demonstrated in this chapter where three different polymorphs of imidazolium lead bromide are studied; IMIPbBr₃ is determined to closely resemble a 4H perovskite polytype, IMI₂PbBr₄ as a perovskitoid and IMI₃PbBr₅ as a true 1D perovskite. All three polymorphs exhibit broadband emission which indicates the existence of self-trapped states in these structures.

Chapter 7 summarizes and presents conclusions based on the work accomplished and connects the important findings of each chapter to the initial objective of the thesis. The impact of this research is reviewed and guidance provided for future work on designing hybrid perovskite structures.

1.5 Findings and Outcomes

The achievement of this research and several novel findings and outcome include:

- i. Evidence for large polaron formation in MAPbI_3 through spectroscopic methods where polaron mobilities and effective mass anisotropy are lower than that of the free carriers.
- ii. The discovery of $\text{API}_2\text{Pb}_3\text{Br}_{10}$, a polymorphic structure of APIPbBr_4 .
- iii. Critical aminoalkyl length of substituted imidazole to form a 2 by 2 corrugated $\langle 110 \rangle$ cut of perovskite is determined.
- iv. Novel polymorphism discovered in imidazole lead bromides showing a structure which resembles 4H-polytype, edge shared lead bromide octahedra which forms a 1-D chain, and a clean 1-D chain of lead bromide octahedra.

The present research starts by studying the prototypical MAPbI_3 and utilizes spectroscopic evidence to prove the formation of polarons. Since polarons are attributed to various properties (e.g. broadband emission) seen in the 2D perovskite series, this research moves onto do a thorough structural characterization of a known APIPbBr_4 , and the whole series in alkyl substituted (and non-substituted) imidazole lead bromide series. These materials are synthesized, followed by the crystallographic characterization through using single crystal X-ray diffraction (XRD), and the solved model validated through powder XRD. This will allow long range structural order to be experimentally verified. Solid State Nuclear Magnetic Resonance (ssNMR) will subsequently be employed to characterize the short-range order (or disorder) and the dynamics of the organic molecule would be probed. The structural phase transitions of the novel perovskites (if present) are also studied at levels which the instruments allow.

Following which, the optical properties of the novel perovskites will be characterized, beginning with the fundamental linear absorption and photoluminescence charted across variable temperature. The correlation between the structural properties with the observed optoelectronic properties will give a preview on the outlook on the role of lead bromide octahedra connectivity.

References

1. Chakhmouradian, A. R.; Woodward, P. M., Celebrating 175 years of perovskite research: a tribute to Roger H. Mitchell. *Physics and Chemistry of Minerals* **2014**, *41* (6), 387-391.
2. Wells, H. L., Über die Cäsium- und Kalium-Bleihalogenide. *Zeitschrift für anorganische Chemie* **1893**, *3* (1), 195-210.
3. Dieter, W., CH₃NH₃PbX₃, ein Pb(II)-System mit kubischer Perowskitstruktur / CH₃NH₃PbX₃, a Pb(II)-System with Cubic Perovskite Structure. *Zeitschrift für Naturforschung B* **1978**, *33* (12), 1443-1445.
4. Weber, D., The Perovskite System CH₃NH₃ [PbnSn₁₋₃X₃] (X = Cl, Br, I). *Zeitschrift für Naturforschung - Section B Journal of Chemical Sciences* **1979**, *34* (7), 939-941.
5. Poglitsch, A.; Weber, D., Dynamic disorder in methylammoniumtrihalogenoplumbates (II) observed by millimeter-wave spectroscopy. *The Journal of Chemical Physics* **1987**, *87* (11), 6373-6378.
6. Wasylishen, R. E.; Knop, O.; Macdonald, J. B., Cation rotation in methylammonium lead halides. *Solid State Communications* **1985**, *56* (7), 581-582.
7. Wu, X.; Trinh, M. T.; Zhu, X. Y., Excitonic Many-Body Interactions in Two-Dimensional Lead Iodide Perovskite Quantum Wells. *The Journal of Physical Chemistry C* **2015**, *119* (26), 14714-14721.
8. Cortecchia, D.; Neutzner, S.; Srimath Kandada, A. R.; Mosconi, E.; Meggiolaro, D.; De Angelis, F.; Soci, C.; Petrozza, A., Broadband Emission in Two-Dimensional Hybrid Perovskites: The Role of Structural Deformation. *J. Am. Chem. Soc.* **2017**, *139* (1), 39-42.

9. Herz, L. M., How Lattice Dynamics Moderate the Electronic Properties of Metal-Halide Perovskites. *The Journal of Physical Chemistry Letters* **2018**, 9 (23), 6853-6863.
10. Lai, M.; Obliger, A.; Lu, D.; Kley, C. S.; Bischak, C. G.; Kong, Q.; Lei, T.; Dou, L.; Ginsberg, N. S.; Limmer, D. T.; Yang, P., Intrinsic anion diffusivity in lead halide perovskites is facilitated by a soft lattice. *Proceedings of the National Academy of Sciences* **2018**, 115 (47), 11929.
11. Slonopas, A.; Foley, B. J.; Choi, J. J.; Gupta, M. C., Charge transport in bulk CH₃NH₃PbI₃ perovskite. *J. Appl. Phys.* **2016**, 119, 074101.
12. La-o-vorakiat, C.; Xia, H.; Kadro, J.; Salim, T.; Zhao, D.; Ahmed, T.; Lam, Y. M.; Zhu, J.-X.; Marcus, R. A.; Michel-Beyerle, M.-E.; Chia, E. E. M., Phonon Mode Transformation Across the Orthorhombic–Tetragonal Phase Transition in a Lead Iodide Perovskite CH₃NH₃PbI₃: A Terahertz Time-Domain Spectroscopy Approach. *J. Phys. Chem. Lett.* **2016**, 7, 1-6.
13. Valverde-Chavez, D. A.; Ponseca, C. S.; Stoumpos, C. C.; Yartsev, A.; Kanatzidis, M. G.; Sundstrom, V.; Cooke, D. G., Intrinsic femtosecond charge generation dynamics in single crystal CH₃NH₃PbI₃. *Energy Environ. Sci* **2015**, 8, 3700-3707.
14. Yin, W.-J.; Shi, T.; Yan, Y., Unusual defect physics in CH₃NH₃PbI₃ perovskite solar cell absorber. *Appl. Phys. Lett.* **2014**, 104, 063903.
15. Brenner, T. M.; Egger, D. A.; Kronik, L.; Hodes, G.; Cahen, D., Hybrid organic—inorganic perovskites: low-cost semiconductors with intriguing charge-transport properties. *Nat. Rev. Mater.* **2016**, 1, 15007.
16. Xing, G.; Mathews, N.; Sun, S.; Lim, S. S.; Lam, Y. M.; Grätzel, M.; Mhaisalkar, S.; Sum, T. C., Long-Range Balanced Electron- and Hole-Transport Lengths in Organic-Inorganic CH₃NH₃PbI₃. *Science* **2013**, 342, 344-347.

Chapter 2

Literature Review

An overview of key progress in the field of 3D HOIP is given, followed by a similar summary for lower dimension layered perovskites and a discussion of their varying definitions.

The flexibility in the engineering of the perovskite structure through exploiting the variation of the organic moiety is demonstrated. The key issues of the structural characterization techniques used for perovskites and their limitations is also examined since structural properties are known to inherently affect the optoelectronic properties.

2.1 Introduction

As mentioned in previous chapter, the term Perovskite, which originally referred to CaTiO_3 was later generalized to include materials which have similar crystal structures with the general formula of ABO_3 or ABX_3 . Distinct from the inorganic oxide perovskites, the organometallic halide perovskites are a much younger field but have become an extensively studied crystalline family of hybrids. In these A is typically an ammonium cation (e.g. methylammonium, phenylethylammonium), B is a divalent metal cation (e.g. Pb^{2+} , Sn^{2+} , Ni^{2+}) and X will be a halide (e.g. Cl^- , Br^- , I^-). Early work regarding hybrid perovskites available in literature dates back to the 1980s¹⁻³ but interest in this material remained relatively dormant for some time, other than range of studies of their structures by Mitzi using a variety of organic cations⁴⁻⁶, and the application of the material to nonlinear optics and electroluminescence (i.e. light emitting diodes, LEDs)^{7, 8}. The earliest report of a halide perovskite being used as a solar light absorber was in 1987 when Salau reported a new compound KPbI_3 which was suitable to be used for such applications in tandem with Cu⁹.

Interest in these materials has increased greatly since 2009. In the quest to search for alternative renewable energy resources, the prototypical HOIP, methylammonium lead iodide (MAPbI_3), was first incorporated into solar cells in the form of quantum dot dyes in dye sensitized solar cells (DSSC) by Miyasaka's group in 2009 with a modest efficiency of 3.8%¹⁰. Subsequently, Park et al improved the efficiency to 6.5%¹¹ in 2011, which was further enhanced to 9.7% by Grätzel et al. in 2012¹². A breakthrough came later that year when Snaith showed that the MAPbI_3 perovskite can also operate independently and behaves as an n-type semiconductor without the need for using it as a dye which led to an increased efficiency of 10.9%¹³. As seen in Figure 2.1, subsequent work led to a dramatic rise in the reported efficiencies of MAPbI_3 based perovskite solar cells, far outperforming other technologies like the dye-sensitized and organic cells, with performances of above 15%¹⁴⁻¹⁶ soon being reported, and further improvement producing the current record certified solar cell efficiency of 25.2%¹⁷.

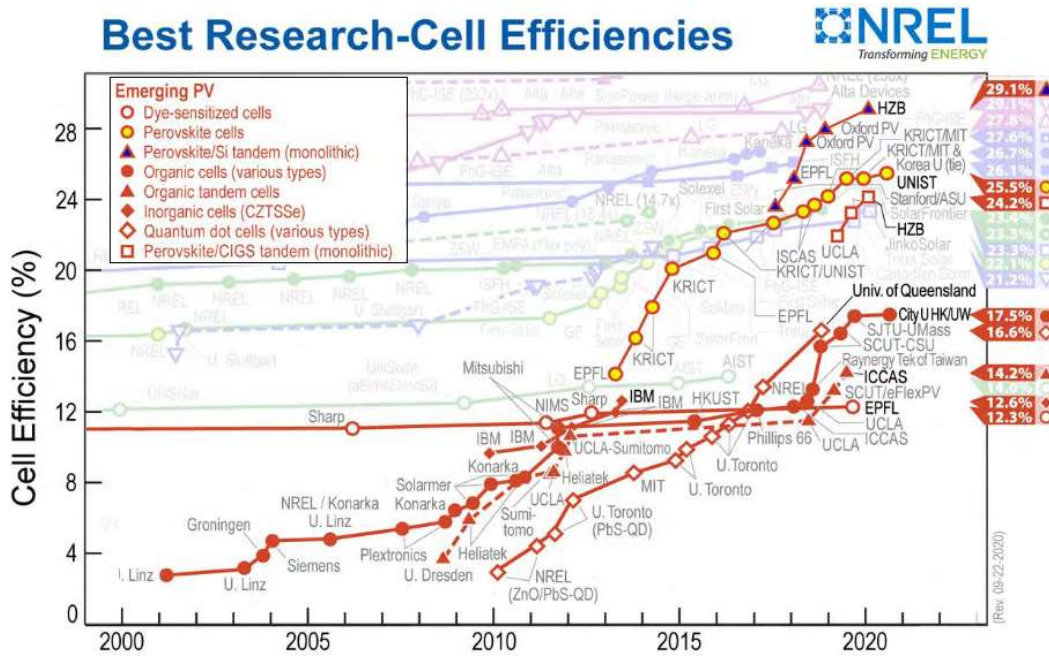


Figure 2.1: Chart detailing the growth of emerging photovoltaics solar cell efficiencies, and a very rapid rate of growth on perovskite cells efficiency is observed. [Taken from NREL, 2020]

The rise of such efficiencies triggered off a search by the scientific community to unravel the reasons behind such exemplary properties with hopes that a better understanding would possibly allow engineering these properties into similar systems. Some of the reported properties include high absorption coefficient¹⁸, long charge carrier diffusion length^{18, 19}, low non-radiative combination rates²⁰, apparent insensitivity to defects^{21, 22}, and having a tunable band gap^{23, 24}. This is further assisted by the simple and low cost fabrication methods and inexpensive raw materials, and the field has been dubbed as the “poor man’s semiconductor” research²⁵. Spearheaded by the success of the hybrid perovskites in solar cells, these perovskites are also increasingly finding various applications such as in LEDs²⁶⁻²⁹, lasing³⁰⁻³⁵, optoelectronics^{30, 36}, thermoelectric³⁷ and multiphoton imaging utilizing a large five photon upconversion effect³⁸. From a structurally perspective, the framework of the hybrid organic-inorganic perovskites (HOIP) is shown to be highly flexible and follows Vergard’s law closely^{39, 40}, which allows a convenient estimate for the tunable band gap. By changing the ratio of all the constituent, A-site, B-site cation and X-site anions, the band gap could be easily tuned while keeping some of the fundamental character of

each system. Therefore the present state-of-the-art perovskite photovoltaic material utilizes a cocktail of ions, which inherits some performance attributes from FA-based system, stability from the MA and Cs based system while the halide substitution tunes the band gap to the sweet spot for photovoltaic conversion. The resultant active solar absorber used in photovoltaic applications is $\text{Cs}_{0.05}(\text{FA}_{0.83}\text{MA}_{0.17})_{0.95}\text{Pb}(\text{I}_{0.82}\text{Br}_{0.18})_3$ ¹⁷.

The class of hybrid perovskites can then be further subdivided into the so-called ‘3D’ and the so-called reduced dimensional perovskites of which undoubtedly, the ‘3D perovskites’ still garner the majority of the research attention. The naming principle for the perovskites here revolves around how the lead halide octahedra are connected. In the ‘3D’ scenario, the lead halide octahedra are connected infinitely over all three axes: like in Figure 2.2, the x-axis, y-axis, and z-axis, as is evident in the prototypical MAPbI_3 and the well-known FAPbI_3 systems.

2.2 3-Dimensional Hybrid Organic-Inorganic Perovskites

The Goldschmidt tolerance factor was developed in 1926⁴¹ to describe the requirements for the perovskite crystal to be intrinsically stable and is written as $t = \frac{r_A + r_0}{\sqrt{2}(r_B + r_0)}$, where r_A is the radius of the A-site cation, r_B is the radius of the B-site cation and r_0 is the radius of the anion. In his work, it was shown that, with a Goldschmidt factor of 0.9 to 1.0, the resulting structure is expected to be an ideal cubic structure while if the factor is in range 0.71-0.9 it would be expected to form orthorhombic structures. If the factor goes below 0.7 or is above 1.0, then the system could be expected to form other close packed structures or hexagonal structures respectively. From the Goldschmidt factor, the anionic radii could be more generalized into any anions with the respective cations; in this chapter, the anions will be halides (Br^- , I^-) and the cation will be lead (Pb^{2+}). Considering only inorganic cations which have to satisfy charge neutrality condition, there can only be a small number of cations which would satisfy the Goldschmidt factor, for example Cesium. However, for organic compounds, which have to satisfy both the charge neutrality and the size condition, there are now a large number of compounds that are suitable. Among the more widely studied cations are the prototypical methylammonium cation, and the next simplest formamidinium cation.

In the development of the Goldschmidt tolerance factor, the A-site cations are assumed to be rigid spheres, which is an accurate approximation in the inorganic perovskites. However, this assumption is increasingly being challenged in HOIPs. While the simplest MA and FA cations are found to be rapidly moving within the inorganic lead-halide framework, so that the approximation to rigid sphere is still valid, this is not true for ring-based organic cations (e.g. pyridine or imidazole) which presents significant limitations to the validity of the assumptions. To further challenge this assumption, organic cations with long alkyl chains or bulky aromatic chains would still crystallize in the perovskite structure, but in the form of “reduced dimensionality”.

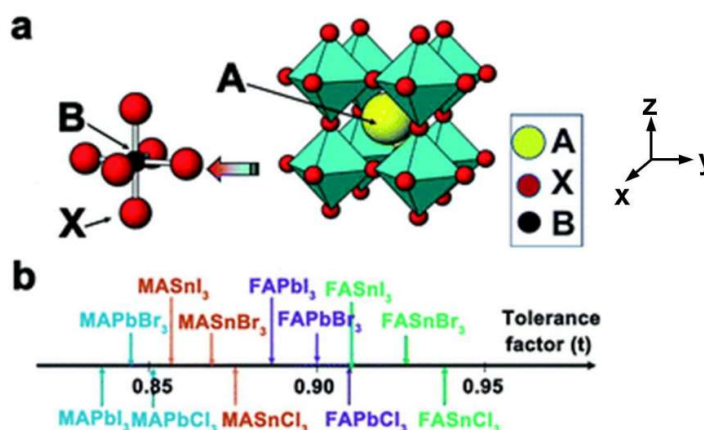


Figure 2.2: Illustration showing the Goldschmidt tolerance factor of the various hybrid perovskite that are well studied in the literature⁴²

There has been a considerable amount of interest in the methylammonium lead iodide system, with some spillover interest in the neighboring lead bromide and a much lesser extent the lead chloride system. Unsurprisingly, optoelectronic studies of MAPbI₃ have been carried out in great details to attempt to unravel the origins of the exceptional properties and to relate them to their structures.

Structural studies of MAPbI₃ have led to a debate on whether it has a centrosymmetric or an acentrosymmetric space group. At first glance, the existence of an inversion centre in the structure would seem insignificant, but the implications run much deeper than might appear. The presence of an inversion centre would favour/not favour certain properties, such as ferroelectricity, etc. so its presence/absence is of crucial importance

in understanding the properties.

Also, different samples of the same material could behave differently; thin film and single crystals can have very different properties. Trap and defect states would greatly influence the measurements done on thin films while the bulk properties would dominate in single crystal samples. The technique used to study the same property also would give a varied response (e.g. thin film, single crystal, THz, microwave, SCLC, capacitance measurements)

Studies carried out on the prototypical MAPbI₃ has seen it exhibit several remarkable transport properties like long charge carrier lifetime⁴³ and diffusion length^{18, 44}, small non-radiative bimolecular recombination coefficient, γ , of the order of $10^{-10} \text{ cm}^3 \text{ s}^{-1}$ which is comparable to crystalline GaAs^{19, 45}, and apparent insensitivity to defects^{21, 22, 46, 47} among many others but the origins of the remarkable charge carrier characteristics are widely under debate. Reported charge carrier mobilities are between 10^{-4} and 10^2 depending on the measurement technique and sample^{43-45, 48-52}, which is in contrast with Langevin model for free charge carrier recombination in semiconductors⁴⁹ and the origin of such inconsistency is being debated.⁵³

Recent works postulates the existence of large polaron in 3D MHPs and point towards the role of electron-phonon coupling in the formation of polarons, where the charge carriers being protected by polaronic characteristic in the perovskite lattice^{54, 55}. The coupling has been probed through electrical conductivity exhibiting power-law temperature dependence,⁵⁶ photoinduced absorption in the visible⁵⁷ and FIR regime⁵⁸, Terahertz measurement^{59, 60}, time resolved optical Kerr effect spectroscopy (TR-OKE)⁶¹, time resolved optical absorption spectroscopy (TR-OAS)⁶². In similar material like MAPbBr₃, there is evidence for screening effects in reorientation of the molecular dipoles and presence of coherent phonon modes generated via displacive excitation^{63, 64} but no proof of their existence. Similarly, polaronic states have been invoked to explain octahedral distortion effects due to coherent vibrations of the Pb-I modes in MAPbI₃,⁶⁵ but the impact of carrier induced lattice distortion on polaron formation and charge transport in optoelectronic devices has remained elusive.⁴³ The importance of understanding the charge carrier behaviour would have strong implications towards the design principles of devices based on MAPbI₃, such as the critical thickness of the MAPbI₃ active layer, and would be addressed in this thesis.

2.3 Structural characterization and the cation dynamics of 3D hybrid perovskite

Structural studies of novel materials have flourished with the use of X-ray diffraction which has grown into a huge and authoritative field where many parts of the analysis can now be automated. A brief outline of this “black box” crystallography is covered in the following experimental section. Notably, diffraction is an average of the unit cells added together, hence is unable to differentiate between dynamic or static disorder present in structures. This limitation has been exposed numerous times and especially so in the hybrid perovskites. Specific to the prototypical MAPbI₃ system, detailed structural studies have shown some anomalies in the structure symmetry.⁶⁶ Furthermore, due to the fast tumbling of the organic methylammonium cation, it is not sufficiently resolved even by neutron diffraction at low temperatures⁶⁶. The apparent difficulty in pinpointing the space group has also sparked off a debate regarding the existence of ferroelectricity in MAPbI₃⁶⁷⁻⁷⁰ where it was concluded experimentally that MAPbI₃ does not show ferroelectric behaviour.^{71, 72}

Solid state nuclear magnetic resonance exploits the effects of local electron density on the magnetic properties of nuclei to characterize the local structure. It is sensitive to changes in the local environment which is useful in characterizing the cation motional dynamics. The study of magnetization decay through various means are then augmented with other experimental observations to draw conclusions on the relative motion of the cations. Furthermore, NMR being highly sensitive to the local environment of nuclei in a structure, means it can also be utilized to verify phase segregation⁷³⁻⁷⁵. ²⁰⁷Pb NMR spectroscopy has been used to characterize the mixed halide perovskites and it was concluded that nonstoichiometric dopants are prevalent regardless of the synthesis methods⁷³. ²⁰⁷Pb spectroscopy was also utilized extensively to probe the solid solution behaviour of ball-milled MAPbX₃. The 2D EXSY NMR spectra provided evidence for the mixed halide system being a solid solution, because phase separated or micro/nano crystalline domains of the different halide systems would not produce any correlations.⁷⁶ It showed that in the mixed halide systems, the structures are highly dependent on the synthesis route used. Similarly, Kubicki et al have conducted a series of studies based on NMR spectroscopy to verify if the common

dopants used in photovoltaics are incorporated into the structural lattices. It was concluded that Cs^+ and guanidinium cations^{74, 77} are incorporated while K^+ , Rb^+ are segregated within its individual grains and not incorporated into the prototypical MAPbX_3 or FAPbX_3 perovskite lattices^{74, 75}. The significance of verifying the incorporation of dopants into the perovskite lattice is immediately obvious because this would modify the crystal structure, and hence the relative energy levels.

On the other hand, the significance of probing the cation dynamics is not immediately obvious. The cation dynamics are shown to influence the crystal structure⁷⁸ and the lifetime of charge carriers⁷⁹ and the cation rotation modulate the electronic band structure and is thought to be responsible for the exceptional properties of MAPbI_3 ⁸⁰. Studies on the dynamics of MAPbI_3 dates back to 1985² and the elucidation of cation dynamics generally rely on two methods; studying the average of anisotropic interaction due to cation motion, such as quadrupole splitting in ^2H and ^{14}N , or examining the relaxation behaviour of the specific nuclei, which this thesis would focus on. As the different relaxation mechanism is sensitive to the nuclei regime of motion, different experiments are utilized to probe the motional dynamics, with T_1 and $T_{1\rho}$, which are also called the spin-lattice relaxation time and the spin-lattice relaxation time in the rotating frame respectively, being more commonly used to probe the motion. T_1 is sensitive to the relaxation through the MHz regime while $T_{1\rho}$ would be sensitive to relaxation through the kHz regime⁸¹.

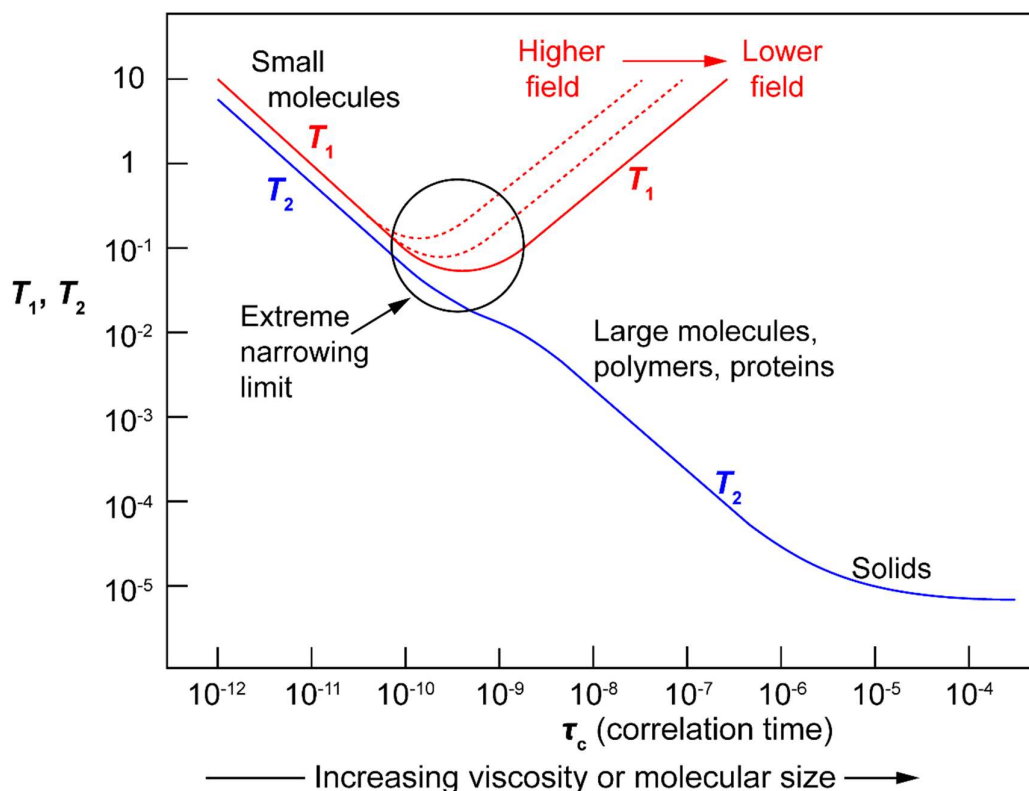


Figure 2.3 the plot of T_1 relaxation time against the correlation time of the process. The molecular correlation time is the time the average molecule completes one radian of rotation. In the very short correlation time, it is suitable for small molecules. At the moderate to long correlation time regime, it is suitable for large molecules like polymers or proteins, or to the extreme limit of solids.⁸²

Through the use of T_1 , NMR has been used as an indirect method to determine correlation time and activation energies in MAPbX_3 systems^{83, 84}. In the work carried out by Xu et al.⁸⁴, detailed analysis on cationic motional mode was carried out, and has shown that rotational tunnelling is the dominant process contributing to the ^1H spin-lattice relaxation which shifts to the thermally activated correlated C_3 -reorientation with increasing temperature for MAPbCl_3 and MAPbI_3 . In a similar way, in MAPbBr_3 , the thermally activated uncorrelated reorientation is the process responsible for ^1H spin-lattice relaxation at higher temperatures.

More recent work also utilized T_1 relaxation to compare FAPbI_3 across the $\alpha - \beta$ -phase transition⁸⁵ which accurately picked up the subtle change in relaxation dynamics which other techniques struggle. Extending this same concept to MAPbI_3 , both ^1H and ^{13}C . ^1H

relaxation was studied across the tetragonal – cubic phase transition.⁸⁶ Although there was no abrupt jump in the T_1 like in FAPbI₃, the rate of change of the T_1 was seen to be distinct. The relaxation dynamics studies from NMR also support the hypothesis that MA⁺ cation motion is dominated by the biaxial rotation about the C – N axis.^{87, 88} and restricted to the ab-plane in the tetragonal phase.⁸⁹ Studies were also carried out on the inorganic lattice, where Nuclear Quadrupole Resonance (NQR) experiments show ¹²⁷I to be oscillating and the frequency is estimated using Bayer theory.⁸⁷ In the same work, Senocrate et al. has proposed that the short ²⁰⁷Pb T_2 relaxation at room temperature is due to cross relaxation with the rapidly relaxing iodine atoms due to quadrupolar interactions. Studies based on NMR spectroscopy has thus far demonstrated its importance to the study of local structure and atom dynamics.

The successful characterization and comparison in 3D perovskites had demonstrated the value of NMR as a complementary technique to diffraction. The characterization of short-range order, along with the capability to probe cation dynamics are shown to be vital and would be extended to several other systems, which will be examined in this thesis.

2.4 Lower dimensional perovskites: layered 2-Dimensional perovskites

In oxide perovskites, layered perovskites are categorized into three main phases; the Ruddlesen-Popper, Dion-Jacobson and Aurivillius phases. The main differences between these involve firstly, the atoms which separate the layers and secondly, the offset of the layers from each other. Ruddlesden-Popper perovskites have a general formula $A_{(n-1)}B_nO_{(3n+1)}$, and the layers are offset by $(\frac{1}{2}, \frac{1}{2})$ ⁹⁰. Aurivillius perovskites have a general formula $(Bi_2O_2)(A_{(n-1)}B_2O_7)$ where the separating layers are strictly Bi_2O_2 and the layers are offset by $(\frac{1}{2}, \frac{1}{2})$ ⁹¹. The Dion-Jacobson phase differs from the others in having an alkali metal (e.g. K⁺, Na⁺) as the separating layer and take on the general formula $M^+ A_{(n-1)}B_nO_{(3n+1)}$, where the layers are offset by $(\frac{1}{2}, 0)$ or $(0, 0)$ ^{92, 93}. In hybrid perovskites, there is a new alternating cation in interlayer (ACI) perovskites⁹⁴. Within the oxide perovskites, the three mentioned class of perovskites are still treated as 3-D perovskite, but in hybrid perovskites, the introduction of organic cations as interlayer ‘spacers’ would turn the systems into 2-D perovskites, as elaborated below.

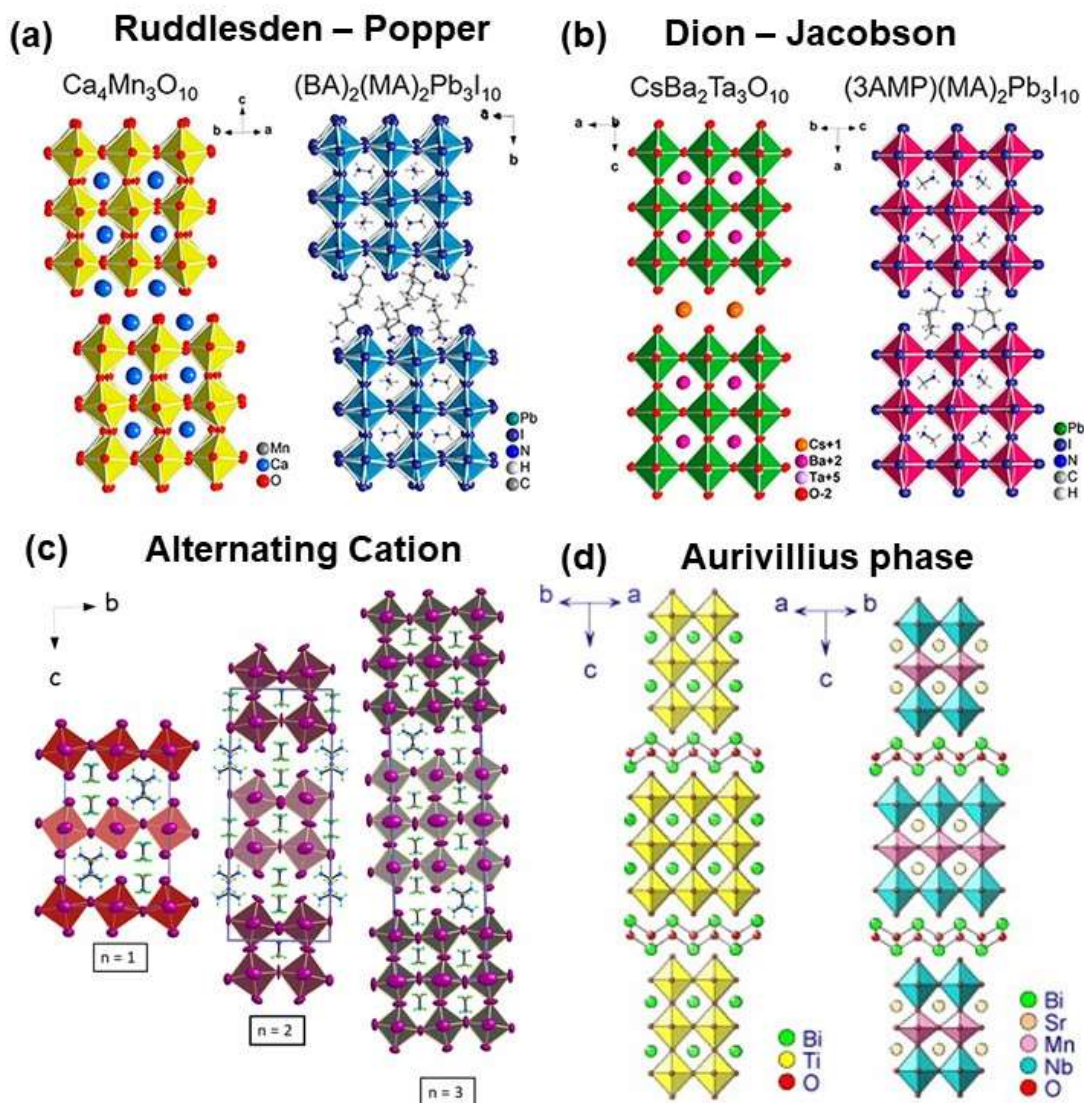


Figure 2.4 Schematic comparison of (a) Ruddlesden – Popper (RP), (b) Dion – Jacobson (DJ) in oxide perovskite against layered hybrid perovskites, and (c) the new alternating cation (ACI) structure unique to hybrid perovskite system. Notably, in RP perovskites, there is an offset of $(\frac{1}{2}, \frac{1}{2})$, while in DJ and ACI, there is no offset of the layers^{94, 95} (d) Oxide perovskite specific Aurivillius phase, with $n = 3$, $\text{Bi}_4\text{Ti}_3\text{O}_{12}$ and $\text{Bi}_2\text{Sr}_2\text{NbMnO}_{12-\delta}$. In Aurivillius phase, the spacer group is strictly Bi_2O_2 .⁹⁶

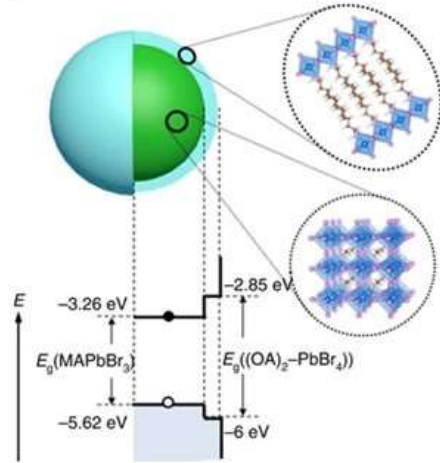
The terminology of ‘reduced dimensional perovskites’ in hybrid perovskites systems has been seen to refer to two different scenarios. One refers to the nanostructuring of 3D perovskites (e.g. MAPbI_3 and FAPbBr_3), into microdisks⁹⁷, nanoplatelets⁹⁸, quantum dots^{99, 100} or just plain nanocrystalline domains¹⁰¹, as seen in Fig 2.5, typically

through the use of ligands to exploit quantum confinement effects for their respective applications (e.g. solar cells, LEDs or lasing) while the other refers to a change in organic A-site cation to force the structure to adopt a reduced dimensional structure, as seen in Fig 2.6. An example would be the Ruddlesden-Popper series of hybrid perovskites, where long alkyl chains (e.g. n-butylammonium) or bulky aromatic chains (e.g. phenylethylammonium) would act as ‘spacers’ to push the layers of lead halide octahedra apart. In this thesis, attention will be given to the latter and ‘low dimensional perovskites’ will refer to these layered structures instead of the nanostructured systems.

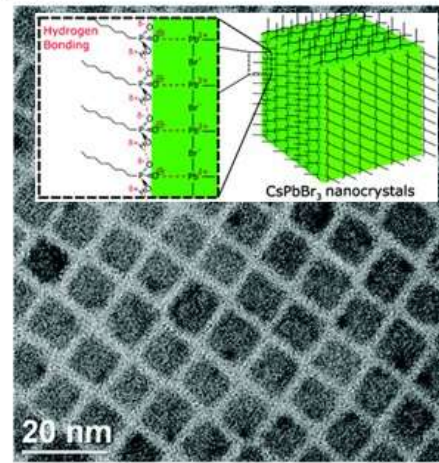
This change to 2D perovskites had been demonstrated in 2001 by Mitzi et al., who also introduced the terminology of naming such 2D perovskites by the direction of the cut¹⁰². In Mitzi’s work, he also coined the terms ‘perovskitizer’ and ‘spacer’ which indicate the role each organic cation plays. As a rule of thumb, a small and spherical cation would generally be a ‘perovskitizer’ since it would help hold the layers together whereas an ammonium cation with either a long aliphatic side chain (e.g. BA), or large bulky aromatic chain (e.g. PEA) would act as a ‘spacer’. The parameter n , would then define the number of lead halide octahedra layers.

Experimentally, in metal-halide perovskites the $\langle 100 \rangle$ oriented perovskite was first demonstrated by Mitzi et al. in the tin iodide series of hybrid perovskites^{4, 103} and has also been found in lead bromide¹⁰⁴ systems. More recently, interest in this area of layered hybrid perovskites has been sparked by the work of Stoumpos et al.¹⁰⁵ where it was demonstrated that the resultant layered perovskites can be obtained on the gram scale¹⁰⁵. The $\langle 100 \rangle$ oriented perovskites can then be further classified by the number of lead halide octahedra layers, n , where $n = 1$ would be a monolayer and $n = 2$ would consist of 2 layers, and $n = \text{infinity}$ would then correspond to the native 3D perovskite structure.

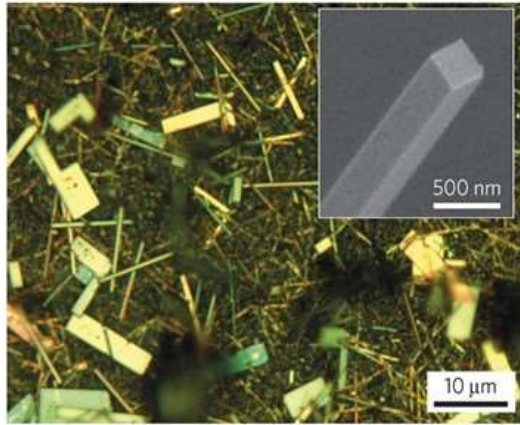
(a) Core-shell structure



(b) Nanocube structure



(c) Nanowire structure



(d) Nanocrystal Structure

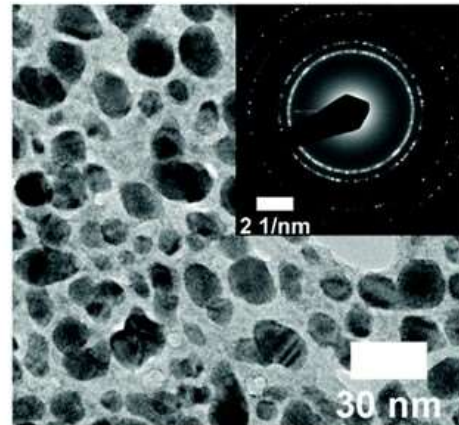


Figure 2.5 One scheme of reduced dimensional perovskite in the form of nanostructured (a) $\text{MAPbBr}_3 - (\text{OA})_2\text{PbBr}_4$ core-shell structure to exploit absorption upconversion effects ³⁸ (b) CsPbBr_3 in nanocube structure in LED device ¹⁰⁶ (c) MAPbI_3 in nanowires for lasing applications and (d) colloidal MAPbBr_3 nanocrystal in LED devices ¹⁰¹

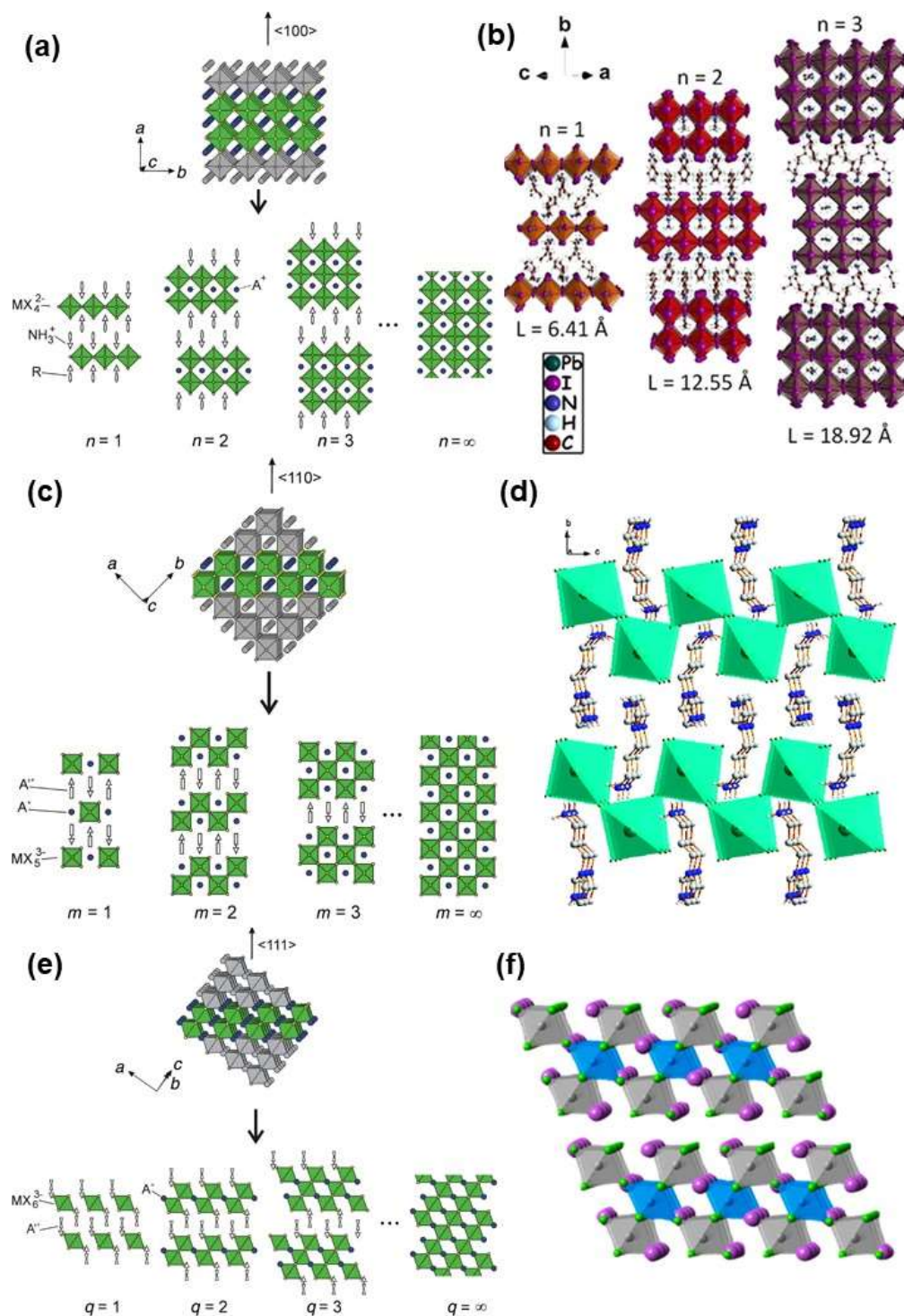


Figure 2.6 (a) schematic diagram showing the relation between 3D perovskites ($n = \infty$) and the $\langle 100 \rangle$ oriented 2D halide layers are indicated by n^{102} (b) $\langle 100 \rangle$ oriented layered hybrid perovskites $(BA)_2PbBr_4$ ¹⁰⁵ (c) schematic showing the layered $\langle 110 \rangle$ oriented perovskite (d) $\langle 110 \rangle$ oriented hybrid perovskite $APIPbBr_4$ ¹⁰⁷ (e) schematic showing the layered $\langle 111 \rangle$ oriented perovskite structure (f) $\langle 111 \rangle$ oriented metal halide perovskite $Cs_4CuSb_2Cl_{12}$ perovskite¹⁰⁸

However, careful attention needs to be paid in using this terminology of “2D perovskites” as there is a debate as to what constitutes a true 2D material. There is no doubt a monolayer of lead halide octahedra (i.e. $n = 1$), should be classified as a 2D material, but classification of the intermediates between 2D to 3D system, e.g. when $n = 5$, it remains highly contentious and a common consensus on the crossover point between 2D and 3D systems is presently missing. To further complicate the naming convention surrounding dimensionality, by using the cations which forms a 3D structure (e.g. MA^+) and 2D structure (e.g. BA^+) together, one forms a layered perovskite structure, which is also sometimes called a “quasi-2D structure”¹⁰⁹⁻¹¹², a “mixed-dimensional structure”¹¹³⁻¹¹⁷, a “multi-dimensional structure”^{38, 118-120}, a “2D/3D heterostructure”^{119, 121}, or even a “2.5D system”.^{122, 123} There is as yet no agreed name for this class of layered perovskite.

Regarding this family of $\langle 100 \rangle$ oriented perovskites, there have been a wide number of studies looking at their optical absorption and emission properties. Work so far generally agrees that with an increase in octahedral tilting and distortion¹²⁴⁻¹²⁷, the emission peak is also generally broadened. In the near ideal geometries such as BA, the photoluminescence emission is exclusively for excitonic emissions, while in the highly distorted geometries, it features more broadband emission. In most intermediate cases, there is a combination of both excitonic and broadband emission. This phenomenon has largely been attributed to localized states, specifically localized excitons. Hence, within the 2D/3D heterostructure subgroup, there is also a generic understanding on the excitonic characteristic being somewhat between the 2D and 3D cases. At the same time, there has also been a slowly increasing interest in the study and exploitation of the natural quantum well structure as seen in the layered perovskite systems¹²⁸⁻¹³⁰ and exploring the Rashba-Dresselhaus spin orbit coupling effect¹³¹⁻¹³⁴.

The distortion of octahedra is frequently measured through a statistical approach and is dependent on several parameters like the bond length, bond angles and the volume of the polyhedron. Three of the widely used parameters are mentioned here. Firstly, $\langle \lambda \rangle$ is also known as the octahedra quadratic elongation parameter¹³⁵ and is defined as

$$\langle \lambda \rangle = \frac{1}{n} \sum_i^n \left(\frac{d_i}{d_{av}} \right)^2 \quad (1)$$

where d_i is the Pb-Br bond length and d_{av} is the average bond length.

Secondly, the bond angle variance from the ideal polyhedron¹³⁵, σ^2 , is defined as

$$\sigma^2 = \frac{1}{m-1} \sum_{i=1}^m (\phi_i - \phi_0)^2 \quad (2)$$

where ϕ_i is the Br – Pb – Br angle and ϕ_0 is the ideal Br-Pb-Br angle and m is the number of Br – Pb – Br angles. In an ideal octahedron $\phi_0 = 90^\circ$ and $m = 12$, thus equation (2) can be simplified into

$$\sigma^2 = \frac{1}{11} \sum_{i=1}^{12} (\phi_i - 90)^2 \quad (3)$$

Lastly, the measure of octahedral distortion¹³⁶, Δd , which is defined as

$$\Delta d = \frac{1}{6} \sum_{i=1}^6 \left(\frac{d_i - d_{av}}{d_{av}} \right)^2 \quad (4)$$

where d_i is the B – X bond length, where B is Pb and X is Br in the scope of this thesis, and d_{av} is the average bond length. It should be noted that each unique octahedron should have its individual distortion rather than averaged across the entire system. Although imperfect, such measurements would give the degree of octahedra distortion some quantitation and further aid the discussion of the origins of broadband emissions.

From the MOP series (MOP = methoxybenzylammonium lead bromide perovskite), it was demonstrated clearly that 2-MOP has a greater octahedra tilting effect, where the dihedral angle is the largest, at 17.6° , as compared to 3-MOP and 4-MOP with a dihedral angle of 3.8° and 5.1° respectively¹³⁷. Consequently, the from the photoluminescence spectra, it can be observed clearly that the emission of 2-MOP is distinctly broader and shows an unusually large Stokes shift of 137 nm, whereas the 3-MOP and 4-MOP shows a much narrower emission profile. Similarly, the role of octahedra distortion in broadband emission had been demonstrated in (BA)PbI₄ and (EDBE)₂PbI₄.¹²⁶ In (BA)PbI₄, λ_{oct} is measured to be 1.0016 and σ^2 is measured to be $5.6 (^\circ)^2$, while in (EDBE)₂PbI₄, λ_{oct} is measured to be 1.0058 and σ^2 is measured to be $14.2 (^\circ)^2$. In the comparison of photoluminescence emission spectra, (EDBE)₂PbI₄ shows a much broader emission, with FWHM = 70 nm as compared to (BA)PbI₄, which only has a

FWHM = 20 nm. In the comparison of (BA)PbBr₄ and (HIS)PbBr₄, (HIS = histammonium, 4-(2-ammonioethyl)-1H-imidazol-3-ium) a similar trend is observed.¹³⁸ The large out-of-plane tilting (22.8 °) is seen to be the main contributor to broadband emission characteristic.

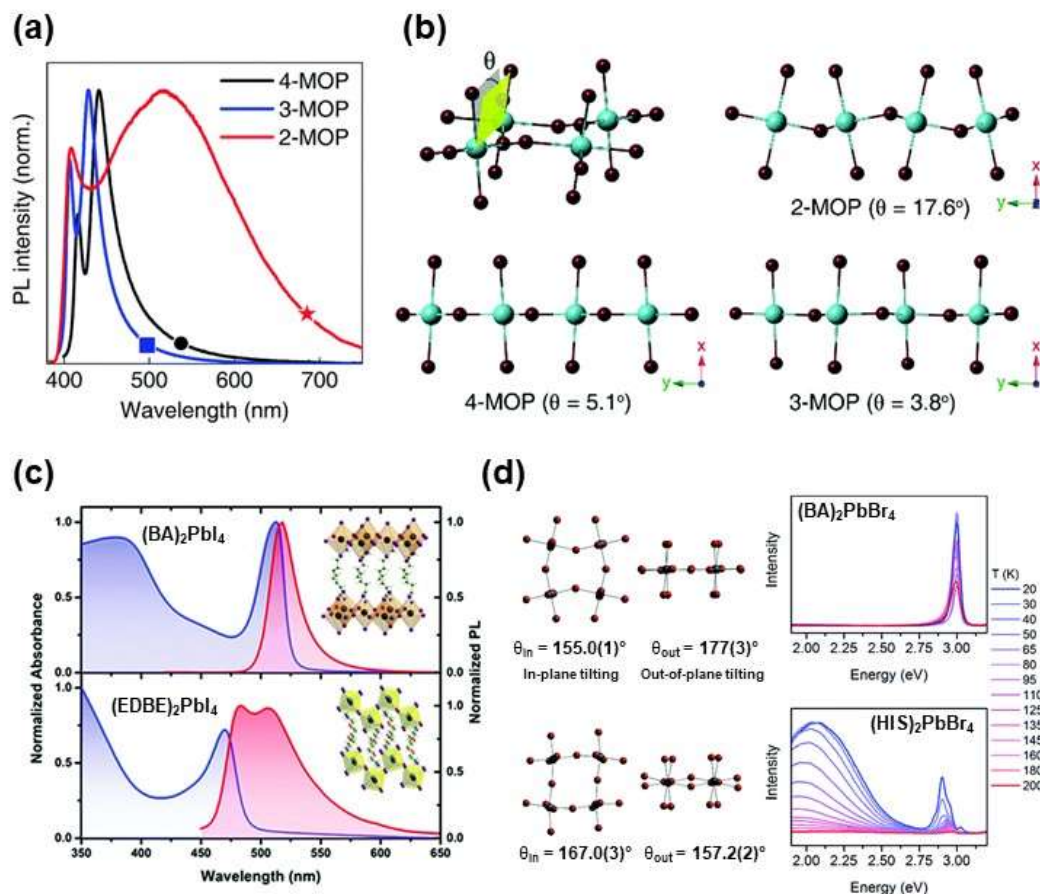


Figure 2.7 (a) photoluminescence of 2 -, 3 -, 4 - MOP at room temperature (b) octahedra tilting of 2 -, 3 -, 4 - MOP samples measured through the dihedral angles¹³⁷ (c) absorption and emission spectra of (BA)₂PbI₄ and (EDBE)PbI₄¹²⁶ (d) structural distortion of (BA)₂PbBr₄ and (HIS)PbBr₄ and the corresponding variable temperature photoluminescence emission profile¹³⁸

The technological importance of such <100> oriented perovskites can be seen in light emitting diodes (LEDs). The earliest report of RP perovskites in LEDs can be traced back to 1994, where a monolayer $n = 1$, PEA₂PbI₄ shows emission at 520 nm under cryogenic temperatures, 78 K.¹³⁹ However, at room temperatures, the efficiencies nosedived and remains a formidable challenge to be addressed. Further advances in

LED applications then focused more on the higher n layers of the $\langle 100 \rangle$ oriented perovskites. These systems shows superior light emission performances and it is proposed that the funnelling effect helps it achieve EQE of 8.8 to 11.7%^{140, 141} and current developments show that the LEDs can achieve an maximum EQE of 10.1%.¹⁴² The proof of concept of using distorted $\langle 100 \rangle$ oriented perovskites as white LEDs has been demonstrated by Hu et al. based on 2-MOP and was shown to have a maximum luminous efficacy of 16.2 lmW^{-1} .¹³⁷ Other potential applications of the $\langle 100 \rangle$ oriented perovskites include devices such as photodetectors^{130, 143-146}, lasing cavities¹⁴⁷, spintronics^{133, 148} and X-ray scintillation and detection¹⁴⁹; notably in lasing applications, it is also nanostructured to further enhance the performance¹⁵⁰⁻¹⁵².

As for the $\langle 110 \rangle$ cut of perovskite, this usually exists in a corrugated form and is typically described as a m by n $\langle 100 \rangle$ oriented perovskite. The most commonly reported of such structures in the lead halide family thus far are 2×2 APIPbBr₄¹⁰⁷, (AETU)PbBr₄¹⁵³, (N-MEDA)PbBr₄¹⁵⁴, (3-APr)PbBr₄¹⁵⁵, (EDBE)PbBr₄¹²⁴ and (IEA)PbBr₄¹²⁷. α -DMEN¹⁵⁶ and (4PNEA)₂PbI₄¹⁵⁷ are the only two 3×3 system reported thus far. [API = N-(3-aminopropyl)imidazole and AETU = S-(aminoethyl)isothiourea, N-MEDA = N1-methylethane-1,2-diammonium, 3APr = 3-aminopyrrolidinium, EDBE = 2,2-(ethylenedioxy)bis(ethylammonium), IEA = 2-(1H-Imidazol-1-yl)ethan ammonium] are the only two 3×3 systems reported thus far. The $\langle 110 \rangle$ oriented perovskites are gaining some attention because they produce broadband white light emission which suggests they have potential application for lighting purposes. Within this class of $\langle 110 \rangle$ oriented perovskite, there is a general consensus that the octahedral structural deformation, as measured through octahedral tilting and octahedral distortion¹³⁵, and the broadness of the photoluminescence peak are correlated but only for the lead bromide family of materials. The lead iodide family of $\langle 110 \rangle$ oriented perovskites, such as (EDBE)PbI₄, does not show any white light emission, although it does show considerable excitonic emission peak broadening with a FWHM = 70 nm¹²⁶. Work to unravel the underlying mechanism is still incomplete but has thus far produced evidence that suggests that self-trapped excitons play a central role in causing the white light emission in the lead bromide family. Theoretical studies have shown how the charges are being delocalized and trapped, thus forming polarons^{125, 158}. When more $\langle 110 \rangle$ oriented perovskites have been discovered, and subjected to detailed spectroscopic studies, the origin might then be better understood.

Lastly, the $\langle 111 \rangle$ -oriented perovskites are much rarer and to the best of my knowledge, have not been reported in hybrid organic-inorganic perovskites. This class is mostly produced by trivalent cations such as in $\text{Cs}_3\text{Sb}_2\text{I}_9$ ^{159, 160}, $\text{Rb}_3\text{Sb}_2\text{I}_9$ ¹⁶⁰ and $\text{Rb}_3\text{Bi}_2\text{I}_9$ ¹⁶¹ with some characteristic broadened emission and have been proposed to have potential applications as radiation detectors.¹⁶⁰

2.5 Lower dimensional perovskites: 1D and other novel perovskite-like structures

Polymorphism, as defined by IUCr, is a crystallographic phenomenon where the compound takes on a same chemical compound, but different crystal structure¹⁶² and an example would be the element carbon existing as either graphite, with a hexagonal structure, or diamond, with a isometric tetrahedral structure. A subset of polymorphism of particular interest is the phenomena of polytypism, which is defined as structures which occurs in several different structural modifications, each of which may be regarded as built up by stacking layers of (nearly) identical structure and composition, and if the modifications differ only in their stacking sequence¹⁶³. This group of polytype structures are most seen using the Ramsdell notation¹⁶⁴ or occasionally with the modified Gard notation in crystallographic journals¹⁶³. Briefly, in the Ramsdell notation, the structures are written as nX , where n would refer to the number of layers per repeat unit, and X would refer to the primitive unit cell; i.e. H for hexagonal, R for rhombohedral, or C for cubic.

The system of classification of 1-D perovskites is less developed than that for layered 2-D perovskites. This is particularly because almost any material in which metal halide octahedra are joined to form a continuous chain is called a 1-D perovskite. These systems take on a variety of names in literature, from “one-dimensional perovskite” (Fig 2.8 a)^{165, 166}, “zigzag edge sharing perovskite” (Fig 2.8c)¹⁶⁷, “double chain one-dimensional perovskite”¹⁶⁸, “face sharing polytype”¹⁶⁹, “bromoplumbate chains” (Fig 2.8 b)¹⁷⁰, “perovskitoid”^{169, 171} and even “1D metal halide nanotube”¹⁷². While Stoumpos et al. first introduced “perovskitoids” as having exclusively face-sharing connectivity between the $[\text{MI}_6]^{4-}$ octahedra¹⁶⁹, the term “perovskitoids” was later broadened to include materials with edge and face sharing connectivity¹⁷¹. The

definition remains vague and does not capture the periodicity effect of the lead halide octahedra connectivity. With the three variants of connectivity, corner, edge and face sharing, there is an almost infinite number of combinations which could result in such a 1-D chain, all of which result in an apparent “nanowire” configuration, yet each structure is distinct. As a result, in this thesis a new notation is proposed in a later chapter, to provide a systematic way of classifying such systems.

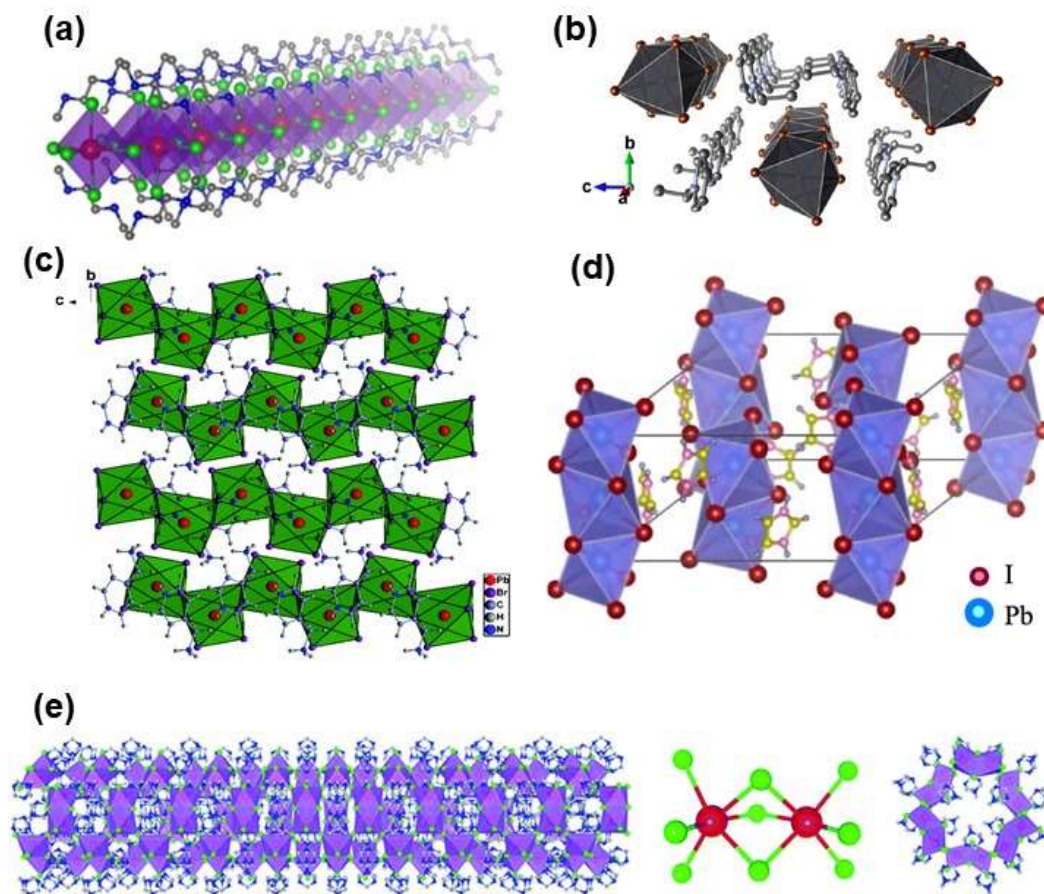


Figure 2.8 Various reported 1D and novel type perovskite or perovskitoid structures (a) one dimensional lead halide perovskite (DMEDA)PbBr₄¹⁶⁵ (b) 1D bromoplumbate 1-(Ethyl)pyridin-1-ium lead bromide¹⁷⁰ (c) one dimensional zigzag edge-sharing perovskite (AMP)PbBr₄¹⁶⁷ (d) one dimensional ImPbI₃¹⁶⁶ and (e) one dimensional nanotube (HMTA)₃Pb₂Br₇¹⁷². [DMEDA = N,N'-dimethylethylenediamine, AMP = 4-(aminomethyl)pyridinium, Im = imidazolium, HMTA = hexamethylenetetramine]

Since this class of material is still underexplored, studies done on this group of 1-D perovskites remain very fragmentary and largely focused on the structural

characterization and exploration of the broadband emission properties which this class of material typically possess¹⁷³⁻¹⁸⁷. There remains a lack of understanding of how a specific configuration of structures, for example strictly face-sharing “perovskitoids” are preferred over the others, and the database of such 1-D systems is only slowly growing. Hopefully with a greater number of organic-inorganic 1-D “perovskitoid” systems being described, there will be more clarity concerning the underlying structural chemistry.

In these reported 1-D systems, the broadband emission, as seen in Fig 2.9, and is typically also accompanied by a large Stokes shift and a long PL lifetime. These experimental observations support the hypothesis that a self-trapped exciton is responsible for the broadband emission although there has been only limited spectroscopic work to provide further experimental evidence of self-trapped excitons (STE)¹⁸⁸, and some theoretical work on multiple site emission¹⁸⁹. On top of the obvious lighting applications for such broadband emitters, when used in LEDs there are also alternative possible applications in the area of non-linear optics¹⁹⁰. In these reported 1-D systems, the broadband emission is typically also accompanied by a heavily Stokes shifted and a long PL lifetime. These experimental observations support the hypothesis that self-trapped exciton is responsible for the broadband emission although there have been limited spectroscopic work to provide further experimental evidence on self-trapped exciton (STE)¹⁸⁸, and theoretical work multiplier site emission¹⁸⁹. On top of the obvious lighting applications in LEDs which such broadband emitter, there are also alternative applications e.g. in the area of non-linear optics¹⁹⁰.

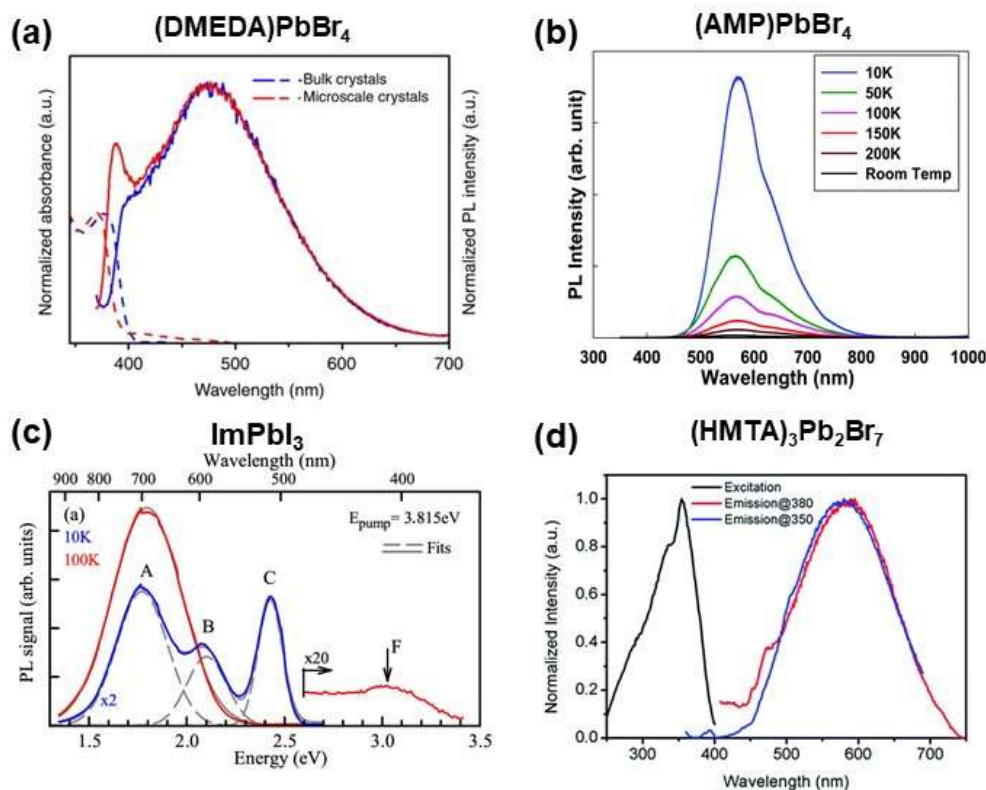


Figure 2.9 Reported photoluminescence spectra of (a) (DMEDA)PbBr₄¹⁶⁵ (b) (AMP)PbBr₄¹⁶⁷ (c) ImPbI₃¹⁶⁶ and (d) (HMTA)₃Pb₂Br₇¹⁷². All the variants of 1D perovskite exhibits varying degree of broadband emission.

References

1. Onoda-Yamamuro, N.; Matsuo, T.; Suga, H., Dielectric study of CH₃NH₃PbX₃ (X = Cl, Br, I). *Journal of Physics and Chemistry of Solids* **1992**, 53 (7), 935-939.
2. Wasylishen, R. E.; Knop, O.; Macdonald, J. B., Cation rotation in methylammonium lead halides. *Solid State Communications* **1985**, 56 (7), 581-582.
3. Weber, D., The Perovskite System CH₃NH₃ [PbnSn1-3X₃] (X = Cl, Br, I). *Zeitschrift fur Naturforschung - Section B Journal of Chemical Sciences* **1979**, 34 (7), 939-941.
4. Mitzi, D. B.; Feild, C. A.; Harrison, W. T. A.; Guloy, A. M., Conducting tin halides with a layered organic-based perovskite structure. *Nature* **1994**, 369, 467.

5. Mitzi, D. B.; Wang, S.; Feild, C. A.; Chess, C. A.; Guloy, A. M., Conducting Layered Organic-inorganic Halides Containing 110 -Oriented Perovskite Sheets. *Science* **1995**, 267 (5203), 1473-1476.
6. Mitzi, D. B., Synthesis, Structure, and Properties of Organic-Inorganic Perovskites and Related Materials. In *Progress in Inorganic Chemistry*, 1999; pp 1-121.
7. Ema, K.; Umeda, K.; Toda, M.; Yajima, C.; Arai, Y.; Kunugita, H.; Wolverson, D.; Davies, J. J., Huge exchange energy and fine structure of excitons in an organic-inorganic quantum well material. *Physical Review B* **2006**, 73 (24), 241310.
8. Ishi, J.; Mizuno, M.; Kunugita, H.; Ema, K.; Iwamoto, S.; Hayase, S.; Kondo, T.; Ito, R., Third-Order Optical Nonlinearity Due to Excitons and Biexcitons in a Self-Organized Quantum-Well Material $(\text{C}_6\text{H}_{13}\text{NH}_3)_2\text{PbI}_4$. *Journal of Nonlinear Optical Physics & Materials* **1998**, 07 (01), 153-159.
9. Salau, A. M.; Kuku, T. A.; Akinnifesi, J. O., Vacuum deposited KPbI_3 films for use in photothermal conversion. *Solar & Wind Technology* **1987**, 4 (2), 151-155.
10. Kojima, A.; Teshima, K.; Shirai, Y.; Miyasaka, T., Organometal Halide Perovskites as Visible-Light Sensitizers for Photovoltaic Cells. *Journal of the American Chemical Society* **2009**, 131 (17), 6050-6051.
11. Im, J.-H.; Lee, C.-R.; Lee, J.-W.; Park, S.-W.; Park, N.-G., 6.5% efficient perovskite quantum-dot-sensitized solar cell. *Nanoscale* **2011**, 3 (10), 4088-4093.
12. Kim, H.-S.; Lee, C.-R.; Im, J.-H.; Lee, K.-B.; Moehl, T.; Marchioro, A.; Moon, S.-J.; Humphry-Baker, R.; Yum, J.-H.; Moser, J. E.; Grätzel, M.; Park, N.-G., Lead Iodide Perovskite Sensitized All-Solid-State Submicron Thin Film Mesoscopic Solar Cell with Efficiency Exceeding 9%. *Scientific Reports* **2012**, 2, 591.
13. Lee, M. M.; Teuscher, J.; Miyasaka, T.; Murakami, T. N.; Snaith, H. J., Efficient Hybrid Solar Cells Based on Meso-Superstructured Organometal Halide Perovskites. *Science* **2012**, 338 (6107), 643-647.
14. Liu, D.; Kelly, T. L., Perovskite solar cells with a planar heterojunction structure prepared using room-temperature solution processing techniques. *Nature Photonics* **2013**, 8, 133.
15. Wang, J. T.-W.; Ball, J. M.; Barea, E. M.; Abate, A.; Alexander-Webber, J. A.; Huang, J.; Saliba, M.; Mora-Sero, I.; Bisquert, J.; Snaith, H. J.; Nicholas, R. J., Low-Temperature Processed Electron Collection Layers of Graphene/ TiO_2 Nanocomposites in Thin Film Perovskite Solar Cells. *Nano Letters* **2014**, 14 (2), 724-730.

16. Wojciechowski, K.; Saliba, M.; Leijtens, T.; Abate, A.; Snaith, H. J., Sub-150 [degree]C processed meso-superstructured perovskite solar cells with enhanced efficiency. *Energy & Environmental Science* **2014**, 7 (3), 1142-1147.
17. Mazzarella, L.; Lin, Y.-H.; Kirner, S.; Morales-Vilches, A. B.; Korte, L.; Albrecht, S.; Crossland, E.; Stannowski, B.; Case, C.; Snaith, H. J.; Schlattmann, R., Infrared Light Management Using a Nanocrystalline Silicon Oxide Interlayer in Monolithic Perovskite/Silicon Heterojunction Tandem Solar Cells with Efficiency above 25%. *Advanced Energy Materials* **2019**, 9 (14), 1803241.
18. Xing, G.; Mathews, N.; Sun, S.; Lim, S. S.; Lam, Y. M.; Grätzel, M.; Mhaisalkar, S.; Sum, T. C., Long-Range Balanced Electron- and Hole-Transport Lengths in Organic-Inorganic CH₃NH₃PbI₃. *Science* **2013**, 342, 344-347.
19. Green, M. A.; Ho-Baillie, A.; Snaith, H. J., The emergence of perovskite solar cells. *Nat. Photonics* **2014**, 8, 506-514.
20. Zhou, H.; Chen, Q.; Li, G.; Luo, S.; Song, T.-b.; Duan, H.-S.; Hong, Z.; You, J.; Liu, Y.; Yang, Y., Interface engineering of highly efficient perovskite solar cells. *Science* **2014**, 345 (6196), 542-546.
21. Yin, W.-J.; Shi, T.; Yan, Y., Unusual defect physics in CH₃NH₃PbI₃ perovskite solar cell absorber. *Appl. Phys. Lett.* **2014**, 104, 063903.
22. Brandt, R. E.; Stevanović, V.; Ginley, D. S.; Buonassisi, T., Identifying defect-tolerant semiconductors with high minority-carrier lifetimes: beyond hybrid lead halide perovskites. *MRS Commun* **2015**, 5, 265-275.
23. D'Innocenzo, V.; Srimath Kandada, A. R.; De Bastiani, M.; Gandini, M.; Petrozza, A., Tuning the Light Emission Properties by Band Gap Engineering in Hybrid Lead Halide Perovskite. *Journal of the American Chemical Society* **2014**, 136 (51), 17730-17733.
24. McMeekin, D. P.; Sadoughi, G.; Rehman, W.; Eperon, G. E.; Saliba, M.; Hörantner, M. T.; Haghighirad, A.; Sakai, N.; Korte, L.; Rech, B.; Johnston, M. B.; Herz, L. M.; Snaith, H. J., A mixed-cation lead mixed-halide perovskite absorber for tandem solar cells. *Science* **2016**, 351 (6269), 151-155.
25. Stoumpos, C. C.; Kanatzidis, M. G., Halide Perovskites: Poor Man's High-Performance Semiconductors. *Advanced Materials* **2016**, 28 (28), 5778-5793.
26. Chin, X. Y.; Cortecchia, D.; Yin, J.; Bruno, A.; Soci, C., Lead iodide perovskite light-emitting field-effect transistor. *Nat. Commun.* **2015**, 6, 7383.

27. Cho, H.; Jeong, S.-H.; Park, M.-H.; Kim, Y.-H.; Wolf, C.; Lee, C.-L.; Heo, J. H.; Sadhanala, A.; Myoung, N.; Yoo, S.; Im, S. H.; Friend, R. H.; Lee, T.-W., Overcoming the electroluminescence efficiency limitations of perovskite light-emitting diodes. *Science* **2015**, *350* (6265), 1222-1225.
28. Wong, A. B.; Lai, M.; Eaton, S. W.; Yu, Y.; Lin, E.; Dou, L.; Fu, A.; Yang, P., Growth and Anion Exchange Conversion of CH₃NH₃PbX₃ Nanorod Arrays for Light-Emitting Diodes. *Nano Lett.* **2015**, *15*, 5519-5524.
29. Tan, Z.-K.; Moghaddam, R. S.; Lai, M. L.; Docampo, P.; Higler, R.; Deschler, F.; Price, M.; Sadhanala, A.; Pazos, L. M.; Credgington, D.; Hanusch, F.; Bein, T.; Snaith, H. J.; Friend, R. H., Bright light-emitting diodes based on organometal halide perovskite. *Nat. Nanotech.* **2014**, *9*, 687-692.
30. Zhu, H.; Fu, Y.; Meng, F.; Wu, X.; Gong, Z.; Ding, Q.; Gustafsson, M. V.; Trinh, M. T.; Jin, S.; Zhu, X. Y., Lead halide perovskite nanowire lasers with low lasing thresholds and high quality factors. *Nat. Mater.* **2015**, *14*, 636-642.
31. Sutherland, B. R.; Hoogland, S.; Adachi, M. M.; Wong, C. T. O.; Sargent, E. H., Conformal Organohalide Perovskites Enable Lasing on Spherical Resonators. *ACS Nano*. **2014**, *8*, 10947-10952.
32. Xing, G.; Mathews, N.; Lim, S. S.; Yantara, N.; Liu, X.; Sabba, D.; Grätzel, M.; Mhaisalkar, S.; Sum, T. C., Low-temperature solution-processed wavelength-tunable perovskites for lasing. *Nat. Mater.* **2014**, *13*, 476.
33. Cadelano, M.; Sarritzu, V.; Sestu, N.; Marongiu, D.; Chen, F.; Piras, R.; Corpino, R.; Carbonaro, C. M.; Quochi, F.; Saba, M.; Mura, A.; Bongiovanni, G., Can Trihalide Lead Perovskites Support Continuous Wave Lasing? *Adv. Opt. Mater.* **2015**, *3*, 1557-1564.
34. Neutzner, S.; Srimath Kandada, A. R.; Lanzani, G.; Petrozza, A., A dual-phase architecture for efficient amplified spontaneous emission in lead iodide perovskites. *J. Mater. Chem. C* **2016**, *4*, 4630-4633.
35. Yuan, F.; Wu, Z.; Dong, H.; Xia, B.; Xi, J.; Ning, S.; Ma, L.; Hou, X., Electric field-modulated amplified spontaneous emission in organo-lead halide perovskite CH₃NH₃PbI₃. *Appl. Phys. Lett.* **2015**, *107*, 261106.
36. Gratzel, M., The light and shade of perovskite solar cells. *Nat. Mater.* **2014**, *13*, 838-842.

37. Filippetti, A.; Caddeo, C.; Delugas, P.; Mattoni, A., Appealing Perspectives of Hybrid Lead–Iodide Perovskites as Thermoelectric Materials. *J. Phys. Chem. C* **2016**, *120*, 28472-28479.
38. Chen, W.; Bhaumik, S.; Veldhuis, S. A.; Xing, G.; Xu, Q.; Grätzel, M.; Mhaisalkar, S.; Mathews, N.; Sum, T. C., Giant five-photon absorption from multidimensional core-shell halide perovskite colloidal nanocrystals. *Nat. Commun.* **2017**, *8*, 15198.
39. Vegard, L., Die Konstitution der Mischkristalle und die Raumfüllung der Atome. *Zeitschrift für Physik* **1921**, *5* (1), 17-26.
40. Denton, A. R.; Ashcroft, N. W., Vegard's law. *Physical Review A* **1991**, *43* (6), 3161-3164.
41. Goldschmidt, V. M., Die Gesetze der Krystallochemie. *Naturwissenschaften* **1926**, *14* (21), 477-485.
42. Dang, Y.; Ju, D.; Wang, L.; Tao, X., Recent progress in the synthesis of hybrid halide perovskite single crystals. *CrystEngComm* **2016**, *18* (24), 4476-4484.
43. Brenner, T. M.; Egger, D. A.; Kronik, L.; Hodes, G.; Cahen, D., Hybrid organic—inorganic perovskites: low-cost semiconductors with intriguing charge-transport properties. *Nat. Rev. Mater.* **2016**, *1*, 15007.
44. Stranks, S. D.; Eperon, G. E.; Grancini, G.; Menelaou, C.; Alcocer, M. J. P.; Leijtens, T.; Herz, L. M.; Petrozza, A.; Snaith, H. J., Electron-Hole Diffusion Lengths Exceeding 1 Micrometer in an Organometal Trihalide Perovskite Absorber. *Science* **2013**, *342*, 341-344.
45. Savenije, T. J.; Ponseca, C. S.; Kunneman, L.; Abdellah, M.; Zheng, K.; Tian, Y.; Zhu, Q.; Canton, S. E.; Scheblykin, I. G.; Pullerits, T.; Yartsev, A.; Sundström, V., Thermally Activated Exciton Dissociation and Recombination Control the Carrier Dynamics in Organometal Halide Perovskite. *J. Phys. Chem. Lett.* **2014**, *5* (13), 2189-2194.
46. Alarousu, E.; El-Zohry, A. M.; Yin, J.; Zhumekenov, A. A.; Yang, C.; Alhabshi, E.; Gereige, I.; AlSaggaf, A.; Malko, A. V.; Bakr, O. M.; Mohammed, O. F., Ultralong Radiative States in Hybrid Perovskite Crystals: Compositions for Submillimeter Diffusion Lengths. *J. Phys. Chem. Lett.* **2017**, *8*, 4386-4390.
47. De Angelis, F.; Petrozza, A., Clues from defect photochemistry. *Nat. Mater.* **2018**, *17* (5), 383-384.

48. Maynard, B.; Long, Q.; Schiff, E. A.; Yang, M.; Zhu, K.; Kottokkaran, R.; Abbas, H.; Dalal, V. L., Electron and hole drift mobility measurements on methylammonium lead iodide perovskite solar cells. *Appl. Phys. Lett.* **2016**, *108* (17), 173505.
49. Wehrenfennig, C.; Eperon, G. E.; Johnston, M. B.; Snaith, H. J.; Herz, L. M., High Charge Carrier Mobilities and Lifetimes in Organolead Trihalide Perovskites. *Adv. Mater.* **2014**, *26* (10), 1584-1589.
50. Ahn, N.; Son, D.-Y.; Jang, I.-H.; Kang, S. M.; Choi, M.; Park, N.-G., Highly Reproducible Perovskite Solar Cells with Average Efficiency of 18.3% and Best Efficiency of 19.7% Fabricated via Lewis Base Adduct of Lead(II) Iodide. *J. Am. Chem. Soc.* **2015**, *137* (27), 8696-8699.
51. Stoumpos, C. C.; Malliakas, C. D.; Kanatzidis, M. G., Semiconducting Tin and Lead Iodide Perovskites with Organic Cations: Phase Transitions, High Mobilities, and Near-Infrared Photoluminescent Properties. *Inorg. Chem.* **2013**, *52* (15), 9019-9038.
52. Chen, Y.; Peng, J.; Su, D.; Chen, X.; Liang, Z., Efficient and Balanced Charge Transport Revealed in Planar Perovskite Solar Cells. *ACS Appl. Mater. Interfaces* **2015**, *7* (8), 4471-4475.
53. Ghosh, T.; Aharon, S.; Etgar, L.; Ruhman, S., Free Carrier Emergence and Onset of Electron-Phonon Coupling in Methylammonium Lead Halide Perovskite Films. *J. Am. Chem. Soc.* **2017**, *139* (50), 18262-18270.
54. Miyata, K.; Meggiolaro, D.; Trinh, M. T.; Joshi, P. P.; Mosconi, E.; Jones, S. C.; De Angelis, F.; Zhu, X.-Y., Large polarons in lead halide perovskites. *Sci. Adv.* **2017**, *3*.
55. Zhu, X. Y.; Podzorov, V., Charge Carriers in Hybrid Organic-Inorganic Lead Halide Perovskites Might Be Protected as Large Polarons. *J. Phys. Chem. Lett.* **2015**, *6*, 4758-4761.
56. Slonopas, A.; Foley, B. J.; Choi, J. J.; Gupta, M. C., Charge transport in bulk CH₃NH₃PbI₃ perovskite. *J. Appl. Phys.* **2016**, *119*, 074101.
57. Yang, X.; Wang, Y.; Li, H.; Sheng, C., Optical Properties of Heterojunction between Hybrid Halide Perovskite and Charge Transport Materials: Exciplex Emission and Large Polaron. *J. Phys. Chem. C* **2016**, *120*, 23299-23303.
58. Ivanovska, T.; Dionigi, C.; Mosconi, E.; De Angelis, F.; Liscio, F.; Morandi, V.; Ruani, G., Long-Lived Photoinduced Polarons in Organohalide Perovskites. *J. Phys. Chem. Lett.* **2017**, *8*, 3081-3086.

59. La-o-vorakiat, C.; Xia, H.; Kadro, J.; Salim, T.; Zhao, D.; Ahmed, T.; Lam, Y. M.; Zhu, J.-X.; Marcus, R. A.; Michel-Beyerle, M.-E.; Chia, E. E. M., Phonon Mode Transformation Across the Orthorhombic–Tetragonal Phase Transition in a Lead Iodide Perovskite $\text{CH}_3\text{NH}_3\text{PbI}_3$: A Terahertz Time-Domain Spectroscopy Approach. *J. Phys. Chem. Lett.* **2016**, *7*, 1-6.
60. Valverde-Chavez, D. A.; Ponseca, C. S.; Stoumpos, C. C.; Yartsev, A.; Kanatzidis, M. G.; Sundstrom, V.; Cooke, D. G., Intrinsic femtosecond charge generation dynamics in single crystal $\text{CH}_3\text{NH}_3\text{PbI}_3$. *Energy Environ. Sci* **2015**, *8*, 3700-3707.
61. Zheng, K.; Abdellah, M.; Zhu, Q.; Kong, Q.; Jennings, G.; Kurtz, C. A.; Messing, M. E.; Niu, Y.; Gosztola, D. J.; Al-Marri, M. J.; Zhang, X.; Pullerits, T.; Canton, S. E., Direct Experimental Evidence for Photoinduced Strong-Coupling Polarons in Organolead Halide Perovskite Nanoparticles. *J. Phys. Chem. Lett.* **2016**, *7*, 4535-4539.
62. Zhu, H.; Miyata, K.; Fu, Y.; Wang, J.; Joshi, P. P.; Niesner, D.; Williams, K. W.; Jin, S.; Zhu, X.-Y., Screening in crystalline liquids protects energetic carriers in hybrid perovskites. *Science* **2016**, *353* (6306), 1409-1413.
63. Batignani, G.; Fumero, G.; Srimath Kandada, A. R.; Cerullo, G.; Gandini, M.; Ferrante, C.; Petrozza, A.; Scopigno, T., Probing femtosecond lattice displacement upon photo-carrier generation in lead halide perovskite. *Nat. Commun.* **2018**, *9* (1), 1971.
64. Park, M.; Neukirch, A. J.; Reyes-Lillo, S. E.; Lai, M.; Ellis, S. R.; Dietze, D.; Neaton, J. B.; Yang, P.; Tretiak, S.; Mathies, R. A., Excited-state vibrational dynamics toward the polaron in methylammonium lead iodide perovskite. *Nat. Commun.* **2018**, *9* (1), 2525.
65. Tsai, H.; Nie, W.; Blancon, J. C.; Stoumpos, C. C.; Soe, C. M. M.; Yoo, J.; Crochet, J.; Tretiak, S.; Even, J.; Sadhanala, A.; Azzellino, G.; Brenes, R.; Ajayan, P. M.; Bulović, V.; Stranks, S. D.; Friend, R. H.; Kanatzidis, M. G.; Mohite, A. D., Stable Light-Emitting Diodes Using Phase-Pure Ruddlesden–Popper Layered Perovskites. *Advanced Materials* **2018**, *30* (6), 1704217.
66. Baikie, T.; Fang, Y.; Kadro, J. M.; Schreyer, M.; Wei, F.; Mhaisalkar, S. G.; Graetzel, M.; White, T. J., Synthesis and crystal chemistry of the hybrid perovskite $(\text{CH}_3\text{NH}_3)\text{PbI}_3$ for solid-state sensitised solar cell applications. *Journal of Materials Chemistry A* **2013**, *1* (18), 5628-5641.

67. Maalej, A.; Abid, Y.; Kallel, A.; Daoud, A.; Lautié, A.; Romain, F., Phase transitions and crystal dynamics in the cubic perovskite $\text{CH}_3\text{NH}_3\text{PbCl}_3$. *Solid State Communications* **1997**, *103* (5), 279-284.
68. Kim, H.-S.; Kim, S. K.; Kim, B. J.; Shin, K.-S.; Gupta, M. K.; Jung, H. S.; Kim, S.-W.; Park, N.-G., Ferroelectric Polarization in $\text{CH}_3\text{NH}_3\text{PbI}_3$ Perovskite. *The Journal of Physical Chemistry Letters* **2015**, *6* (9), 1729-1735.
69. Leguy, A. M. A.; Frost, J. M.; McMahon, A. P.; Sakai, V. G.; Kockelmann, W.; Law, C.; Li, X.; Foglia, F.; Walsh, A.; O'Regan, B. C.; Nelson, J.; Cabral, J. T.; Barnes, P. R. F., The dynamics of methylammonium ions in hybrid organic-inorganic perovskite solar cells. *Nature Communications* **2015**, *6* (1), 7124.
70. Li, L.; Shang, X.; Wang, S.; Dong, N.; Ji, C.; Chen, X.; Zhao, S.; Wang, J.; Sun, Z.; Hong, M.; Luo, J., Bilayered Hybrid Perovskite Ferroelectric with Giant Two-Photon Absorption. *Journal of the American Chemical Society* **2018**, *140* (22), 6806-6809.
71. Fan, Z.; Xiao, J.; Sun, K.; Chen, L.; Hu, Y.; Ouyang, J.; Ong, K. P.; Zeng, K.; Wang, J., Ferroelectricity of $\text{CH}_3\text{NH}_3\text{PbI}_3$ Perovskite. *The Journal of Physical Chemistry Letters* **2015**, *6* (7), 1155-1161.
72. Hoque, M. N. F.; Yang, M.; Li, Z.; Islam, N.; Pan, X.; Zhu, K.; Fan, Z., Polarization and Dielectric Study of Methylammonium Lead Iodide Thin Film to Reveal its Nonferroelectric Nature under Solar Cell Operating Conditions. *ACS Energy Letters* **2016**, *1* (1), 142-149.
73. Rosales, B. A.; Men, L.; Cady, S. D.; Hanrahan, M. P.; Rossini, A. J.; Vela, J., Persistent Dopants and Phase Segregation in Organolead Mixed-Halide Perovskites. *Chemistry of Materials* **2016**, *28* (19), 6848-6859.
74. Kubicki, D. J.; Prochowicz, D.; Hofstetter, A.; Zakeeruddin, S. M.; Grätzel, M.; Emsley, L., Phase Segregation in Cs-, Rb- and K-Doped Mixed-Cation $(\text{MA})_x(\text{FA})_{1-x}\text{PbI}_3$ Hybrid Perovskites from Solid-State NMR. *Journal of the American Chemical Society* **2017**, *139* (40), 14173-14180.
75. Kubicki, D. J.; Prochowicz, D.; Hofstetter, A.; Zakeeruddin, S. M.; Grätzel, M.; Emsley, L., Phase Segregation in Potassium-Doped Lead Halide Perovskites from ^{39}K Solid-State NMR at 21.1 T. *Journal of the American Chemical Society* **2018**, *140* (23), 7232-7238.
76. Karmakar, A.; Askar, A. M.; Bernard, G. M.; Terskikh, V. V.; Ha, M.; Patel, S.; Shankar, K.; Michaelis, V. K., Mechanochemical Synthesis of Methylammonium Lead

Mixed-Halide Perovskites: Unraveling the Solid-Solution Behavior Using Solid-State NMR. *Chemistry of Materials* **2018**, *30* (7), 2309-2321.

77. Kubicki, D. J.; Prochowicz, D.; Hofstetter, A.; Saski, M.; Yadav, P.; Bi, D.; Pellet, N.; Lewiński, J.; Zakeeruddin, S. M.; Grätzel, M.; Emsley, L., Formation of Stable Mixed Guanidinium-Methylammonium Phases with Exceptionally Long Carrier Lifetimes for High-Efficiency Lead Iodide-Based Perovskite Photovoltaics. *Journal of the American Chemical Society* **2018**, *140* (9), 3345-3351.

78. Mosconi, E.; Amat, A.; Nazeeruddin, M. K.; Grätzel, M.; De Angelis, F., First-Principles Modeling of Mixed Halide Organometal Perovskites for Photovoltaic Applications. *The Journal of Physical Chemistry C* **2013**, *117* (27), 13902-13913.

79. Gong, J.; Yang, M.; Ma, X.; Schaller, R. D.; Liu, G.; Kong, L.; Yang, Y.; Beard, M. C.; Lesslie, M.; Dai, Y.; Huang, B.; Zhu, K.; Xu, T., Electron-Rotor Interaction in Organic-Inorganic Lead Iodide Perovskites Discovered by Isotope Effects. *The Journal of Physical Chemistry Letters* **2016**, *7* (15), 2879-2887.

80. Motta, C.; El-Mellouhi, F.; Kais, S.; Tabet, N.; Alharbi, F.; Sanvito, S., Revealing the role of organic cations in hybrid halide perovskite CH₃NH₃PbI₃. *Nature Communications* **2015**, *6* (1), 7026.

81. Wilkening, M.; Heitjans, P., Li jump process in h-Li_{0.7}TiS₂ studied by two-time ⁷Li spin-alignment echo NMR and comparison with results on two-dimensional diffusion from nuclear magnetic relaxation. *Physical Review B* **2008**, *77* (2), 024311.

82. Bloembergen, N.; Purcell, E. M.; Pound, R. V., Relaxation Effects in Nuclear Magnetic Resonance Absorption. *Physical Review* **1948**, *73* (7), 679-712.

83. Knop, O.; Wasylishen, R. E.; White, M. A.; Cameron, T. S.; Oort, M. J. M. V., Alkylammonium lead halides. Part 2. CH₃NH₃PbX₃ (X = Cl, Br, I) perovskites: cuboctahedral halide cages with isotropic cation reorientation. *Canadian Journal of Chemistry* **1990**, *68* (3), 412-422.

84. Xu, Q.; Eguchi, T.; Nakayama, H.; Nakamura, N.; Kishita, M., Molecular Motions and Phase Transitions in Solid CH₃NH₃PbX₃ (X = Cl, Br, I) as Studied by NMR and NQR. In *Zeitschrift für Naturforschung A*, 1991; Vol. 46, p 240.

85. Fabini, D. H.; Siaw, T. A.; Stoumpos, C. C.; Laurita, G.; Olds, D.; Page, K.; Hu, J. G.; Kanatzidis, M. G.; Han, S.; Seshadri, R., Universal Dynamics of Molecular Reorientation in Hybrid Lead Iodide Perovskites. *Journal of the American Chemical Society* **2017**, *139* (46), 16875-16884.

86. Baikie, T.; Barrow, N. S.; Fang, Y.; Keenan, P. J.; Slater, P. R.; Piltz, R. O.; Gutmann, M.; Mhaisalkar, S. G.; White, T. J., A combined single crystal neutron/X-ray diffraction and solid-state nuclear magnetic resonance study of the hybrid perovskites $\text{CH}_3\text{NH}_3\text{PbX}_3$ ($\text{X} = \text{I}, \text{Br}$ and Cl). *Journal of Materials Chemistry A* **2015**, 3 (17), 9298-9307.
87. Senocrate, A.; Moudrakovski, I.; Kim, G. Y.; Yang, T.-Y.; Gregori, G.; Grätzel, M.; Maier, J., The Nature of Ion Conduction in Methylammonium Lead Iodide: A Multimethod Approach. *Angewandte Chemie International Edition* **2017**, 56 (27), 7755-7759.
88. Bernard, G. M.; Wasylishen, R. E.; Ratcliffe, C. I.; Terskikh, V.; Wu, Q.; Buriak, J. M.; Hauger, T., Methylammonium Cation Dynamics in Methylammonium Lead Halide Perovskites: A Solid-State NMR Perspective. *The Journal of Physical Chemistry A* **2018**, 122 (6), 1560-1573.
89. Franssen, W. M. J.; van Es, S. G. D.; Dervişoğlu, R.; de Wijs, G. A.; Kentgens, A. P. M., Symmetry, Dynamics, and Defects in Methylammonium Lead Halide Perovskites. *The Journal of Physical Chemistry Letters* **2017**, 8 (1), 61-66.
90. Ruddlesden, S. N.; Popper, P., The compound $\text{Sr}_3\text{Ti}_2\text{O}_7$ and its structure. *Acta Crystallographica* **1958**, 11 (1), 54-55.
91. Aurivillius, B., Mixed bismuth oxides with layer lattices. II. Structure of $\text{Bi}_4\text{Ti}_3\text{O}_{12}$. *Arkiv for Kemi* **1949**, 1 (54), 463-480.
92. Jacobson, A. J.; Johnson, J. W.; Lewandowski, J. T., Interlayer chemistry between thick transition-metal oxide layers: synthesis and intercalation reactions of $\text{K}[\text{Ca}_2\text{N}_{3n-3}\text{Nb}_n\text{O}_{3n+1}]$ ($3 \leq n \leq 7$). *Inorganic Chemistry* **1985**, 24 (23), 3727-3729.
93. Dion, M.; Ganne, M.; Tournoux, M., Nouvelles familles de phases $\text{MIMII}_2\text{Nb}_3\text{O}_{10}$ a feuillets "perovskites". *Materials Research Bulletin* **1981**, 16 (11), 1429-1435.
94. Soe, C. M. M.; Stoumpos, C. C.; Kepenekian, M.; Traoré, B.; Tsai, H.; Nie, W.; Wang, B.; Katan, C.; Seshadri, R.; Mohite, A. D.; Even, J.; Marks, T. J.; Kanatzidis, M. G., New Type of 2D Perovskites with Alternating Cations in the Interlayer Space, $(\text{C}(\text{NH}_2)_3)(\text{CH}_3\text{NH}_3)_n\text{Pb}_n\text{I}_{3n+1}$: Structure, Properties, and Photovoltaic Performance. *Journal of the American Chemical Society* **2017**, 139 (45), 16297-16309.

95. Mao, L.; Ke, W.; Pedesseau, L.; Wu, Y.; Katan, C.; Even, J.; Wasielewski, M. R.; Stoumpos, C. C.; Kanatzidis, M. G., Hybrid Dion–Jacobson 2D Lead Iodide Perovskites. *Journal of the American Chemical Society* **2018**, *140* (10), 3775–3783.
96. Mandal, T. K.; Sivakumar, T.; Augustine, S.; Gopalakrishnan, J., Heterovalent cation-substituted Aurivillius phases, $\text{Bi}_2\text{SrNaNb}_2\text{TaO}_{12}$ and $\text{Bi}_2\text{Sr}_2\text{Nb}_{3-x}\text{M}_x\text{O}_{12}$ ($\text{M}=\text{Zr}, \text{Hf}, \text{Fe}, \text{Zn}$). *Materials Science and Engineering: B* **2005**, *121* (1), 112–119.
97. Yuan, Z.; Shu, Y.; Tian, Y.; Xin, Y.; Ma, B., A facile one-pot synthesis of deep blue luminescent lead bromide perovskite microdisks. *Chemical Communications* **2015**, *51* (91), 16385–16388.
98. Liang, D.; Peng, Y.; Fu, Y.; Shearer, M. J.; Zhang, J.; Zhai, J.; Zhang, Y.; Hamers, R. J.; Andrew, T. L.; Jin, S., Color-Pure Violet-Light-Emitting Diodes Based on Layered Lead Halide Perovskite Nanoplates. *ACS Nano* **2016**, *10* (7), 6897–6904.
99. Deng, W.; Fang, H.; Jin, X.; Zhang, X.; Zhang, X.; Jie, J., Organic–inorganic hybrid perovskite quantum dots for light-emitting diodes. *Journal of Materials Chemistry C* **2018**, *6* (18), 4831–4841.
100. Jin, X.; Zhang, X.; Fang, H.; Deng, W.; Xu, X.; Jie, J.; Zhang, X., Facile Assembly of High-Quality Organic–Inorganic Hybrid Perovskite Quantum Dot Thin Films for Bright Light-Emitting Diodes. *Advanced Functional Materials* **2018**, *28* (11), 1705189.
101. Chandran, B. K.; Veldhuis, S. A.; Chin, X. Y.; Bruno, A.; Yantara, N.; Chen, X.; Mhaisalkar, S., Precursor non-stoichiometry to enable improved $\text{CH}_3\text{NH}_3\text{PbBr}_3$ nanocrystal LED performance. *Physical Chemistry Chemical Physics* **2018**, *20* (8), 5918–5925.
102. Mitzi, D. B., Templating and structural engineering in organic-inorganic perovskites. *Journal of the Chemical Society, Dalton Transactions* **2001**, (1), 1–12.
103. Mitzi, D. B.; Dimitrakopoulos, C. D.; Kosbar, L. L., Structurally Tailored Organic–Inorganic Perovskites: Optical Properties and Solution-Processed Channel Materials for Thin-Film Transistors. *Chemistry of Materials* **2001**, *13* (10), 3728–3740.
104. Calabrese, J.; Jones, N. L.; Harlow, R. L.; Herron, N.; Thorn, D. L.; Wang, Y., Preparation and characterization of layered lead halide compounds. *Journal of the American Chemical Society* **1991**, *113* (6), 2328–2330.
105. Stoumpos, C. C.; Cao, D. H.; Clark, D. J.; Young, J.; Rondinelli, J. M.; Jang, J. I.; Hupp, J. T.; Kanatzidis, M. G., Ruddlesden–Popper Hybrid Lead Iodide Perovskite 2D Homologous Semiconductors. *Chemistry of Materials* **2016**, *28* (8), 2852–2867.

106. Brown, A. A. M.; Hooper, T. J. N.; Veldhuis, S. A.; Chin, X. Y.; Bruno, A.; Vashishtha, P.; Tey, J. N.; Jiang, L.; Damodaran, B.; Pu, S. H.; Mhaisalkar, S. G.; Mathews, N., Self-assembly of a robust hydrogen-bonded octylphosphonate network on cesium lead bromide perovskite nanocrystals for light-emitting diodes. *Nanoscale* **2019**, *11* (25), 12370-12380.
107. Li, Y. Y.; Lin, C. K.; Zheng, G. L.; Cheng, Z. Y.; You, H.; Wang, W. D.; Lin, J., Novel $\langle 110 \rangle$ -Oriented Organic-Inorganic Perovskite Compound Stabilized by N-(3-Aminopropyl)imidazole with Improved Optical Properties. *Chemistry of Materials* **2006**, *18* (15), 3463-3469.
108. Vargas, B.; Ramos, E.; Pérez-Gutiérrez, E.; Alonso, J. C.; Solis-Ibarra, D., A Direct Bandgap Copper-Antimony Halide Perovskite. *Journal of the American Chemical Society* **2017**, *139* (27), 9116-9119.
109. Byun, J.; Cho, H.; Wolf, C.; Jang, M.; Sadhanala, A.; Friend, R. H.; Yang, H.; Lee, T.-W., Efficient Visible Quasi-2D Perovskite Light-Emitting Diodes. *Advanced Materials* **2016**, *28* (34), 7515-7520.
110. Papadatos, D.; Vassilakopoulou, A.; Koutselas, I., Energy transfer yellow light emitting diodes based on blends of quasi-2D perovskites. *Journal of Luminescence* **2017**, *188*, 567-576.
111. Chen, Y.; Sun, Y.; Peng, J.; Tang, J.; Zheng, K.; Liang, Z., 2D Ruddlesden-Popper Perovskites for Optoelectronics. *Advanced Materials* **2018**, *30* (2), 1703487.
112. Shang, Y.; Liao, Y.; Wei, Q.; Wang, Z.; Xiang, B.; Ke, Y.; Liu, W.; Ning, Z., Highly stable hybrid perovskite light-emitting diodes based on Dion-Jacobson structure. *Science Advances* **2019**, *5* (8), eaaw8072.
113. Koh, T. M.; Shanmugam, V.; Schlipf, J.; Oesinghaus, L.; Müller-Buschbaum, P.; Ramakrishnan, N.; Swamy, V.; Mathews, N.; Boix, P. P.; Mhaisalkar, S. G., Nanostructuring Mixed-Dimensional Perovskites: A Route Toward Tunable, Efficient Photovoltaics. *Advanced Materials* **2016**, *28* (19), 3653-3661.
114. Chaudhary, B.; Koh, T. M.; Febriansyah, B.; Bruno, A.; Mathews, N.; Mhaisalkar, S. G.; Soci, C., Mixed-Dimensional Naphthylmethylammonium-Methylammonium Lead Iodide Perovskites with Improved Thermal Stability. *Scientific Reports* **2020**, *10* (1), 429.
115. Li, Z.; Liu, X.; Xu, J.; Yang, S.; Zhao, H.; Huang, H.; Liu, S. F.; Yao, J., 2D-3D $\text{Cs}_2\text{PbI}_2\text{Cl}_2\text{-CsPbI}_{2.5}\text{Br}_{0.5}$ Mixed-Dimensional Films for All-Inorganic

Perovskite Solar Cells with Enhanced Efficiency and Stability. *The Journal of Physical Chemistry Letters* **2020**, *11* (10), 4138-4146.

116. Krishna, A.; Gottis, S.; Nazeeruddin, M. K.; Sauvage, F., Mixed Dimensional 2D/3D Hybrid Perovskite Absorbers: The Future of Perovskite Solar Cells? *Advanced Functional Materials* **2019**, *29* (8), 1806482.

117. Liu, G.; Zheng, H.; Xu, X.; Zhu, L.-Z.; Zhang, X.; Pan, X., Design of High-Efficiency and Environmentally Stable Mixed-Dimensional Perovskite Solar Cells Based on Cesium-Formamidinium Lead Halide Component. *Chemistry of Materials* **2018**, *30* (21), 7691-7698.

118. Koh, T. M.; Thirumal, K.; Soo, H. S.; Mathews, N., Multidimensional Perovskites: A Mixed Cation Approach Towards Ambient Stable and Tunable Perovskite Photovoltaics. *ChemSusChem* **2016**, *9* (18), 2541-2558.

119. Zhang, F.; Kim, D. H.; Zhu, K., 3D/2D multidimensional perovskites: Balance of high performance and stability for perovskite solar cells. *Current Opinion in Electrochemistry* **2018**, *11*, 105-113.

120. Cortecchia, D.; Lew, K. C.; So, J.-K.; Bruno, A.; Soci, C., Cathodoluminescence of Self-Organized Heterogeneous Phases in Multidimensional Perovskite Thin Films. *Chemistry of Materials* **2017**, *29* (23), 10088-10094.

121. Qin, Z.; Dai, S.; Gajjela, C. C.; Wang, C.; Hadjiev, V. G.; Yang, G.; Li, J.; Zhong, X.; Tang, Z.; Yao, Y.; Guloy, A. M.; Reddy, R.; Mayerich, D.; Deng, L.; Yu, Q.; Feng, G.; Calderon, H. A.; Robles Hernandez, F. C.; Wang, Z. M.; Bao, J., Spontaneous Formation of 2D/3D Heterostructures on the Edges of 2D Ruddlesden–Popper Hybrid Perovskite Crystals. *Chemistry of Materials* **2020**, *32* (12), 5009-5015.

122. Pellegrino, G.; D'Angelo, S.; Deretzis, I.; Condorelli, G. G.; Smecca, E.; Malandrino, G.; La Magna, A.; Alberti, A., From PbI₂ to MAPbI₃ through Layered Intermediates. *The Journal of Physical Chemistry C* **2016**, *120* (35), 19768-19777.

123. Yang, Z.; Wei, M.; Voznyy, O.; Todorovic, P.; Liu, M.; Quintero-Bermudez, R.; Chen, P.; Fan, J. Z.; Proppe, A. H.; Quan, L. N.; Walters, G.; Tan, H.; Chang, J.-W.; Jeng, U. S.; Kelley, S. O.; Sargent, E. H., Anchored Ligands Facilitate Efficient B-Site Doping in Metal Halide Perovskites. *Journal of the American Chemical Society* **2019**, *141* (20), 8296-8305.

124. Cortecchia, D.; Yin, J.; Bruno, A.; Lo, S.-Z. A.; Gurzadyan, G. G.; Mhaisalkar, S.; Bredas, J.-L.; Soci, C., Polaron self-localization in white-light emitting hybrid perovskites. *J. Mater. Chem. C* **2017**, *5* (11), 2771-2780.

125. Yin, J.; Li, H.; Cortecchia, D.; Soci, C.; Brédas, J.-L., Excitonic and Polaronic Properties of 2D Hybrid Organic–Inorganic Perovskites. *ACS Energy Lett.* **2017**, *2*, 417-423.
126. Cortecchia, D.; Neutzner, S.; Srimath Kandada, A. R.; Mosconi, E.; Meggiolaro, D.; De Angelis, F.; Soci, C.; Petrozza, A., Broadband Emission in Two-Dimensional Hybrid Perovskites: The Role of Structural Deformation. *J. Am. Chem. Soc.* **2017**, *139* (1), 39-42.
127. Febriansyah, B.; Giovanni, D.; Ramesh, S.; Koh, T. M.; Li, Y.; Sum, T. C.; Mathews, N.; England, J., Inducing formation of a corrugated, white-light emitting 2D lead-bromide perovskite via subtle changes in templating cation. *Journal of Materials Chemistry C* **2020**, *8* (3), 889-893.
128. Blancon, J. C.; Stier, A. V.; Tsai, H.; Nie, W.; Stoumpos, C. C.; Traoré, B.; Pedesseau, L.; Kepenekian, M.; Katsutani, F.; Noe, G. T.; Kono, J.; Tretiak, S.; Crooker, S. A.; Katan, C.; Kanatzidis, M. G.; Crochet, J. J.; Even, J.; Mohite, A. D., Scaling law for excitons in 2D perovskite quantum wells. *Nature Communications* **2018**, *9* (1), 2254.
129. Wu, X.; Trinh, M. T.; Zhu, X. Y., Excitonic Many-Body Interactions in Two-Dimensional Lead Iodide Perovskite Quantum Wells. *The Journal of Physical Chemistry C* **2015**, *119* (26), 14714-14721.
130. Zhou, J.; Chu, Y.; Huang, J., Photodetectors Based on Two-Dimensional Layer-Structured Hybrid Lead Iodide Perovskite Semiconductors. *ACS Applied Materials & Interfaces* **2016**, *8* (39), 25660-25666.
131. Manchon, A.; Koo, H. C.; Nitta, J.; Frolov, S. M.; Duine, R. A., New perspectives for Rashba spin–orbit coupling. *Nature Materials* **2015**, *14* (9), 871-882.
132. Dresselhaus, G.; Kip, A. F.; Kittel, C., Spin-Orbit Interaction and the Effective Masses of Holes in Germanium. *Physical Review* **1954**, *95* (2), 568-569.
133. Zhai, Y.; Baniya, S.; Zhang, C.; Li, J.; Haney, P.; Sheng, C.-X.; Ehrenfreund, E.; Vardeny, Z. V., Giant Rashba splitting in 2D organic-inorganic halide perovskites measured by transient spectroscopies. *Science Advances* **2017**, *3* (7), e1700704.
134. Long, G.; Jiang, C.; Sabatini, R.; Yang, Z.; Wei, M.; Quan, L. N.; Liang, Q.; Rasmita, A.; Askerka, M.; Walters, G.; Gong, X.; Xing, J.; Wen, X.; Quintero-Bermudez, R.; Yuan, H.; Xing, G.; Wang, X. R.; Song, D.; Voznyy, O.; Zhang, M.; Hoogland, S.; Gao, W.; Xiong, Q.; Sargent, E. H., Spin control in reduced-dimensional chiral perovskites. *Nature Photonics* **2018**, *12* (9), 528-533.

135. Robinson, K.; Gibbs, G. V.; Ribbe, P. H., Quadratic Elongation: A Quantitative Measure of Distortion in Coordination Polyhedra. *Science* **1971**, *172* (3983), 567-570.
136. Alonso, J. A.; Martínez-Lope, M. J.; Casais, M. T.; Fernández-Díaz, M. T., Evolution of the Jahn–Teller Distortion of MnO₆ Octahedra in RMnO₃ Perovskites (R = Pr, Nd, Dy, Tb, Ho, Er, Y): A Neutron Diffraction Study. *Inorganic Chemistry* **2000**, *39* (5), 917-923.
137. Hu, H.; Morris, S. A.; Qiao, X.; Zhao, D.; Salim, T.; Chen, B.; Chia, E. E. M.; Lam, Y. M., Molecular engineering of two-dimensional hybrid perovskites with broadband emission for white light-emitting diodes. *Journal of Materials Chemistry C* **2018**, *6* (38), 10301-10307.
138. Smith, M. D.; Jaffe, A.; Dohner, E. R.; Lindenberg, A. M.; Karunadasa, H. I., Structural origins of broadband emission from layered Pb-Br hybrid perovskites. *Chemical Science* **2017**, *8* (6), 4497-4504.
139. Era, M.; Morimoto, S.; Tsutsui, T.; Saito, S., Organic-inorganic heterostructure electroluminescent device using a layered perovskite semiconductor (C₆H₅C₂H₄NH₃)₂PbI₄. *Applied Physics Letters* **1994**, *65* (6), 676-678.
140. Yuan, M.; Quan, L. N.; Comin, R.; Walters, G.; Sabatini, R.; Voznyy, O.; Hoogland, S.; Zhao, Y.; Beauregard, E. M.; Kanjanaboos, P.; Lu, Z.; Kim, D. H.; Sargent, E. H., Perovskite energy funnels for efficient light-emitting diodes. *Nature Nanotechnology* **2016**, *11* (10), 872-877.
141. Zhang, S.; Yi, C.; Wang, N.; Sun, Y.; Zou, W.; Wei, Y.; Cao, Y.; Miao, Y.; Li, R.; Yin, Y.; Zhao, N.; Wang, J.; Huang, W., Efficient Red Perovskite Light-Emitting Diodes Based on Solution-Processed Multiple Quantum Wells. *Advanced Materials* **2017**, *29* (22), 1606600.
142. Vashishtha, P.; Ng, M.; Shivarudraiah, S. B.; Halpert, J. E., High Efficiency Blue and Green Light-Emitting Diodes Using Ruddlesden–Popper Inorganic Mixed Halide Perovskites with Butylammonium Interlayers. *Chemistry of Materials* **2019**, *31* (1), 83-89.
143. Li, L.; Sun, Z.; Wang, P.; Hu, W.; Wang, S.; Ji, C.; Hong, M.; Luo, J., Tailored Engineering of an Unusual (C₄H₉NH₃)₂(CH₃NH₃)₂Pb₃Br₁₀ Two-Dimensional Multilayered Perovskite Ferroelectric for a High-Performance Photodetector. *Angewandte Chemie International Edition* **2017**, *56* (40), 12150-12154.

144. Fu, Q.; Wang, X.; Liu, F.; Dong, Y.; Liu, Z.; Zheng, S.; Chaturvedi, A.; Zhou, J.; Hu, P.; Zhu, Z.; Bo, F.; Long, Y.; Liu, Z., Ultrathin Ruddlesden–Popper Perovskite Heterojunction for Sensitive Photodetection. *Small* **2019**, *15* (39), 1902890.
145. Leng, K.; Abdelwahab, I.; Verzhbitskiy, I.; Telychko, M.; Chu, L.; Fu, W.; Chi, X.; Guo, N.; Chen, Z.; Chen, Z.; Zhang, C.; Xu, Q.-H.; Lu, J.; Chhowalla, M.; Eda, G.; Loh, K. P., Molecularly thin two-dimensional hybrid perovskites with tunable optoelectronic properties due to reversible surface relaxation. *Nature Materials* **2018**, *17* (10), 908-914.
146. Han, S.; Yao, Y.; Liu, X.; Li, B.; Ji, C.; Sun, Z.; Hong, M.; Luo, J., Highly Oriented Thin Films of 2D Ruddlesden–Popper Hybrid Perovskite toward Superfast Response Photodetectors. *Small* **2019**, *15* (39), 1901194.
147. Raghavan, C. M.; Chen, T.-P.; Li, S.-S.; Chen, W.-L.; Lo, C.-Y.; Liao, Y.-M.; Haider, G.; Lin, C.-C.; Chen, C.-C.; Sankar, R.; Chang, Y.-M.; Chou, F.-C.; Chen, C.-W., Low-Threshold Lasing from 2D Homologous Organic–Inorganic Hybrid Ruddlesden–Popper Perovskite Single Crystals. *Nano Letters* **2018**, *18* (5), 3221-3228.
148. Kepenekian, M.; Even, J., Rashba and Dresselhaus Couplings in Halide Perovskites: Accomplishments and Opportunities for Spintronics and Spin–Orbitronics. *The Journal of Physical Chemistry Letters* **2017**, *8* (14), 3362-3370.
149. Birowosuto, M. D.; Cortecchia, D.; Drozdowski, W.; Brylew, K.; Lachmanski, W.; Bruno, A.; Soci, C., X-ray Scintillation in Lead Halide Perovskite Crystals. *Scientific Reports* **2016**, *6*, 37254.
150. Li, M.; Wei, Q.; Muduli, S. K.; Yantara, N.; Xu, Q.; Mathews, N.; Mhaisalkar, S. G.; Xing, G.; Sum, T. C., Enhanced Exciton and Photon Confinement in Ruddlesden–Popper Perovskite Microplatelets for Highly Stable Low-Threshold Polarized Lasing. *Advanced Materials* **2018**, *30* (23), 1707235.
151. Zhang, H.; Liao, Q.; Wu, Y.; Zhang, Z.; Gao, Q.; Liu, P.; Li, M.; Yao, J.; Fu, H., 2D Ruddlesden–Popper Perovskites Microring Laser Array. *Advanced Materials* **2018**, *30* (15), 1706186.
152. Zhang, H.; Wu, Y.; Liao, Q.; Zhang, Z.; Liu, Y.; Gao, Q.; Liu, P.; Li, M.; Yao, J.; Fu, H., A Two-Dimensional Ruddlesden–Popper Perovskite Nanowire Laser Array based on Ultrafast Light-Harvesting Quantum Wells. *Angewandte Chemie International Edition* **2018**, *57* (26), 7748-7752.

153. Li, Y.; Zheng, G.; Lin, J., Synthesis, Structure, and Optical Properties of a Contorted <110>-Oriented Layered Hybrid Perovskite: $\text{C}_3\text{H}_{11}\text{SN}_3\text{PbBr}_4$. *European Journal of Inorganic Chemistry* **2008**, 2008 (10), 1689-1692.
154. Dohner, E. R.; Hoke, E. T.; Karunadasa, H. I., Self-Assembly of Broadband White-Light Emitters. *Journal of the American Chemical Society* **2014**, 136 (5), 1718-1721.
155. Li, X.; Guo, P.; Kepenekian, M.; Hadar, I.; Katan, C.; Even, J.; Stoumpos, C. C.; Schaller, R. D.; Kanatzidis, M. G., Small Cyclic Diammonium Cation Templated (110)-Oriented 2D Halide (X = I, Br, Cl) Perovskites with White-Light Emission. *Chemistry of Materials* **2019**, 31 (9), 3582-3590.
156. Mao, L.; Wu, Y.; Stoumpos, C. C.; Wasielewski, M. R.; Kanatzidis, M. G., White-Light Emission and Structural Distortion in New Corrugated Two-Dimensional Lead Bromide Perovskites. *Journal of the American Chemical Society* **2017**, 139 (14), 5210-5215.
157. Tremblay, M.-H.; Thouin, F.; Leisen, J.; Bacsá, J.; Srimath Kandada, A. R.; Hoffman, J. M.; Kanatzidis, M. G.; Mohite, A. D.; Silva, C.; Barlow, S.; Marder, S. R., (4NPEA) 2PbI_4 (4NPEA = 4-Nitrophenylethylammonium): Structural, NMR, and Optical Properties of a 3×3 Corrugated 2D Hybrid Perovskite. *Journal of the American Chemical Society* **2019**, 141 (11), 4521-4525.
158. Neutzner, S.; Thouin, F.; Cortecchia, D.; Petrozza, A.; Silva, C.; Srimath Kandada, A. R., Exciton-polaron spectral structures in two-dimensional hybrid lead-halide perovskites. *Physical Review Materials* **2018**, 2 (6), 064605.
159. Ivanov, Y. N.; Sukhovskii, A. A.; Lisin, V. V.; Aleksandrova, I. P., Phase Transitions of $\text{Cs}_3\text{Sb}_2\text{I}_9$, $\text{Cs}_3\text{Bi}_2\text{I}_9$, and $\text{Cs}_3\text{Bi}_2\text{Br}_9$ Crystals. *Inorganic Materials* **2001**, 37 (6), 623-627.
160. McCall, K. M.; Stoumpos, C. C.; Kostina, S. S.; Kanatzidis, M. G.; Wessels, B. W., Strong Electron-Phonon Coupling and Self-Trapped Excitons in the Defect Halide Perovskites $\text{A}_3\text{M}_2\text{I}_9$ (A = Cs, Rb; M = Bi, Sb). *Chemistry of Materials* **2017**, 29 (9), 4129-4145.
161. Chang, J.-H.; Doert, T.; Ruck, M., Structural Variety of Defect Perovskite Variants $\text{M}_3\text{E}_2\text{X}_9$ (M = Rb, Tl, E = Bi, Sb, X = Br, I). *Zeitschrift für anorganische und allgemeine Chemie* **2016**, 642 (13), 736-748.
162. Crystallography, I. U. o.

163. Guinier, A.; Bokij, G. B.; Boll-Dornberger, K.; Cowley, J. M.; Durovic, S.; Jagodzinski, H.; Krishna, P.; de Wolff, P. M.; Zvyagin, B. B.; Cox, D. E.; Goodman, P.; Hahn, T.; Kuchitsu, K.; Abrahams, S. C., Nomenclature of polytype structures. Report of the International Union of Crystallography Ad hoc Committee on the Nomenclature of Disordered, Modulated and Polytype Structures. *Acta Crystallographica Section A* **1984**, *40* (4), 399-404.
164. Ramsdell, L. S., Studies on silicon carbide. *American Mineralogist* **1947**, *42*, 64.
165. Yuan, Z.; Zhou, C.; Tian, Y.; Shu, Y.; Messier, J.; Wang, J. C.; van de Burgt, L. J.; Kountouriotis, K.; Xin, Y.; Holt, E.; Schanze, K.; Clark, R.; Siegrist, T.; Ma, B., One-dimensional organic lead halide perovskites with efficient bluish white-light emission. *Nature Communications* **2017**, *8*, 14051.
166. Seth, C.; Jana, D.; Jindal, V.; Khushalani, D.; Ghosh, S., One-Dimensional Behavior of Imidazolium Lead Iodide. *The Journal of Physical Chemistry C* **2019**, *123* (26), 16449-16455.
167. Jung, M.-H., Broadband white light emission from one-dimensional zigzag edge-sharing perovskite. *New Journal of Chemistry* **2020**, *44* (1), 171-180.
168. Jodlowski, A. D.; Yépez, A.; Luque, R.; Camacho, L.; de Miguel, G., Benign-by-Design Solventless Mechanochemical Synthesis of Three-, Two-, and One-Dimensional Hybrid Perovskites. *Angewandte Chemie International Edition* **2016**, *55* (48), 14972-14977.
169. Stoumpos, C. C.; Mao, L.; Malliakas, C. D.; Kanatzidis, M. G., Structure–Band Gap Relationships in Hexagonal Polytypes and Low-Dimensional Structures of Hybrid Tin Iodide Perovskites. *Inorganic Chemistry* **2017**, *56* (1), 56-73.
170. Febriansyah, B.; Neo, C. S. D.; Giovanni, D.; Srivastava, S.; Lekina, Y.; Koh, T. M.; Li, Y.; Shen, Z. X.; Asta, M.; Sum, T. C.; Mathews, N.; England, J., Targeted Synthesis of Trimeric Organic–Bromoplumbate Hybrids That Display Intrinsic, Highly Stokes-Shifted, Broadband Emission. *Chemistry of Materials* **2020**, *32* (11), 4431-4441.
171. Li, X.; He, Y.; Kepenekian, M.; Guo, P.; Ke, W.; Even, J.; Katan, C.; Stoumpos, C. C.; Schaller, R. D.; Kanatzidis, M. G., Three-Dimensional Lead Iodide Perovskitoid Hybrids with High X-ray Photoresponse. *Journal of the American Chemical Society* **2020**, *142* (14), 6625-6637.

172. Lin, H.; Zhou, C.; Tian, Y.; Besara, T.; Neu, J.; Siegrist, T.; Zhou, Y.; Bullock, J.; Schanze, K. S.; Ming, W.; Du, M.-H.; Ma, B., Bulk assembly of organic metal halide nanotubes. *Chemical Science* **2017**, 8 (12), 8400-8404.
173. Hoffman, J. M.; Che, X.; Sidhik, S.; Li, X.; Hadar, I.; Blancon, J.-C.; Yamaguchi, H.; Kepenekian, M.; Katan, C.; Even, J.; Stoumpos, C. C.; Mohite, A. D.; Kanatzidis, M. G., From 2D to 1D Electronic Dimensionality in Halide Perovskites with Stepped and Flat Layers Using Propylammonium as a Spacer. *Journal of the American Chemical Society* **2019**, 141 (27), 10661-10676.
174. Barkaoui, H.; Abid, H.; Zelewski, S.; Urban, J.; Baranowski, M.; Mlayah, A.; Triki, S.; Plochocka, P.; Abid, Y., Negative Thermal Quenching of Efficient White-Light Emission in a 1D Ladder-Like Organic/Inorganic Hybrid Material. *Advanced Optical Materials* **2019**, 7 (20), 1900763.
175. Bakthavatsalam, R.; Haris, M. P. U.; Shaikh, S. R.; Lohar, A.; Mohanty, A.; Moghe, D.; Sharma, S.; Biswas, C.; Raavi, S. S. K.; Gonnade, R. G.; Kundu, J., Ligand Structure Directed Dimensionality Reduction (2D \rightarrow 1D) in Lead Bromide Perovskite. *The Journal of Physical Chemistry C* **2020**, 124 (3), 1888-1897.
176. Sun, C.; Yue, Y.-D.; Zhang, W.-F.; Sun, X.-Y.; Du, Y.; Pan, H.-M.; Ma, Y.-Y.; He, Y.-C.; Li, M.-T.; Jing, Z.-H., [DMEDA]PbCl₄: a one-dimensional organic lead halide perovskite with efficient yellow emission. *CrystEngComm* **2020**, 22 (8), 1480-1486.
177. Sun, C.; Guo, Y.-H.; Yuan, Y.; Chu, W.-X.; He, W.-L.; Che, H.-X.; Jing, Z.-H.; Yue, C.-Y.; Lei, X.-W., Broadband White-Light Emission in One-Dimensional Organic-Inorganic Hybrid Silver Halide. *Inorganic Chemistry* **2020**, 59 (7), 4311-4319.
178. Li, D.; Wu, W.; Wang, S.; Zhang, X.; Li, L.; Yao, Y.; Peng, Y.; Luo, J., A one-dimensional dual emissive hybrid perovskite with flexibly tunable white-light emission. *Journal of Materials Chemistry C* **2020**, 8 (20), 6710-6714.
179. Zhang, W.; Tao, K.; Ji, C.; Sun, Z.; Han, S.; Zhang, J.; Wu, Z.; Luo, J., (C₆H₁₃N)₂BiI₅: A One-Dimensional Lead-Free Perovskite-Derivative Photoconductive Light Absorber. *Inorganic Chemistry* **2018**, 57 (8), 4239-4243.
180. Febriansyah, B.; Koh, T. M.; John, R. A.; Ganguly, R.; Li, Y.; Bruno, A.; Mhaisalkar, S. G.; England, J., Inducing Panchromatic Absorption and Photoconductivity in Polycrystalline Molecular 1D Lead-Iodide Perovskites through π -Stacked Viologens. *Chemistry of Materials* **2018**, 30 (17), 5827-5830.

181. Yue, C.-Y.; Lin, N.; Gao, L.; Jin, Y.-X.; Liu, Z.-Y.; Cao, Y.-Y.; Han, S.-S.; Lian, X.-K.; Hu, B.; Lei, X.-W., Organic cation directed one-dimensional cuprous halide compounds: syntheses, crystal structures and photoluminescence properties. *Dalton Transactions* **2019**, 48 (27), 10151-10159.
182. Duong, T.-M. H.; Nobusue, S.; Tada, H., Face-shared structures of one-dimensional organic–inorganic lead iodide perovskites. *Applied Physics Express* **2018**, 11 (11), 115502.
183. Lin, H.; Zhou, C.; Neu, J.; Zhou, Y.; Han, D.; Chen, S.; Worku, M.; Chaaban, M.; Lee, S.; Berkwits, E.; Siegrist, T.; Du, M.-H.; Ma, B., Bulk Assembly of Corrugated 1D Metal Halides with Broadband Yellow Emission. *Advanced Optical Materials* **2019**, 7 (6), 1801474.
184. Biswas, A.; Bakthavatsalam, R.; Shaikh, S. R.; Shinde, A.; Lohar, A.; Jena, S.; Gonnade, R. G.; Kundu, J., Efficient Broad-Band Emission from Contorted Purely Corner-Shared One Dimensional (1D) Organic Lead Halide Perovskite. *Chemistry of Materials* **2019**, 31 (7), 2253-2257.
185. Zhou, C.; Tian, Y.; Khabou, O.; Worku, M.; Zhou, Y.; Hurley, J.; Lin, H.; Ma, B., Manganese-Doped One-Dimensional Organic Lead Bromide Perovskites with Bright White Emissions. *ACS Applied Materials & Interfaces* **2017**, 9 (46), 40446-40451.
186. García-Espejo, G.; Rodríguez-Padrón, D.; Pérez-Morales, M.; Luque, R.; de Miguel, G.; Camacho, L., Mechanochemical synthesis of one-dimensional (1D) hybrid perovskites incorporating polycyclic aromatic spacers: highly fluorescent cation-based materials. *Journal of Materials Chemistry C* **2018**, 6 (28), 7677-7682.
187. Barkaoui, H.; Abid, H.; Yangu, A.; Triki, S.; Boukheddaden, K.; Abid, Y., Yellowish White-Light Emission Involving Resonant Energy Transfer in a New One-Dimensional Hybrid Material: (C₉H₁₀N₂)PbCl₄. *The Journal of Physical Chemistry C* **2018**, 122 (42), 24253-24261.
188. Gautier, R.; Paris, M.; Massuyeau, F., Exciton Self-Trapping in Hybrid Lead Halides: Role of Halogen. *Journal of the American Chemical Society* **2019**, 141 (32), 12619-12623.
189. Du, M.-H., Emission Trend of Multiple Self-Trapped Excitons in Luminescent 1D Copper Halides. *ACS Energy Letters* **2020**, 5 (2), 464-469.

190. Yuan, C.; Li, X.; Semin, S.; Feng, Y.; Rasing, T.; Xu, J., Chiral Lead Halide Perovskite Nanowires for Second-Order Nonlinear Optics. *Nano Letters* **2018**, *18* (9), 5411-5417.

Chapter 3

Experimental Methodology

Experimental details and rationales for synthetic techniques are discussed in detail; synthesis via the hydrohalic acid route was favoured due to its higher yields. Subsequently, the various characterization techniques are discussed in greater detail. While structural analysis revolves around X-ray diffraction and solid state Nuclear Magnetic Resonance spectroscopy, optoelectronic properties were probed by laser-based techniques.

3.1 Synthesis

There are three main synthesis routes which have been reported in literature to obtain isolated single crystals of inorganic-organic hybrid perovskites, namely inverse temperature crystallization, antisolvent vapor assisted crystallization and crystallization from hydrohalic acid. The medium in which the techniques utilizes varies; in the first two mentioned technique, the salts are dissolved in stoichiometric ratios in organic solvent, most commonly DMF, while in the hydrohalic acid route, the reaction is carried out in excess acid, and hence, is in an aqueous medium. The synthetic route from hydrohalic acid is the preferred choice in this thesis because of its relative synthetic ease and the ability to obtain crystals on the gram scale.

3.1.1 Crystallization from hydrohalic acid

The synthesis of 2D Ruddlesden-Popper hybrid perovskites are generally very successful and proceed in high yield. In the early work done by Stoumpos et al¹, it was demonstrated that the hybrid perovskites are capable of crystallizing as the mixed-dimension forms by utilizing stoichiometric amounts of 2D to 3D hybrid perovskite cations. In general, the starting precursors are added to hydrobromic acid in stoichiometric amounts and the solution is heated to obtain complete dissolution, then cooled to obtain the desired crystals.

By extension of these synthetic principles, this method was utilized in this work for the synthesis of $\text{API}_2\text{Pb}_3\text{Br}_{10}$, IEAPbBr_4 and the various polymorphs of imidazole lead bromide. This technique is favoured because the samples could be facilely synthesized and isolated on the gram scale. Slow cooling of the supersaturated solution would further yield high quality crystals on which further studies by single crystal X-ray diffraction could be carried out. Notably, as will be described below the ratio of the initial concentrations of the imidazole to lead oxide was found to greatly affect the purity of the product giving rise to the discovery of polymorphs.

During the synthesis, 10 mmol of PbO was added to 20 mmol of hydrobromic acid with gentle heating and stirring. Upon complete dissolution of PbO , the reaction vessel was cooled in an ice bath and 10 mmol of amine (e.g. 1,3-aminopropyl imidazole) was

added to the reaction vessel with gentle. Stirring. White precipitates were observed instantaneously, and the solution was then gently heated while stirring until the precipitate had dissolved. The solution was then cooled, whereupon the crystals slowly formed. The crystals were isolated by suction filtration and dried under reduced pressure for 12 hours.

The preparation of IEABr was synthesized as reported elsewhere² with some slight modification. Imidazole (1.63 g, 24 mmol), 2-chloroethylamine hydrochloride (3.00 g, 25.9 mmol), NaOH (3.45) and tetrabutylammonium hydrogensulfate catalyst (0.3 g) was reacted in acetonitrile (75 ml) under reflux for 24 hours. The solution was subsequently filtered under reduced pressure using a Buchner funnel with sintered disc. The filtrate was concentrated on a rotary evaporator and placed under reduced pressure ($\sim 5 \times 10^{-2}$ torr) for around 6 h to remove ACN whereupon it yielded an oil (3.16 g). Hydrobromic acid 48% aqueous (5 ml) was added to the oil to convert IEA from the free base form into the IEABr salt. Ethanol (20 ml) was added to the solution and white IEABr salt was precipitated by adding diethyl ether. The process of re-dispersing in ethanol and precipitating with diethyl ether was repeated twice. White precipitates of IEABr were harvested and dried under reduced pressure to yield IEABr salt (1.37 g, 29.6%). Solution NMR (^1H and ^{13}C) was performed by dissolving the salt in DMSO- d_6 to verify the signature of IEABr using a Bruker AVANCE I 400 MHz spectrometer. For the imidazole lead bromides, a starting PbO to imidazole ratio of 1:2 yielded approximately 60% IMIPbBr₃ and 40% IMI₂PbBr₄. The crystals could be separated by hand while viewing them under a polarizing microscope based on the morphology and shape of the crystal. Using a starting PbO to imidazole ratio of 1:4 yielded approximately 60% IMI₂PbBr₄ and 40% IMI₃PbBr₅. However, the two polymorphs, IMI₂PbBr₄ and IMI₃PbBr₅, cannot be physically distinguished. Therefore, further analysis attempts to subtract the influence of IMI₂PbBr₄ from the bulk of IMI₃PbBr₅ since this would be a physical mixture.

3.1.2 Preparation of thin films

Thin films on the order of several hundreds of nanometers to a few microns thick can be prepared through a variety of methods. In hybrid perovskites, these films are easily obtainable through the process of spincoating. This is a highly cost effective technique

and requires a spincoater and a hotplate to do post-deposition annealing. For the preparation of MAPbI₃ thin films, the precursor solutions of MAI and lead iodide (1:1) with the desired concentrations were prepared by dissolving stoichiometric amounts of methylammonium iodide (MAI, Dyesol Inc) and lead iodide (PbI₂, 99.99%, TCI) in anhydrous N,N-dimethylformamide (DMF, Sigma-Aldrich). Calcium fluoride and intrinsic (undoped) silicon substrates were sonicated in a mixture of acetone and isopropyl alcohol (IPA) for 15 minutes followed by 30 minutes of UV/ozone treatment. The substrates were then transferred into a nitrogen filled glovebox with water and oxygen levels <1 ppm. The mixed precursor solution was spin-coated on the substrates at 4000 rpm for 30 s; toluene dripping was performed after 4 s to obtain smooth, high-quality films. The substrates were subsequently annealed at 100 °C for 15 minutes.

3.2 Material Characterization

Most of the structural characterization utilises XRD and ssNMR. This is because these techniques are complementary to each other and with the incorporation of DFT simulations, can provide a very comprehensive picture of the solved crystallographic structure. XRD is an absolute technique while ssNMR is a relative technique and each has their own limitations. Furthermore, XRD probes long range order (or disorder) of the sample whereas sNMR probes the short range interactions, and hence elucidates short range order (or disorder). They can both be augmented through DFT calculations. Further probing of optoelectronic properties involves techniques such as photoluminescence, FTIR and femtosecond transient absorption spectroscopy.

3.2.1 X-ray Diffraction: Single Crystal Diffraction (scXRD)

Diffraction refers to the physical phenomena of the spreading of waves when they pass through an opening, or around an obstacle into regions where we would not expect them. Diffraction occurs if a wave encounters an object and if the wavelength is approximately on the same order of magnitude as the object's size. This phenomenon can be seen in everyday life, for example the sun appearing red during sunset because sunlight gets diffracted by dust particles in the atmosphere or when water waves in a ripple passes through a gap in a barrier and comes out as a curved wave on the other

side. In structural analysis, X-rays are used as the source because the wavelength of X-rays are comparable to the interatomic distances of around 10^{-10} m.

Hence, if the path difference is an integer number of the wavelength, a constructive interference would be obtained; similarly, if the path difference is $n + \frac{1}{2}$ times of the wavelength, a destructive interference would be obtained. Thus, using a geometrical approach and consider the row of atoms with a d_{hkl} space apart, when in-phase incident X-ray approach the atoms at an angle θ , the path difference between the first and second row of atoms is seen to be 2Δ . Using geometrical relation of a right angled triangle, it is obvious that $\Delta = d \sin\theta$. For constructive interference to occur, this path difference would have to be an integer number of the wavelength. This would then produce the well-known Bragg equation, $2d \sin\theta = \lambda$.

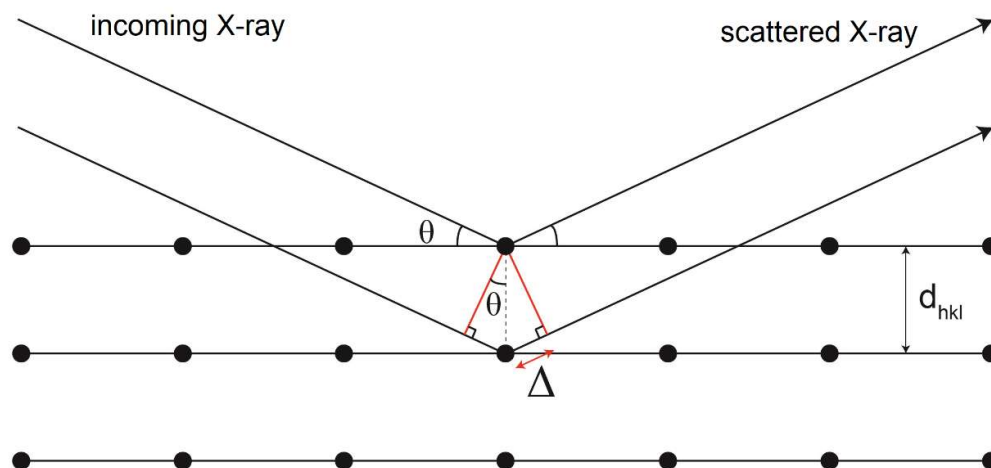


Figure 3.1 schematic showing the principles behind XRD, and Bragg's law

It should be noted, however, that this notion can be misleading on several fronts. Firstly, these X-rays are not reflected by the planes like light rays from optical mirrors but are scattered by the electrons bound to the discrete atoms. Hence, heavier atoms which consequently have more electrons are stronger scattering centres and this is quantitatively described through the structure factor, S_f . The concept of reciprocal lattice has to be introduced for detailed discussion regarding the structure factor where the reciprocal lattice is a mathematical construct invented by physicists and crystallographers to give a very convenient and succinct representation of the physics of diffraction by a crystal. Secondly, these Miller planes which are often central to the

discussion of diffraction, are only mathematical tools which help crystallographers to reconstruct and model the structure of the interested compound. The interested readers are directed to the authoritative textbooks³⁻⁵ on the detailed discussion on the derivation of reciprocal lattice and structural factor. The end objective of X-ray diffraction studies, be it single crystal or powder diffraction, is to create a chemically sensible model to describe the structure and this may require additional input of chemical knowledge from the operator. In summary, a general workflow for single-crystal X-ray diffraction is seen as follow:

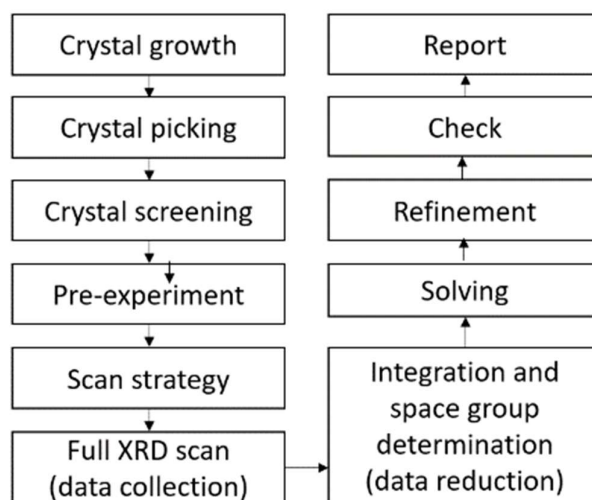


Figure 3.2 a schematic of the general flow of work for single crystal XRD studies

3.2.1.1 The Phase Problem

In the modern crystallographic analysis, most of these analyses is now turned into a black box where the user would just have to push a couple of buttons to obtain the results. The objective of this section is to quickly summarize the main techniques used, and the underlying operating principles behind the black box. In short, the phase problem arises because when incident X-rays are scattered by the atoms, the structural factor, F , which describes the properties of the X-ray contains both a real and imaginary component. However, when the scattered X-rays are collected at the detector, only the real component is captured, while the imaginary component is lost. Therefore, there is a need to retrieve the phase, which is a component of the imaginary component. Three main methods are commonly used in today's crystallographic communities, and they

are the family of Direct methods, Patterson method, and the current overwhelmingly popular dual space charge flipping method (e.g. Superflip⁶ or SHELXT⁷). Detailed mathematical treatment of the mentioned methods will not be covered in this thesis and the interested reader is directed to the textbooks^{4,8}. Each solution method has its own strength and weaknesses.

In brief, the direct methods exploit several phenomena to tackle the phase problem and is the oldest branch of methods. If the electron densities were arbitrary, then the phase problem would be unsolvable, however, it is common knowledge that the electron density is positive everywhere (*positivity constraint*) and that crystal structures are composed of point-like atoms (*atomicity constraint*). Therefore, the electron density only contains only a limited number of significant peaks while the rest of the unit cell is filled by almost zero density. Generalizing this condition would mean that the significant density is grouped into separated point and peaks; this would be known as the *sparseness constraint*. These constraints are then formulated into mathematical statements like Karle-Hauptman determinant⁹, Sayre's equation¹⁰, structure invariants and tangent formula. The general procedure would start by preparing the data, such as looking at Wilson plots and intensity statistics, then set up phase relationships through looking at triplets, then assigning the starting phases through fixing the origin and then symbolic addition. The phases are then determined using the tangent formula and lastly, checked against a figure of merit.

The Patterson method tackles the phase problem in a different approach. The structure factor magnitudes alone contain some information about the spacing of the atoms in the structure. This is done by multiplying by its complex conjugate, F_{hkl}^* , and thereby “setting” the phases to zero and the coefficient are $|F_{obs}|^2$. By intuitive inspection, the Patterson method would find itself most useful when there are a few heavy atoms among many light atoms or when a significant proportion of the molecular structure is expected to have a well-defined and known rigid geometry. It should be noted that in the Patterson map, the peaks correspond to interatomic vectors instead of the position of the atoms. However, the Patterson method effectiveness falls quickly as the number of atoms increases. A structure with N atoms will contain $N(N-1)$ interatomic vectors, and hence, becomes unsuitable for a structure with more than 50 atoms.

Lastly, in the charge flipping method, it can be thought of as a ‘brute force’ method and has been gaining popularity since the computation power is cheaply available on almost everyone’s desks. Dual space algorithms reconstruct the scattering density by modifying the scattering density in both direct and reciprocal space and by combining these modifications in an iteration scheme. The modification in both spaces are equally important and neither space can solve the phase problem alone. The fundamental idea in dual space algorithms is to start off from a random image and then reconstructed by iterations imposing known constraints upon the previous image. Thus, leaning on the constraints as highlighted in the earlier section, the *positivity constraint*, *sparseness constraint* and *atomicity constraint* in the direct space and the knowledge of the diffraction patterns (*amplitude constraint*) in the reciprocal space; in fulfilling these constraints in both the real space and reciprocal space, the algorithm iterates until it converges. One key feature of the dual space method is solving the structure in the triclinic *P1* space group, and then determines the symmetry after the structure solution. This advantage is crucial because the analysis is based on the experimental amplitudes and reconstructed phases rather than only on the amplitudes. Hence, the analysis does not suffer from ambiguities between centrosymmetric and non-centrosymmetric space groups. However, for all the advantages offered by this method, a critical condition that needs to be met is the completeness of the dataset because charge flipping would require atomic resolution to work. With the requirement of modern CIFs to have a resolution of 0.8 Å, this would usually not be a problem but would need to be kept in mind when working under extreme conditions. There are also instances where the solution is not sufficiently accurate to detect small deviations from a higher symmetry. This can be seen in cases where a large part of the structure is strongly dominated by the scattering from the heavy elements, but only a few light atoms break the symmetry. Hence, to overcome this limitation, it would be best practice to combine both standard symmetry analysis and the analysis of the electron density reconstructed by charge flipping.

To conclude, each of these techniques should be regarded as complementary techniques to each other, rather than competitors. Though dual space methods are much more popular due to the advantages that come with them, direct methods would still be a suitable choice if the structure is very large with light atoms only, or if the dataset is

incomplete, or because dual space methods fail.

3.2.1.2 Twinning

The phenomena of twinning is not uncommon in crystallography. Here, a quick introduction to twinning is examined in this section and the interested reader is directed to the textbooks for a more detailed mathematical treatment of the subject⁴. The terminology of ‘twinning’ has been loosely used to describe a manifestation of samples which are not a true single crystal, which would include flawed crystal giving split peaks, or polycrystalline segregates. However, it does carry a very specific meaning where the twinned crystal is has two (or more) orientations or mirror images of the same structure occurring together in a well-defined relationship to each other. It tends to happen more often in structures with certain configurations, such as in a monoclinic structure with β close to 90° , or when the cell axis of a is approximately the same as c . Twinning can then be understood as the result of from the ‘mistakes’ in putting the blocks of unit cells together to form the large crystal, where some regions have a different but related orientation from the other. Therefore, a mathematical treatment to describe such relationship is through a twin law, which can be expressed as a 3×3 matrix that relates the two sets of unit cell axis vectors and hence, the two sets of reflection indices. The main challenge is to firstly recognize that the diffraction is twinned, and subsequently finding the twin law. There are several types of twinning: merohedral twinning, pseudo-merohedral twinning and non-merohedral twinning.

In merohedral twinning, the two component lattices coincide exactly so reflections belonging to the two components are superimposed and each measured intensity is the sum of two separate reflection intensities with different indices related by the twin law. A particular case of merohedral twinning which can occur in any crystal system would be racemic twinning. In this scenario, the non-centrosymmetric structure is twinned with its inverted version and results in the superposition of the reflection hkl with $\overline{h}\overline{k}\overline{l}$ when Freidel’s law do not apply.

In the pseudo-merohedral twinning, the reflections almost overlap each other. This occurs when the twin operation is not a valid symmetry operation of the true crystal system but is an operation of a higher crystal system to which the lattice approximates.

An example would be a monoclinic structure with β close to 90° . A twofold rotation about either the a or c axis is not valid in the monoclinic system but valid in the orthorhombic system, where α , β and γ are all 90° .

Lastly, there would be the instance of non-merohedral twinning, and it occurs when the two lattices for twin components do not coincide at all points and only some reflections are overlapped. This form of twinning can be easily recognized by problems in unit cell determination or through visual inspection of the intensity-weighted reciprocal lattice. Once identified, the two components should be related by a simple rotation to obtain a twin law and proceed with the subsequent analysis, i.e. integration, solving and refining. As a result of twinning, the experimentally observed diffraction patterns may have higher symmetry than the true crystal structure and hence, the combination of systematic absences may appear to be impossible. Furthermore, the strong and weak reflections sometimes overlap, resulting in an averaging of intensity statistics. Often, the structure not giving a sensible solution or refinement is the main reason for looking whether the structure into twinning.

3.2.1.3 Least Squares Refinement

Least squares refinement finds its origin in statistics and the interested reader is directed to the relevant textbooks for a detailed statistical treatment of least squares refinement^{11, 12}, this section gives a brief overview on the refinement strategy. In the instance where there are more observations than the number of variables, the variables can be ‘*overdetermined*’. The quantity minimized in the refinement, the residual, is given by the expression

$$S = \sum_i w (y_o - y_c)^2 \quad (3.1)$$

where w is the assigned weighting factor for the reflection, y_o is the observed intensity and y_c is the calculated intensity from the structure model. The location of the minima of functions is usually done through calculus by setting the differential of the function to zero. Extending these same principles to non-linear least square refinements, the set of equations obtained typically cannot be solved directly. Hence, there is a need to use an initial value of the parameters (i.e. a starting model) and iterate it towards a better solution. Since there is only a small shift in the parameters, the function can be

approximated by a Taylor's expansion if the function is differentiable. Care must be taken to ensure the global minimum is reached rather than a local one and this requires the starting point of the refinement to be sufficiently close to the correct model.

Restraint and constraints which are included in the refinement stage are very helpful as it allows us to input certain knowledge into the refinements and help to reduce any uncertainties involved. Although from a daily usage, the two terms would have similar meaning, but in crystallographic refinements the fundamental difference lies in restraints being an additional observation, and the relative weight of this observation can be set, while a constraint is one where the condition is absolute. Without going through the mathematical formalism, an example on restraint and constraint is given here: in a cubic structure, $a = b = c$, $\alpha = \beta = \gamma = 90^\circ$ would be a *constraint* because this is the very definition of a cubic structure. In a refinement between two aliphatic carbon, the C-C distance is *restrained* to 1.54 Å because deviation from the ideal 1.54 Å do occur and this 'additional knowledge' have to compete with the intensity data reach a reasonable refinement.

At the end of the refinements, the residuals are defined in several ways. Overall residuals commonly used in X-ray crystallography are shown in Table 3.1.

Table 3.1 definition of the various parameters utilized in single crystal XRD

Parameter	Definition
R-factor (R_{obs})	$R_{obs} = \frac{\sum F_o - F_c }{\sum F_o }$
Generalized R-factor (wR)	$wR = \left(\frac{\sum w (F_o^2 - F_c^2)^2}{\sum w (F_o)^2} \right)^{\frac{1}{2}}$
Goodness of fit (GoF)	$GoF = S = \left[\frac{\sum w (F_o^2 - F_c^2)^2}{N - P} \right]^{\frac{1}{2}}$

R_{obs} is long established as the traditional ‘R-factor’ accorded general reverence far in excess of its real significance and is most often reported R-value. wR is the ‘generalized R-factor’ and is also sometimes called R' , RG or R_w which is in accordance with the current *Acta Crystallographica* usage. S is also called the ‘goodness of fit’ or GoF, which should have a value of 1 if the model is a true representation of the X-ray scattering power of the structure; if $S > 1$, it would indicate it is a bad model or bad data-to-parameters ratio; if $S < 1$, it would indicate the model is better than the data and certain aspects like absorption correction or space group determination should be looked into. As a rule of thumb, the model would be accepted when $R < 0.05$, $wR < 0.10$ and $GoF \cong 1$. However, careful considerations would still have to be taken and check if the structure makes sense from a chemical perspective. One particular area to take note would be the on the area of thermal ellipsoids and was even regarded as an ‘error dustbin’¹³. An usually large or anisotropic ellipsoid may sometimes genuinely represent unusual thermal motion, such as a long side chain not stabilized by a secondary interaction like hydrogen bonds, but if there is no other evidence or chemical knowledge that suggests so, the ellipsoid should be regarded with doubt. Often, the thermal ellipsoids are mopping up some systematic error, such as absorption, incorrect space group, or a likelier instance of disorder within the structure.

3.2.1.4 Reporting and Validation

Following the analysis and refinements, the output crystallographic information file (CIF) are then generated. The CIF file would contain all the atomic parameters and essential details like the chemical name, author information and others.

Checked with checkCIF for correct syntax and meets all the IUCr requirements. However, as cautioned by the checkCIF, the service should be used as a tool instead of replacing the role of an experienced crystallographer.

3.2.1.5 Software and hardware utilized

The crystals dispersed in Fomblin ® and are hand-picked under a polarizing microscope and mounted onto MiTeGen microloops of the appropriate size for room temperature X-ray diffraction investigations or mounted onto a glass fiber approximately 100 µm in diameter to reduce the likelihood of crystal frosting for measurements at low temperatures ($T < 200$ K). The X-ray initialization and early processing was done together using software package CrysAlisPro on the Rigaku Gemini diffractometer and

Rigaku SuperNova diffractometer using Mo K_{α} = 0.71 Å. The collection strategy and integration were as suggested through CrysAlis. The structure solution and refinement were done with SHELXT⁷ and Olex2¹⁴ respectively, and further validated with PLATON¹⁵ and IUCr CheckCIF service. The structural visuals were plotted using Mercury¹⁶.

3.2.2 X-ray Diffraction: powder X-ray Diffraction(pXRD)

3.2.2.1 Bragg-Brentano and Transmission geometry

The Bragg-Brentano geometry is by far the most commonly seen configuration in modern laboratories. The X-ray tube is aligned in a focusing circle with the detector and sample, as in the schematic shown. Usually, the sample is fixed in position while the tube and detector move along the circle; however, it is also geometrically possible to fix the position of the X-ray source and detector while the sample stage is set to rotate. To get good powder average, the sample stage is usually set to spin about the axis normal to the flat sample stage. The divergence of the source X-ray beam can be controlled by a soller slit and divergence slit to reduce the axial divergence and height divergence (beam spread) of the source X-ray. The X-ray then reach the sample and when it satisfies the Bragg equation, a peak is observed. Between the sample and detector, there are also several optics component which helps to reduce the divergence. The anti-scatter slit, which reduces height divergence and air scattering, soller slit, which similarly reduces axial divergence and the receiving slit, which removes diffuse scattering from all the previous optical elements and reduces beam height divergence. While the slits are helpful, it has to be kept in mind that a 'better' slit would result in a reduced signal. Hence, a reasonable balance between the desired signal-to-noise and acceptable divergence would need to be struck. There are many similarities with the optics of the Bragg-Brentano geometry the transmission mode. Generally, samples are loaded onto a bulk sample holder for the Bragg-Brentano geometry whereas samples are usually packed into capillaries for experiments done in the transmission geometry.

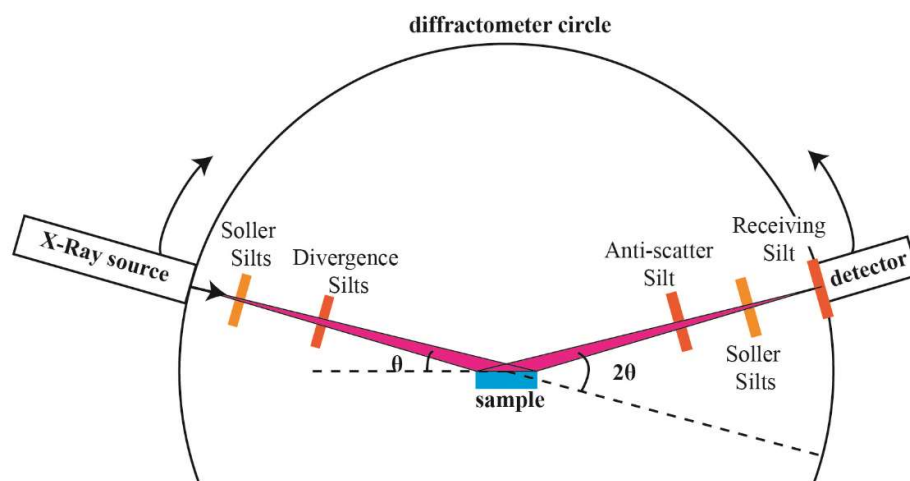


Figure 3.3 schematic of a diffractometer in the Bragg-Brentano geometry

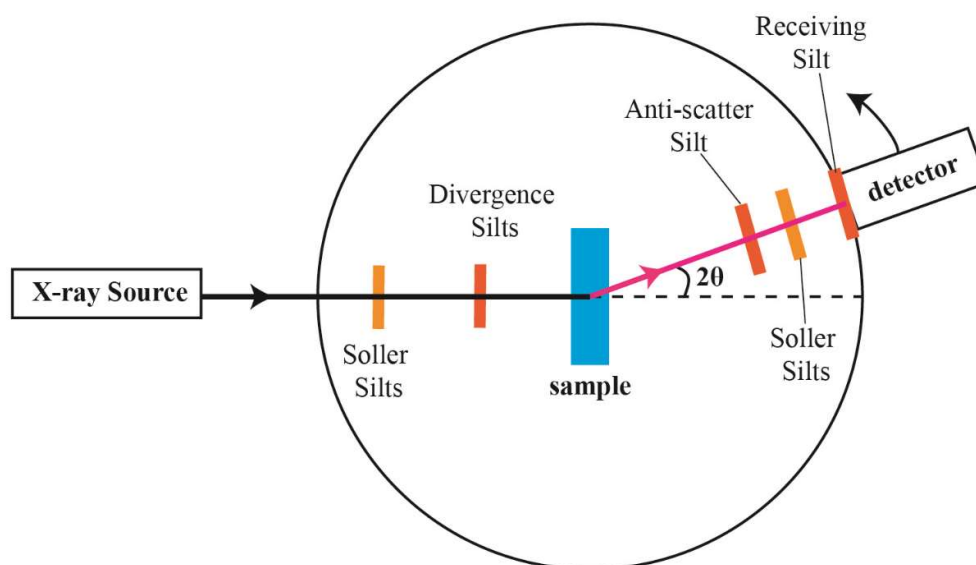


Figure 3.4 schematic of a diffractometer in the transmission geometry

3.2.2.2 Rietveld Refinements

The diffraction patterns are post processed and a Rietveld refinement is done on them. This method of refinement is done on the whole diffraction pattern and the initial development was made by Rietveld.¹⁷ The powder patterns are refined against a known model and various parameters are refined to obtain a best fit through the least squares method. The calculated pattern is given by the equation,

$$y_{ci} = sf \sum_K L_K |F_K|^2 \phi(2\theta_i - 2\theta_K) P_K A + y_{bi} \quad (3.2)$$

where sf is the scale factor, K represents the Miller indices, hkl for a Bragg reflection, L_k contains the Lorentz polarization and multiplicity factor, $\phi(2\theta_i - 2\theta_K)$ is the reflection profile function, P_k is the preferred orientation factor, A is the absorption factor, F_k is the structure factor of the K th Bragg reflection and y_{bi} is the background intensity at the i th step. At the end of the least squares refinement, the commonly listed R-values related to powder XRD refinements are shown in the Table 3.2, with R_{wp} be the meaningful amongst the list because the same expression as the residual being minimized and hence, provides a good measure of the quality of refinement.

Table 3.2 definition of the various parameters utilized in pRXD refinements

Parameter	Definition
R- weighted pattern	$R_{wp} = \left(\frac{\sum w_i (y_{oi} - y_{ci})^2}{\sum w_i (y_{oi} - y_{bi})^2} \right)^{0.5}$
R-Bragg	$R_{Bragg} = \frac{\sum I_{oK} - I_{cK} }{\sum I_{oK}}$
R-pattern	$R_{wp} = \left(\frac{\sum y_{oi} - y_{ci} }{\sum y_{oi} - y_{bi} } \right)^{0.5}$
Goodness of fit (GoF)	$GoF = S = \chi^2 = \left[\frac{\sum w (y_o^2 - y_c^2)^2}{N - P} \right]^{\frac{1}{2}}$

There are two main types of variables which are refined in the Rietveld refinements; parameters related to the experimental setup and parameters which are specific to the samples. Of the ones related to the experimental setup, instrumental variables like the diffractometer geometry, incident beam properties and detector effects are typically pre-determined against a reference sample, like LaB₆ or Silicon, and fixed in the actual refinement of the samples.

A variety of peak shapes have been used to fit the measured Bragg peaks and are examined by Young et al ¹⁸. The commonly used profiles are the Gaussian, Lorentzian and the Thompson-Cox-Hastings (TCHZ) pseudo-Voigt profile, where the mixing

parameter η controls the relative combination of the Gaussian-Lorentzian shape¹⁹ The expressions, and refined parameters, which defines the shape and width of the and TCHZ peaks are listed below.

Table 3.3 definition of the various parameters utilized in Rietveld refinements

Peak Function	Definition
Gaussian	$G(x) = \left(\frac{2\sqrt{\frac{\ln(2)}{\pi}}}{FWHM} \right) \exp\left(\frac{-4\ln(2)x^2}{FWHM^2}\right)$
Lorentzian	$L(x) = \frac{\left(\frac{\frac{2}{\pi}}{FWHM}\right)}{\left(\frac{1+4x^2}{FWHM^2}\right)}$
Pseudo-Voigt	$F(x) = \eta L(x) + (1 - \eta) G(x)$
TCHZ	
TCHZ FWHM expression	$\eta = 1.36603 \frac{\Gamma_L}{\Gamma} - 0.47719 \left(\frac{\Gamma_L}{\Gamma}\right)^2 + 0.1116 \left(\frac{\Gamma_L}{\Gamma}\right)^3$ $FWHM = \Gamma = (\Gamma_G^5 + A\Gamma_G^4\Gamma_L + B\Gamma_G^3\Gamma_L^2 + C\Gamma_G^2\Gamma_L^3 + D\Gamma_G\Gamma_L^4 + \Gamma_L^5)^{0.2}$ $\Gamma_G = \left(U \tan^2\theta + V \tan\theta + W + \frac{Z}{\cos^2\theta} \right)^{0.5}$ $\Gamma_L = X \tan\theta + \frac{Y}{\cos\theta}$
with U, V, W, Y, Z as parameters to be refined	

3.3 Nuclear Magnetic Resonance (NMR)

3.3.1 Solid State Nuclear Magnetic Resonance (SSNMR)

Nuclear magnetic resonance exploits the spin and magnetic properties intrinsic to every nuclei in the material. All atomic nuclei can be characterized by a nuclear spin quantum

number, I , where I can be any multiple of $\frac{1}{2}$ (i.e. 0, $\frac{1}{2}$, 1, $\frac{3}{2}$, 2, $\frac{5}{2}$ etc). This spin quantum number arises from the relative numbers of protons and neutrons in the nucleus and is in discrete quantized units. Nuclei for which $I = 0$ (e.g. ^{12}C) are called ‘NMR silent’ or non-NMR active nuclei, while the remaining nuclei where $I \neq 0$ possess spin, charge and angular momentum.

The non-zero spin angular momentum will also give rise to the magnetic moment of a nucleus μ , and the assemblies of such magnetic moments give rise to nuclear paramagnetism. The magnetic moment is related to nuclear spin quantum number,

$$\mu = \gamma \hbar I \quad (3.3)$$

where γ is the gyromagnetic ratio and \hbar is the reduced Planck’s constant.

From quantum mechanics, a nucleus of spin I will have $2I + 1$ possible orientation. As an illustration, for a spin $\frac{1}{2}$ nuclei, this would give two possible levels as seen in Fig 3.5. In the absence of an external magnetic field, these orientations are of equal energy but if a magnetic field is applied, the energy levels will be split, and each level is given a magnetic quantum number, m . The interaction of the nuclear magnetic moment with the external magnetic field is known as the Zeeman interaction, and the interaction energy is known as the Zeeman energy, which is given by

$$E = -\mu \cdot B_0 = -\gamma \hbar I \cdot B_0 \quad (3.4)$$

$$E = -\gamma \hbar B_0 m_I \quad (3.5)$$

where $mI = -I, +I, I+1$, etc. Therefore, the energy level difference between the upper and lower levels can be written as

$$\Delta E = -\gamma \hbar B_0 m_{+I} - (-\gamma \hbar B_0 m_{-I}) = \gamma \hbar B_0 \quad (3.6)$$

Thus, if the incoming radiation $\hbar\omega_0 = \gamma \hbar B_0$, it would correspond to the ‘resonance’ of the transition and the characteristic frequency, ω_0 , which gives the Larmor equation,

$$\omega_0 = -\gamma B_0 \quad (3.7)$$

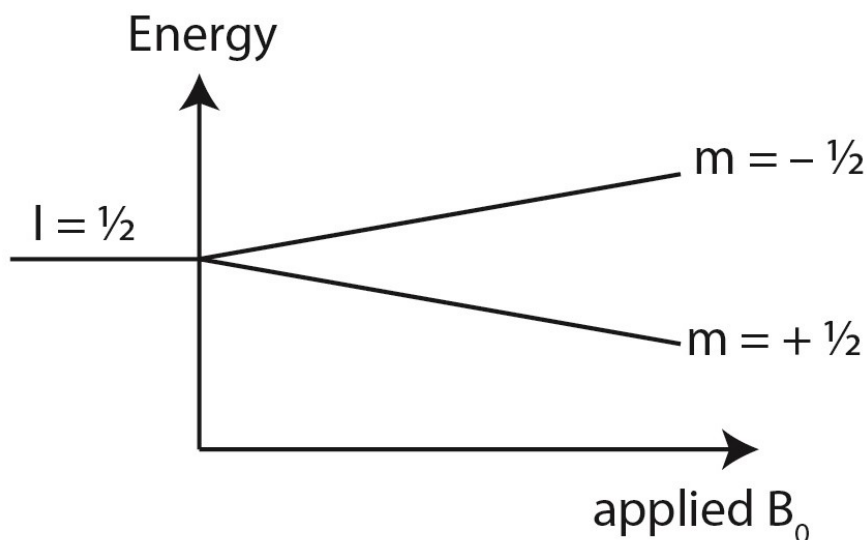


Figure 3.5 schematic of energy level. Energy splitting increases with increasing B_0

The low energy required for an NMR transition has two important consequence:

1. Since the population difference between the two energy levels is very small, approximately 1 part in 10^6 , the actual population difference can be calculated from Boltzmann's relationship:

$$\frac{N_{upper}}{N_{lower}} = e^{-\frac{\Delta E}{kT}} \approx 1 - \frac{\gamma \hbar B}{kT} \quad (3.8)$$

Thus, NMR spectroscopy is a relatively insensitive technique because of the small excess of spins in the ground state. Due to the low sensitivity, the most common technique utilized to improve signal-to-noise ratio is to increase the number of scans to obtain better signal averaging.

2. Since the lifetime of the excited state can be relatively long, NMR would give access to much slower dynamics than any other physical probes, on the order of milliseconds to seconds.

The effect of the applying a radiofrequency pulse is the basis to allow NMR observations to be made. To understand this effect, we will consider the precessing magnetic moments of a nuclei sitting in an applied magnetic field, B_0 . The net magnetization, M_0 , of the nuclei would align in the same direction of B_0 ,

$$M_0 = \mu_0 \frac{N \gamma^2 I(I+1) B_0}{3 k_B T} \quad (3.9)$$

A radiofrequency pulse then applies a torque to the magnetization vector which would

drive it to the x-y plane from equilibrium. This radiofrequency pulse would perturb the magnetic moments away from the alignment with the huge applied B_0 . In many NMR experiments, the duration of the radiofrequency pulse is chosen such that the magnetization vector rotates by 90° onto the x-y plane because the detection of the magnetization is possible only on the x-y plane.

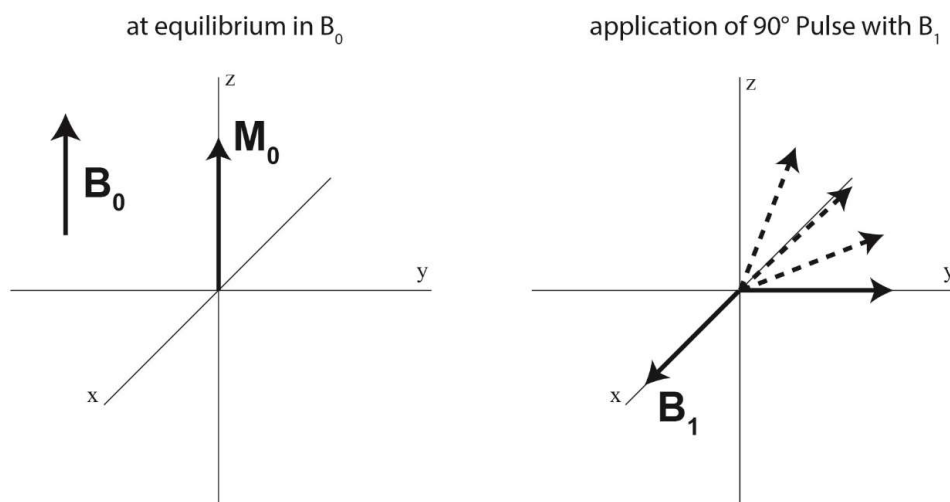


Figure 3.6 schematic of magnetization vectors (a) at equilibrium when placed in a magnetic field B_0 , (b) when the system is perturbed by the application of B_1 , the magnetization vector is rotated onto the x-y plane, which can then be detected.

With the magnetization now being perturbed onto the x-y plane, the magnetization would relax and return to the initial M_0 in the z-direction (aligned with B_0). The two main relaxation processes are spin-lattice relaxation, also called T_1 relaxation or longitudinal relaxation and the other is a spin-spin relaxation, also called the T_2 relaxation or transverse relaxation. The detected signal is collected as a free induction decay (FID) and is then Fourier transformed to obtain a spectrum.

The spin-lattice relaxation occurs by the transfer of energy to its surrounding (i.e. 'lattice'). Because nuclei in the surrounding are in constant vibrational and rotational motion, this creates a complex magnetic field. The interaction between the lattice field and the excited state nuclei will cause them to lose energy, thereby returning to the lower state. This relaxation time, T_1 , would dictate how fast the NMR experiment can be recycled. At $1 \times T_1$, the recovery of the magnetization is 63% of the original M_0 and would be fully relaxed at $5 \times T_1$. However, should a full relaxation for quantitation not

be required, experiments can also be recycled at 1.3 to 1.5 times of T_1 to obtain the best signal per unit time.

The spin-spin relaxation describes the interaction between neighboring nuclei with identical precessional frequencies but have different magnetic quantum states. It can also be described as the spins becoming de-phased where the spin-spin relaxation causes a cumulative loss in phase resulting in transverse magnetization decay. There is no net change in the population of the excited and ground energy states, but the average lifetime of a nucleus in the excited state will decrease, and thus result in line broadening. Using a more holistic approach to describe a system in an NMR experiment, the Hamiltonian of a system can be described as follows:

$$H_{\text{total}} = H_{\text{external}} + H_{\text{internal}}, \quad (3.10)$$

where

$H_{\text{external}} = H_z$ (Zeeman interaction) + H_{RF} (Radiofrequency pulse) and

$H_{\text{internal}} = H_{\text{CS}}$ (chemical shielding) + H_{Quad} (quadrupolar) + H_{D} (dipolar) + H_{J} (scalar spin-spin) + H_{P} (paramagnetic) + H_{K} (Knight's shift)

The contributions to the H_{external} has been outlined in the earlier section and this section will focus on the H_{internal} , with more detailed discussion for H_{CS} . The Hamiltonian for the chemical shift (H_{CS}) contains a spin and spatial component which is written as follows:

$$H_{\text{cs}} = \frac{1}{3} \left\{ \sum_{j=1}^3 \sigma_j + \sum_{j=1}^3 (3 \cos \theta - 1) \sigma_j \right\} \gamma I_z B_0 \quad (3.11)$$

where σ_j is the chemical shift tensor, γ the gyromagnetic ratio, I_z is the spin angular momentum B_0 the applied magnetic field. Therefore, it can be seen clearly here that the spatial term of $(3 \cos \theta - 1)$ can reduce the magnitude of the interaction to zero at a very specific “magic angle”, 54.736° . However, just by putting the crystallites in this “magic angle” with respect to the external magnetic field B_0 , is insufficient. To remove the broadening in powder samples, all the crystallites have to assume this orientation simultaneously. Therefore, the sample needs to be spun sufficiently fast to obtain this orientation “simultaneously”. If the two mentioned conditions are fulfilled, the anisotropic chemical shift broadening contributions are averaged to zero and the isotropic chemical shift is retained. Qualitatively, chemical shift measures the amount

of ‘shielding’ the nucleus experiences from B_0 , and it is highly dependent on the local environment of the nucleus. The amount of ‘shielding’ is relative, and would therefore, be referenced to a specific system. For ^1H , ^{13}C and ^{29}Si , these nuclei are referenced to tetramethylsilane.

3.3.2 Solution NMR

This is a more specific case than solid-state NMR, where the tumbling of molecules in the solution averages out several interactions, namely chemical shift anisotropy, and thus, sharp peaks are typically seen in solution NMR spectra. Therefore, J-coupling and dipolar coupling interactions can be seen in most spectra.

The multiplicity of the peaks will be in $2nI + 1$ peaks, where I is the spin and n is the number of neighbouring nuclei. The relative intensities of the peak would follow that in a Pascal’s triangle. In the most widely studied nuclei, ^1H , $I = \frac{1}{2}$, hence a ^1H coupled with one other ^1H would give a doublet, ^1H coupled with two other ^1H would give a triplet, etc. It should be noted that the peak splitting only occurs between non-equivalent hydrogens and splitting primarily occurs between ^1H atoms that are separated by three bonds. In the example shown in Fig 3.7a, 1,1,2-trichloroethane $\text{H}_{\text{a}1}$ and $\text{H}_{\text{a}2}$ are chemically equivalent hydrogen and does not split each other and would be a doublet because there is only one neighbouring H_{b} ; similarly H_{b} would be a triplet due to the presence of two H_{a} . In Fig 3.7b, ethyl acetate, H_{a} is a singlet and is not affected by coupling from H_{b} or H_{c} because it is more than three bonds away. Solution NMR (^1H and ^{13}C) were performed on a Bruker AVANCE I 400 MHz spectrometer.

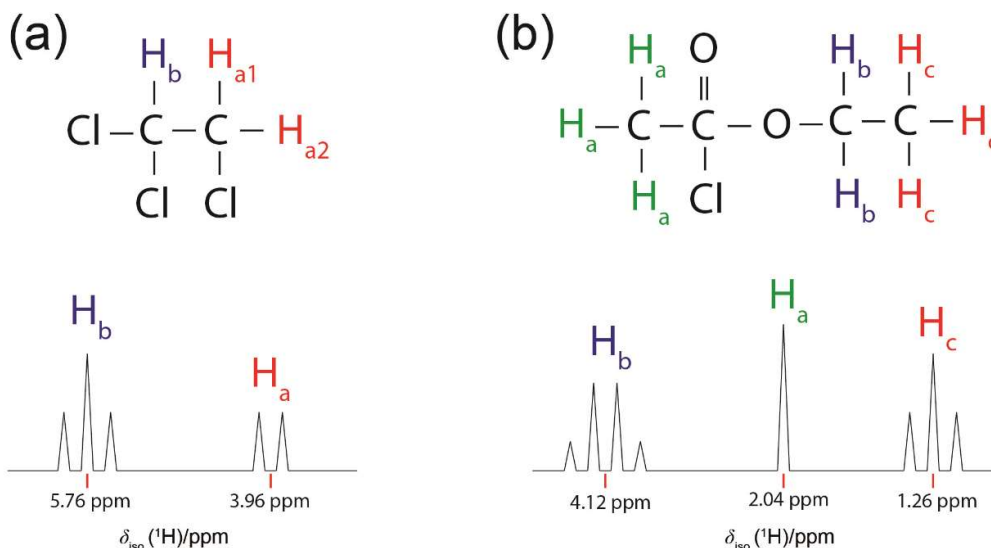


Figure 3.7 (a) peak splitting due to spin-spin coupling in 1,1,2-trichloroethane. H_{a1} and H_{a2} are chemically equivalent hydrogen and does not split each other. H_b would be split into a triplet due to the presence of two H_a . (b) H_a in ethyl acetate is not affected by coupling more than three bonds away, and hence is a singlet. H_b and H_c , are triplets and quartets respectively.

3.3.4 1D NMR pulse sequences: One pulse, CPMAS, Hahn Echo, Saturation Recovery, $T_{1\rho}$

The one pulse NMR experiment is the simplest and most straightforward NMR experiment. The two most important parameters would be the duration of the radiofrequency 90° pulse and the recycle delay, which would ideally be taken to at $5 \times T_1$ to obtain a quantitative spectrum. The spectrum can then be deconvoluted into the individual chemical shifts through DMFit²⁰. In this thesis, one pulse experiments are done on ^1H .

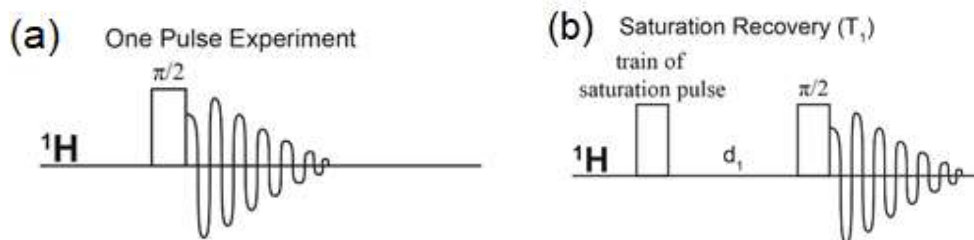


Figure 3.8 (a) schematic of the pulse sequence in a one pulse and (b) saturation recovery experiment to measure the T_1

As an extension to the one pulse experiment, the saturation recovery experiment is also done using the same principles. The samples are first saturated by a train of radiofrequency pulses such that no signal is observed, then after a stipulated delay time, a one pulse experiment is carried out (i.e. 90° pulse, followed by observation). After collecting a series of spectra with varied delay time, spectra is plotted on a 2-dimensionally and the recovery of NMR signal is fitted to an exponential function, $I(\tau) = I_0 \left(1 - e^{-\frac{\tau}{T_1}}\right)$, to obtain the T_1 of the individual chemical shifts.

$T_{1\rho}$ is sometimes also known as the spin-lattice relaxation in the rotating frame and is the time constant for the decay of magnetization along the applied radiofrequency field, B_1 , of an applied spin locking pulse in the rotating frame of reference. It is analogous to T_1 except it describes relaxation along the radio frequency field of the pulse (which is static in the rotating frame) rather than relaxation along B_0 . The $T_{1\rho}$ is measured by first applying a 90° pulse to an equilibrium magnetization vector and a spin locking pulse is then applied. During the spin locking pulse, the large magnetization vector, which was initially polarized in B_0 , decays to its equilibrium value in the much smaller field, B_1 , with time constant, $T_{1\rho}$. The $T_{1\rho}$ is measured by analysing the intensity of the NMR signal in the spectra collected as a function of the duration of the spin locking pulse and fitted to exponential the function,

$$I(\tau) = I_0 e^{-\frac{\tau}{T_{1\rho}}} \quad (3.12)$$

Since motion in the various regime affects relaxation in various ways, it is crucial to probe the spin relaxation dynamics across the various regimes to obtain a comprehensive understanding of the molecule's motion²¹. More relevant to this thesis, T_1 is sensitive motion in the MHz regime while $T_{1\rho}$ is sensitive to motion in kHz regime.

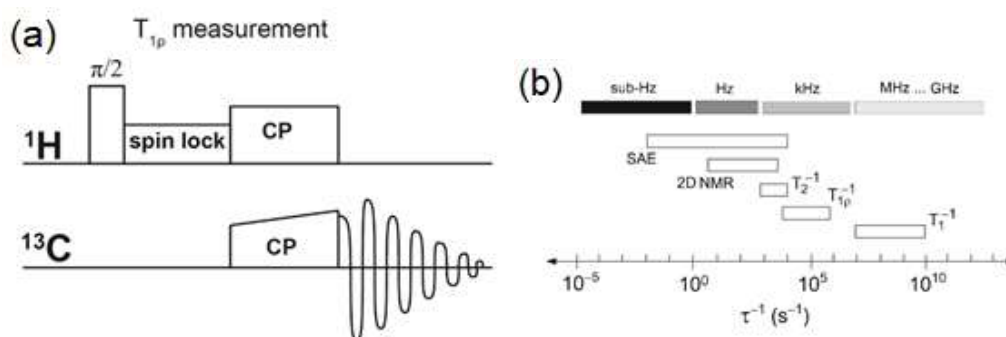


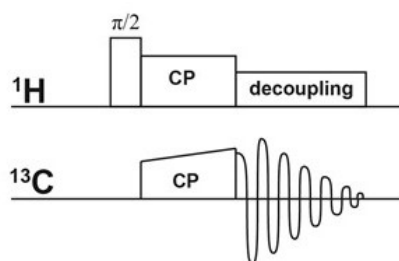
Figure 3.9 (a) schematic of the pulse sequence in $T_{1\rho}$ measurements. (b) illustration showing the various regimes of motion which correlates to the various relaxation mechanisms and the

type of experiments²¹

In cross-polarization magic angle spinning (CPMAS), also called proton-enhanced nuclear induction spectroscopy, this pulse sequence utilizes the more naturally abundant spin like ^1H , to increase the polarization of a less abundant spin e.g. ^{13}C . In brief, the experiment starts by exciting the ^1H with a 90° pulse, then the polarization of ^1H is transferred to ^{13}C by matching the Hartman-Hahn condition²², then acquiring the signal on ^{13}C while pulsing the ^1H channel with a decoupling sequence. The added advantage is that the experiment can now be recycled at the T_1 of the more abundant spin, like ^1H , instead of the observed nuclei ^{13}C . However, the disadvantage would be CPMAS is no longer quantitative like in the one pulse experiment, and the acquisition time would very often be limited by the decoupling duration on ^1H channel.

In the Hahn echo pulse sequence, the spin magnetization is refocused using an electromagnetic radiation pulse. The main advantage is to bypass the very fast decays of the spin relaxation and dephasing which shorter than the instrument response time. By introducing a recoupling 180° pulse, the inhomogeneous dephasing can be removed and the signal can be recorded.

(a) Cross Polarization MAS



(b) Spin Echo Experiment

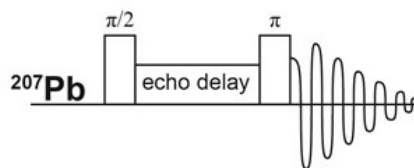


Figure 3.10 (a) schematic of the pulse sequence in CPMAS and (b) a spin echo experiment

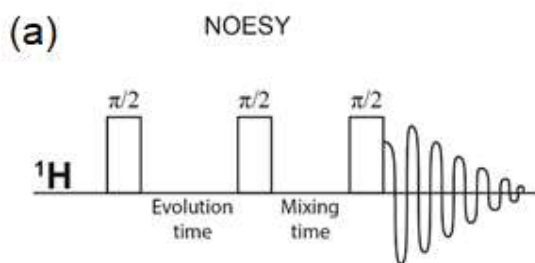
3.3.5 2D pulse sequences

A two dimensional variation of NMR was first proposed by Jeener²³ and the main objective is to add an additional experimental variable, and thus introducing a second dimension to the resulting spectrum, providing data that is easier to interpret and often

more informative. This is particularly helpful in large and complex molecules or in the scope of this thesis, make the assignment more rigorous. 2D experiments vary from 1D experiments with an additional step. In general, 2D experiments consist of three stages, the preparation, evolution/mixing, detection, of which the evolution/mixing stage is not observed in a typical 1D experiment. In a oversimplified description of each stage, the preparation can be understood as doing something to the nuclei, the evolution/mixing stage as allowing the nuclei precess freely and allowing the nuclei to ‘talk’ to each other, and the detection of the results. During the evolution/mixing stage, the spins can precess freely for a given time. During this time, the magnetization is labelled with the chemical shift of the first nucleus. During the mixing time magnetization is then transferred from the first nucleus to a second one.

3.3.5.1 2D Homonuclear correlation experiment: NOESY and BABA

Mixing sequences utilize two mechanisms for magnetization transfer: scalar coupling or dipolar interaction like the Nuclear Overhauser Effect (NOE). Data are acquired at the end of the experiment and during this time the magnetization is labelled with the chemical shift of the second nucleus. Since NOESY utilizes dipolar interaction NOE effect, the spectra obtained can be understood as a $^1\text{H} - ^1\text{H}$ through-space correlation. In the BABA experiment, the dipolar interaction is also being exploited, the main phenomena is slightly different; BABA looks at the multiple quantum transition, or specifically double quantum-single quantum coherences and the signal being recoupled in the rotor synchronized manner. The two different pulse sequences depends on the same dipolar interaction albeit in a different manner and would allow the correlations made be more accurate.



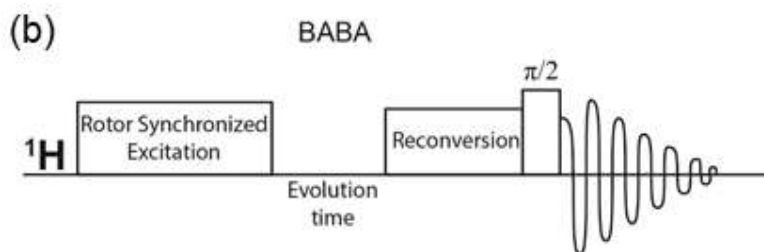


Figure 3.11 (a) schematic of the pulse sequence in a 2D NOESY (b) 2D BABA experiment

3.3.5.2 2D Heteronuclear Correlation experiment (HETCOR); hCH and FSLG

Similarly, in the heteronuclear correlation (HETCOR) pulse sequences, the transfer of magnetization can also either be through scalar coupling or dipolar interaction. The specific pulse sequence utilized in this thesis, the hCH and FSLG both utilizes the dipolar interaction. Therefore, similar to NOESY, hCH and FSLG provides $^1\text{H} - ^{13}\text{C}$ through space correlations. The FSLG differ from hCH in that multi-pulse decoupling on the ^1H channel during acquisition of the FID that would otherwise appear too broad because of the low MAS. The advantage from hCH comes from the increased sensitivity because the magnetization is first transferred from ^1H to ^{13}C and back to ^1H because ^1H have a greater natural abundance and larger γ compared to ^{13}C . FSLG on the other hand transfers the magnetization from ^1H to ^{13}C and detection is done on ^{13}C while applying a multi pulse decoupling on the ^1H channel. The decoupling would improve the resolution on the indirect axis (F1) instead of using MAS to gain resolution.

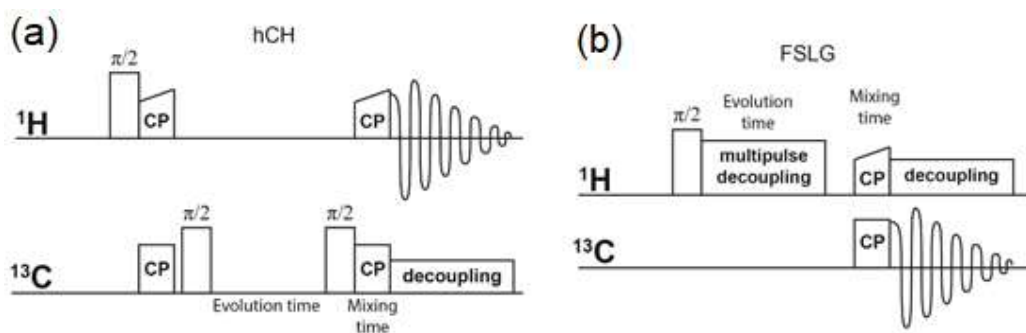


Figure 3.12 (a) schematic of the pulse sequence in a 2D hCH HETCOR and (b) 2D FSLG HETCOR experiment

3.4 Optoelectronic Characterization

3.4.1 Fundamentals of Fourier Transformed Infrared Spectroscopy (FTIR)

The FTIR spectroscopy is a technique based on interferometry. Light is emitted from a source and collimated by the mirror R1 onto a beamsplitter, which splits the light into two beams of equal intensity. The two beams are then reflected by a flat mirror (M1 and M2) and recombine on the mirror R2, which then refocuses the combined beam onto the detector. The difference in optical path would result in the interference patterns. If the radiation is monochromatic, it would result in a constructive interference when the path difference is equal to $n\lambda$ and conversely result in destructive interference when the path difference is $(n+\frac{1}{2})\lambda$, where n is an integer. Following a series of derivation beginning from the electric field of a monochromatic radiation propagating along a direction, it can be derived that

$$F(\delta) = K \int_{-\infty}^{\infty} S(\bar{\nu}) e^{i(2\pi\bar{\nu}\delta)} d\bar{\nu} \quad (3.13)$$

where $F(\delta)$ is the light intensity (i.e. the interferogram), K is a constant, $S(\bar{\nu})$ is average radiation energy per unit area and time at the detector, δ is the path difference of the two beams. This is the fundamental relation in FTIR spectroscopy, where the interferogram is Fourier transform of the source spectrum, and the converse is also true; i.e.

$$S(\bar{\nu}) = K' \int_{-\infty}^{\infty} F(\delta) e^{-i(2\pi\bar{\nu}\delta)} d\delta \quad (3.14)$$

where K' is a constant.

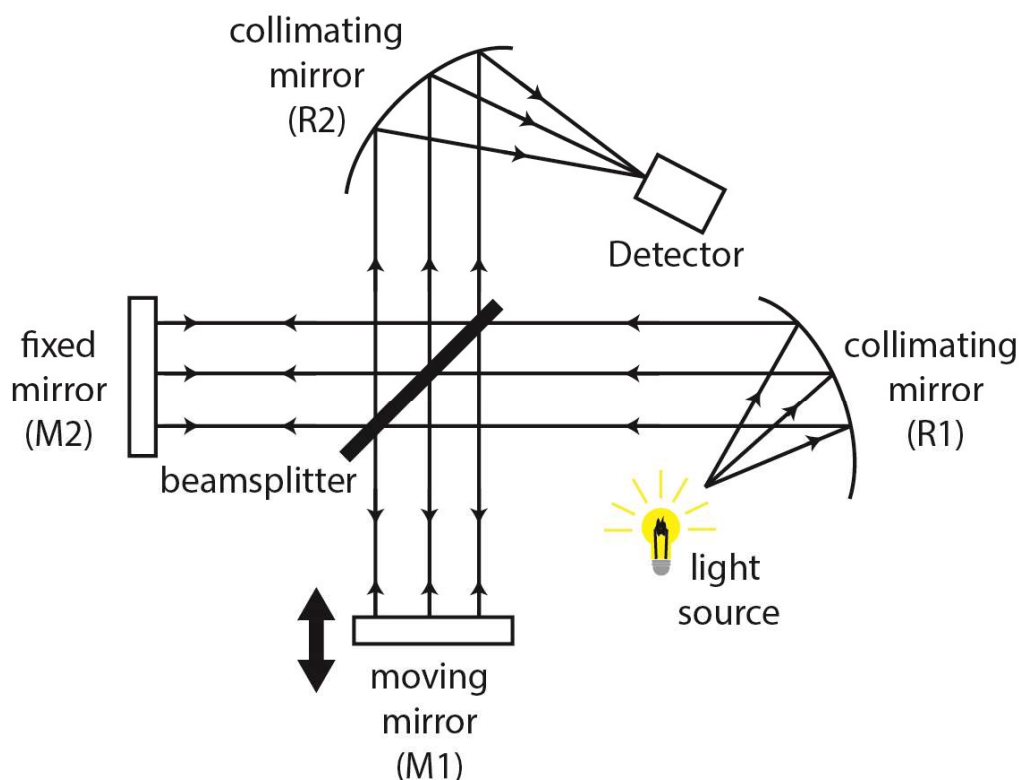


Figure 3.13 schematic of a Michelson interferometer, which is the basis of an FTIR. R1 and R2 are collimating mirrors and M1 and M2 are flat mirrors.

The interferogram $F(\delta)$ is collected by varying the scanning the position of the moving plain mirror in the interferometer and recording the light intensity as a function of the retardation δ . A Fourier transformation is then applied to the interferogram and the spectrum is thus obtained.

FTIR has several advantages over conventional dispersive ones and is briefly summarized here, and the interested readers are directed to the available textbooks.²⁴⁻²⁶ The spectral resolution can be improved just by increasing the scanning range of the moving mirror because the resolution is inversely proportional to the maximum difference of the optical path. Next, the whole spectrum is acquired within a single scan of the moving mirror, hence, in a fixed time, it is possible to take an average of multiples scans thus improving the signal to noise ratio considerably. These are also known as the Fellgett and Jacquinot advantages. In the FTIR, a HeNe laser is used as a wavelength scale reference which is much more stable and precise than in dispersive instruments

where the scale depends on the mechanical movement of diffraction gratings and this is also known as the Connes advantage. The measurements were done on the Bruker V80v, and the schematic of the instrument is shown in Fig 3.14.

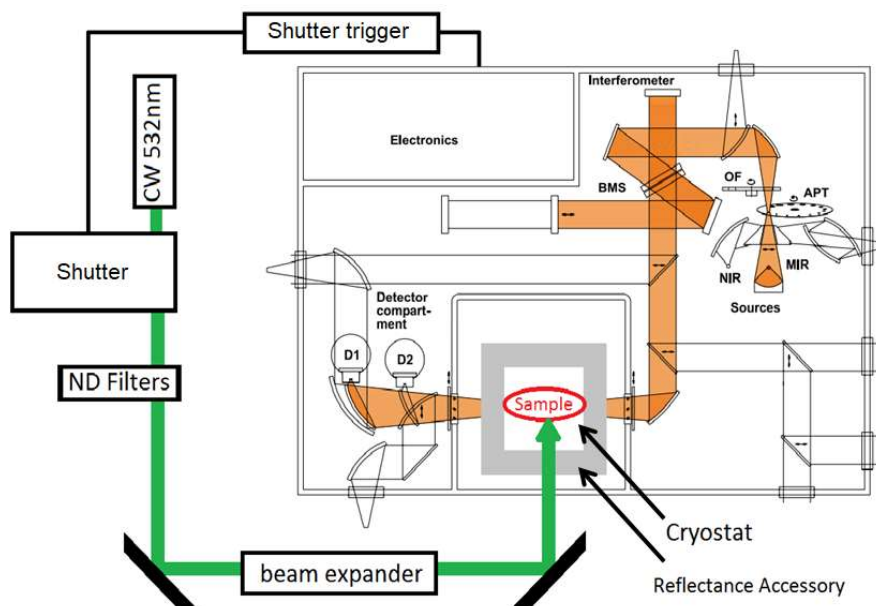


Figure 3.14 schematic of the Bruker V80v FTIR, with laser add-on for cw-PIA measurement.

When the system is photoexcited, it may create new electronic states within the band gap. This would result in photoinduced transitions with a redistribution of the oscillator strength. The photoexcitation can be studied in the visible, NIR and MIR by measuring the photoinduced absorption by exciting with a continuous wave laser or by pump-probe techniques. The photoabsorption levels can be seen thorough the relative differential transmittance, that is

$$-\frac{\Delta T}{T} = \frac{T - T_{exc}}{T} \quad (3.15)$$

where T and T_{exc} are the sample transmittance in the ground state (no photoexcitation) and excited state (with photoexcitation) respectively. In a simplified schematic of the energy states as shown in Fig 3.15, level 1 would be the ground state, level 3 would be the excited state and level 2 would be the photoinduced energy state. When the differential, $-\Delta T/T$, is taken two key characteristics would be seen in the spectrum. Due to the population depletion in the ground state under photoexcitation (i.e. electrons excited from 1 to 3), the differential spectrum will show a negative peak at the energy

corresponding to transition from $1 \rightarrow 3$, and this is known as photobleaching. Due to the photoexcitation, a virtual photoexcited state 2 would form within the band gap and a positive peak would be shown at the energy corresponding to the transition from $2 \rightarrow 3$, and this is known as photoabsorption. If selection rules permit, the transition from $1 \rightarrow 2$ could also be observed. In hybrid perovskite systems, the linear absorption occurs in the visible spectral regime and the intra-gap photoinduced energy would have exhibit the signatures at a lower energy, typically in the NIR to MIR region and the region can be probed easily through FTIR spectroscopy.

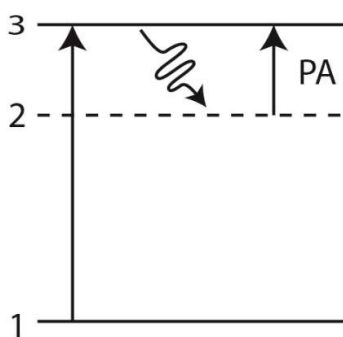


Figure 3.15 schematic of band diagram and the formation of absorption band due to photoexcitation

3.4.2 Ultrafast spectroscopy: Transient absorption

Femtochemistry was pioneered by the Nobel laureate Ahmed Hassan Zewail²⁷⁻²⁹ who recorded ‘snapshots’ of chemical reactions using an ultrafast femtosecond transient absorption technique. In the transient absorption experiment, a first laser pulse ‘pumps’ the system into an excited state and the excited states relaxes back to the ground state on the femto to picosecond timescale. During the relaxation, a second laser pulse is then used to ‘probe’ the population of the excited states at different time delays with respect to the excitation. Hence, this method of analysis is termed as pump-probe spectroscopy. From the principle of turning still pictures into movies, if sufficient snapshots with a short time delay (e.g. 30 still pictures per second or 3.3 ms apart) are played continuously one after another, a video would be obtained. Similarly, in pump-probe spectroscopy, this “video” is obtained by collecting the ‘probe’ at different time delays,

and subsequently the data are put together to obtain a “movie” which shows the rate of relaxation of the system. Pump-probe techniques provides a direct method to probe the changes to the absorption and refractive index with sub-picosecond resolution. In the schematics shown in Fig 3.16, the different time delays are controlled by a precise moving optical delay stage; since the speed of light, c , is a constant, and a change in the laser path length by 0.1 mm will be equivalent to a delay of 333 fs.

A commercial regenerative amplifier system (Quantronix Integra-C) was used as the laser source with a repetition rate of 1 kHz at 810 nm and pulse width of around 100 fs. A commercial spectrometer, Jobin Yvon CP140-104, equipped with a silicon photodiode array was used to record the transient absorption spectra (Entwicklungsbüro Stresing). A portion of the laser beam was split to generate the 400 nm pump beam using a 1 mm thick BBO crystal cut at 29.2°. White probe light was generated using a sapphire crystal coupled with a 750 nm short pass filter just sufficient to attenuate 800 nm generation beam without saturating the camera and thus, the output spectrum was sensitive from 550 to 830 nm. An additional long pass filter with cut-off wavelength of 450 nm was used after the sample to avoid saturation of the camera by the intense pump beam. The collected data are then post processed through a global fitting of the resulting spectral decays using the R-package TIMP on Glotaran³⁰. This allows for a more holistic fitting of the data since the full data is taken into consideration. The processes are then fitted through characteristic lifetimes and interpreted. Similar to the processes in steady state PIA, the phenomena of photobleaching and photoabsorption follows the same argument and principles; photobleaching arises at the band edge due to the reduced occupancy of the ground state and partial occupancy of the excited state while photoabsorption could originate from a variety of responses.

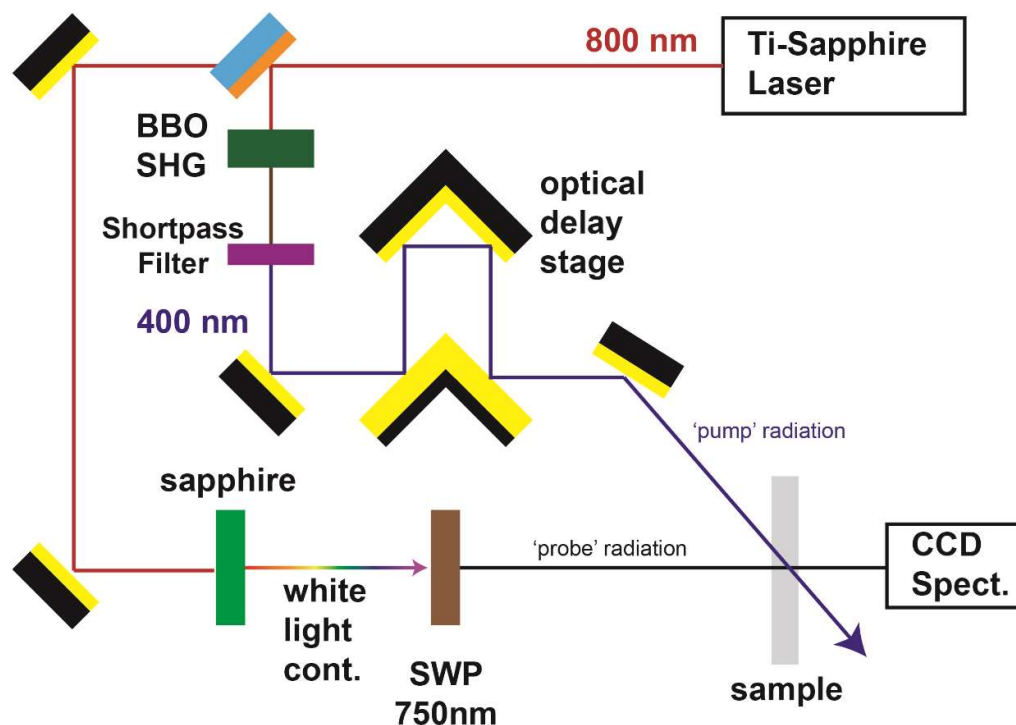


Figure 3.16 schematic of the experimental setup for ultrafast transient absorption spectroscopy

3.4.3 Linear Absorption and Photoluminescence

The understanding of interband absorption is based on the quantum mechanical treatment and of light-matter interaction to the band state of solids. From the nearly-free electron model of semiconductors, the valence and conduction bands, sometimes also referred to as the highest occupied molecular orbital (HOMO) and lowest unoccupied molecular orbital (LUMO), respectively, and these energy levels can be approximated by a parabolic dispersion in an E - k relationship plot.

By the principle of conservation of energy, $E_f = E_i + \hbar\omega$ where E_i is the energy of the electron in the valence band, E_f is the energy of the electron in the upper band and $\hbar\omega$ is the photon energy. Since there is a continuous range of energy states in the within the upper and lower band, the transition is possible over a range of excitation energies. It also therefore, apparent that the minimum value of $E_f - E_i$ is E_g ; this would imply that that the absorption shows a threshold behaviour and interband transitions will be not possible unless $\hbar\omega > E_g$. Interband transitions therefore give rise to a continuous

absorption from the low energy threshold E_g to an upper value set by the extreme limits set of the bands that participates in the optical transition.

Upon excitation, the excited charge carriers can relax through either through intraband or interband states. In the former, it occurs during carrier cooling within the respective conduction or valance bands, while in the latter the recombination can occur radiatively to give photoluminescence or non-radiatively through trap-assisted recombination.

In the direct band gap material, photons are emitted when electrons at the bottom of the conduction band and holes at the top of the valence band combine radiatively. The radiative lifetime are short and typically in the range of 10^{-9} s and luminescent efficiency are expected to be high. Photons are first absorbed from an excitation source, like an arc lamp or laser, exciting many electrons into the conduction band and holes into the valence band when the excitation energy is greater than E_g . The electrons excited to states high up into the valence bands do not remain in that initial state for a long time as it can lose energy rapidly through emission of phonons, as allowed by selection rules and conservation laws. In a typical solid, the electron-phonon coupling is very strong and hence, the scattering events take places on the time scale of $\sim 10^{-13}$ s, which is much faster than the radiative recombination lifetimes. This would, therefore, allow the electrons to relax to the bottom of the conduction band the electron and hole recombine radiatively.

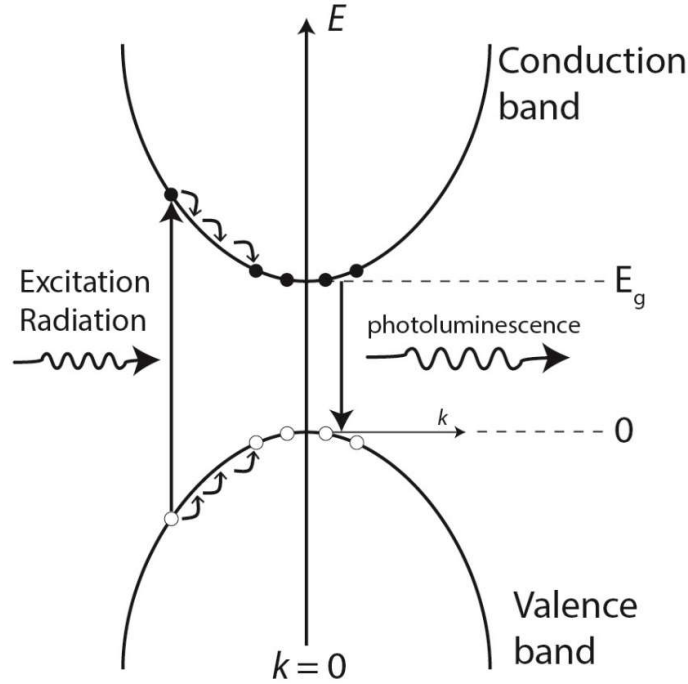


Figure 3.17 schematic of the band diagram from a nearly-free electron model. The photoexcitation would create electron-hole pairs which relaxes to the bottom of the conduction band and top of the valence band. There, it can recombine radiatively to emit a photon, which is observed as photoluminescence.

In thin film configuration, absorption coefficient and intensity are related through the Beer-Lambert equation,

$$I(z) = I_0 e^{-\alpha z} \quad (3.16)$$

where I_0 is the incident intensity, α is the material's absorption coefficient and z is the thickness of the film. Hence, when the film thickness, z , and reference intensity is known, the material absorption coefficient can be determined. However, in the measurement of bulk samples the diffuse reflection, rather than the change in transmission is utilized. In diffuse reflection, the intensity of diffusely reflected light is independent of the angle of incidence, and results to multiple scattering within the sample. Kubelka-Munk function is used to determine the absorption coefficient of the material³¹ The theory is based on a model where the radiation field is approximated by two different fluxes, one travelling from the illuminated sample surface and the other is radiation travelling toward the illuminated surface and assumes that the background is black (i.e. no reflection from background) and the sample is infinitely thick, the

derived result would be the well known Kubelka-Munk function,

$$F(R_{\infty}) = \frac{(1 - R_{\infty})^2}{2R_{\infty}} \propto \frac{\alpha}{S} \quad (3.17)$$

where R is the reflectance, α is the absorption coefficient and S is the scattering coefficient.

The Tauc plot is then used to estimate the material's band gap. For a direct band gap material, the plot of $F(R)^2$, which is proportional to $(\alpha h\nu)^{\frac{1}{2}}$, against $h\nu$, is taken and the E_g is extracted where the slope extrapolated to zero. However, it should be noted that the widely used Tauc plot only provides a very crude approximation which does not have a comprehensive theoretical basis in determining the band gap because it assumes free carriers, rather than excitonic or absorption edges. As such, in the hybrid perovskites systems, the plot provides an underestimate of the E_g ; the plot determines the E_g minus excitonic binding energy and a thermal broadening parameter³²

3.4.4 Basic Concepts of Photoconductivity

The classical Drude model can be used to express the conductivity for a semiconductor. With only one type of charge carrier, e.g. electrons, n in the dark, in the presence of an applied electric field $F = V/l$, where V is the voltage applied across the length, l , the expression can be written as:

$$J = nev \quad (3.18)$$

where J is the current density, e the elementary charge and v the drift velocity of the charge carrier. Since the drift velocity is directly proportional to the applied electric field, $v = \mu F$, the current density will also be proportional to the applied field, i.e.

$$J = \sigma F \quad (3.19)$$

where $\sigma = ne\mu$, which is the conductivity of the material.

When the sample is under illumination, a change in the conductivity might occur due to either a change in the carrier concentration Δn or to a change in the carrier mobility $\Delta\mu$:

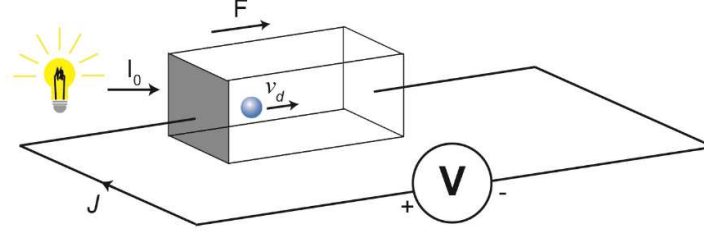


Figure 3.18 schematic of the various quantities which determines the photoconductivity process in based on Drude model. I_0 is the illumination intensity, F is the applied electric field, J is the current density and v_d is the charge carrier drift velocity.

$$\Delta\sigma = \sigma_{light} - \sigma_{dark} = e(\mu\Delta n + n\Delta\mu) \quad (3.20)$$

In general,

$$J_{PC} = eF[\mu(t)\Delta n(t) + n(t)\Delta\mu(t)] \quad (3.21)$$

where J_{PC} is the photocurrent. It should be noted that both the mobility and carrier density are a function of time. If $\Delta n \gg \Delta\mu$, as verified in many semiconductors, and the time dependence of mobility can be neglected, then the photoconductivity can be written as

$$J_{PC}(t) = \Delta\sigma eF = e\mu\Delta n(t)F \quad (3.22)$$

At low light injection levels, it can be assumed that there is a constant quantum yield of free charges per photon absorbed. Hence, the spatial dependence of the intensity is described by Beer-Lambert law. For absorption in the z -direction, Beer-Lambert's law reads:

$$\frac{dI}{dz} = -\alpha I, I(z) = I_0 e^{-\alpha z} \quad (3.23)$$

where α is the absorption coefficient and I_0 the illumination intensity. Therefore, the optical generation rate of the free carriers, g , can be written as

$$g(z) = -\eta \frac{1}{\hbar\omega} \frac{dI}{dz} = \eta(1-R) \frac{1}{\hbar\omega} \alpha I_0 e^{-\alpha z} \quad (3.24)$$

where η is the charge carrier generation quantum efficiency, $\hbar\omega$ is the photon energy, and R is the reflectance. It should be noted that η , α and R are dependent on photon energy. These photoexcited carriers will eventually relax back to the ground state with a characteristic lifetime, τ . Therefore, under constant illumination at the steady state condition,

$$\Delta n(t) = g\tau = \text{constant} \quad (3.25)$$

Hence, it follows that the photoconductivity is given by

$$\Delta\sigma = ge(\mu\tau) \quad (3.26)$$

Therefore, the total steady state photocurrent for a given photon energy can be written as:

$$J_{PC} = \Delta\sigma F = e\mu\tau F \int_0^d g(z)dz = \eta(1-R)(1-e^{-\alpha d}) \frac{I_0}{\hbar\omega} e\mu\tau F \quad (3.27)$$

where d is the sample thickness in the absorption direction. The above equation can be generalized to the scenario where both charge carriers, i.e. electron and holes with charge carrier density n and p respectively, contribute to the photocurrent response:

$$J_{PC} = \eta(1-R)(1-e^{-\alpha d}) \frac{I_0}{\hbar\omega} eF(\mu_n\tau_n + \mu_p\tau_p) \quad (3.28)$$

Steady state photocurrent is largely dictated by long lifetimes processes often associated with defects or disorder (e.g. trapping) and would therefore not be the true material lifetime. Additionally, a challenge remains on disentangling the mobility-lifetime effects from the photogeneration effects. In transient photocurrent measurements, the carriers are generated by a short radiation pulse and the photocurrent decay is recorded as a function of time. If the optical pulse duration is short compared to the carrier lifetime, the initial photogenerated carrier density will be given by

$$N(t=0) = (1-R)(1-e^{-\alpha d})\eta \frac{P}{d} \quad (3.29)$$

where P is the number of photons per pulse per unit area, d is the sample thickness, and η is the charge carrier photogeneration quantum efficiency. If the density of carrier photogenerated by the pulsed excitation is large, compared to the intrinsic carriers, then the photocurrent density can be written by eq 3.22, with $\Delta n(t) \cong N(t)$,

$$J_{PC}(t) = N(t)e\mu F \quad (3.30)$$

Hence, the transient photocurrent waveform will reflect the kinetics of the charge carrier density after photoexcitation.

The expression for peak photocurrent can then be written as

$$I_{peak} = \eta\phi\mu(1-R)(1-e^{-\alpha d}) \frac{E_p e V}{\hbar\omega d^2} \quad (3.31)$$

Thus, the early time mobility can be extracted from the plot of peak photocurrent against the applied voltage when an estimate of the quantum yield, $\eta\phi$, is available.

Experimentally, the sample transient photoconductivity measurements were done on the Auston switch setup as seen in Fig 3.19. The geometry of the stripline determines the impedance of the transmission line, Z_0 , and has to match the 50 Ω input impedance

required by the acquisition system. The impedance is given by the empirical relation,

$$Z_0(\varepsilon, h, w, t) = \frac{87}{\sqrt{\varepsilon + 1.41}} \ln \frac{5.98h}{0.8w + t} \quad (3.32)$$

here w and t are the line width and thickness, h and ε are the thickness and dielectric constant of the substrate respectively. A nominal 50Ω impedance is obtained with these parameters:

$$\varepsilon = 10.6$$

$$h = 0.625 \text{ mm}$$

$$w = 0.625 \text{ mm}$$

$$t = 0.01 \text{ mm}$$

The small gap, which would be the active area of the switch, d , is 0.1 mm. The incoming ultrafast laser pulse would hit on this gap under an external DC bias and the photogenerated carriers are driven across the gap by the applied electric field. This photocurrent pulse would then be recorded in the oscilloscope. While a decrease in gap size would consequently increase the capacitance logarithmically, the photosensitivity is increased proportionally to d . Hence, by using very small gaps, the sensitivity can be increased without a loss of bandwidth. For the given above parameters, the capacitance, $C_g = 0.02 \text{ pF}$, and the effective time constant for this Auston switch is $2Z_0C_g \sim 2 \text{ ps}$.

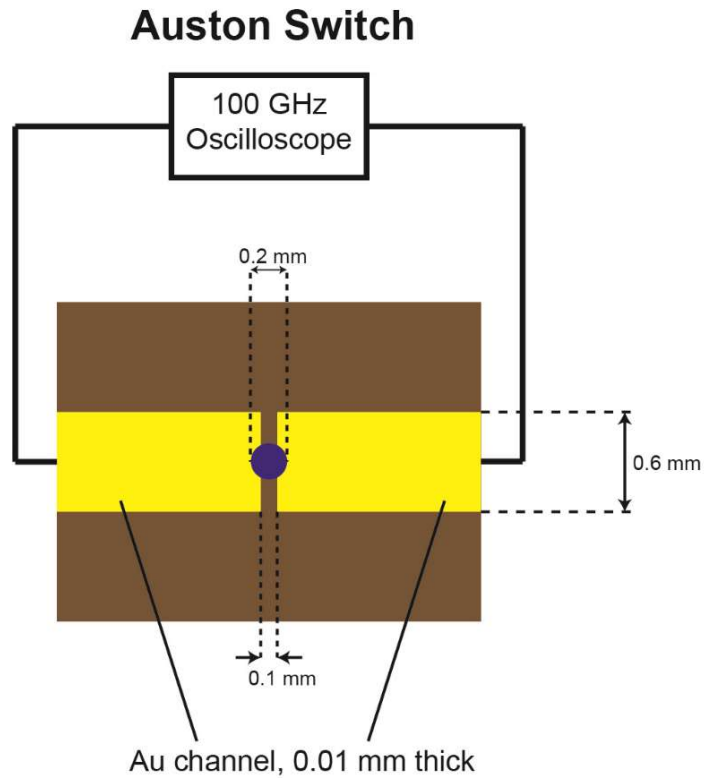


Figure 3.19 schematic of the transient photocurrent setup. The photoelectrons are generated

with an optical excitation source of 400 nm pulsed laser with a beam diameter of 0.2mm, and is collected by applying a bias across the gold channel and recorded with an 100 GHz oscilloscope

References

1. Stoumpos, C. C.; Cao, D. H.; Clark, D. J.; Young, J.; Rondinelli, J. M.; Jang, J. I.; Hupp, J. T.; Kanatzidis, M. G., Ruddlesden–Popper Hybrid Lead Iodide Perovskite 2D Homologous Semiconductors. *Chemistry of Materials* **2016**, 28 (8), 2852-2867.
2. Cuadro, A. M.; Matia, M. P.; Garcia, J. L.; Vaquero, J. J.; Alvarez-Builla, J., Synthesis of N- (Aminoethyl) Azoles Under Phase Transfer Catalysis. *Synthetic Communications* **1991**, 21 (4), 535-544.
3. Kittel, C., *Introduction to Solid State Physics*. Wiley: 2004.
4. Clegg, W.; Blake, A. J., *Crystal structure analysis principles and practice*. 2nd ed. ed.; Oxford University Press: Oxford, 2009.
5. Ashcroft, N. W., *Solid state physics*. Revised edition. ed.; Cengage Learning Asia Pte Ltd: Singapore, 2016.
6. Palatinus, L.; Chapuis, G., SUPERFLIP - a computer program for the solution of crystal structures by charge flipping in arbitrary dimensions. *Journal of Applied Crystallography* **2007**, 40 (4), 786-790.
7. Sheldrick, G., SHELXT - Integrated space-group and crystal-structure determination. *Acta Crystallographica Section A* **2015**, 71 (1), 3-8.
8. Giacovazzo, C., *Fundamentals of crystallography*. 3rd ed. ed.; Oxford University Press: Oxford, 2011.
9. Karle, J.; Hauptman, H., The phases and magnitudes of the structure factors. *Acta Crystallographica* **1950**, 3 (3), 181-187.
10. Sayre, D., The squaring method: a new method for phase determination. *Acta Crystallographica* **1952**, 5 (1), 60-65.
11. Sivia, D. S., *Data analysis : a Bayesian tutorial*. 2nd ed. ed.; Oxford University Press: Oxford, 2006.
12. Hughes, I., *Measurements and their uncertainties : a practical guide to modern error analysis*. New York: Oxford, 2010.

13. Jones, P. G., Crystal structure determination: a critical view. *Chemical Society Reviews* **1984**, *13* (2), 157-172.
14. Dolomanov, O. V.; Bourhis, L. J.; Gildea, R. J.; Howard, J. A. K.; Puschmann, H., OLEX2: a complete structure solution, refinement and analysis program. *Journal of Applied Crystallography* **2009**, *42* (2), 339-341.
15. Spek, A., Structure validation in chemical crystallography. *Acta Crystallographica Section D* **2009**, *65* (2), 148-155.
16. Macrae, C. F.; Sovago, I.; Cottrell, S. J.; Galek, P. T. A.; McCabe, P.; Pidcock, E.; Platings, M.; Shields, G. P.; Stevens, J. S.; Towler, M.; Wood, P. A., Mercury 4.0: from visualization to analysis, design and prediction. *Journal of Applied Crystallography* **2020**, *53* (1), 226-235.
17. Rietveld, H., A profile refinement method for nuclear and magnetic structures. *Journal of Applied Crystallography* **1969**, *2* (2), 65-71.
18. Young, R. A.; Wiles, D. B., Profile shape functions in Rietveld refinements. *Journal of Applied Crystallography* **1982**, *15* (4), 430-438.
19. Thompson, P.; Cox, D. E.; Hastings, J. B., Rietveld refinement of Debye-Scherrer synchrotron X-ray data from Al₂O₃. *Journal of Applied Crystallography* **1987**, *20* (2), 79-83.
20. Massiot, D.; Fayon, F.; Capron, M.; King, I.; Le Calvé, S.; Alonso, B.; Durand, J.-O.; Bujoli, B.; Gan, Z.; Hoatson, G., Modelling one- and two-dimensional solid-state NMR spectra. *Magnetic Resonance in Chemistry* **2002**, *40* (1), 70-76.
21. Wilkening, M.; Heitjans, P., Li jump process in h-Li_{0.7}TiS₂ studied by two-time ⁷Li spin-alignment echo NMR and comparison with results on two-dimensional diffusion from nuclear magnetic relaxation. *Physical Review B* **2008**, *77* (2), 024311.
22. Hartmann, S. R.; Hahn, E. L., Nuclear Double Resonance in the Rotating Frame. *Physical Review* **1962**, *128* (5), 2042-2053.
23. Jeener, J.; Meier, B. H.; Bachmann, P.; Ernst, R. R., Investigation of exchange processes by two-dimensional NMR spectroscopy. *The Journal of Chemical Physics* **1979**, *71* (11), 4546-4553.
24. Griffiths, P. R., *Fourier transform infrared spectrometry*. Wiley: New York, 1986.
25. Smith, B. C., *Fundamentals of Fourier transform infrared spectroscopy*. CRC Press: Boca Raton, 1996.

26. Rees, O. J., *Fourier transform infrared spectroscopy : developments, techniques, and applications*. Nova Science Publishers: New York, 2010.
27. Zewail, A. H., Laser Femtochemistry. *Science* **1988**, 242 (4886), 1645.
28. Zhong, D.; Pal, S. K.; Wan, C.; Zewail, A. H., Femtosecond dynamics of a drug–protein complex: Daunomycin with Apo riboflavin-binding protein. *Proceedings of the National Academy of Sciences* **2001**, 98 (21), 11873.
29. Pal, S. K.; Peon, J.; Bagchi, B.; Zewail, A. H., Biological Water: Femtosecond Dynamics of Macromolecular Hydration. *The Journal of Physical Chemistry B* **2002**, 106 (48), 12376-12395.
30. Snellenburg, J. J.; Liptonok, S.; Seger, R.; Mullen, K. M.; van Stokkum, I. H. M., Glotaran: A Java-Based Graphical User Interface for the R Package TIMP. *J. Stat. Softw* **2012**, 49, 22.
31. Kubelka, P.; Munk, F., Ein Beitrag zur Optik der Farbanstriche. *Z. Tech. Phys. (Leipzig)* **1931**, 12, 593-601.
32. Green, M. A.; Ho-Baillie, A. W. Y., Pushing to the Limit: Radiative Efficiencies of Recent Mainstream and Emerging Solar Cells. *ACS Energy Letters* **2019**, 4 (7), 1639-1644.

Chapter 4

Large polaron self-trapped states in 3D MAPbI₃ *

The nature of technologically relevant 3D MHP are studied extensively in this chapter. This chapter utilizes a combination of DFT and spectroscopy across the entire optical frequency range to pin down polaron features because large electron-phonon coupling characteristics are expected to dominate in HOIPs. The formation dynamics of the polaron signature are seen on the order of nanoseconds, with a portion living up into the milliseconds, which is probed extensively by steady state photoinduced absorption. The MIR spectral features show the photogeneration of states associated with low energy intragap electronic transition with lifetime in the millisecond regime, and vibrational mode renormalization in both frequency and amplitude where DFT supports the assignments, thus proving the existence of large polarons through both theoretical and experimental works.

*This section is published substantially as Walter P. D. Wong, Jun Yin, Bhumika Chaudhary, Xin Yu Chin, Daniele Cortecchia, Shu-Zee A. Lo, Andrew C. Grimsdale, Omar F. Mohammed, Guglielmo Lanzani, and Cesare Soci. Large Polaron Self-Trapped States in Three-Dimensional Metal-Halide Perovskites. *ACS Materials Letters*. **2020** 2, (1), 20-27. Reprinted with permission. Copyright (2020) American Chemical Society.

4.1 Introduction

Metal halide perovskites have attracted enormous interest since 2015 because the material is very easily processable^{1, 2} and exhibits numerous remarkable properties as highlighted in the earlier chapter³⁻⁹ and there are some evidence pointing towards the possibility of charge carriers being protected by polaronic characteristic in the perovskite lattice^{10, 11}. The highly deformable and polar nature of the metal halide framework can cause charge carriers to self-trap into phonon dressed localized states¹²⁻¹⁴. In lower dimensional perovskites, e.g. 2D perovskites, Coulombic interactions are enhanced through reduced dielectric screening and quantum confinement effects giving rise to the formation of self-trapped excitons (small polarons) and manifests in apparent radiative recombination effects like white light emission in compounds like (EDBE)PbBr₄^{14, 15}, where *ab initio* simulations indicates that the excess charge is spatially confine to one crystal unit cell or less. Hence, the photoexcitation induces localized distortions of the lead-halide framework¹⁴⁻¹⁷ which is associated with to polaron-exciton states, with a characteristic fine structure in the absorption line-shapes¹⁸. Conversely, for charge carriers in 3D perovskites, the polarons may extend over several lattice sites¹⁹ because of the long-range electron phonon interaction typically observed in ionic crystals. Large polarons are expected to exhibit band-like transport with mobility greater than $1 \text{ cm}^2 \text{ V}^{-1} \text{ s}^{-1}$, that falls with increasing temperature^{11, 20}. Furthermore, electrostatic screening from the polar lattice deformation could hinder Coulomb mediated processes such as Auger cooling and Langevin recombination²¹.

Recent works point towards the role of electron-phonon coupling which contributes to the formation of polarons²²⁻²⁸. In similar materials like MAPbBr₃, there is evidence for screening effects in reorientation of the molecular dipoles and presence of coherent phonon modes generated via displacive excitation^{29, 30} but this is not a proof of their existence. Polaronic states have been invoked to explain octahedral distortion effects due to coherent vibrations of the Pb-I modes in MAPbI₃³¹ but the impact of carrier induced lattice distortion on polaron formation and charge transport in optoelectronic devices has remained elusive.³ From a structural perspective, the structure of MAPbI₃ has been thoroughly examined and debated.³²⁻⁴³ Although the methylammonium cation cannot be accurately modelled based on diffraction studies, this dynamic disorder is

further observed through other indirect techniques like nuclear magnetic resonance.^{38, 42, 44, 45} Furthermore, the inorganic framework, which dominates most of the diffraction results, is seen to be consistent across several studies^{33, 35, 39-41}. Therefore, this work starts off by exploring polaronic effects through first principles DFT calculation built upon the current understanding of the structural properties of MAPbI₃ and these theoretical predictions are further tested through experimental observations in the IR continuous-wave photoinduced absorption (cw-PIA) spectroscopy. Lastly, this work further explores the formation dynamics of polarons through ultrafast transient and photocurrent spectroscopy.

4.2 Experimental Methods

4.2.1 Computational methods: polaronic and free carrier mobility

The first principles density functional theory (DFT) calculations were carried out at generalized gradient approximation/Perdew-Burke-Enzerhof (PBE) level using the projector-augmented wave (PAW) method as implemented in the Vienna Ab initio simulation (VASP) package^{46, 47}. The plane-wave basis set cutoff of the wavefunctions were set to 400 eV and a uniform grid of 6×6×6 k -mesh in the Brillouin zone was employed to optimize the crystal structure of MAPbI₃. The van der Waals function (vdW-DF) was included during the structural optimization and calculation of electronic properties. The resulting crystallographic parameters of the tetragonal-phase MAPbI₃ is $a = 8.68 \text{ \AA}$, $b = 8.67 \text{ \AA}$, $c = 12.8 \text{ \AA}$. Thereafter, a 3×3×3 supercell containing 1296 atoms were used for the large polaron simulations and the Brillouin zones were sampled by the Γ point. The atomic positions of MAPbI₃ supercells in the neutral and charged, or photoexcited, states were fully relaxed until each atom in the supercells experience forces of less than 0.01 eV/Å. The charge density distribution of valence band maximum (VBM) or conduction band minimum (CBM) for MAPbI₃ supercells were used to describe the positive or negative polaron features. The effective masses for the electron (m_e^*) and hole (m_h^*) were estimated by fitting the dispersion relation of $m^* = \hbar^2 \left[\frac{\partial^2 \varepsilon(k)}{\partial k^2} \right]^{-1}$ from the band structures (Fig 4.1 a and 4.1b) along the directions Γ -X, Γ -Z and Γ -M for tetragonal phase and Γ -X and Γ -Z for orthorhombic phase. The

optical dielectric function was simulated using random phase approximation (RPA) method as implemented in VASP.

Infrared and Raman vibronic mode position and intensities were calculated using *Phonon* code as implemented in *Quantum Espresso* package⁴⁸ at the Γ point of the first Brillouin zone. The local density approximation (LDA) exchange-correlation functional with norm-conserving pseudopotential were utilized based on the optimized neutral and charged structures. The plane-wave expansion cutoff for the wavefunctions were set at 100 Ry where the uniform grids of 12x12x8 Monkhorst-Pack scheme were used for the k-point sampling with a self-consistency threshold of 10^{-14} Ry

Free carrier mobility is calculated by the semi-classical Boltzmann transport theory where only the contribution of acoustic phonon were considered in the evaluation of the scattering lifetime. The charge carrier density (n) and mobility (μ) are approximated as^{49, 50}

$$n = \frac{(2m^*k_B T)^{\frac{3}{2}}}{2\pi^2\hbar^3} {}_0F_0^{\frac{3}{2}} \quad (4.1)$$

$$\mu = \frac{2\pi\hbar^4 e B}{m_l^* (2m_b^* k_B T)^{\frac{3}{2}} \Xi^2} \frac{{}_3^0 F_{-2}^1}{{}_0F_0^{\frac{3}{2}}} \quad (4.2)$$

where

$${}_n F_l^m = \int_0^\infty \left(-\frac{\partial f}{\partial \zeta} \right) \zeta^n (\zeta + \alpha \zeta^2)^m [(1 + 2\alpha \zeta)^2 + 2]^{\frac{l}{2}} d\zeta \quad (4.3)$$

$$f = \frac{1}{(e^{\zeta - \xi} + 1)}; \frac{\alpha = k_B T}{E_g}, \quad (4.4)$$

where k_B is the Boltzmann constant, e is the elementary charge, T is the temperature, $2\pi\hbar$ is the Planck constant, and ξ is the reduced chemical potential; m^* is the density of state effective mass, m_l^* is the conductivity effective mass, m_b^* is the band effective mass; B is the bulk modulus ($B = \frac{\partial^2 E}{\partial V^2}$), $\Xi_{e-p/h-p}$ is the electron-phonon (or hole-phonon) coupling energy ($\Xi_{e-p/h-p} = V_0 \left(\frac{\Delta E_{CBM}}{\frac{VB M}{\Delta V}} \right)$), n , m , and l power integer indices, E_g is the electronic band gap, and ζ is the reduced carrier energy.

Electron phonon coupling is described by the dimensionless Frohlich parameter, α ,

$$\alpha = \frac{1}{4\pi\epsilon_0} \frac{e^2}{\hbar} \left(\frac{1}{\epsilon_\infty} - \frac{1}{\epsilon_s} \right) \sqrt{\frac{m}{2\hbar\omega_p}} \quad (4.5)$$

where ϵ_0 is the dielectric constant of vacuum; ϵ_∞ and ϵ_s are optical and static dielectric constants, respectively; e is the charge of carrier; $2\pi\hbar$ is Planck's constant; m is the bare electron band effective mass and ω_p is the characteristic angular frequency of the longitudinal optical (LO) phonon mode. ω_p is obtained from the $\text{Im}[1/\epsilon(\omega_p)]$ spectra in far-infrared region, as presented in Fig 4.2.

The finite-temperature free energies of the coupling electron-phonon system are taken from the expression derived by Ōsaka, which is an extension of Feynman's athermal variational solution. The self-free energy of polaron F , is under the phono occupation factor $\beta = \omega_p/k_B T$, and was calculated with two parameters: v and w , where v is a unit of ω , the frequency of relation motion between a charge and a coupled LO phonon; w is a unit of ω_p ^{51, 52}. Thereafter, v and w were numerically solved by giving the minimum $F = -(A + B + C)$ ¹⁰, where

$$A = \frac{3}{\beta} \left[\ln\left(\frac{v}{w}\right) - \frac{\ln(2\pi\beta)}{2} - \ln \frac{\sinh\left(\frac{v\beta}{2}\right)}{\sinh\left(\frac{w\beta}{2}\right)} \right] \quad (4.6)$$

$$B = \frac{\alpha v}{\sqrt{\pi[\exp(\beta) - 1]}} \int_0^{\frac{\beta}{2}} \frac{\exp(\beta - x) + \exp(x)}{\sqrt{w^2 x \left(1 - \frac{x}{\beta}\right) + \frac{Y(x)(v^2 - w^2)}{v}}} dx \quad (4.7)$$

$$Y(x) = \frac{1}{1 - \exp(-v\beta)} [1 + \exp(-v\beta) - \exp(-vx) - \exp\{v(x - \beta)\}] \quad (4.8)$$

$$C = \frac{3(v^2 - w^2)}{4v} \left(\coth\left(\frac{v\beta}{2}\right) - \frac{2}{v\beta} \right) \quad (4.9)$$

Therefore, the expression for polaron mobility can be described as^{53, 54}

$$\mu = \frac{3\sqrt{\pi}e}{2\pi\omega m\alpha_{e-ph}} \frac{\sinh\left(\frac{\beta}{2}\right)}{\beta^{\frac{5}{2}}} \frac{w^3}{v^3} \frac{1}{K} \quad (4.10)$$

where

$$K = \int_0^\infty \frac{\cos(u)}{(u^2 + a^2 - b\cos(vu))^{\frac{3}{2}}} du \quad (4.11)$$

$$a^2 = \left(\frac{\beta}{2}\right)^2 + \left(\frac{v^2 - w^2}{w^2 v}\right) \beta \coth\left(\frac{\beta v}{2}\right) \quad (4.12)$$

$$b = \left(\frac{v^2 - w^2}{w^2 v}\right) \frac{\beta}{\sinh\left(\frac{\beta v}{2}\right)} \quad (4.13)$$

4.2.2 FTIR Spectroscopy and Continuous-Wave Photoinduced Absorption

Photoinduced absorption measurements were carried out in a Bruker V80v FTIR spectrometer using a solid-state pump laser at 532 nm with an intensity of ~200 mW/cm², modulated by a Thorlabs shutter. The samples fabricated from 20 wt % precursor solutions were utilized for the visible regime while the samples fabricated from 40 wt % solutions were utilized in the NIR and MIR range. cw-PIA measurements were carried out at room temperatures (298 K) or at low temperatures (78 K) in a Helitran cryostat, which is cooled by liquid nitrogen with a base pressure of around 5.0×10^{-5} mbar. Four different detectors were used to probe the three distinct spectral regimes: Deuterated Triglycine Sulfate (DTGS) and Mercury Cadmium Telluride (MCT) to probe the mid-infrared regime, Indium Gallium Arsenide (InGaAs) to probe near-infrared, and Silicon to probe the visible regime. A notch filter at 532 nm was used for measurements in the visible regime to eliminate pump laser scattering, while a 650 nm band pass filter or a double-polished Silicon wafer were utilized for NIR and MIR measurements, respectively. The FTIR spectrometer operated in rapid scan mode. Transmittance spectra were recorded under photoexcitation, T_{on} , and without photoexcitation, T_{off} to obtain the PIA, $-\Delta T/T$. Approximately 8000 T_{on} and T_{off} scans each were collected and averaged to obtain the desired signal-to-noise ratio.

4.2.3 Transient Absorption

A commercial regenerative amplifier system (Quantronix Integra-C) was used as the laser source with a repetition rate of 1 kHz at 810 nm and pulse width of around 100 fs. A commercial spectrometer, Jobin Yvon CP140-104, equipped with a silicon photodiode array was used to record the transient absorption spectra (Entwicklungsbüro

Stresing). A portion of the laser beam was split to generate the 400 nm pump beam using a 1 mm thick BBO crystal cut at 29.2°. White probe light was generated using a sapphire crystal coupled with a 750 nm short pass filter just sufficient to attenuate 800 nm generation beam without saturating the camera and thus, the output spectrum was sensitive from 550 to 830 nm. An additional long pass filter with cut-off wavelength of 450 nm was used after the sample to avoid saturation of the camera by the intense pump beam. A schematic of the experimental setup is seen in Fig 3.16. The intensity of pump laser is measured to be 5 nJ per pulse. The results were subsequently processed through a global fitting of the resulting spectral decays was performed using the R-package TIMP on Glotaran interface⁵⁵, with multiple sequential exponential decays. Dispersion compensation was conducted by fitting 2nd order dispersion relationship central at 755 nm in conjunction with the interested multiple exponential decay function. Convergence of the numerical fitting is ensured by multiple rounds of numerical fitting using calculated parameters from previous round, until all parameters stabilize. Overall goodness of the fitting is indicated by the final residual error of 0.489 after stabilization, with no temporal and spectral trend in residue plots.

4.2.4 Transient and steady state photocurrent

The setup utilizes the same femtosecond pump laser as for transient absorption measurements, frequency doubled to the excitation wavelength of 400 nm. Gold contacts were deposited via a shadow mask to form a 50 Ω Auston photoconductive switch. Measurements were performed in a vacuum chamber focusing 5 mW laser beam power on a 1.5×10^{-3} cm² spot size. External bias of 5 V to 30 V was supplied by a picoammeter/voltage source (Keithley 6487). The transient photocurrent signal was recorded using a real-time high-speed oscilloscope (Teledyne Lecroy LabMaster 10 Zi-A) equipped with a 100 GHz sampling channel, connected after a Mini-Circuit DC-AC splitter to prevent DC current leakage.

Steady state photocurrent measurements were performed using conventional amplitude modulation technique in a setup equipped with a Xe lamp source, a monochromator (Horiba iHR550) which disperses light in the wavelength range of 300-900 nm, a mechanical chopper (Stanford SR570), a voltage source (Keithley 6487), and a lock-in amplifier (Stanford SR830). The chopper modulation frequency was set to 138 Hz, and

the lock-in time constant was 300 ms, corresponding to 0.42 Hz equivalent noise bandwidth. Before the measurement, the monochromatic light power was obtained using a reference calibrated Si photodiode.

4.3 Results

4.3.1 Computational results

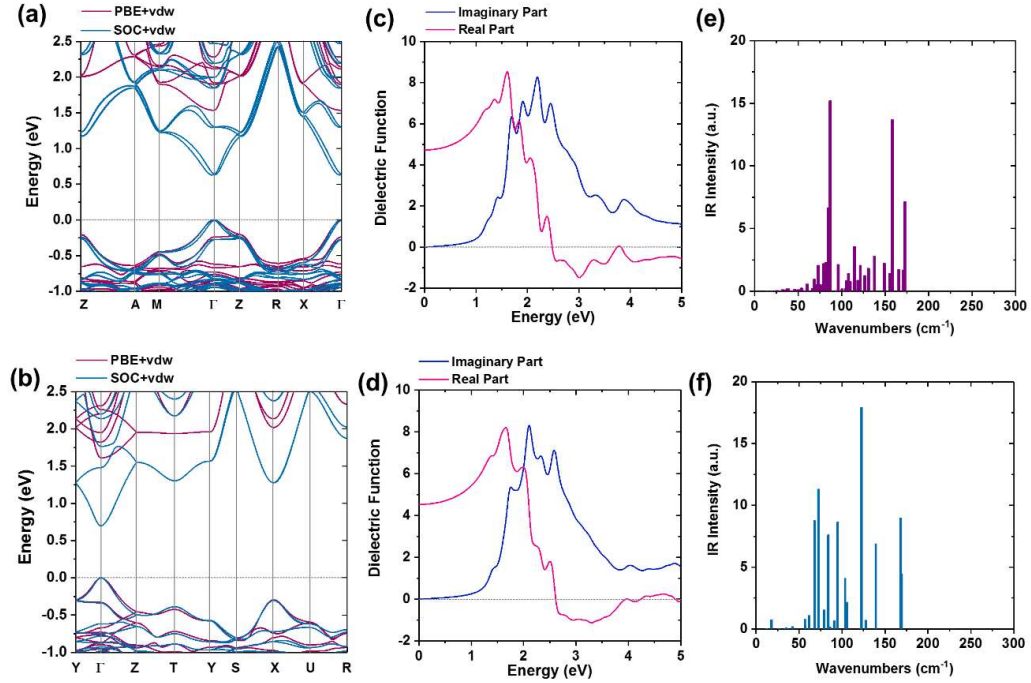


Figure 4.1. Electronic and optical properties of MAPbI₃. (a, b) calculated electronic band structures, (c, d) real part (in red) and imaginary part (in blue) of dielectric function, and (e, f) far-infrared vibrational modes and intensity for tetragonal-phase (up) and orthorhombic-phase (down) MAPbI₃.

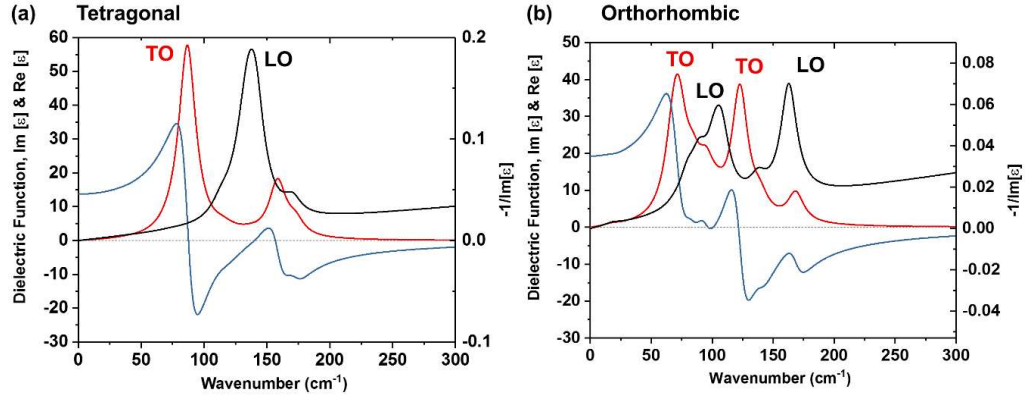


Figure 4.2. Far-infrared optical response of MAPbI₃. Calculated real part (in red), imaginary part (in blue) of dielectric function, and imaginary part of the inverse dielectric function (in black) for (a) tetragonal-phase and (b) orthorhombic-phase MAPbI₃.

The calculated electronic band structure is as shown in Figure 4.1 (a) and (b) where the plots show a direct comparison of the spin-orbit coupling (SOC) effects while using the same Perdew–Burke–Ernzerhof (PBE) function; the pink plot without SOC effect, while the blue plot is with SOC effects. A comparison of the two methods against experimental results are seen in the next section. The dielectric function taken from the same calculation and shown in Fig 4.1 (c) and (d) and is subsequently used in the simulation of free carrier and polaronic properties. The far infrared (FIR) vibrational modes were also calculated and are shown in Fig 4.1 (e) and (f), which shows that most of the vibrational modes are between 50 cm⁻¹ and 200 cm⁻¹. Zooming into the FIR region of the dielectric function of MAPbI₃, it can be seen that the specific transverse optical (TO) phonon mode can be seen from the real part of the dielectric function and longitudinal optical (LO) phonon modes from the inverse dielectric function. The LO modes are then utilized to calculate the free carrier and polaronic mobilities, as outlined in the earlier section. The key parameters for calculating the free carrier and polaronic mobilities and results are summarized in Table 4.1 and Table 4.2, while the important results of the effective mass and mobility are summarized in Table 4.3.

Table 4.1. The parameters for calculating free carrier mobility. Band (m_b^*), conductivity (m_l^*) and density of state (m^*) effective mass, hole/electron-phonon coupling (Ξ), bulk modulus (B), and free hole/electron mobility (μ_{carrier}) for tetragonal and orthorhombic phase MAPbI₃.

Compound	Type	m_b^*	m_l^*	m^*	Ξ	B	μ_{carrier} (cm ² /V·s)
MAPbI ₃ (300K, Tetragonal)	Positive	0.198	0.196	0.210	10.268	3.303	332.2
	Negative	0.185	0.184	0.200	7.975		630.5
MAPbI ₃ (78K, Orthorhombic)	Positive	0.220	0.215	0.210	10.869	3.427	1491.6
	Negative	0.171	0.166	0.187	8.051		5122.0

Table 4.2. The parameters for calculating polaron mobility. Optical and static dielectric constants (ϵ_∞ and ϵ_s), angular frequencies of a characteristic LO phonon mode (ω), average hole/electron effective masses of bare electron bands (m^*), electron-phonon coupling constant (α), phonon occupation factor (β), hole/electron polaron mass (m_{polaron}^*) and hole/electron polaron mobility (μ_{polaron}) for tetragonal- and orthorhombic-phase MAPbI₃.

Compound	Type	ϵ_∞	ϵ_s	$\omega/2\pi$ (THz)	m^* ($\times m_0$)	α	β	m_{polaron}^* ($\times m_0$)	μ_{polaron} (cm ² /V·s)
MAPbI ₃ (300K, Tetragonal)	Positive	4.73	27.31	4.11	0.210	2.356	0.661	0.507	215.38
	Negative				0.200	2.299		0.492	225.93
MAPbI ₃ (78K, Orthorhombic)	Positive	4.53	23.59	4.86	0.210	2.208	1.396	0.468	497.93
	Negative				0.187	2.084		0.435	550.68

Table 4.3. Calculated effective mass (m^* , $\times m_0$) and mobility ($\text{cm}^2/\text{V}\cdot\text{s}$, average of different crystallographic directions) of free charges and polarons in tetragonal and orthorhombic phase MAPbI₃ (spin-orbit coupling effects included)

Type	Tetragonal			Orthorhombic		
	Effective Mass ($\times m_0$)		Mobility ($\text{cm}^2/\text{V}\cdot\text{s}$)	Effective Mass ($\times m_0$)		Mobility ($\text{cm}^2/\text{V}\cdot\text{s}$)
	M(Y) $\rightarrow\Gamma$	$\Gamma\rightarrow\text{Z}$		M(Y) $\rightarrow\Gamma$	$\Gamma\rightarrow\text{Z}$	
Free Hole	0.240	0.180	332.2	0.166	0.253	1491.6
Hole Polaron	1.411	1.058	215.4	0.976	1.487	497.9
Free Electron	0.220	0.107	630.5	0.121	0.204	5122.0
Electron Polaron	1.293	0.629	225.9	0.711	1.199	550.7

Importantly, the results here show how the effective masses and charge mobility are anisotropic across both the high temperature tetragonal and low temperature orthorhombic phases. The polaron effective masses are approximately 5 times larger than the free carrier effective mass and thus the polaronic mobilities are between 1.5 to 8 times smaller than the free carrier mobilities. Furthermore, the results presented here also shows that the polaronic effective mass anisotropy is smaller than the free carrier anisotropy. This is an indication that the polaronic mobility anisotropy would consequently be smaller than in the free carriers. While there are numerous limitations arising from *ab initio* simulations, the results here show that polaronic effects cannot be ignored during device design and operations because the difference can be up to an order of magnitude. Similarly, the anisotropic charge carrier properties would obscure charge carrier comparisons done on polycrystalline and single crystal samples. Therefore, polaronic effects cannot be ignored in MAPbI₃ and rigorous experimental evidence is needed, and this is thoroughly discussed in the subsequent section.

4.3.2 Comparison of DFT results against steady state UV-Vis and photocurrent

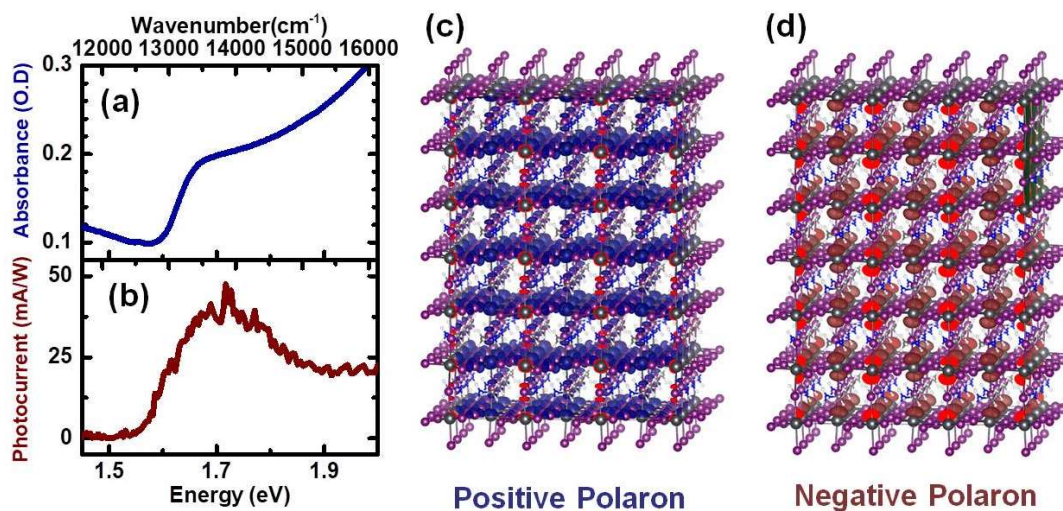


Figure 4.3 (a) Experimental steady state absorption and (b) steady state photocurrent results showing good agreement with the *ab initio* band structure without SOC effects, (Fig 4.1a, pink line). Schematic of (c) positive and (d) negative polaron charge density from DFT simulations

The *ab initio* DFT results was compared against experimental steady state UV-Vis and steady state photocurrent results in Fig 4.3 (a) and (b), where it is evident that calculations without SOC effects better reproduces experimental conditions with a simulated band gap of 1.61 eV, which is comparable to the experimentally observed 1.64 eV. However, with the inclusion of SOC effects, the band gap deviates significantly to 0.7 eV (Fig 4.1 a blue plot), but this is attributed to band splitting effect when SOC effects are included. The better approximation without SOC effects is attributed the error cancellation effects but inclusion of SOC would capture the contributions of the heavy elements.

The charge carriers are then simulated by removing an electron Fig 4.3 (c) and by including an additional electron Fig 4.3 (d) into the neutral lattice and allowed to spontaneously relax into the equilibrium geometry giving rise to the formation of such positive and negative polaronic states. Utilizing the parameters outlined in the Table 4.2, the new half-filled energy levels are associated to the negative polaron lies 0.187 eV below the conduction band minimum while energy level associated the positive polaron likes 0.235 eV above the valance band maximum. The resulting charge density

distribution shows the polarons to be localized within 2-3 inorganic atomic layers, and hence, would be a large polaron. This is comparable with that also observed in 3D and 2D perovskites. Accordingly, the charge carrier characteristics are also calculated and summarized in Table 4.3, where the effective masses and mobility are anisotropic.

As a result of polaronic formation, several critical observations which can be probed experimentally would be expected; firstly, partially filled states appear within the band gap and hence, gives rise to new optical transitions. Secondly, the vibrational mode frequencies are renormalized by the change in bond geometries, including the spectator modes (e.g. organic moiety and inorganic lattice). Thirdly, the geometric distortion induces local symmetry breaking what relaxes vibration selection rules and could activates vibrational modes that are silent for bare states. To further test these predictions, a photoinduced IR-absorption is measured over a broad IR range, from the visible regime deep into MIR.

4.3.3 Continuous-Wave Photoinduced Absorption

Low temperature steady state cw-PIA was carried out as described in the experimental section where the MAPbI₃ thin films synthesized from 40 wt% precursor solutions were used for regions I, II and III, to enhance the signal to noise ratio, while those produced using 20 wt% solutions were used for region IV to probe the region around PB and energy levels just above the band gap. cw-PIA measurements shows clear evidence for the generation of long-lived photoexcited states, with lifetimes on the order of milliseconds and there are four distinct regions of interest as highlighted in Fig 4.4a. In region I (500-2500 cm⁻¹), it shows two photoabsorption peaks P₀, which is assigned to trap states, and P₁, which is assigned to PIA states. In region II (3000 – 3300 cm⁻¹), a photomodulated vibronic mode, in region III which shows a broad transition P_n, and region IV, which shows the PA and PB. The disappearance of P₁ P₂ and P_n with increasing temperatures suggests that these spectral features have a common origin. Based on the spectral assignments, an oversimplified band schematic of MAPbI₃ is presented in Fig 4.4 c where P₁ and P₂ arising from the intra-gap polaronic states, P₀ from the trap states, P_n to higher level transitions and PB as expected from MAPbI₃. Due to the formation of the new intra-gap polaronic states, the optical transitions arising from it must exist as a high and low energy pair, as seen in the case of conjugated

polymers^{56,57}. Hence, P_1 and P_2 satisfy this condition nicely which is further supported by the values derived from first principles DFT calculations.

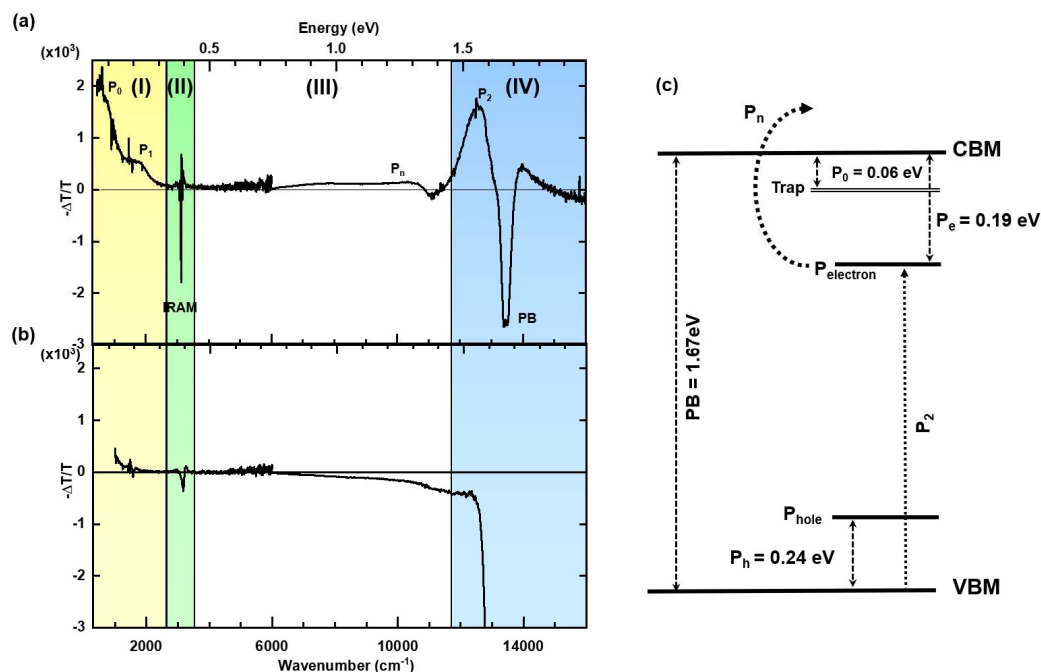


Figure 4.4 (a) Full PIA spectra at 78 K showing key photoabsorption feature and are subdivided into regions I, II, IV and III (b) full PIA spectrum at 298 K showing the concurrent disappearance of these key photoabsorption features (c) schematic energy level diagram of the photoexcited states. P_0 would correspond to the trap states, P_1 and P_2 corresponding to a high-low energy photoabsorption pair, which is a signature of polarons. P_n is assigned to the higher-level energy transitions of the photoinduced states.

Focusing on the PIA spectrum at region I, it features two photoinduced absorption bands centred around 516 cm^{-1} (P_0) and 1650 cm^{-1} (P_1), as determined by Gaussian fitting curves in red, and a series of small features at 620 cm^{-1} , 908 cm^{-1} , 1254 cm^{-1} , 1460 cm^{-1} and 1570 cm^{-1} (solid black lines running across Fig 4.5) which corresponds to the amplitude modulation of the main IR active (IRAV) vibrational modes of the organic CH_3NH_3^+ cation.⁵⁸ The feature at 600 cm^{-1} is an exception, which is within the range of C-N vibrational modes of the organic moiety, corresponds to an IR inactive Raman mode. This would indicate that the inversion symmetry that governs mutually exclusive Raman and IR mode selection rules is broken due to the local distortion of the lattice in the presence of the self-trapped charge.⁵⁸

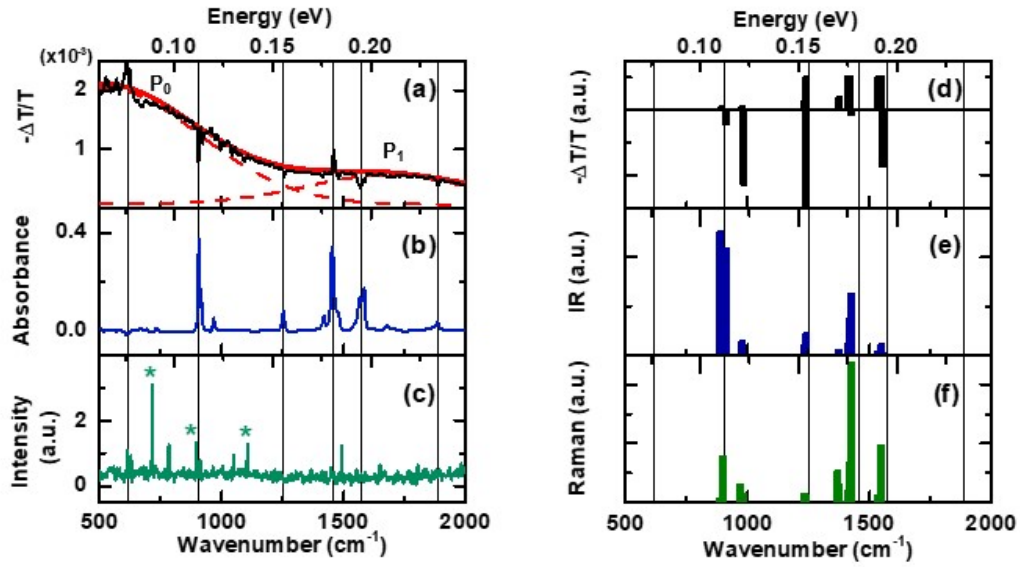


Figure 4.5 Experimental and simulated infrared active vibrational (IRAV) and Raman modes. (a) PIA spectrum ($T = 78$ K) fitted to two Gaussian peaks centred at 1650 cm^{-1} and 516 cm^{-1} (red dashed lines), (b) FTIR spectrum ($T = 78$ K), and (c) Raman spectrum ($\lambda_{\text{exc}} = 1024\text{ nm}$, $T = 300$ K), where green asterisks denote peaks from the CaF_2 substrate. (d) Simulated photoinduced absorption modes are obtained as $-(\Delta T/T) = -(IR_{\text{neut}} - IR_{\text{exc}})/IR_{\text{neut}}$, where IR_{exc} and IR_{neut} are the IR mode intensities of excited and ground states, respectively. (e, f) Calculated IR and Raman mode intensity spectra of orthorhombic MAPbI_3 . The main vibrational modes are indicated by black vertical lines, showing the correspondence between IRAV modes and Raman modes, which become IR-active under photoexcitation.

DFT calculations accurately accounts for two main experimental observations in region I of the spectrum; the broader photoabsorption band, P_1 , and the signs of the IRAV modes. The broad P_1 centred at 1650 cm^{-1} (0.204 eV) corresponds to a convolution of electronic transitions from negative and positive polaron states at $P_e = 0.187\text{ eV}$ below the CBM and $P_h = 0.235\text{ eV}$ above the VBM, respectively. Conversely, the P_0 peak centred at 516 cm^{-1} (0.06 eV), that does not emerge from the calculations, is likely due to the presence of trap states.⁹ Fig 4.5 (e) and (f) show the calculated IR and Raman spectra, which corresponds to the experimental modes assigned to the organic moiety. The photoinduced modulation of the IRAV modes from 750 cm^{-1} to 2000 cm^{-1} are reproduced reasonably well by the calculations. Fig 4.5 (d) shows the spectrum obtained by computing the difference between the spectra calculated in the undistorted

(i.e. neutral) and distorted (i.e. charged) perovskite lattices. The modulation sign is in agreement with the experiment for each mode, accounting for amplitude increase or decrease of the vibrational transitions upon polaron formation. This would suggest that the negative photoabsorption dips are due to a decrease of the vibrational transition oscillator strength, rather than originating from Fano resonances due to quantum interference of electronic and vibrational transitions.⁵⁹

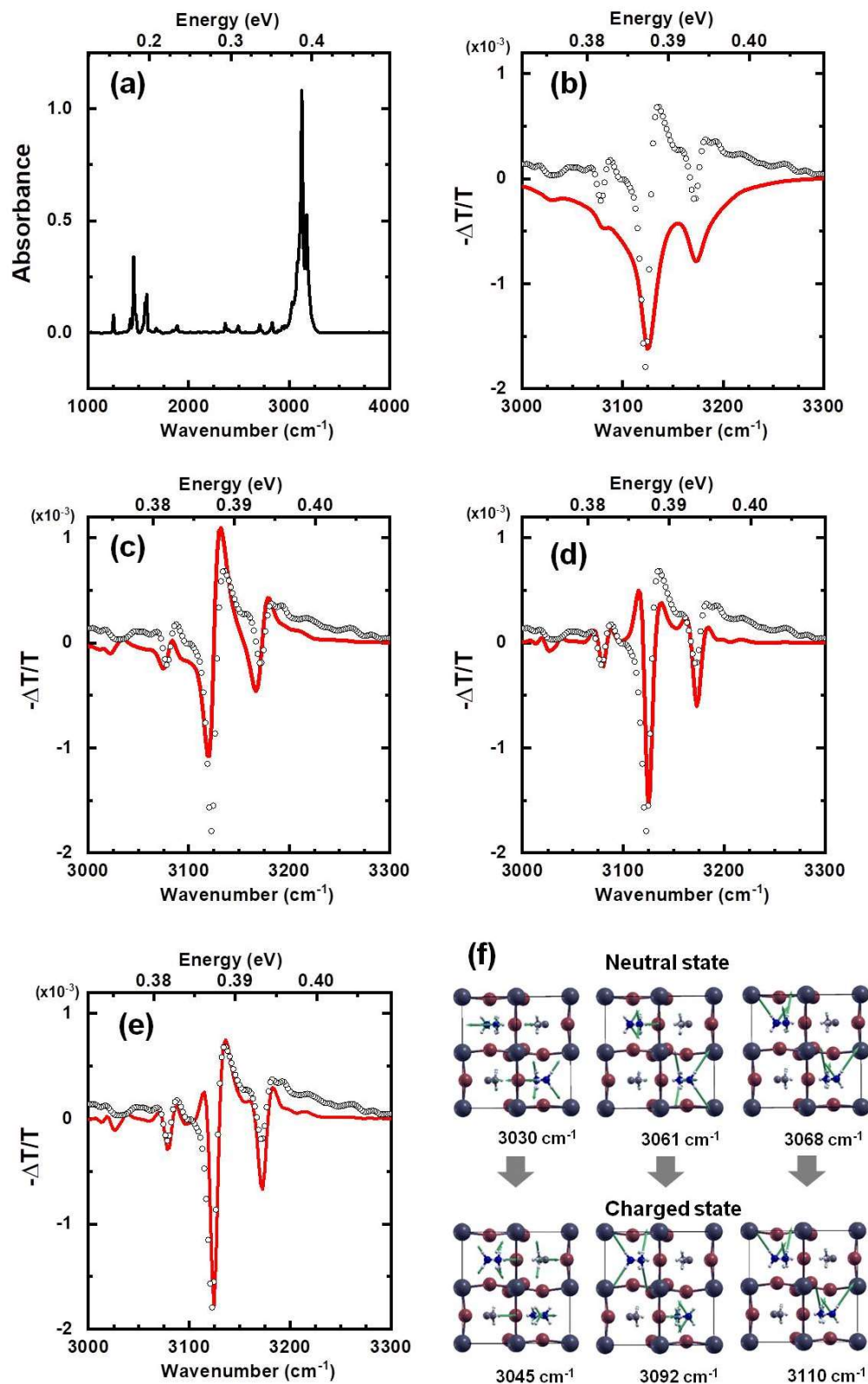


Figure 4.6 The Infrared active modulation (IRAM) of C – H and N – H stretching mode. (a) the FTIR absorbance spectrum of MAPbI₃, $f(\bar{\nu})$, (b) the fitted results (red line) against

experimental results (black open circles) with only the 0th order derivative, $f(\bar{\nu}) = -0.0015 f(\bar{\nu})$, (c) only the 1st order derivative, $f(\bar{\nu}) = -0.02 f'(\bar{\nu})$, (d) only the 2nd order derivative, $f(\bar{\nu}) = 0.11 f''(\bar{\nu})$ (d) best fit of this region with a combination of 1st and 2nd order derivative $f(\bar{\nu}) = -0.0075 f'(\bar{\nu}) + 0.1 f''(\bar{\nu})$. (e) the representative IR vibrational frequencies and displacement vectors obtained from phonon calculations, and corresponding blue-shift of IR-active-mode frequencies in the charged state.

Moving onto region II, in the low temperature orthorhombic-phase, MAPbI₃ shows several IR peaks in the spectral region between 3000 cm⁻¹ and 3300 cm⁻¹, which is assigned to both C – H and N – H stretching modes of the organic methylammonium cations. The photoinduced modulation of these modes in region II is of particular interest. The experimental PA data in this region is fitted to the zeroth, first and second derivative of the steady-state IR spectrum (Fig 4.6 a). The first derivative component of the absorption spectrum gives an indication of the spectral blue shift of the peak, while the second derivative component is related to the peak broadening⁶⁰. As seen from Fig 4.6 c and Fig 4.6 d, fitting only to the first derivative or to the second derivative only would not sufficiently reproduce the experimental spectrum. Both the blue shifting and peak broadening effects are attributed to the modulation of C – H and N – H bonds induced by the polarons. In the process of distorting the perovskite lattice locally, it has indirectly affected their vibrational potential through the hydrogen bonds between hydrogen atoms of –NH₃ and iodine atoms in charged MAPbI₃ (*spectator modes*). Thermal modulation cannot account for this effect as it determines an opposite red shift of the mode frequency (mode softening). DFT predicts that the mode in the neutral state at 3030 cm⁻¹, 3061 cm⁻¹ and 3068 cm⁻¹ would be shifted to 3045 cm⁻¹, 3092 cm⁻¹ and 3110 cm⁻¹ respectively, when in the charged state. In spite of the slight mismatch of calculated and experimental IR mode frequencies in both neutral and excited states (Fig 4.6 f), the blue shift induced by the lattice distortion on the vibrational modes is correctly reproduced by the DFT calculations. Thus, the observed long-lived vibrational frequency renormalization upon photoexcitation is a clear fingerprint of the generation of a geometrically relaxed state.

4.3.4 Transient dynamics

The concomitant photoinduced electronic spectrum, with intragap transitions, corroborate the assignment to photogenerated polarons. Details of the cw-PIA spectrum of region IV are shown in the Fig. 4.7 (a). The spectrum is then fitted to four Gaussian curves, labelled P₂ (centred at ~1.56 eV), PB (centred at ~1.67 eV) and a sum of two Gaussians at (centred at ~1.61 eV and ~1.69 eV) to model the effect of the change in refractive index as reported by Price et al.⁶¹ P₂ corresponds well to the energetics determined for ground state to polaron transitions, while the PB peak are assigned to valence to conduction band, which is in close agreement with that reported in literature.^{32, 62, 63} Photoabsorption peak assignments are summarized in Fig 4.4 (c).

Steady-state spectroscopy results thus far points to large polarons being the primary photoexcitations in 3D MAPbI₃. To determine their generation and relaxation dynamics, ultrafast (fs) transient absorption and fast (ps) transient photocurrent measurements were carried out. The time evolution of the transient photoinduced absorption (TPA) spectrum upon pulsed laser excitation is shown in the 2D contour plot in Fig. 4.7 (b) and shows two key features; first, a broad absorption peak from 1.7 to 2.0 eV (13700 to 16100 cm⁻¹) and secondly, a sharp peak centred at 1.64 eV (13200 cm⁻¹), which corresponds to the ground-state bleaching of MAPbI₃. Comparison of the cw-PIA and TPA spectra of MAPbI₃ (Figs. 4.7a, b) shows good qualitative agreement, with coexistence of PIA and PB components at different relative positions. The red-shift of the photobleaching peak in cw-PIA relative to the transient data is likely due to change in bandgap from 1.67 eV to 1.64 eV from the high temperature tetragonal phase to the low temperature orthorhombic phase,⁶⁴ since cw-PIA was collected at ~80 K whereas TPA was obtained at room temperature. Moreover, the TPA spectrum contains contributions from both neutral excitons and charged polarons.

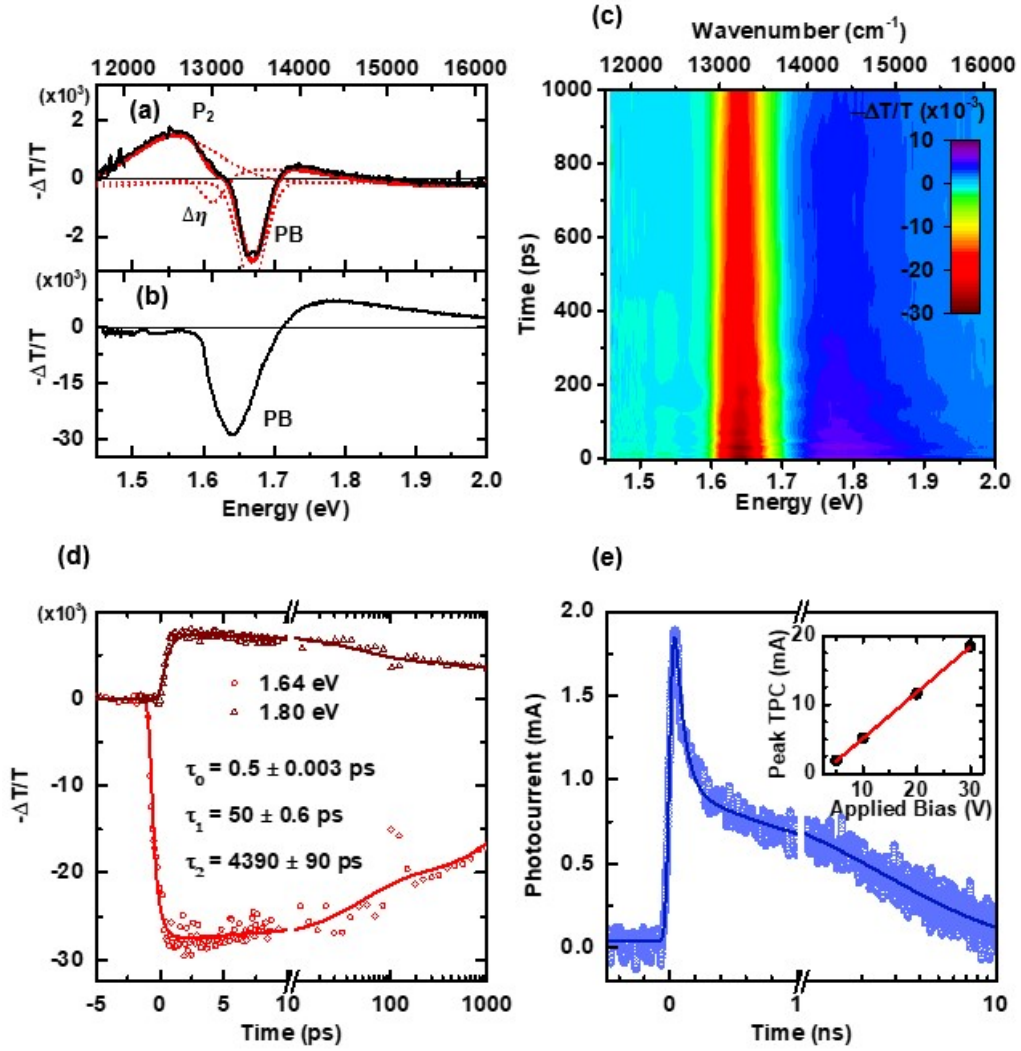


Figure 4.7 (a) Steady state PIA taken at 80 K compared against (b) transient PA taken at 298 K and $t=1.5$ ps. (c) ultrafast transient absorption map of MAPbI₃ (d) shows the slice at 1.64 eV, which is the band gap and subsequent global fitting shows three distinct lifetimes. Detailed discussion are in the text. (e) transient photocurrent and insert shows the linear dependence of peak photocurrent against the applied bias. Note the change in timescale from linear to logarithmic in (d) and (e) marked by breaks.

The correspondence between early-time TPA and cw-PIA spectra indicates that the long-lived polaronic species are generated at ultrafast time scale ($t < 100$ fs). From the global fitting of the spectral decays (see representative dynamics in Fig 4.7d) we determined three distinctive time constants of $\tau_0 = 0.500 \pm 0.003$ ps, $\tau_1 = 50.0 \pm 0.6$ ps, and $\tau_2 = 4390 \pm 90$ ps for sequential exponential decays. The ultrafast

relaxation process of 0.500 ps is attributed to lattice thermalization, and the longer time constants to polaron population decay. The recombination process is outside of our experimental temporal range, suggesting a long lived polaron population that is consistent with the observation up to the millisecond time domain. Note that transient features between 1.7 eV and 2.0 eV have also been previously observed in MAPbI₃ films,⁶⁵⁻⁶⁸ and assigned to band filling effects by Manser *et al.*,⁶⁷ while Zhai *et al.* ascribed them to the photogeneration of free carriers.⁶⁸ The long lived decay was also detected in an earlier study, but was not then attributed to specific features.⁶⁶

To further deduce the nature of the photogenerated species, a transient photocurrent is carried out. The picosecond transient photocurrent (TPC) generated from a femtosecond laser pulse in a photoconductive switch was measured with a 100 GHz real-time sampling channel oscilloscope and the results are shown in Fig 4.7e. Unlike photoinduced absorption measurements where all-optical transitions are observed, including the signatures of neutral (e.g. excitonic) photogenerated species, fast TPC waveforms measures only charge carrier generation and decay dynamics, which correlates directly with transport characteristics of photovoltaic devices. The fast rise time of the TPC signal, which is limited by the instrument response function, is consistent with the sub-picosecond polaron generation inferred from TPA measurements. The characteristic photocurrent decay times obtained through a biexponential fit with $\tau_1 = 101 \pm 1$ ps and $\tau_2 = 4220 \pm 20$ ps and this extracted lifetime compares well against the long-lived polaron lifetimes observed in transient absorption with, $\tau_1 = 50.0 \pm 0.6$ ps, and $\tau_2 = 4390 \pm 90$ ps. The initial dynamics of TPA, τ_1 is likely to include exciton decay, which accounts for its faster early time constant. The inset of Fig 4.7e shows the linear relation between peak transient photocurrent and applied voltage, which enables the extraction of charge carrier mobility in the linear regime. The early-time mobility was estimated from the peak transient photocurrent (eq 3.31),

$$I_{peak} = \eta \phi \mu (1 - R) \frac{E_p e V}{\hbar \omega d^2},$$

Assuming unitary charge generation, unitary quantum yield and with an excitation density is on the order of 10^{18} cm⁻³, the estimated the probability to escape fast recombination is 0.1.⁶⁹ The estimated reflectance is then taken from Fresnel equation,

$$R = \left| \frac{1 - \eta}{1 + \eta} \right|^2$$

By taking $\eta = 2.3$,⁷⁰ $(1 - R) = 0.84$. Experimental values for the excitation fluence is 0.64 mJ cm^{-2} and $d = 100 \text{ }\mu\text{m}$, the early time mobility is derived, $\mu \approx 10 \text{ cm}^2 \text{ V}^{-1} \text{ s}^{-1}$. In contrast, steady-state photocurrent was utilized to estimate trap-limited (long-time) charge carrier mobility using the classical Drude model. Steady-state photocurrent is given by (eq 3.27),

$$J_{PC}(t) = e\mu\tau F \int_0^d g(z) dz = \frac{I_0 e}{\hbar\omega} F\mu\tau.$$

As such, with experimental illumination intensity of $I_0 = 18.5 \text{ }\mu\text{Wcm}^{-2}$ at photon energy of 1.68 eV , the corresponding mobility-lifetime product is of the order of $\mu\tau = 2.0 \times 10^{-3} \text{ cm}^2 \text{ V}^{-1}$. Assuming a carrier lifetime of $\tau \approx 1 - 10 \text{ ms}$ (limited by the cw-PIA modulation frequency), the steady-state mobility is estimated, $\mu_{ss} = 0.2 - 2 \text{ cm}^2 \text{ V}^{-1} \text{ s}^{-1}$.

The difference in mobility from the two techniques are expected because steady-state mobility carrier mobility are dominated by thermally activated trapping and detrapping,⁷¹ whereas early-time (pre-trapping) carrier mobility are closer to band-like mobility which is estimated by first principle calculations.⁵⁰ When compared to the values found in literature, the findings here are comparable and consistent with other polycrystalline thin film samples which are between 0.5 and $80 \text{ cm}^2 \text{ V}^{-1} \text{ s}^{-1}$.^{65, 66, 72} Comparing the mobility values predicted by DFT against measurements done on single crystals would be more accurate because the contribution from other processes, such as trapping, are greatly reduced. The mobilities of single crystals reported in literature are seen to vary from 2.5 to $600 \text{ cm}^2 \text{ V}^{-1} \text{ s}^{-1}$,^{26, 72-76} based on the technique used, going from THz (ps time scale) through microwave reflectivity (μs time scale) to Space Charged Limited Current (ms time scale). This is comparable to the mobility values obtained through our DFT calculations at around $200 - 500 \text{ cm}^2 \text{ V}^{-1} \text{ s}^{-1}$.

4.4 Conclusion

In conclusion, this work has provided evidence that the lattice relaxation process

responsible for the photogeneration of small polarons in low dimensional perovskites is also present in the 3D metal halide perovskite MAPbI₃. However, in MAPbI₃, the electronic energy and the lattice elastic energy are constrained by the limit of the extent to which the lattice can deform. In this scenario, large polarons with radius extending over a few lattice sites are formed through the phonon dressed self-trapped states. Such large polarons are generated at the ultrafast time scale and are long lived, with a portion of the initial population surviving up to the milliseconds time domain, which is evident in the cw-PIA spectra, indicating vibrational mode frequency renormalization. Small charge symmetry breaking, yielding ambipolar transport even in the polaron regime are also expected, and observed experimentally. The charge carrier recombination is also affected by their polaronic nature because the phonon cloud surrounding the carrier in 3D ionic crystals increases charge screening thereby reduces Coulombic interactions. All these evidences, from theoretical to steady-state and femtosecond spectroscopy, validates the idea that large polarons are responsible for the anomalous transport characteristics of metal halide perovskites. Hence, polaronic effects would also be responsible for the experimental observations such as the lowering of carrier mobility through an apparent rescaling of the effective mass, apparent insusceptibility to carrier scattering, and suppression of Langevin, or bimolecular, recombination channels.

References

1. Jeon, N. J.; Noh, J. H.; Kim, Y. C.; Yang, W. S.; Ryu, S.; Seok, S. I., Solvent engineering for high-performance inorganic–organic hybrid perovskite solar cells. *Nat. Mater.* **2014**, *13*, 897-903.
2. Zhao, Y.; Zhu, K., Solution Chemistry Engineering toward High-Efficiency Perovskite Solar Cells. *J. Phys. Chem. Lett* **2014**, *5*, 4175-4186.
3. Brenner, T. M.; Egger, D. A.; Kronik, L.; Hodes, G.; Cahen, D., Hybrid organic—inorganic perovskites: low-cost semiconductors with intriguing charge-transport properties. *Nat. Rev. Mater.* **2016**, *1*, 15007.
4. Savenije, T. J.; Ponseca, C. S.; Kunneman, L.; Abdellah, M.; Zheng, K.; Tian, Y.; Zhu, Q.; Canton, S. E.; Scheblykin, I. G.; Pullerits, T.; Yartsev, A.; Sundström, V., Thermally Activated Exciton Dissociation and Recombination Control the Carrier

Dynamics in Organometal Halide Perovskite. *J. Phys. Chem. Lett.* **2014**, 5 (13), 2189-2194.

5. Green, M. A.; Ho-Baillie, A.; Snaith, H. J., The emergence of perovskite solar cells. *Nat. Photonics* **2014**, 8, 506-514.

6. Yin, W.-J.; Shi, T.; Yan, Y., Unusual defect physics in CH₃NH₃PbI₃ perovskite solar cell absorber. *Appl. Phys. Lett.* **2014**, 104, 063903.

7. Brandt, R. E.; Stevanović, V.; Ginley, D. S.; Buonassisi, T., Identifying defect-tolerant semiconductors with high minority-carrier lifetimes: beyond hybrid lead halide perovskites. *MRS Commun* **2015**, 5, 265-275.

8. Alarousu, E.; El-Zohry, A. M.; Yin, J.; Zhumekenov, A. A.; Yang, C.; Alhabshi, E.; Gereige, I.; AlSaggaf, A.; Malko, A. V.; Bakr, O. M.; Mohammed, O. F., Ultralong Radiative States in Hybrid Perovskite Crystals: Compositions for Submillimeter Diffusion Lengths. *J. Phys. Chem. Lett.* **2017**, 8, 4386-4390.

9. De Angelis, F.; Petrozza, A., Clues from defect photochemistry. *Nat. Mater.* **2018**, 17 (5), 383-384.

10. Miyata, K.; Meggiolaro, D.; Trinh, M. T.; Joshi, P. P.; Mosconi, E.; Jones, S. C.; De Angelis, F.; Zhu, X.-Y., Large polarons in lead halide perovskites. *Sci. Adv.* **2017**, 3.

11. Zhu, X. Y.; Podzorov, V., Charge Carriers in Hybrid Organic–Inorganic Lead Halide Perovskites Might Be Protected as Large Polarons. *J. Phys. Chem. Lett.* **2015**, 6, 4758-4761.

12. Cortecchia, D.; Yin, J.; Bruno, A.; Lo, S.-Z. A.; Gurzadyan, G. G.; Mhaisalkar, S.; Bredas, J.-L.; Soci, C., Polaron self-localization in white-light emitting hybrid perovskites. *J. Mater. Chem. C* **2017**, 5 (11), 2771-2780.

13. Cortecchia, D.; Neutzner, S.; Srimath Kandada, A. R.; Mosconi, E.; Meggiolaro, D.; De Angelis, F.; Soci, C.; Petrozza, A., Broadband Emission in Two-Dimensional Hybrid Perovskites: The Role of Structural Deformation. *J. Am. Chem. Soc.* **2017**, 139 (1), 39-42.

14. Yin, J.; Li, H.; Cortecchia, D.; Soci, C.; Brédas, J.-L., Excitonic and Polaronic Properties of 2D Hybrid Organic–Inorganic Perovskites. *ACS Energy Lett.* **2017**, 2, 417-423.

15. Smith, M. D.; Karunadasa, H. I., White-Light Emission from Layered Halide Perovskites. *Acc. Chem. Res.* **2018**, 51 (3), 619-627.

16. Cortecchia, D.; Yin, J.; Petrozza, A.; Soci, C., White light emission in low-dimensional perovskites. *Journal of Materials Chemistry C* **2019**, 7 (17), 4956-4969.
17. Lin, H.; Zhou, C.; Tian, Y.; Siegrist, T.; Ma, B., Low-Dimensional Organometal Halide Perovskites. *ACS Energy Lett.* **2018**, 3 (1), 54-62.
18. Neutzner, S.; Thouin, F.; Cortecchia, D.; Petrozza, A.; Silva, C.; Srimath Kandada, A. R., Exciton-polaron spectral structures in two-dimensional hybrid lead-halide perovskites. *Physical Review Materials* **2018**, 2 (6), 064605.
19. Emin, D., Optical properties of large and small polarons and bipolarons. *Phys. Rev. B* **1993**, 48, 13691-13702.
20. Emin, D., Large-polaron transport. In *Polarons*, Emin, D., Ed. Cambridge University Press: Cambridge, 2012; pp 86-94.
21. Fu, J.; Xu, Q.; Han, G.; Wu, B.; Huan, C. H. A.; Leek, M. L.; Sum, T. C., Hot carrier cooling mechanisms in halide perovskites. *Nat. Commun.* **2017**, 8 (1), 1300.
22. Slonopas, A.; Foley, B. J.; Choi, J. J.; Gupta, M. C., Charge transport in bulk CH₃NH₃PbI₃ perovskite. *J. Appl. Phys.* **2016**, 119, 074101.
23. Yang, X.; Wang, Y.; Li, H.; Sheng, C., Optical Properties of Heterojunction between Hybrid Halide Perovskite and Charge Transport Materials: Exciplex Emission and Large Polaron. *J. Phys. Chem. C* **2016**, 120, 23299-23303.
24. Ivanovska, T.; Dionigi, C.; Mosconi, E.; De Angelis, F.; Liscio, F.; Morandi, V.; Ruani, G., Long-Lived Photoinduced Polarons in Organohalide Perovskites. *J. Phys. Chem. Lett.* **2017**, 8, 3081-3086.
25. La-o-vorakiat, C.; Xia, H.; Kadro, J.; Salim, T.; Zhao, D.; Ahmed, T.; Lam, Y. M.; Zhu, J.-X.; Marcus, R. A.; Michel-Beyerle, M.-E.; Chia, E. E. M., Phonon Mode Transformation Across the Orthorhombic–Tetragonal Phase Transition in a Lead Iodide Perovskite CH₃NH₃PbI₃: A Terahertz Time-Domain Spectroscopy Approach. *J. Phys. Chem. Lett.* **2016**, 7, 1-6.
26. Valverde-Chavez, D. A.; Ponseca, C. S.; Stoumpos, C. C.; Yartsev, A.; Kanatzidis, M. G.; Sundstrom, V.; Cooke, D. G., Intrinsic femtosecond charge generation dynamics in single crystal CH₃NH₃PbI₃. *Energy Environ. Sci* **2015**, 8, 3700-3707.
27. Zheng, K.; Abdellah, M.; Zhu, Q.; Kong, Q.; Jennings, G.; Kurtz, C. A.; Messing, M. E.; Niu, Y.; Gosztola, D. J.; Al-Marri, M. J.; Zhang, X.; Pullerits, T.; Canton, S. E., Direct Experimental Evidence for Photoinduced Strong-Coupling

Polarons in Organolead Halide Perovskite Nanoparticles. *J. Phys. Chem. Lett.* **2016**, *7*, 4535-4539.

28. Zhu, H.; Miyata, K.; Fu, Y.; Wang, J.; Joshi, P. P.; Niesner, D.; Williams, K. W.; Jin, S.; Zhu, X.-Y., Screening in crystalline liquids protects energetic carriers in hybrid perovskites. *Science* **2016**, *353* (6306), 1409-1413.

29. Batignani, G.; Fumero, G.; Srimath Kandada, A. R.; Cerullo, G.; Gandini, M.; Ferrante, C.; Petrozza, A.; Scopigno, T., Probing femtosecond lattice displacement upon photo-carrier generation in lead halide perovskite. *Nat. Commun.* **2018**, *9* (1), 1971.

30. Park, M.; Neukirch, A. J.; Reyes-Lillo, S. E.; Lai, M.; Ellis, S. R.; Dietze, D.; Neaton, J. B.; Yang, P.; Tretiak, S.; Mathies, R. A., Excited-state vibrational dynamics toward the polaron in methylammonium lead iodide perovskite. *Nat. Commun.* **2018**, *9* (1), 2525.

31. Tsai, H.; Nie, W.; Blancon, J. C.; Stoumpos, C. C.; Soe, C. M. M.; Yoo, J.; Crochet, J.; Tretiak, S.; Even, J.; Sadhanala, A.; Azzellino, G.; Brenes, R.; Ajayan, P. M.; Bulović, V.; Stranks, S. D.; Friend, R. H.; Kanatzidis, M. G.; Mohite, A. D., Stable Light-Emitting Diodes Using Phase-Pure Ruddlesden–Popper Layered Perovskites. *Advanced Materials* **2018**, *30* (6), 1704217.

32. Baikie, T.; Fang, Y.; Kadro, J. M.; Schreyer, M.; Wei, F.; Mhaisalkar, S. G.; Graetzel, M.; White, T. J., Synthesis and crystal chemistry of the hybrid perovskite (CH₃NH₃)PbI₃ for solid-state sensitised solar cell applications. *Journal of Materials Chemistry A* **2013**, *1* (18), 5628-5641.

33. Kawamura, Y.; Mashiyama, H.; Hasebe, K., Structural Study on Cubic–Tetragonal Transition of CH₃NH₃PbI₃. *Journal of the Physical Society of Japan* **2002**, *71* (7), 1694-1697.

34. Fang, H.-H.; Raissa, R.; Abdu-Aguye, M.; Adjokatse, S.; Blake, G. R.; Even, J.; Loi, M. A., Photophysics of Organic–Inorganic Hybrid Lead Iodide Perovskite Single Crystals. *Advanced Functional Materials* **2015**, *25* (16), 2378-2385.

35. Poglitsch, A.; Weber, D., Dynamic disorder in methylammoniumtrihalogenoplumbates (II) observed by millimeter-wave spectroscopy. *The Journal of Chemical Physics* **1987**, *87* (11), 6373-6378.

36. Ong, K. P.; Goh, T. W.; Xu, Q.; Huan, A., Structural Evolution in Methylammonium Lead Iodide CH₃NH₃PbI₃. *The Journal of Physical Chemistry A* **2015**, *119* (44), 11033-11038.

37. Leguy, A. M. A.; Frost, J. M.; McMahon, A. P.; Sakai, V. G.; Kockelmann, W.; Law, C.; Li, X.; Foglia, F.; Walsh, A.; O'Regan, B. C.; Nelson, J.; Cabral, J. T.; Barnes, P. R. F., The dynamics of methylammonium ions in hybrid organic–inorganic perovskite solar cells. *Nature Communications* **2015**, *6* (1), 7124.
38. Baikie, T.; Barrow, N. S.; Fang, Y.; Keenan, P. J.; Slater, P. R.; Piltz, R. O.; Gutmann, M.; Mhaisalkar, S. G.; White, T. J., A combined single crystal neutron/X-ray diffraction and solid-state nuclear magnetic resonance study of the hybrid perovskites CH₃NH₃PbX₃ (X = I, Br and Cl). *Journal of Materials Chemistry A* **2015**, *3* (17), 9298-9307.
39. Weller, M. T.; Weber, O. J.; Henry, P. F.; Di Pumpo, A. M.; Hansen, T. C., Complete structure and cation orientation in the perovskite photovoltaic methylammonium lead iodide between 100 and 352 K. *Chemical Communications* **2015**, *51* (20), 4180-4183.
40. G, S.; Mahale, P.; Kore, B. P.; Mukherjee, S.; Pavan, M. S.; De, C.; Ghara, S.; Sundaresan, A.; Pandey, A.; Guru Row, T. N.; Sarma, D. D., Is CH₃NH₃PbI₃ Polar? *The Journal of Physical Chemistry Letters* **2016**, *7* (13), 2412-2419.
41. Dang, Y.; Liu, Y.; Sun, Y.; Yuan, D.; Liu, X.; Lu, W.; Liu, G.; Xia, H.; Tao, X., Bulk crystal growth of hybrid perovskite material CH₃NH₃PbI₃. *CrystEngComm* **2015**, *17* (3), 665-670.
42. Franssen, W. M. J.; van Es, S. G. D.; Dervişoğlu, R.; de Wijs, G. A.; Kentgens, A. P. M., Symmetry, Dynamics, and Defects in Methylammonium Lead Halide Perovskites. *The Journal of Physical Chemistry Letters* **2017**, *8* (1), 61-66.
43. Franz, A.; Többsen, D. M.; Schorr, S., Interaction between cation orientation, octahedra tilting and hydrogen bonding in methylammonium lead triiodide. *Crystal Research and Technology* **2016**, *51* (9), 534-540.
44. Roiland, C.; Trippe-Allard, G.; Jemli, K.; Alonso, B.; Ameline, J.-C.; Gautier, R.; Bataille, T.; Le Polles, L.; Deleporte, E.; Even, J.; Katan, C., Multinuclear NMR as a tool for studying local order and dynamics in CH₃NH₃PbX₃ (X = Cl, Br, I) hybrid perovskites. *Physical Chemistry Chemical Physics* **2016**, *18* (39), 27133-27142.
45. Bernard, G. M.; Wasylishen, R. E.; Ratcliffe, C. I.; Terskikh, V.; Wu, Q.; Buriak, J. M.; Hauger, T., Methylammonium Cation Dynamics in Methylammonium Lead Halide Perovskites: A Solid-State NMR Perspective. *The Journal of Physical Chemistry A* **2018**, *122* (6), 1560-1573.

46. Kresse, G.; Furthmüller, J., Efficiency of ab-initio total energy calculations for metals and semiconductors using a plane-wave basis set. *Comp Mater Sci* **1996**, *6* (1), 15-50.
47. Kresse, G.; Joubert, D., From ultrasoft pseudopotentials to the projector augmented-wave method. *Physical Review B* **1999**, *59* (3), 1758-1775.
48. Giannozzi, P.; Baroni, S.; Bonini, N.; Calandra, M.; Car, R.; Cavazzoni, C.; Ceresoli, D.; Chiarotti, G. L.; Cococcioni, M.; Dabo, I.; Dal Corso, A.; de Gironcoli, S.; Fabris, S.; Fratesi, G.; Gebauer, R.; Gerstmann, U.; Gougoussis, C.; Kokalj, A.; Lazzeri, M.; Martin-Samos, L.; Marzari, N.; Mauri, F.; Mazzarello, R.; Paolini, S.; Pasquarello, A.; Paulatto, L.; Sbraccia, C.; Scandolo, S.; Sclauzero, G.; Seitsonen, A. P.; Smogunov, A.; Umari, P.; Wentzcovitch, R. M., QUANTUM ESPRESSO: a modular and open-source software project for quantum simulations of materials. *Journal of Physics: Condensed Matter* **2009**, *21* (39), 395502.
49. He, Y.; Galli, G., Perovskites for Solar Thermoelectric Applications: A First Principle Study of CH₃NH₃AI₃ (A = Pb and Sn). *Chemistry of Materials* **2014**, *26* (18), 5394-5400.
50. Chin, X. Y.; Cortecchia, D.; Yin, J.; Bruno, A.; Soci, C., Lead iodide perovskite light-emitting field-effect transistor. *Nat. Commun.* **2015**, *6*, 7383.
51. Feynman, R. P., Slow Electrons in a Polar Crystal. *Physical Review* **1955**, *97* (3), 660-665.
52. Ôsaka, Y., Polaron Mobility at Finite Temperature (Weak Coupling Limit). *Journal of the Physical Society of Japan* **1966**, *21* (3), 423-433.
53. Frost, J. M., Calculating polaron mobility in halide perovskites. *Physical Review B* **2017**, *96* (19), 195202.
54. Wang, H.; Pei, Y.; LaLonde, A. D.; Snyder, G. J., Weak electron-phonon coupling contributing to high thermoelectric performance in n-type PbSe. *Proceedings of the National Academy of Sciences* **2012**, *109* (25), 9705.
55. Snellenburg, J. J.; Laptinok, S.; Seger, R.; Mullen, K. M.; van Stokkum, I. H. M., Glotaran: A Java-Based Graphical User Interface for the R Package TIMP. *J. Stat. Softw* **2012**, *49*, 22.
56. Jiang, X. M.; Österbacka, R.; Korovyanko, O.; An, C. P.; Horovitz, B.; Janssen, R. A. J.; Vardeny, Z. V., Spectroscopic Studies of Photoexcitations in Regioregular and Regiorandom Polythiophene Films. *Advanced Functional Materials* **2002**, *12* (9), 587-597.

57. Westerling, M.; Vijila, C.; Österbacka, R.; Stubb, H., Bimolecular recombination in regiorandom poly(3-hexylthiophene). *Chemical Physics* **2003**, *286* (2), 315-320.
58. Miranda, P. B.; Moses, D.; Heeger, A. J., Ultrafast photogeneration of charged polarons in conjugated polymers. *Physical Review B* **2001**, *64* (8), 081201.
59. Narra, S.; Chung, C.-C.; Diau, E. W.-G.; Shigeto, S., Simultaneous Observation of an Intraband Transition and Distinct Transient Species in the Infrared Region for Perovskite Solar Cells. *J. Phys. Chem. Lett.* **2016**, *7*, 2450-2455.
60. Lanzani, G., *The Photophysics behind Photovoltaics and Photonics*. John Wiley & Sons: 2012.
61. Price, M. B.; Butkus, J.; Jellicoe, T. C.; Sadhanala, A.; Briane, A.; Halpert, J. E.; Broch, K.; Hodgkiss, J. M.; Friend, R. H.; Deschler, F., Hot-carrier cooling and photoinduced refractive index changes in organic–inorganic lead halide perovskites. *Nature Communications* **2015**, *6* (1), 8420.
62. Stoumpos, C. C.; Malliakas, C. D.; Kanatzidis, M. G., Semiconducting Tin and Lead Iodide Perovskites with Organic Cations: Phase Transitions, High Mobilities, and Near-Infrared Photoluminescent Properties. *Inorg. Chem.* **2013**, *52* (15), 9019-9038.
63. Quarti, C.; Mosconi, E.; Ball, J. M.; D'Innocenzo, V.; Tao, C.; Pathak, S.; Snaith, H. J.; Petrozza, A.; De Angelis, F., Structural and optical properties of methylammonium lead iodide across the tetragonal to cubic phase transition: implications for perovskite solar cells. *Energy & Environmental Science* **2016**, *9* (1), 155-163.
64. Kong, W.; Ye, Z.; Qi, Z.; Zhang, B.; Wang, M.; Rahimi-Iman, A.; Wu, H., Characterization of an abnormal photoluminescence behavior upon crystal-phase transition of perovskite CH₃NH₃PbI₃. *Phys. Chem. Chem. Phys.* **2015**, *17*, 16405-16411.
65. Xing, G.; Mathews, N.; Sun, S.; Lim, S. S.; Lam, Y. M.; Grätzel, M.; Mhaisalkar, S.; Sum, T. C., Long-Range Balanced Electron- and Hole-Transport Lengths in Organic-Inorganic CH₃NH₃PbI₃. *Science* **2013**, *342*, 344-347.
66. Stranks, S. D.; Eperon, G. E.; Grancini, G.; Menelaou, C.; Alcocer, M. J. P.; Leijtens, T.; Herz, L. M.; Petrozza, A.; Snaith, H. J., Electron-Hole Diffusion Lengths Exceeding 1 Micrometer in an Organometal Trihalide Perovskite Absorber. *Science* **2013**, *342*, 341-344.

67. Manser, J. S.; Kamat, P. V., Band filling with free charge carriers in organometal halide perovskites. *Nat. Photonics* **2014**, *8*, 737-743.
68. Zhai, Y.; Sheng, C. X.; Zhang, C.; Vardeny, Z. V., Ultrafast Spectroscopy of Photoexcitations in Organometal Trihalide Perovskites. *Adv. Funct. Mater.* **2016**, *26*, 1617-1627.
69. D'Innocenzo, V.; Grancini, G.; Alcocer, M. J. P.; Kandada, A. R. S.; Stranks, S. D.; Lee, M. M.; Lanzani, G.; Snaith, H. J.; Petrozza, A., Excitons versus free charges in organo-lead tri-halide perovskites. *Nature Communications* **2014**, *5* (1), 3586.
70. Löper, P.; Stuckelberger, M.; Niesen, B.; Werner, J.; Filipič, M.; Moon, S.-J.; Yum, J.-H.; Topič, M.; De Wolf, S.; Ballif, C., Complex Refractive Index Spectra of CH₃NH₃PbI₃ Perovskite Thin Films Determined by Spectroscopic Ellipsometry and Spectrophotometry. *The Journal of Physical Chemistry Letters* **2015**, *6* (1), 66-71.
71. Moses, D.; Soci, C.; Chi, X.; Ramirez, A. P., Mechanism of Carrier Photogeneration and Carrier Transport in Molecular Crystal Tetracene. *Phys. Rev. Lett.* **2006**, *97* (6), 067401.
72. Herz, L. M., Charge-Carrier Mobilities in Metal Halide Perovskites: Fundamental Mechanisms and Limits. *ACS Energy Letters* **2017**, *2* (7), 1539-1548.
73. Wehrenfennig, C.; Eperon, G. E.; Johnston, M. B.; Snaith, H. J.; Herz, L. M., High Charge Carrier Mobilities and Lifetimes in Organolead Trihalide Perovskites. *Adv. Mater.* **2014**, *26* (10), 1584-1589.
74. Saidaminov, M. I.; Abdelhady, A. L.; Murali, B.; Alarousu, E.; Burlakov, V. M.; Peng, W.; Dursun, I.; Wang, L.; He, Y.; Maculan, G.; Goriely, A.; Wu, T.; Mohammed, O. F.; Bakr, O. M., High-quality bulk hybrid perovskite single crystals within minutes by inverse temperature crystallization. *Nature Communications* **2015**, *6*, 7586.
75. Dong, Q.; Fang, Y.; Shao, Y.; Mulligan, P.; Qiu, J.; Cao, L.; Huang, J., Electron-hole diffusion lengths > 175 μm in solution-grown CH₃NH₃PbI₃ single crystals. *Science* **2015**, *347* (6225), 967-970.
76. Shi, D.; Adinolfi, V.; Comin, R.; Yuan, M.; Alarousu, E.; Buin, A.; Chen, Y.; Hoogland, S.; Rothenberger, A.; Katsiev, K.; Losovyj, Y.; Zhang, X.; Dowben, P. A.; Mohammed, O. F.; Sargent, E. H.; Bakr, O. M., Low trap-state density and long carrier diffusion in organolead trihalide perovskite single crystals. *Science* **2015**, *347* (6221), 519.

Chapter 5

Localized effects in polymorphic <110> oriented 2-D layered perovskites *

This chapter moves away from the traditional 3D perovskite to layered 2D perovskites, where this class of layered 2D perovskites are finding opportunities in lighting application. The design principle to obtain the corrugated <110> oriented layered 2D perovskite is examined closely, where a slight mismatch would turn the inorganic framework into a 1D 'perovskitoid'. The structural and bulk optical properties along with the cation dynamics of the 2D layered perovskite and 'perovskitoid' are studied extensively which are tallied against theoretical DFT predictions. The results hints at the significance of the localized cation dynamics in bulk optical properties of materials.

*Results from this chapter are currently being prepared for publication

5.1 Introduction

The structural properties of hybrid perovskites are remarkably flexible, and are semi-empirically determined by the Goldschmidt tolerance factor¹. Therefore, other than the widely popular prototypical MAPbI₃ system, which is being actively explored for application in photovoltaics²⁻⁴, there are other much studied systems such as MAPbBr₃^{5, 6} and MAPbCl₃^{7, 8} which show rather different optical properties despite being structurally similar. Early work showed that mixtures of these systems follow Vegard's law of solid solution^{9, 10}. Hence, this opened the possibility of band gap tuning which was shown to be an effective strategy¹¹. Similarly, upon substituting the A-site cation with another similar organic cation, such as formamidinium (FA) and guanidinium (GA), the system would also follow Vegard's law. This possibility of tuning eventually resulted in the magical development of the mixed cation and halide Cs_{0.05}(FA_{0.83}MA_{0.17})_{0.95}Pb(I_{0.82}Br_{0.18})₃ as the frontrunner for photovoltaics application with an impressive 25.2% efficiency¹².

At around the same time, this possibility of band gap tuning also opened up another potential application: lighting. The concept of using hybrid perovskites for lighting applications is very similar to their use in a solar cell; the former recombines an electron and hole radiatively to emit a photon while the latter absorbs a photon and separates the resulting exciton into electron-hole pairs which are then harvested or stored. The possibility was first demonstrated by Xing et al. arising from the potential lasing application in perovskites¹³, the proof of concept was then demonstrated through light emitting diodes (LEDs)¹⁴ and light emitting field effect transistors (LEFET)¹⁵. However, there are major differences in the device architecture of a solar cell and a LED. Most significantly, a lighting application typically requires the band gap of the active material to be within the visible regime while photovoltaics requires the material of the active material to be ideally between 1.0 and 1.7 eV, according to the Shockley – Queisser limit, which is in the red or near-infrared¹⁶. Hence, MAPbI₃ with a band gap of 1.67 eV (750 nm, red colour) would be ideal for photovoltaic applications, and for making a red LED, while the bromide series, e.g. MAPbBr₃ with a band gap of 2.18 eV (568 nm, green colour) or FAPbBr₃ with a band gap of 2.13 eV (582 nm, green colour) would be better suited for lighting application. Intrinsically blue light emitters remain elusive in the field of hybrid perovskites. With the three basic component of colours being

sufficiently addressed, the three parts can be combined to generate a white light emitter. The importance of the blue emitter for obtaining full colour emission cannot be understated, as shown by the award of the Nobel prize in physics for 2014, to Professors Isamu Akasaki, Hiroshi Amano and Shuji Nakamura for their invention of the blue LED.¹⁷

At the same time, within the field of hybrid perovskites, there are several systems which shows promising preliminary results as an active layer which intrinsically emits white light which can potentially bypass the need for a blue emitter. Among the early systems which are reported to be white light emitters, are APIPbBr₄¹⁸ (API = 1-(3-Aminopropyl)imidazole), (EDBE)PbBr₄¹⁹ (EDBE = 2,2'-(ethylenedioxy)bis(ethylammonium)) and others¹⁹⁻²¹, and there is a general trend that these intrinsic white light emitting systems are either highly distorted perovskites²²⁻²⁴, or are in the reduced dimensional corrugated <110> cut of perovskites^{25, 26}.

As highlighted in chapter 2, the terminology of ‘reduced dimensionality’ has to be used carefully because it can refer to two different scenarios. Briefly, in one instance, the reduction of 3D to 2D perovskites can be understood as layering using a different cation, e.g. n-butylammonium (BA) cation instead of methylammonium cation. The other instance would involve the nanostructuring of the ‘traditional’ 3D methylammonium metal halide perovskite with ligands into nanocubes, nanowires,²⁷ nanorods or core-shell structure for their various application²⁸⁻³⁵. This chapter will focus only on the former, which involves altering the A-site cations from a quasi-spherical MA or FA cation to other cations to obtain a reduced dimensional structure.

While there has been developed some understanding of the underlying mechanism of white light emission, evidence only point towards a structural correlation of octahedral tilting and octahedra distortion towards the broadness of the photoluminescence emission²²⁻²⁴. There is still a lack of understanding of the contribution of the short range interaction and (dis)order, particularly from the organic cations, to the long range order of the crystal structure. The short-range dynamics can be readily probed through solid state nuclear magnetic resonance (SSNMR), while the long-range order can be probed through X-ray diffraction studies. The complementary results from both SSNMR and XRD would then allow a more holistic approach towards understanding the observed

bulk optoelectronic properties, such as the observed optical band gap and photoluminescence spectra.

This chapter revisits the pioneer <110> cut material, APIPbBr₄, and aimed to establish an understanding of the structure-property relationships, particularly the correlation of short- and long-range order, with the observed bulk photoluminescence. However, during this work, it was discovered that the bulk APIPbBr₄ exists in a polymorph in the form of a truncated 1-dimensional inorganic chain, also called a “1D perovskitoid” with a different structural formula of API₂Pb₃Br₁₀, instead of the reported <110> cut. Further analysis showed API₂Pb₃Br₁₀ undergoes a phase transition at lower temperatures but that it does not revert to the reported <110> oriented perovskite. Instead the cation displaces slightly and distorts the symmetry from monoclinic to triclinic. Upon inspection of the structure, it was hypothesized that the aliphatic propylammonium tail is too long, and thus an aliphatic ethylammonium tail would be more suitable. Therefore, the organic 2-(1H-Imidazol-1-yl)ethanammonium (IEA) cation was synthesized and crystallized using the same procedure as was used to prepare API₂Pb₃Br₁₀. In this case the <110> cut of perovskite was obtained. The short-range dynamics and long-range order were studied extensively on both systems through SSNMR and XRD, respectively, and unsurprisingly the cation dynamics were found to be considerably different. The phase transition in API₂Pb₃Br₁₀ was also thoroughly characterized and it was found to be due to a reorganization of the aliphatic section of API cation, which breaks the symmetry of the crystal. IEAPbBr₄ on the other hand does not show any phase transition.

DFT calculations were then performed on these systems to study the band structure where the calculated results agree with the experimentally observed optical band gap, and thus validates the approximations. Furthermore, the ¹H and ¹³C chemical shifts in NMR was also predicted through DFT calculations and it shows close agreement with experimental values.

5.2 Experimental

5.2.1 X-ray diffraction

The crystals were dispersed in Fomblin ® and were hand-picked under a polarizing microscope and mounted onto MiTeGen microloops of the appropriate size for room temperature X-ray diffraction investigations or mounted onto a glass fiber approximately 100 µm in diameter to reduce the likelihood of crystal frosting for measurements at low temperatures ($T < 200$ K). The X-ray initialization and early processing was done together using software package CrysAlisPro on the Rigaku Gemini diffractometer using $\text{Mo K}\alpha = 0.71 \text{ \AA}$. The collection strategy and integration were carried out in CrysAlis. The structure solution and refinement were done with SHELXT³⁶ and Olex2³⁷. The solutions are checked with PLATON³⁸, and verified with IUCr CheckCIF. Powder XRD was carried out in Diamond light source beamline I11 with radiation of 0.825 \AA (15 keV). Samples were packed into 0.1mm capillaries and referenced against SiO_2 for Rietveld refinements. Sequential refinements were carried out on variable temperature XRD to obtain the relative percentage and lattice parameters of individual phases.

5.2.2 Nuclear Magnetic Resonance

NMR experiments were performed using a suite of different magnets. Variable temperature ^1H T_1 , ^{13}C CPMAS, hCH HETCOR and ^{207}Pb measurements were mainly done on Bruker 600 MHz Advance III 1.9mm probe; ^1H T_1 measurements was also carried out on Bruker 300 MHz Advance III HD 1.3mm probe. ^1H NOESY, ^1H BABA, ^1H One Pulse were carried out on Bruker 700 MHz Advance III 1.3mm probe. $T_{1\rho}$ was carried out on Bruker 400 MHz Advance II 4mm probe. Density Functional Theory (DFT) calculations were performed using with a plane wave basis set using CASTEP 17 to predict individual ^1H and ^{13}C chemical shifts. Ultrasoft pseudopotentials and Perdew, Burke, Ernzerhof (PBE) exchange functionals have been used; kinetic energy cutoff for wave functions of 900 eV and k-point spacing equivalent to $2 \times 3 \times 3$ for all systems.

5.2.3 Calorimetric characterization

Differential Scanning Calorimetry (DSC) was performed on TA Instruments DSC Q10 with powdered samples crimped in an aluminium pan. Thermogravimetric analysis

(TGA) was done on TA Instruments Q500 with powdered samples placed in an alumina crucible. The crucible is then placed on a platinum pan.

5.2.4 Steady-state absorption and photoluminescence

Variable temperature absorption was measured on a PerkinElmer Lambda 1050 with the Linkam stage purged with N₂ as the temperature controller stage. Powdered samples were placed in a BaSO₄ filled crucible and the absorption spectra are referenced against pure BaSO₄. Variable temperature photoluminescence was carried out on a Horiba Fluorolog Spectrophotometer. Samples were mounted onto sticky carbon tape in an Oxford system cryostat evacuated to 4×10^{-4} mbar. Excitation wavelengths was set at 290 nm, while the second order effects are filtered off with a Schott WG-320nm long pass filter.

5.2.5 Theoretical analysis using Density Functional Theory

To determine the electronic structure of the imidazole-based hybrid materials, Density Functional Theory calculations were performed on the experimentally determined structures using the CASTEP plane-wave pseudopotential code. The PBE parameterisation of the Generalised Gradient Approximation (GGA) and the rSCAN meta-GGA exchange-correlation functionals were implemented in this study. In these calculations, a 800 eV plane-wave cutoff was used and the Brillouin zone was sampled using Monkhorst-Pack k-point grids at a spacing of 0.03 Å⁻¹ or less. On-the-fly generated ultrasoft pseudopotentials were employed throughout, which included scalar-relativistic effects approximated by the Koelling-Harmon scheme. Band structure calculations including spin-orbit coupling were also performed employing the PBE functional and norm-conserving pseudopotentials. All dispersion interactions were approximated using the many-body dispersion scheme. Starting from the single crystal X-ray determined structures, the atomic coordinates and the lattice parameters using the PBE and rSCAN functionals were relaxed to tolerances of 0.05 eV/Å for forces and 0.05 GPa for stresses. In the cases where the X-ray results indicated partial occupancies of the atomic sites associated with the imidazolium cations, initial structures with randomly oriented imidazolium cations were generated which were subsequently relaxed. The band structure calculations were performed on the relaxed structures, and

the resulting total, partial and joint density of states were computed using the OptaDOS program. The calculation of the NMR parameters was undertaken using the gauge-including projector augmented wave (GIPAW) approach on the rSCAN relaxed structures.

5.3 Results and Discussion

5.3.1 X-ray Structural Characterization

The results of the single crystal XRD and the key parameters for both $\text{API}_2\text{Pb}_3\text{Br}_{10}$ and IEAPbBr_4 systems are shown in Table 5.1 where the projections of the two phases of $\text{API}_2\text{Pb}_3\text{Br}_{10}$ are shown. In Fig 5.1 (a), the high temperature $I2$ phase and in Fig 5.1 (b), the low temperature $P\bar{1}$ phase. The octahedral connectivity is considerably different from that previously reported for APIPbBr_4 , which was exclusively corner shared, whereas $\text{API}_2\text{Pb}_3\text{Br}_{10}$ exhibits an edge-face-face-edge sharing sequence to form a distorted one-dimensional chain of lead bromide octahedra. Consequently, $\text{API}_2\text{Pb}_3\text{Br}_{10}$ should be classified as a ‘perovskitoid’ – a detailed discussion on the naming nomenclature will follow in the next chapter.

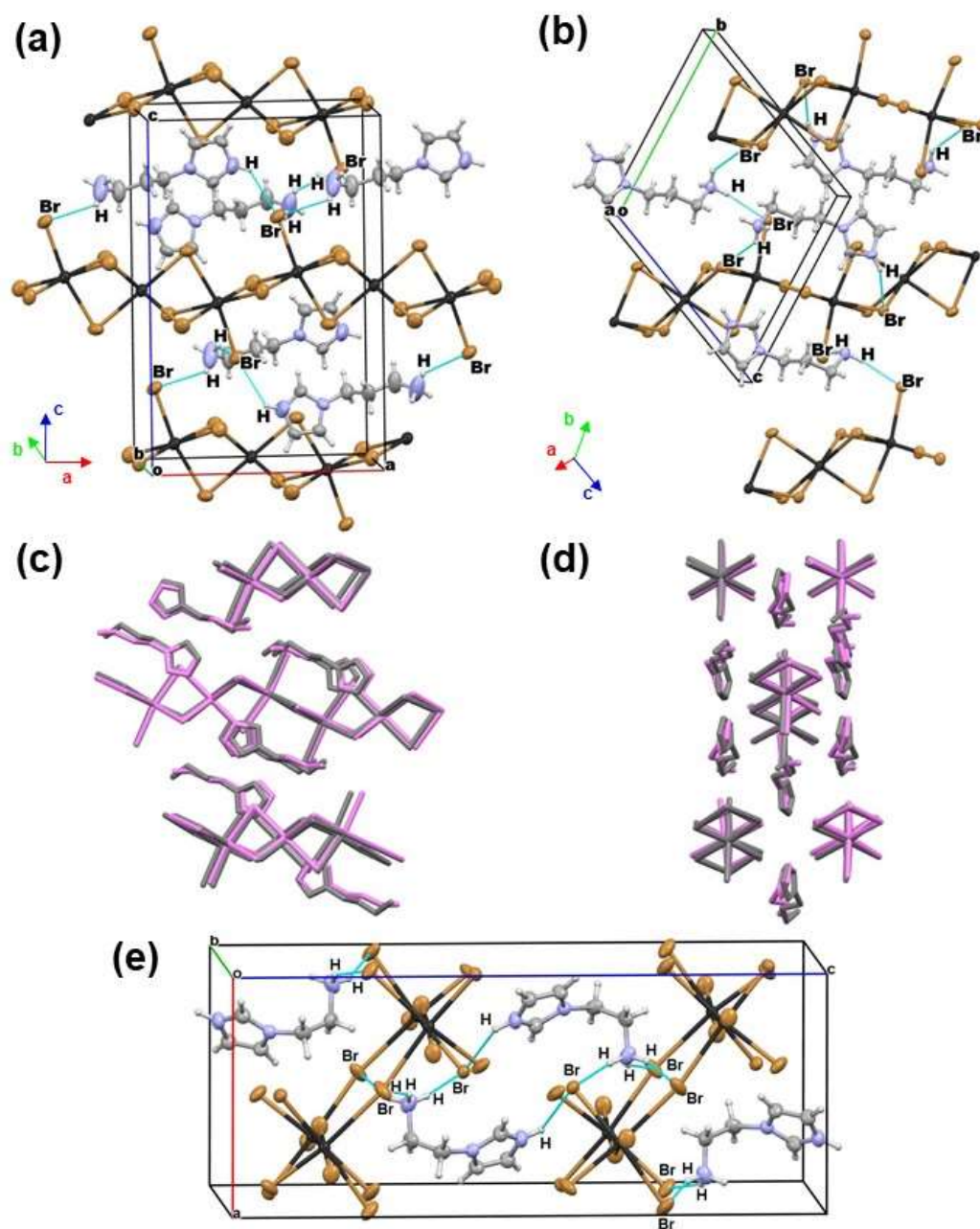


Figure 5.1 (a) $\text{API}_2\text{Pb}_3\text{Br}_{10}$ in the high temperature $I2$ phase, (b) $\text{API}_2\text{Pb}_3\text{Br}_{10}$ in the low temperature $P\bar{1}$ phase (standard unit cell), (c) an overlay of the high (in pink) and low temperature (in grey) viewed down the b -axis and (d) down the a -axis of the monoclinic cell. (e) API cation in the low temperature $P\bar{1}$ phase and (f) high temperature $I2$ phase. (g) projection of IEAPbBr_4 which is in a <110> oriented 2D layered perovskite structure.

Table 5.1 Selected parameters to the solution and refinement of scXRD results

Sample name	API ₂ Pb ₃ Br ₁₀	API ₂ Pb ₃ Br ₁₀	IEAPbBr ₄
Empirical formula	C ₆ H ₁₃ N ₃ Br ₅ Pb _{1.5}	C ₆ H ₁₃ N ₃ Br ₅ Pb _{1.5}	C ₅ H ₁₁ N ₃ Br ₄ Pb
Formula wt	835.53	837.53	640
Temp (K)	298(2)	240(2)	298(2)
Crystal system	monoclinic	triclinic	orthorhombic
Space group	<i>I</i> 2	<i>P</i> $\bar{1}$	<i>Pbca</i>
unit cell dimensions			
a (Å)	11.7516(4)	8.0475(4)	9.5868(5)
b (Å)	8.0414(3)	11.1003(6)	11.8741(7)
c (Å)	17.7814(6)	11.2081(6)	23.709(1)
α (°)	90	108.009(5)	90
β (°)	90.108(3)	106.605(4)	90
γ (°)	90	107.141(5)	90
Volume (Å ³)	1680.33(10)	827.93(8)	2699.0(3)
Z	4	2	8
ρ_{calc} (g cm ³)	3.311	3.36	3.150
μ (mm ⁻¹)	26.896	27.294	24.313
F(000)	1472	736	2272
Crystal size (mm ³)	0.191 × 0.138 × 0.091	0.271 × 0.231 × 0.082	0.177 × 0.116 × 0.073
2 Θ range (°)	6.14 to 54.242	6.624 to 55.068	6.454 to 66.658
	-15 ≤ h ≤ 15	-10 ≤ h ≤ 10	-14 ≤ h ≤ 12
Index ranges	-10 ≤ k ≤ 10	-14 ≤ k ≤ 14	-18 ≤ k ≤ 7
	-22 ≤ l ≤ 21	-14 ≤ l ≤ 14	-36 ≤ l ≤ 16
Refln collected	11919	7452	9501
Refinement method		<i>full-matrix least squares on F²</i>	
	3721	7452	4790
Indep reflns	(R _{int} = 0.0272, R _{sigma} = 0.0256)	(R _{sigma} = 0.0188)	(R _{int} = 0.0449, R _{sigma} = 0.0588)
Data/restraints/param	3721/1/143	7452/0/144	4790/0/119
GoF on F ²	1.046	1.077	1.008
Final R indexes [I ≥ 2 σ (I)]	R ₁ = 0.0218, wR ₂ = 0.0529	R ₁ = 0.0457, wR ₂ = 0.1211	R ₁ = 0.0417, wR ₂ = 0.0759
Final R indexes [all data]	R ₁ = 0.0236, wR ₂ = 0.0539	R ₁ = 0.0502, wR ₂ = 0.1224	R ₁ = 0.0772, wR ₂ = 0.0888
Fourier difference max and min (e Å ⁻³)	0.72 and -0.82	3.31 and -3.04	2.33 and -2.11
Flack parameter	0.020(5)	-	-

The phase transition exhibited by $\text{API}_2\text{Pb}_3\text{Br}_{10}$ is not transformative and does not revert the $\text{API}_2\text{Pb}_3\text{Br}_{10}$ structure into <110> oriented APIPbBr_4 . The overlay of the two different phases is seen in Fig 5.1 (c) and Fig 5.1 (d), where the pink wires represent the high temperature $I2$ phase and the grey wires represent the low temperature $P\bar{1}$ phase. Upon close inspection of the overlay map, a subtle difference can be seen in the orientation of the organic API cation while the inorganic lead-bromide framework remains almost unchanged. As seen in Fig 5.1 (d), the imidazole heads of API are displaced at an angle with respect to each other, as can be clearly seen in Fig 5.1 c, the aliphatic tail undergoes a displacive rearrangement. The high temperature API cation has a larger thermal ellipsoid and the organic tail, particularly from $^1\text{H}/^{13}\text{C} - 6$ and $^1\text{H}/^{13}\text{C} - 8$, that the arrangement is noticeably distorted.

The phase transition from high temperature $I2$ would always result in approximately 50% twinning, rotated 180° about the c -axis (17\AA) in the low temperature $P\bar{1}$ phase, which likely originate from the very small deviation of the beta angle in $I2$ phase. Even in the standard $C2$ space group, the beta angle deviates only slightly from the ideal 120° by 3.5° . In the low temperature $P\bar{1}$ phase, $\text{API}_2\text{Pb}_3\text{Br}_{10}$ is prepared in both the standard unit cell, with a cell volume of 827 \AA^3 and the non-standard unit cell with a volume of 1657 \AA^3 . The non-standard unit cell would allow a better and direct comparison on the phase transition, while the standard unit cell would be the basis of theoretical DFT analysis. Although the two systems are crystallographically identical, the difficulties during post processing and detwinning of the results has affected the accuracy of the atomic thermal displacement parameters in the non-standard unit cell. Further detailed discussion of the phase transition will follow in the subsequent section.

An in-depth inspection shows that the critical difference between the $\text{API}_2\text{Pb}_3\text{Br}_{10}$ and APIPbBr_4 structures lies in the charge distribution of the organic cation, and hence, the lead halide octahedra connectivity. In $\text{API}_2\text{Pb}_3\text{Br}_{10}$, the charge from the organic dication is distributed linearly along the 1-dimensional chain of lead halide octahedra while in APIPbBr_4 the organic dication charges are distributed between two layers. Hence, another cation, IEA, with a shorter aliphatic chain was synthesized and a material was crystallized using a method similar to that used to make $\text{API}_2\text{Pb}_3\text{Br}_{10}$. In IEAPbBr_4 , it is evident that the 2×2 corrugated <110> oriented perovskite was obtained and is

structurally very similar to the APIPbBr₄ and is consistent with earlier reports³⁹. Notably, the lead halide octahedra in IEAPbBr₄ are highly distorted indicating that IEA is likely to be at the limits for the formation of a corrugated <110> oriented 2D layered perovskite. This is in contrast with (EDBE)PbBr₄ where the presence of oxygen atoms in the EDBE provided torsional flexibility in the formation of the structure^{19, 20}. While there has been a consistent linkage between the amount of octahedral distortion and the degree of possible broadness in the photoluminescence emission, IEAPbBr₄ shows that there is likely to be a limit to the degree of broadness in the emission. The results of cross comparison with other corrugated <110> oriented hybrid perovskites are summarized in Table 5.2. The key parameters to measure octahedra distortion are $\langle\lambda\rangle$, which the quadratic elongation parameter⁴⁰, Δd which is the measure of octahedra distortion⁴¹ and σ^2 which measures the bond angle variance from the idea polyhedron⁴⁰. Calorimetric analysis was also carried out on IEAPbBr₄ and it does not exhibit any phase transition up to the point of thermal disintegration showing the robustness of the inorganic framework.

Table 5.2 Distortion parameter in corrugated <110> oriented 2D layered perovskites

Sample Name	Structure Type	$\langle\lambda\rangle$	Δd ($\times 10^{-4}$)	σ^2	Emission Centre /nm	Emission FWHM /nm (± 30 nm)
IEAPbBr ₄ ^{this work}	2 \times 2 (110)	1.0170	23.1	51.3	405	40
APIPbBr ₄ ¹⁸	2 \times 2 (110)	1.0088	13.7	20.8	500	300
3APr PbBr ₄ ⁴²	2 \times 2 (110)	1.0075	9.86	21.1	600	100
(EDBE)PbBr ₄ ¹⁹	2 \times 2 (110)	1.0090	13.7	23.9	575	150
N-MEDA PbBr ₄ ²¹	2 \times 2 (110)	1.0080	10.8	24.5	570	100
a-DMENPbBr ₄ ²⁵	3 \times 3 (110)	1.0107	30.8	Pb1 25.8	520	150
		1.0030	3.92	Pb2 8.87		
(4PNEA)PbI ₄ ²⁶	3 \times 3 (110)	1.0046	1.28	Pb3 15.1	500	100
		1.0067	31.1	Pb1 11.8		
		1.0021	1.01	Pb2 6.80		

Variable temperature powder XRD was carried out using synchrotron radiation on API₂Pb₃Br₁₀ while IEAPbBr₄ was examined only at room temperature. Due to the

difference in experiment setup, the $\text{API}_2\text{Pb}_3\text{Br}_{10}$ was measured in slow mode, while IEAPbBr_4 was measured in quick scan mode, hence, the counts are notably different, and the R_{exp} in $\text{API}_2\text{Pb}_3\text{Br}_{10}$ is significantly lower at approximately 0.6 compared to 13.8 for IEAPbBr_4 . Rietveld refinement was carried out on the samples and the refinement stability of the variable temperature $\text{API}_2\text{Pb}_3\text{Br}_{10}$ XRD can be seen in Fig 5.2 (c). The dips in R_{wp} at around 0 °C and 20 °C are attributed to the phase transition where both $I2$ and $P\bar{1}$ phases are observed to both be present in considerable amounts. The gradual change of $I2$ phase cell volume with respect to the temperature shows the reversibility of this phase transition.

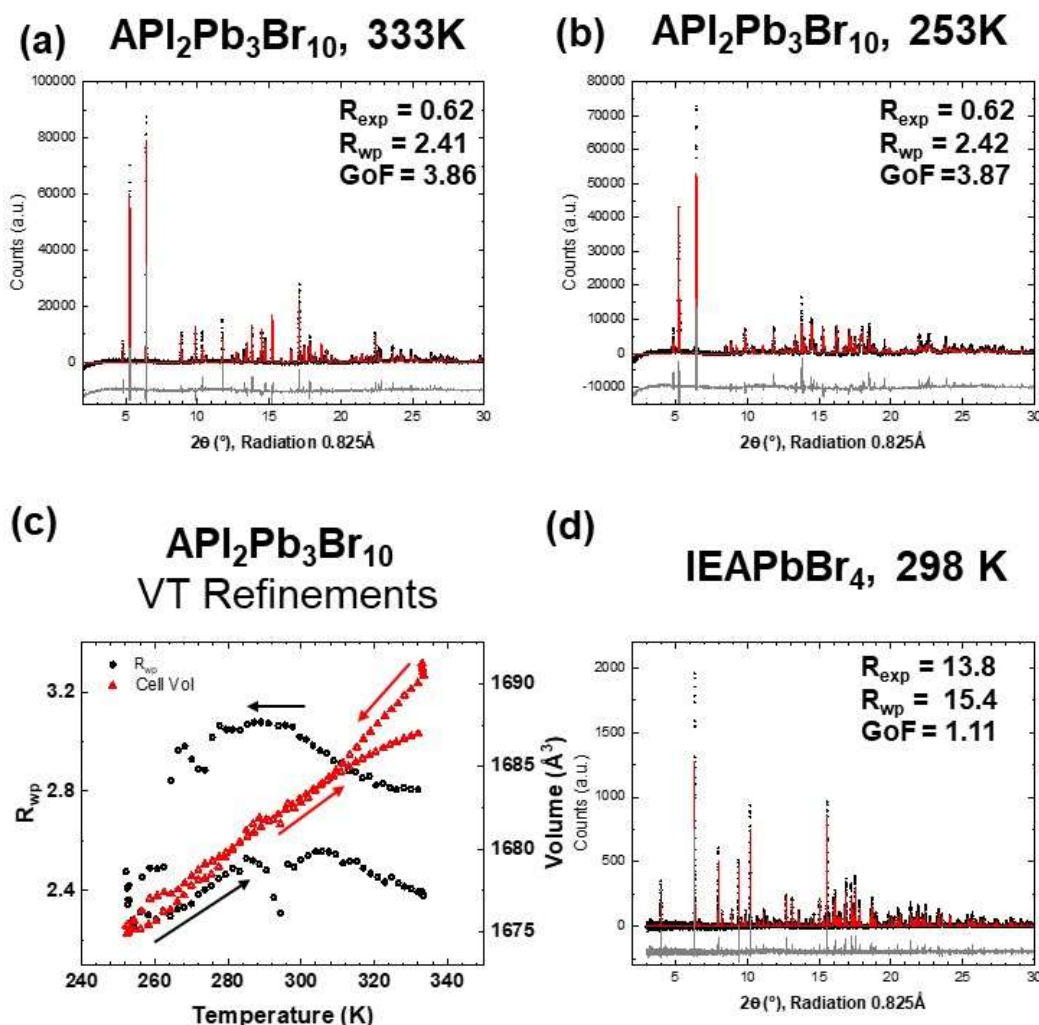


Figure 5.2 Powder XRD Rietveld refinement of (a) $\text{API}_2\text{Pb}_3\text{Br}_{10}$ in the room temperature $I2$ phase, and (b) $\text{API}_2\text{Pb}_3\text{Br}_{10}$ in the low temperature $P\bar{1}$ phase. (c) The plot of R_{wp} and unit cell volume of the $I2$ phase. A dip in R_{wp} can be observed at 273 K and 290 K. This is attributed to

the phase transition where both $I2$ and $P\bar{1}$ phases are observed to be in considerable amounts of each other. (d) Rietveld refinement of IEAPbBr₄ with an X-ray radiation of 0.825°Å.

The phase transition from $I2$ to $P\bar{1}$ is not allowed in the group-subgroup relationship tree and it is immediately obvious that $I2$ would have only a 2₁ screw-axis as the symmetry operator and would be non-centrosymmetric whereas $P\bar{1}$ would only have only inversion centre as the symmetry operator and would be centrosymmetric. This displacive phase transition giving an apparent mismatch is likely to originate from the behaviour of the organic cation and thus, group-subgroup relation of phase transition is unlikely to be applicable to such hybrid perovskite systems with non-spherical organic cations.

5.3.2 NMR Characterization

The long-range structure characterization is unquestionably best characterized through XRD, while NMR is best utilized to study the local structural properties of the systems. The complementary techniques of both XRD and NMR thus give a thorough understanding of both the atomic positions, and the atomic dynamics, particularly for the organic cations. ¹H, ¹³C and ²⁰⁷Pb NMR spectroscopy was carried out and the results are shown in Figures 5.3 and 5.4.

Fig 5.3 shows the one pulse ¹H spectra, along with the atomic assignment and deconvolution (blue curves), which are used to produce the simulated curve (red curve) which is compared against the experimentally obtained (black curve). As the experiment is conducted at an interval of five times T_1 , each peak will be quantitative. In ¹³C spectra, each peak is sufficiently resolved to not require any experimental deconvolution, and furthermore, the individual peak area is not quantitative under CPMAS conditions. A comparison in the ¹H spectra of the high and low temperature phase of API₂Pb₃Br₁₀ would reveal that the low temperature peaks are typically broader and this is expected because an increase in temperature would result in an increased tumbling and vibration of the organic cation, and hence the ¹H atoms. Therefore, this would average out the dipolar interactions, much like effects of magic angle spinning, to give a more resolved linewidth in the high temperature phase. This is further

supported by $T_{1\rho}$ measurements as seen in Table 5.3, where the $T_{1\rho}$ of the high and low temperature phases are almost identical; around 9 ms in both high temperature $I2$ and low temperature $P\bar{1}$ phase. In the ^{13}C spectra, it can be seen clearly that a new peak appears in the low temperature $P\bar{1}$ phase, but this would be more appropriately interpreted as a peak splitting because of the phase transition. This is supported by the spectra shown in Fig 5.4 (c), which charts the respective nuclei across the phase transition regime.

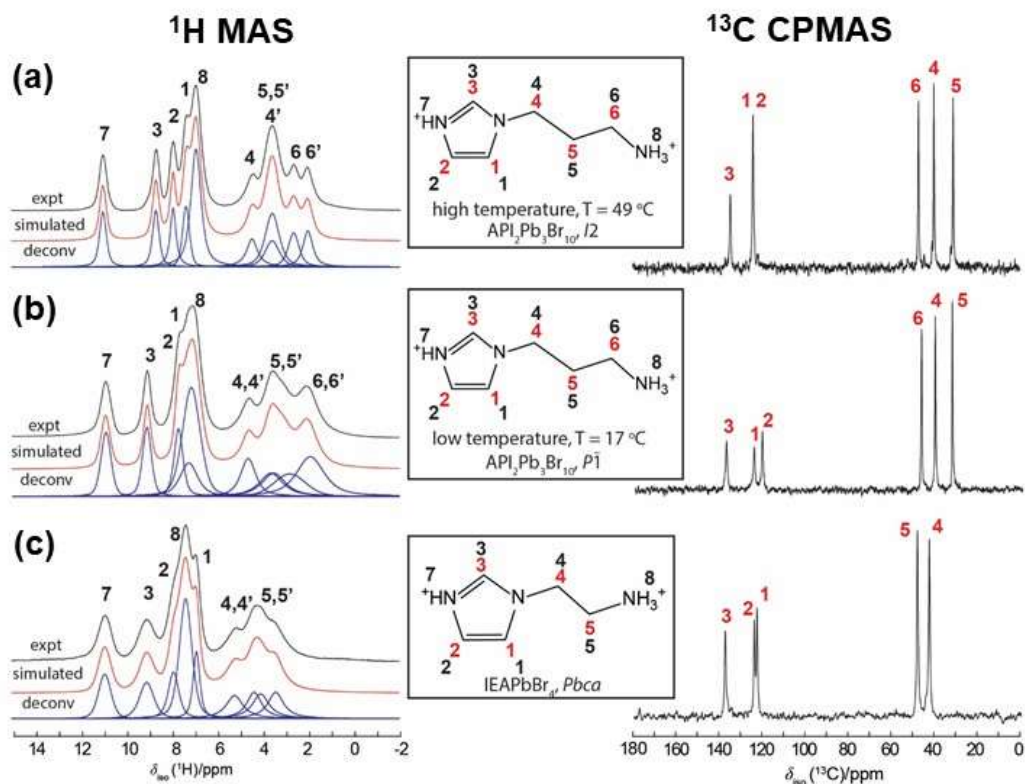


Figure 5.3 ^1H (left) and ^{13}C (right) SSNMR spectra of (a) $\text{API}_2\text{Pb}_3\text{Br}_{10}$ in the high temperature $I2$ phase, (b) $\text{API}_2\text{Pb}_3\text{Br}_{10}$ in the low temperature $P\bar{1}$ phase (c) IEAPbBr_4 assigned to the individual atoms.

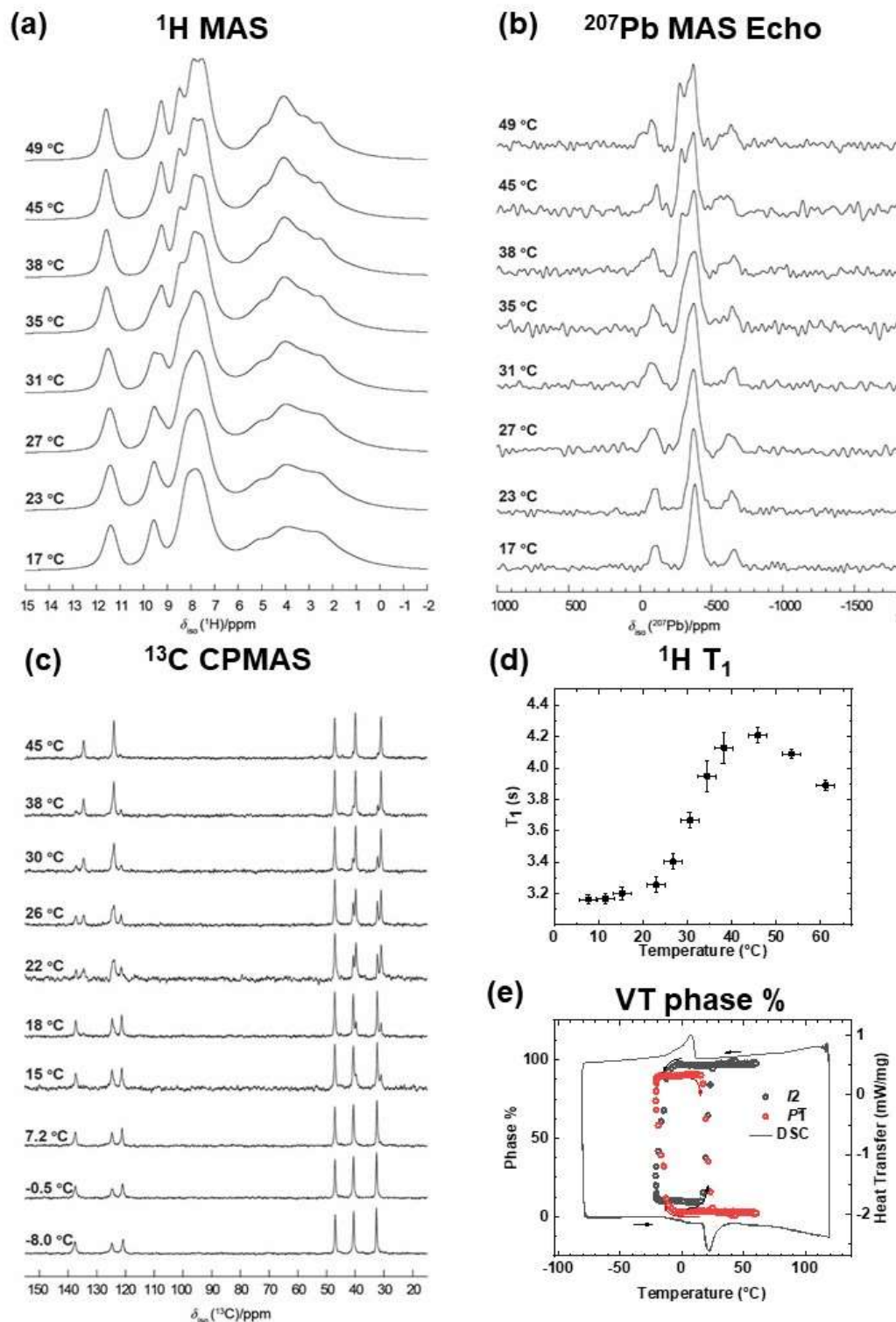


Figure 5.4 Variable temperature sweep of $\text{API}_2\text{Pb}_3\text{Br}_{10}$ and ^1H , ^{13}C and ^{207}Pb showing a clear correlation with XRD results. ^1H T_1 shows three distinct regions, below 20 °C, the intermediate 20 °C – 40 °C, and after 45 °C. Phase transition confirmed through XRD, NMR and calorimetric methods.

Across the phase transition temperature, Fig 5.4 shows the changes of the ^1H , ^{13}C and ^{207}Pb NMR spectra of $\text{API}_2\text{Pb}_3\text{Br}_{10}$. Focusing on ^{13}C spectra (Fig 5.4 c), the chemical shift of peak 4 and peak 5 gradually change from 40.5 ppm to 40.1 ppm and 32.6 to 31.1 ppm respectively going from the low to high temperatures. The effect of the change in chemical shift is also replicated by DFT calculation and presented in Table 5.2. Similarly, ^1H spectra show a gradual change from peak 3 from 9.1 ppm to 8.7 ppm, and an increased resolution as temperature increases. For the region between 7 ppm and 9 ppm, there would be a combination of effects of narrower peaks linewidths and gradual shifts of the peak positions. Although small, the deconvolution shows that the ^1H peaks 8, 1, 2 has changed from 7.2 ppm to 6.9 ppm, 7.3 ppm to 7.4 ppm and 7.8 ppm to 7.9 ppm respectively. Notably, the consistent overestimation of the ammonium ^1H , i.e. $^1\text{H} - 7$ and $^1\text{H} - 8$ for both $\text{API}_2\text{Pb}_3\text{Br}_{10}$ and IEAPbBr_4 system is attributed to the estimation errors from the DFT functionals. Interestingly, the ^1H chemical shifts obtained from DFT based on the original reported APIPbBr_4 obtained from DFT is very similar to the experimentally obtained $\text{API}_2\text{Pb}_3\text{Br}_{10}$, as can be seen in Table 5.2. On the other hand, the ^{13}C chemical shifts obtained from DFT show some characteristic differences from $\text{API}_2\text{Pb}_3\text{Br}_{10}$ and are closer to those in IEAPbBr_4 . This gives an indication that the chemical environment of ^1H is less sensitive to the variations in the lead bromide framework as compared to the chemical environment of ^{13}C . Hence, unsurprisingly, the difference in chemical shifts in the phase transition is seen more visibly in the ^{13}C spectra, which is further aided by the much narrower linewidths. Further evidence for the structural reconfiguration of API cation will be discussed in the subsequent section on 2D NMR.

The ^1H dynamics were also followed across the phase transition regime and the results are shown in Fig 5.4 d, which displays three distinct regions based on the slope profile; below 20 °C, above 40 °C, and the intermediate between 20 °C and 40 °C. T_1 has been linked to the nuclei dynamics and earlier work has examined in details the relationship between T_1 relaxation and the activation energy of the mode of motion through an Arrhenius relationship^{43, 44}. Recent works on the prototypical MAPbI_3 has seen an increasing T_1 relaxation time with increasing temperature⁴⁵.

From the slope profile, the three regimes of T_1 in $\text{API}_2\text{Pb}_2\text{Br}_{10}$ are different. Remarkably,

the slope profile of the low and high temperature is in direct contrast with each other; in the low temperature phase T_1 increase with increasing temperature while in the high temperature phase T_1 decrease with increasing temperature. The continuous change in T_1 is also consistent with the nature of the phase transition, unlike the MAPbX₃ series studied by Xu et al.⁴⁴, where the T_1 shows a discontinuous jump across the phase transition. The different slope profile of T_1 indicates a likely crossover in the dominant molecular motional mode responsible for the relaxation although further analysis is beyond the scope of this work. Such a crossover of behaviour was observed in early works on MAPbX₃ by Xu et al.⁴⁴ where it was determined that the T_1 relaxation was first dominated by correlated C₃-reorientation at higher temperatures, which changed to the regime dominated by the uncorrelated C₃-reorientation of MA cation past the deep T_1 minimum in MAPbBr₃ at lower temperatures. Similarly, in MAPbCl₃ and MAPbI₃, Xu et al. demonstrated that the T_1 relaxation was dominated by rotational tunnelling motion in the high temperature which transited into the regime dominated by correlated C₃-reorientation of MA cation at lower temperatures.

In the ²⁰⁷Pb spectra, it can be observed that the single peak at low temperature gradually splits into two peaks, starting from -400 ppm to two peaks with a peak intensity of approximately 2:1 ratio at -371 ppm and -280 ppm. The relative intensities of the peak are also supported by XRD results, where the peak at -371 ppm corresponds to the lead with face-edge sharing (fully occupied Pb01) while -280 ppm would be due to the lead with face-face sharing (partial occupied Pb02). Pb01 sits on a general position in the unit cell, and hence, is fully occupied while Pb02 sits on a special position, and hence is partially occupied (0.5). Furthermore, from an NMR shielding perspective, in the face-face shared octahedra, the bromine is less effective in shielding the Pb atoms, while in the face-edge shared octahedra, the edge shared bromine atoms can contribute more to the shielding. Therefore, the relative ratio of 1:0.5 can then be written as 2:1 and thus give a good agreement between the observed ²⁰⁷Pb NMR spectra and crystallographic results.

Combining the results through both short- and long-range structural techniques and indirect calorimetric studies, the phase transition of API₂Pb₃Br₁₀ from $P\bar{1}$ to $I2$ is thoroughly characterized. From NMR, the change in chemical shift would highlight the change in structural configuration. Consequently, the effect of the displacive phase

transition can be seen in Fig 5.1 (c) and (d), where the overlay of the two phases does show a small deviation from each other, particularly the orientation of the aliphatic tail group and the relative planar angles of the imidazole head group. The relative percentage of phases are, as mentioned in the earlier section, refined sequentially, and plotted on the same temperature range with DSC results, as seen in Fig 5.4 €. The implications of the phase transition on the bulk absorption and photoluminescence properties would be examined in the subsequent section.

Under the same experimental conditions, the high temperature ^1H spectra of the $\text{API}_2\text{Pb}_3\text{Br}_{10}$ /2 phase is visibly more resolved than that of IEAPbBr_4 , particularly in the aliphatic region between 2 ppm and 4 ppm. This hints at the faster tumbling of the API cation compared to the IEA cation, which is also supported by $T_{1\rho}$ measurements. A shorter $T_{1\rho}$, around 10 ms in $\text{API}_2\text{Pb}_3\text{Br}_{10}$, can be interpreted as a faster molecular motion in the kHz regime as compared to 200 ms in IEAPbBr_4 . This would therefore allow a more efficient averaging of the $^1\text{H} - ^1\text{H}$ dipolar interaction in $\text{API}_2\text{Pb}_3\text{Br}_{10}$ which results in the narrower ^1H linewidths under same experimental conditions. The T_1 measured across the different field is also in consistent with that measured for most other hybrid perovskite systems.

The characteristic of the polymorphed $\text{API}_2\text{Pb}_3\text{Br}_{10}$ remains critical in our understanding of the molecular engineering of <110> oriented perovskites because the example of $\text{API}_2\text{Pb}_3\text{Br}_{10}$ and IEAPbBr_4 shows that there is a critical chain length which contributes towards the formation of <110> oriented perovskites. The work of Febriansyah et al⁴⁶ shows the importance of the imidazole head group, as a change to a pyridinium head would change the structure into a <100> oriented lead bromide perovskite. As seen in $(4\text{PNEA})\text{PbI}_4$ system, the nitro-nitro and nitro-I interactions would stabilize the corrugated structure while the ammonium moieties anchor the lead halide sheets together²⁶. In another 3×3 a-DMEN, the authors attributed the driving force to a ‘chelating’ effect by the cation to the bromine atoms through hydrogen bond²⁵. The work presented in this chapter would also complement the observation by Mao et al.²⁵, which also concluded that the length of the diamine remains critical to for formation of corrugated structures.

Table 5.3 ^1H chemical shifts of $\text{API}_2\text{Pb}_3\text{Br}_{10}$, APIPbBr_4 and IEAPbBr_4 as determined

experimentally and predicted through DFT simulation

API ₂ Pb ₃ Br ₁₀ High Temp (I2)					API ₂ Pb ₃ Br ₁₀ Low Temp (P1)				APIPbBr ₄ (P2 ₁ /c) ^a	IEAPbBr ₄ (Pbca)			
¹ H site	¹ H δ_{iso} Expt /ppm	¹ H DFT δ_{iso} /ppm	Rel. Int. /% (\pm 1%)	$T_{1\rho}$ /ms	¹ H δ_{iso} Expt /ppm	¹ H DFT δ_{iso} /ppm	Rel. Int. /% (\pm 1%)	$T_{1\rho}$ /ms	¹ H δ_{iso} Calc. DFT /ppm	¹ H δ_{iso} Expt /ppm	¹ H DFT δ_{iso} /ppm	Rel. Int. /% (\pm 1%)	$T_{1\rho}$ /ms
6'	2.0	1.8	7.8	9.5	2.0	1.8	15.3	9.8	2.3				
6	2.6	2.9	7.5			2.5			2.9				
5	3.6	3.2		8.4	2.9	3.0	8.1	10.4	3.5	3.4	3.6	9.3	148
5'		3.4	14.7		3.6	3.5	7.7		3.7	3.9	3.9	9.3	
4	3.6	4.0	7.4	9.7	3.6	3.6	7.7	9.5	4.7	4.5	4.4	8.7	135
4'	4.5	4.7	7.3		4.7	4.8	7.9		5.3	5.2	5.4	8.7	
8	6.9	6.2	23.8	-	7.2	5.5	22.7	-	6.0	7.0	7.2	9.0	177
		7.0				8.7			7.0	7.4	6.3	27.6	-
		9.9				8.9			8.3		7.3		
1	7.4	7.4	8.0	7.6	7.3	7.7	7.9	9.4	7.8		8.9		
2	7.9	8.4	8.2		7.8	8.1	7.6	6.5	8.1	7.9	8.5	9.4	158
3	8.7	9.4	7.6	7.4	9.1	8.8	7.5	7.7	8.8	9.1	9.3	9.6	134
7	11.0	13.4	7.7	-	10.9	12.4	7.6	-	13.5	10.9	11.2	9.5	-

Table 5.4 ¹³C chemical shifts of API₂Pb₃Br₁₀, APIPbBr₄ and IEAPbBr₄ as determined experimentally and predicted through DFT simulations

API ₂ Pb ₃ Br ₁₀ High Temp (I2)			API ₂ Pb ₃ Br ₁₀ Low Temp (P1)		APIPbBr ₄ (P2 ₁ /c) ^a	IEAPbBr ₄ (Pbca)	
¹³ C site	¹³ C δ_{iso} Expt /ppm	¹³ C δ_{iso} Calc. DFT /ppm	¹³ C δ_{iso} Expt /ppm	¹³ C δ_{iso} Calc. DFT /ppm	¹³ C δ_{iso} DFT /ppm	¹³ C δ_{iso} Expt /ppm	¹³ C δ_{iso} Calc. DFT /ppm
5	31.1	31.9	32.6	36.8	41.2	42.0	43.0
4	40.1	39.5	40.5	47.6	46.1	50.1	48.7
6	47.2	48.7	47.0	49.2	48.5	122.3	125.6
2	123.8	124.0	120.8	123.4	122.1	126.3	125.8
1	123.8	125.8	124.8	132.3	131.5	136.7	138.8
3	134.9	135.6	137.6	141.7	144.0		

Table 5.5 T_1 and $T_{1\rho}$ of API₂Pb₃Br₁₀ and IEAPbBr₄ at different magnetic field strength

API ₂ Pb ₃ Br ₁₀ High Temp (I2)					API ₂ Pb ₃ Br ₁₀ Low Temp (P1̄)			IEAPbBr ₄ (Pbca)				
¹ H site	¹ H δ _{iso} Expt. /ppm	T ₁ 14.1T /s (±0.5s)	T ₁ 7.1T /s (±0.5s)	T _{1ρ} 9.4T /ms (±1ms)	T ₁ 14.1T /s (±0.5s)	T ₁ 7.1T /s (±0.5s)	T _{1ρ} 9.4T /ms (±1ms)	¹ H site	¹ H δ _{iso} Expt. /ppm	T ₁ 14.1T /s (±0.5s)	T ₁ 7.1T /s (±0.5s)	T _{1ρ} 9.4T /ms (±20ms)
6	2.0 2.6	4.0	2.1	9.47	3.0	2.1	9.82	5	3.4 3.9	1.4	2.4	135
5	3.6	4.1	2.1	9.72	3.1	2.1	9.47	4	4.5	1.4	2.4	148
4	3.6 4.5	4.1 4.0	2.1 2.0	8.44	3.1 3.0	2.1 2.0	10.4	2	5.2 7.0	1.4	2.3	158
8	6.9	3.8	2.1	-	3.1	2.2		8	7.4	1.4	2.3	
1	7.4	4.0	2.2	7.6	3.1	2.2	6.54	1	7.9	1.4	2.3	177
2	7.9	4.1	2.2	7.6	3.1	2.2	9.35	3	9.1	1.4	2.3	134
3	8.7	4.3	2.3	7.4	3.1	2.3	7.73	7	10.9	1.3	2.3	
7	11.0	4.2	2.3		3.1	2.2						

Both homonuclear and heteronuclear 2D NMR was carried out and the results are shown in Figure 5.5 and Figure 5.6. The heteronuclear correlation provides definitive evidence supporting the assignment of the aromatic imidazole group, particularly for $^1\text{H} - 7, 3$ and $^{13}\text{C} - 1, 2, 3$ and it also provides further evidence that $^{13}\text{C} - 4, 5, 6$ and $^1\text{H} - 4, 5, 6$ are within the expected regions.

5.3.3 Analysis of API cation across the phase transition by XRD and NMR

A homonuclear $^1\text{H} - ^1\text{H}$ BABA 2D NMR experiment provided additional evidence for the structural reconfiguration of the API cation. In Fig 5.5 c and d, the $^1\text{H} 1 - 4$ correlation is not seen in the low temperature phase but is seen in the high temperature phase. Since a BABA experiment revolves around the single quantum – double quantum transition, it is highly sensitive to the interatomic distances. Thus, the lack of $^1\text{H} 1 - 4$ correlation at the high temperature indicates that the imidazole plane had tilted away from the $^{13}\text{C} - 4$. However, from the NOESY results, with a sufficiently long contact time of 100 ms, the $^1\text{H} 1 - 4$ correlation peak appears very weakly, and hence, is an indication that the displacement of the ^1H atoms are just outside the resonance sensitivity of the BABA experiment. This is also substantiated from the XRD results, where Fig 5.6 shows the ORTEP diagram of the API cation, and the idealized $^1\text{H} - 4$ atoms in the low temperature phase (Fig 5.6 a, b) is pushed away from the imidazole ring than in the higher temperature phase (Fig 5.6 c, d). Based on the idealized structure, the $^1\text{H} 1 - 4$ distance is measured to be 2.690 Å in the low temperature phase and 2.859 Å in the high temperature phase, and the $^1\text{H} 3 - 4$ distance is measured to be 2.592 Å in the low temperature phase and 2.549 Å in the high temperature phase. Although the difference in $^1\text{H} 3 - 4$ interatomic distance is considerably smaller, it should be noted that the ^1H atoms are modelled to be in the idealized position. Therefore, crystallographic and NMR spectroscopic evidence supports the observation of slight displacement of the aliphatic tail in API cation due to the phase transition.

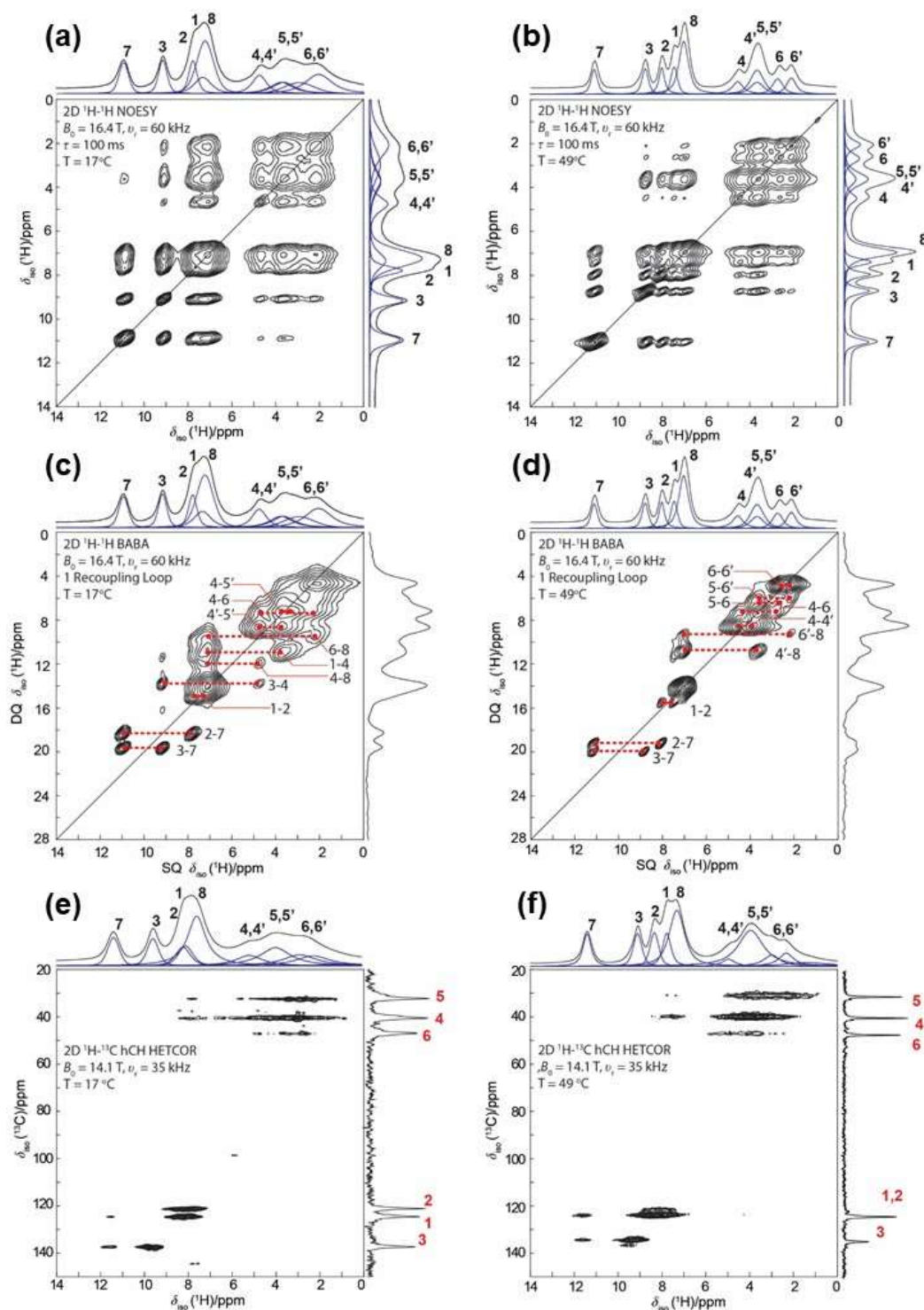


Figure 5.5 2D NMR spectra of $\text{API}_2\text{Pb}_3\text{Br}_{10}$ in the low (left) and high temperature (right) phase. (a,b) homonuclear NOESY (c, d) BABA and (e, f) heteronuclear hCH experiment

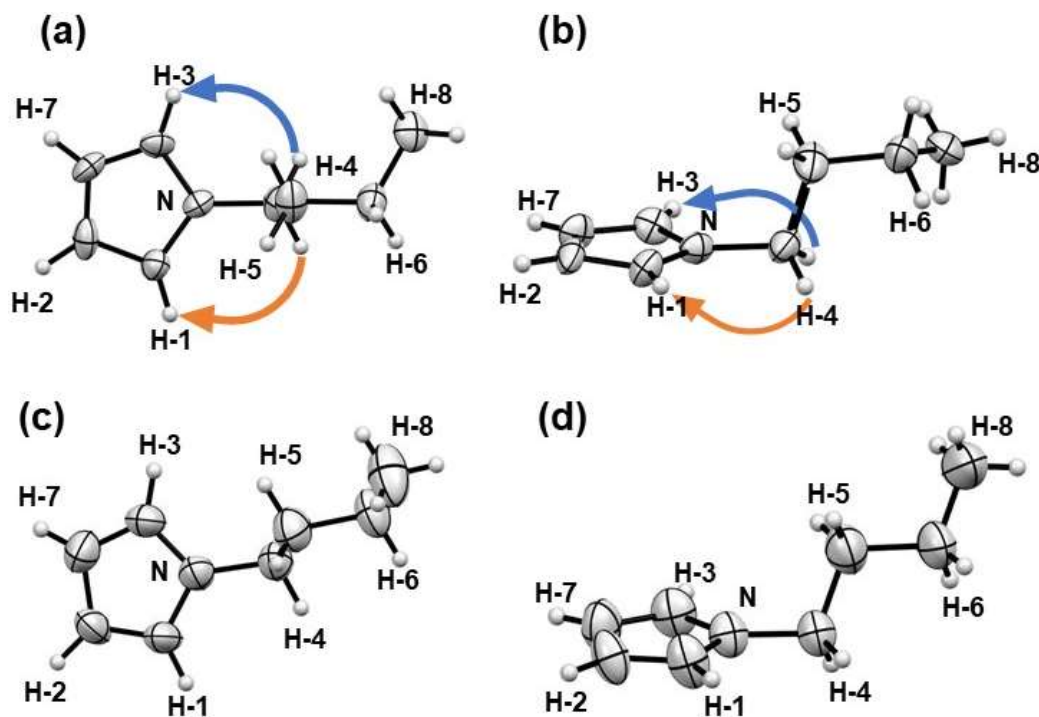


Figure 5.6 ORTEP diagram of the 1-(3-aminopropyl)imidazolium (API) cation in the low temperature ($P\bar{1}$) phase viewed (a) down the imidazolium plane, (b) almost parallel to the imidazolium plane, and high temperature $I2$ phase viewed (c) down the imidazolium plane, (d) almost parallel to the imidazolium plane. The orange and blue arrows show the two correlation, which was observed in the ^1H – ^1H BABA homonuclear NMR correlation experiment at the low temperature phase but absent in the high temperature phase.

Table 5.5 idealized ^1H – ^1H interatomic distance in the high and low temperature phase. Highlighted in bold are the two specific correlation which is seen in the ^1H – ^1H BABA homonuclear NMR correlation experiment at the low temperature phase but absent in the high temperature phase due to interatomic distances.

^1H	^1H	distance in $I2$ phase/ Å	distance in the $P\bar{1}$ phase/ Å
7	3	2.365	2.379
7	2	2.457	2.351
2	1	2.413	2.487
3	4	2.549	2.592
1	4	2.859	2.690
4	5	2.263	2.358
5	6	2.325	2.329
6	8	2.324	2.442

Comparing these results with those from $\text{API}_2\text{Pb}_3\text{Br}_{10}$ and IEAPbBr_4 , the differences

between them are also, unsurprisingly, similar to those seen in the 1D spectra in Fig 5.3. The noticeable broader ^1H spectra in IEAPbBr₄ is seen in the 2D homonuclear NOESY and heteronuclear hCH. No doubt the broader region in hCH does not give the desired resolution to differentiate $^1\text{H} - 4$ and $^1\text{H} - 5$, it nevertheless proves that $^1\text{H} - 4$ and $^1\text{H} - 5$ are correlated to $^{13}\text{C} - 4$ and $^{13}\text{C} - 5$. Further elucidation comes from BABA spectra, through the different peak positions, and further substantiated through DFT calculations and the 1D deconvolution fitting.

Since ^1H NOESY and BABA exploit the dipolar interaction, the relative intensity of the peaks provides an indication of the interatomic distance, and thus, allows the disentanglement of the aliphatic $^1\text{H} - 4,5,6$ and the ammonium $^1\text{H} - 8$ and $^1\text{H} - 1$, especially in the more resolved API₂Pb₃Br₁₀ spectrum. All the assignments were also corroborated by DFT calculations, as shown in Table 5.2 and 5.3. Notably, NOESY allows intermolecular correlations to be shown while BABA only shows intramolecular correlations. Hence, the weak correlations observed in NOESY, like $^1\text{H} - 3$ to $^1\text{H} - 4,5,6,6'$, $^1\text{H} - 2$ to $^1\text{H} - 4',5,5'$ and $^1\text{H} - 1$ to $^1\text{H} - 4,4',5,5',6$ are intermolecular. In the idealised model (Fig 5.1 a,b) the mentioned ^1H intermolecular distances typically span between 3 Å to 4 Å, which is on the upper limit for a reasonable range for the dipolar interaction. Similarly, this is also observed in IEAPbBr₄, although to a lesser extent because of a decreased resolution. For IEAPbBr₄, the same observation can also be seen in $^1\text{H} - 3$ to $^1\text{H} - 4,4',5,5'$, $^1\text{H} - 2$ to $^1\text{H} - 4,4',5,5'$ and $^1\text{H} - 1$ to $^1\text{H} - 4,4',5,5'$.

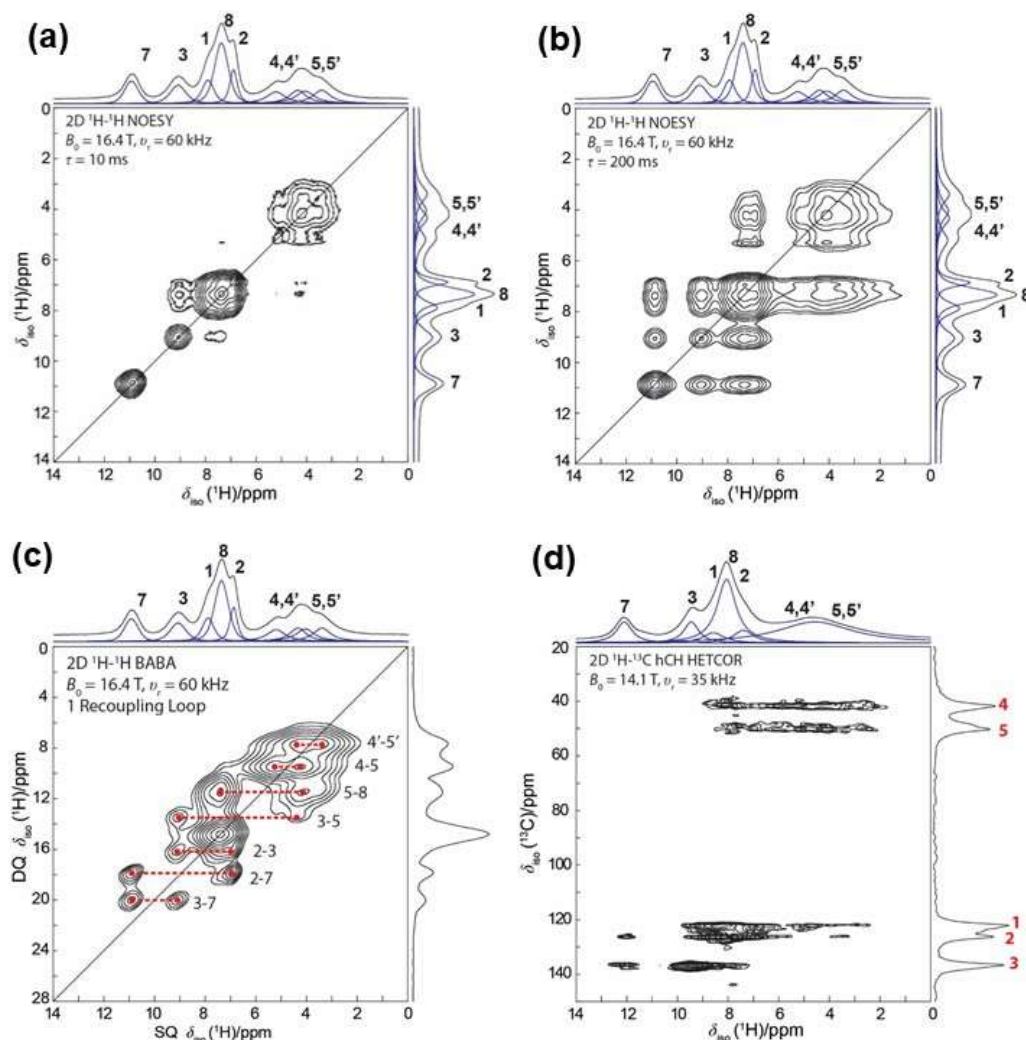


Figure 5.7 2D NMR spectra of IEAPbBr₄ in the low (left) and high temperature (right) phase. (a) homonuclear NOESY with contact time 10 ms, (b) NOESY with contact time 200 ms (c) homonuclear BABA and (d) heteronuclear hCH experiment.

5.3.4 Band structure predicted by Density Functional Theory and validated experimentally through steady-state absorption and photoluminescence

Based on the single crystal XRD results, the obtained CIF files are utilized to calculate the Density of State (DOS) and the Joint Density of States, as shown in Fig 5.8. A summary of the calculated band gaps (using the CASTEP DFT code) and measured band gaps (from the photoluminescence and absorbance data) are compared in table 5.6; the high and low temperature API₂Pb₃Br₁₀ phases are indirect band gap materials, while IEAPbBr₄ is a direct band gap material. However, it should be noted that in API₂Pb₃Br₁₀

the band dispersions are around the valence band to conduction band transition is very flat, and only shows a small momentum mismatch of around 0.01 eV. From table 5.6, the calculated band gaps can be seen to depend on the lead bromide framework structure connectivity. The trend here shows that the band gap of corner shared perovskites (i.e. IEAPbBr₄, and APIPbBr₄) is consistently smaller than the face shared perovskitoids (i.e. API₂Pb₃Br₁₀). The results also show that by accounting for the spin-orbit coupling effects in the hybrid perovskites, the energy levels of Pb and Br *p*-orbitals are lowered and thus decreasing the band gap. The PBE functionals are known to underestimate the band gaps⁴⁷, hence, the differing band gaps predicted by rSCAN and PBE functionals. The implementation of SOC effects in DFT bandgap calculations is non-trivial^{48, 49}; the inclusion of SOC to the rSCAN functional is likely to yield predicted band gap values that would agree closely with the experimental results. Nevertheless, the DFT estimations provides a good benchmark against the obtained experimental values.

The results of steady state absorption and photoluminescence spectroscopy are shown in Fig 5.9. Distinctly broadband emission can be observed from both API₂Pb₃Br₁₀ and IEAPbBr₄, which is experimental evidence for the effects of charge localization in hybrid perovskites. The absorption measurements were carried out in reflectance mode, and hence, is plotted with the Kubelka-Munk function against the excitation energy. Assuming that the materials are a direct band gap material, a Tauc plot is used to estimate the band gap of the two systems and the results are plotted in the insert of the absorption spectra. Even though DFT calculations showed that API₂Pb₃Br₁₀ are indirect band gaps, due to the slight momentum mismatch, and coupled with a very flat band dispersion around the VB – CB transition region, it is fair to approximate the material to one that has a direct band gap. The linear absorption profile seen in Fig 5.9 corroborates well with the Joint Density of State calculation of API₂Pb₃Br₁₀ and IEAPbBr₄ thus further validating the strong theoretical models with experimental results.

In the photoluminescence spectra, a strong baseline is observed and is the result of an experimentally challenging condition. The excitation energies have to be greater than 3.3 eV (375 nm) to excite the charge carriers above the band gap, and consequently, would require a long pass filter to remove any second order effects arising from the monochromator of the source lamp. Commercially, such filters are not available and

the Schott WG320 is the only available filter with a cut-off (transmittance $< 10^{-4}$) at 290 nm (4.28 eV). Furthermore, a cryostat is required to control the temperature of the sample and additional optics and parts would be added to the experimental setup. Hence, by using such high excitation energy, even optically transparent components like CaF_2 windows of the cryostat and the instrument's mirrors would also begin to fluoresce to give the baseline (labelled in black). Consequently, the incomplete filtering from the long pass filter resulted in the presence of a second order peak at 580 nm arising from the monochromator, which is labelled by an asterisk in the photoluminescence spectra.

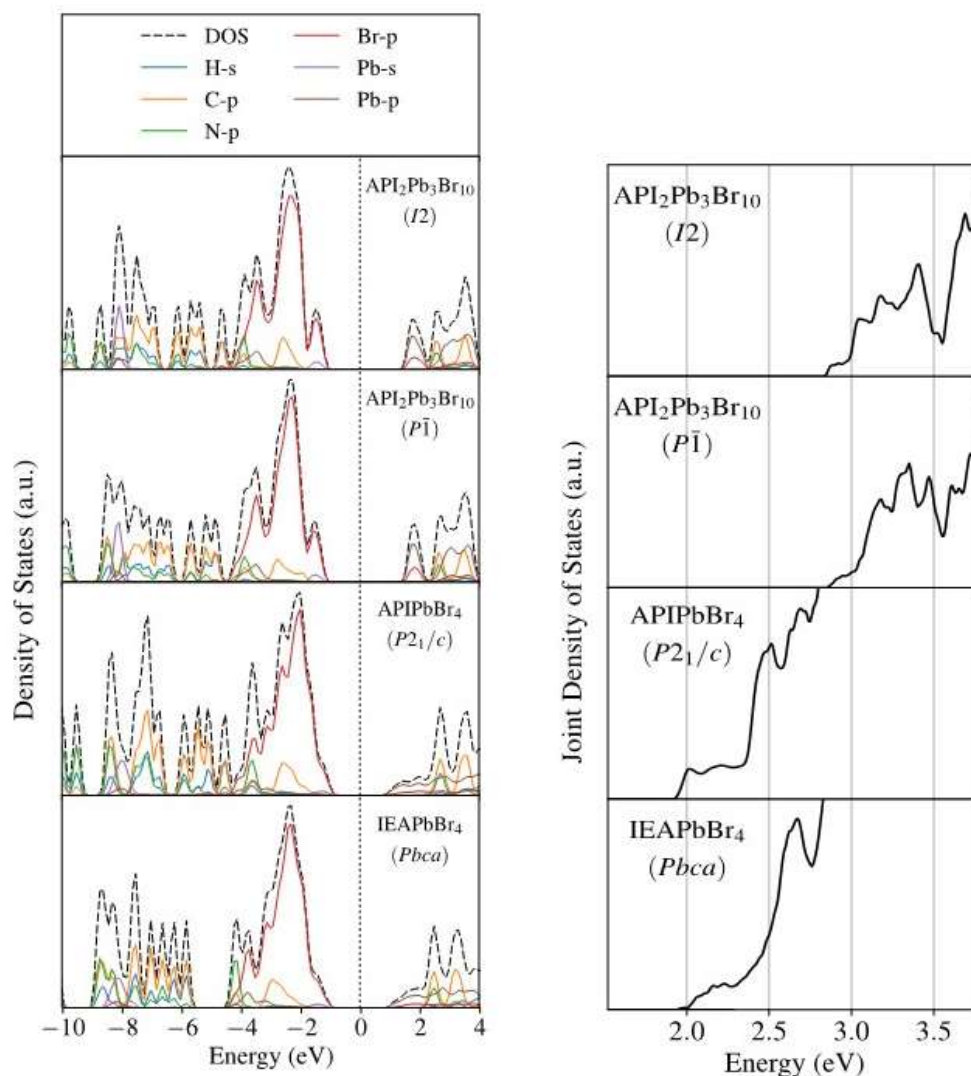


Figure 5.8 The density of states (left) and joint density of states (right) of $\text{API}_2\text{Pb}_3\text{Br}_{10}$, APIPbBr_4 , and IEAPbBr_4 as calculated by Density Functional Theory (DFT) using the Perdew–Burke–Ernzerhof (PBE) with Spin Orbit Coupling (SOC) functional.

Table 5.6 Band gaps obtained from DFT simulations. The inclusion of SOC effects gives a better estimate of the band gap. Corner shared octahedra, as in APIPbBr₄ and IEAPbBr₄, shows a consistently smaller band gap than the face and edge shared API₂Pb₃Br₁₀ perovskitoid.

Sample	E_g / eV (rSCAN)	E_g / eV (PBE)	E_g / eV (PBE-SOC)	E_g / eV (Experimental)
API ₂ Pb ₃ Br ₁₀ (<i>I</i> 2)	3.75	3.38	2.84	3.02 (40 °C)
API ₂ Pb ₃ Br ₁₀ (\bar{P} 1)	3.82	3.43	2.86	3.06 (-20 °C)
APIPbBr ₄ (<i>P</i> 2 ₁ /c)	2.83	2.46	1.96	Not Applicable
IEAPbBr ₄ (<i>Pbca</i>)	2.86	2.53	2.02	3.08 (20 °C)

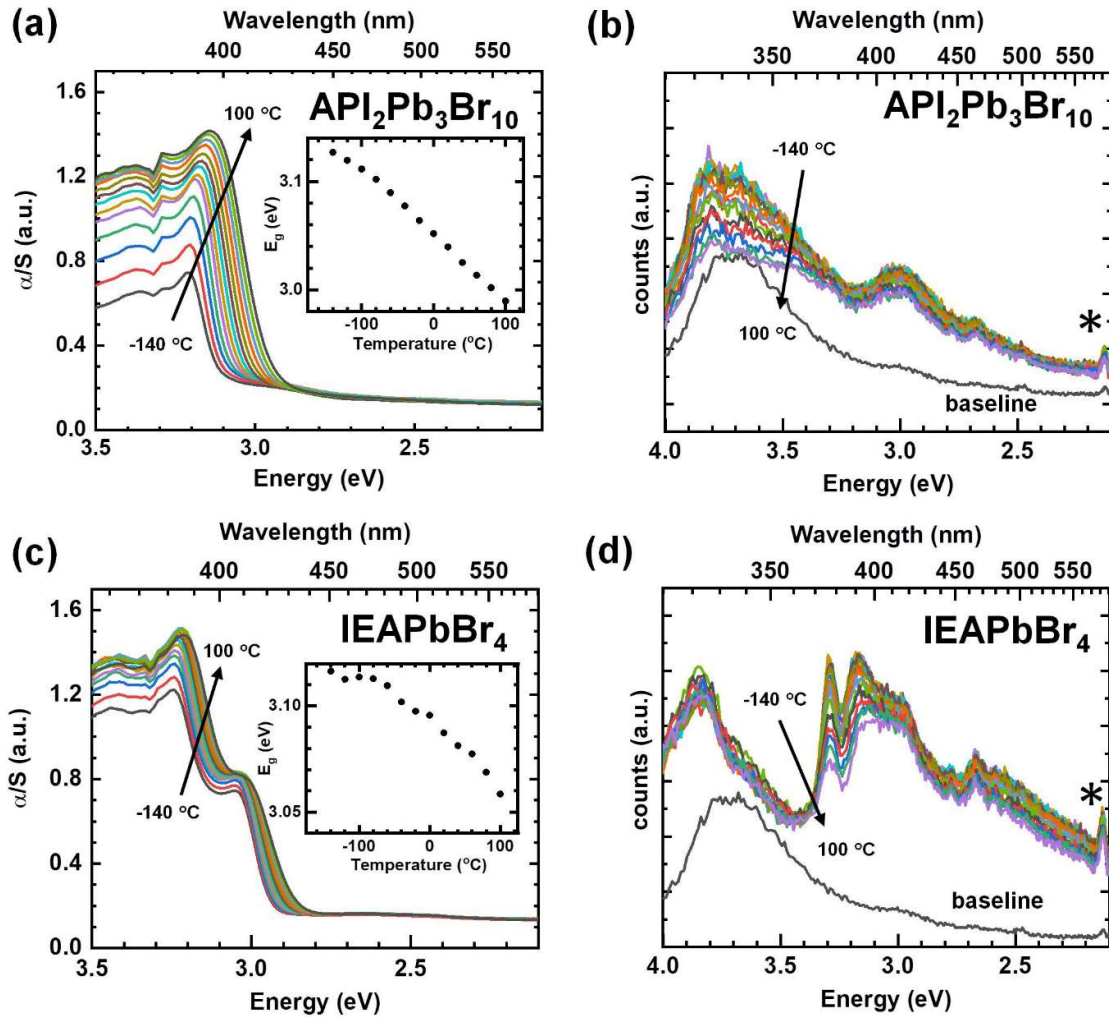


Figure 5.9 Absorption and photoluminescence results. Asterisk marks the spectral artefact arising from the second order effects arising from the monochromator while using the source radiation (290 nm), which has not filtered out by long pass filter (Schott 320).

Table 5.7 Table of key optical properties extracted from photoluminescence results

API₂Pb₃Br₁₀ (I2/P1)		IEAPbBr₄ (Pbca)	
PL centre/nm	430	PL centre/nm	410
PL FWHM /nm	80±10	PL FWHM /nm	30±10
T/°C	E_g/eV	T/°C	E_g/eV
-140	3.13	-140	3.11
-120	3.12	-120	3.11
-100	3.11	-100	3.11
-80	3.10	-80	3.11
-60	3.09	-60	3.11
-40	3.08	-40	3.10
-20	3.06	-20	3.10
0	3.05	0	3.10
20	3.04	20	3.09
40	3.02	40	3.08
60	3.01	60	3.08
80	3.00	80	3.07
100	2.99	100	3.06

In the optical characterization of API₂Pb₃Br₁₀, it can be observed that the effects of the phase transition are not distinct in all the observed optical properties. The shape profile of the absorption is consistent and is a linear correlation of the band gap with the temperature. The band gap is expectedly red shifts as expected with increasing temperature and is attributed to the lattice expansion effects. Similarly, in the photoluminescence spectra, there is no visible change in either the emission profile or the absolute emission intensity. Although the photoluminescence results have a strong influence from the background, a broadband component can still be observed from 400 nm to 550 nm. The presence of such broadband emission character in hybrid perovskites has very frequently been attributed to the presence of self-trapped states.^{20, 22} Notably, there is no definite evidence for the existence of excitons even at low temperatures.

In IEAPbBr₄, a strong emission peak is seen at 377 nm, which decreases with increasing

temperature. Given that the high excitation energy of 290 nm is used for this measurement, it remains inconclusive whether this would be an excitonic feature or other interband transition. However, the broad feature between 380 nm and 550 nm gives as indication of the presence of self-trapped charge electrons and holes^{20, 22}.

5.4 Conclusion

In conclusion, this chapter has shown that the prototypical APIPbBr₄ can exist as a polymorph, API₂Pb₃Br₁₀ in the bulk. While this does not invalidate the earlier reported structure, this work shows an important, but also known, weakness in single crystal diffraction technique, where crystal picked for diffraction could be different from the bulk sample. This error can be avoided by further validating the obtained structure by carrying out powder XRD.

The structural phase transition seen in API₂Pb₃Br₁₀ is thoroughly characterized through XRD and NMR and the results agree with calorimetric studies, which shows that the phase transition from $P\bar{1}$ to $I2$ is at around 20 °C and the transition from $I2$ to $P\bar{1}$ is at around 0 °C. No structural phase transition is observed in IEAPbBr₄ up to the point of thermal degradation.

The phase transition exhibited by API₂Pb₃Br₁₀ warrants further investigation into the difference in the various properties, e.g. mechanical, optoelectronic, or magnetic properties, because very few materials exhibits phase transition at around room temperatures. With a better understanding of the various properties, suitable applications can then be suggested, and this material could find application in temperature sensitive switching devices.

From the structural formation perspective, it is demonstrated that there are two main competing stabilization-destabilization factors to be considered when engineering the <110> cut of perovskite. When the carbon tail length is too long and does not have any other interactions to stabilize the spacing, like API₂Pb₃Br₁₀, the perovskite connectivity will undergo a reconstructive transformation and the di-cationic charges would be spread out along a chain. At an optimal two carbon chain length, the <110> oriented

perovskite is formed.

From the NMR studies, the structural properties corroborate with X-ray diffraction, particularly, from the BABA correlation experiment in $\text{API}_2\text{Pb}_3\text{Br}_{10}$. The cation dynamics of API and IEA are seen to be distinct between the two systems and provides evidence that the localized disorder has to be considered while probing the bulk properties of each system.

It is further demonstrated in this chapter that broadband emission is present in both $\text{API}_2\text{Pb}_3\text{Br}_{10}$ and IEAPbBr_4 , which is an indication of the presence of self-trapped charge carriers even though the structural configuration of the lead halide octahedra are distinctly different. No doubt there are differences in the photoluminescence spectra between the two, where IEAPbBr_4 shows sharp feature accompanied by a broadband white light emission whereas $\text{API}_2\text{Pb}_3\text{Br}_{10}$, shows a low photoluminescence quantum yield as the counts is considerably lower than IEAPbBr_4 and has a different emission profile. However, the two systems both exhibits broadband photoluminescence emission, which indicates the presence of self-trapped carriers.

References

1. Goldschmidt, V. M., Die Gesetze der Krystallochemie. *Naturwissenschaften* **1926**, 14 (21), 477-485.
2. Kim, H.-S.; Lee, C.-R.; Im, J.-H.; Lee, K.-B.; Moehl, T.; Marchioro, A.; Moon, S.-J.; Humphry-Baker, R.; Yum, J.-H.; Moser, J. E.; Grätzel, M.; Park, N.-G., Lead Iodide Perovskite Sensitized All-Solid-State Submicron Thin Film Mesoscopic Solar Cell with Efficiency Exceeding 9%. *Scientific Reports* **2012**, 2, 591.
3. Lee, M. M.; Teuscher, J.; Miyasaka, T.; Murakami, T. N.; Snaith, H. J., Efficient Hybrid Solar Cells Based on Meso-Superstructured Organometal Halide Perovskites. *Science* **2012**, 338 (6107), 643-647.
4. Im, J.-H.; Lee, C.-R.; Lee, J.-W.; Park, S.-W.; Park, N.-G., 6.5% efficient perovskite quantum-dot-sensitized solar cell. *Nanoscale* **2011**, 3 (10), 4088-4093.
5. Saidaminov, M. I.; Abdelhady, A. L.; Murali, B.; Alarousu, E.; Burlakov, V. M.; Peng, W.; Dursun, I.; Wang, L.; He, Y.; Maculan, G.; Goriely, A.; Wu, T.;

Mohammed, O. F.; Bakr, O. M., High-quality bulk hybrid perovskite single crystals within minutes by inverse temperature crystallization. *Nature Communications* **2015**, *6*, 7586.

6. Swainson, I. P.; Hammond, R. P.; Soullière, C.; Knop, O.; Massa, W., Phase transitions in the perovskite methylammonium lead bromide, CH₃ND₃PbBr₃. *Journal of Solid State Chemistry* **2003**, *176* (1), 97-104.

7. Maculan, G.; Sheikh, A. D.; Abdelhady, A. L.; Saidaminov, M. I.; Haque, M. A.; Murali, B.; Alarousu, E.; Mohammed, O. F.; Wu, T.; Bakr, O. M., CH₃NH₃PbCl₃ Single Crystals: Inverse Temperature Crystallization and Visible-Blind UV-Photodetector. *The Journal of Physical Chemistry Letters* **2015**, *6* (19), 3781-3786.

8. Maalej, A.; Abid, Y.; Kallel, A.; Daoud, A.; Lautié, A.; Romain, F., Phase transitions and crystal dynamics in the cubic perovskite CH₃NH₃PbCl₃. *Solid State Communications* **1997**, *103* (5), 279-284.

9. Vegard, L., Die Konstitution der Mischkristalle und die Raumfüllung der Atome. *Zeitschrift für Physik* **1921**, *5* (1), 17-26.

10. Denton, A. R.; Ashcroft, N. W., Vegard's law. *Physical Review A* **1991**, *43* (6), 3161-3164.

11. Stranks, S. D.; Eperon, G. E.; Grancini, G.; Menelaou, C.; Alcocer, M. J. P.; Leijtens, T.; Herz, L. M.; Petrozza, A.; Snaith, H. J., Electron-Hole Diffusion Lengths Exceeding 1 Micrometer in an Organometal Trihalide Perovskite Absorber. *Science* **2013**, *342*, 341-344.

12. Mazzarella, L.; Lin, Y.-H.; Kirner, S.; Morales-Vilches, A. B.; Korte, L.; Albrecht, S.; Crossland, E.; Stannowski, B.; Case, C.; Snaith, H. J.; Schlattmann, R., Infrared Light Management Using a Nanocrystalline Silicon Oxide Interlayer in Monolithic Perovskite/Silicon Heterojunction Tandem Solar Cells with Efficiency above 25%. *Advanced Energy Materials* **2019**, *9* (14), 1803241.

13. Xing, G.; Mathews, N.; Lim, S. S.; Yantara, N.; Liu, X.; Sabba, D.; Grätzel, M.; Mhaisalkar, S.; Sum, T. C., Low-temperature solution-processed wavelength-tunable perovskites for lasing. *Nat. Mater.* **2014**, *13*, 476.

14. Tan, Z.-K.; Moghaddam, R. S.; Lai, M. L.; Docampo, P.; Higler, R.; Deschler, F.; Price, M.; Sadhanala, A.; Pazos, L. M.; Credgington, D.; Hanusch, F.; Bein, T.; Snaith, H. J.; Friend, R. H., Bright light-emitting diodes based on organometal halide perovskite. *Nat. Nanotech.* **2014**, *9*, 687-692.

15. Chin, X. Y.; Cortecchia, D.; Yin, J.; Bruno, A.; Soci, C., Lead iodide perovskite light-emitting field-effect transistor. *Nat. Commun.* **2015**, *6*, 7383.
16. Shockley, W.; Queisser, H. J., Detailed Balance Limit of Efficiency of p-n Junction Solar Cells. *Journal of Applied Physics* **1961**, *32* (3), 510-519.
17. Johnston, H., Blue LED research wins Nobel prize. *Physics World* **2014**, *27* (11), 6-7.
18. Li, Y. Y.; Lin, C. K.; Zheng, G. L.; Cheng, Z. Y.; You, H.; Wang, W. D.; Lin, J., Novel <110> -Oriented Organic-Inorganic Perovskite Compound Stabilized by N-(3-Aminopropyl)imidazole with Improved Optical Properties. *Chemistry of Materials* **2006**, *18* (15), 3463-3469.
19. Dohner, E. R.; Jaffe, A.; Bradshaw, L. R.; Karunadasa, H. I., Intrinsic White-Light Emission from Layered Hybrid Perovskites. *Journal of the American Chemical Society* **2014**, *136* (38), 13154-13157.
20. Cortecchia, D.; Yin, J.; Bruno, A.; Lo, S.-Z. A.; Gurzadyan, G. G.; Mhaisalkar, S.; Bredas, J.-L.; Soci, C., Polaron self-localization in white-light emitting hybrid perovskites. *J. Mater. Chem. C* **2017**, *5* (11), 2771-2780.
21. Dohner, E. R.; Hoke, E. T.; Karunadasa, H. I., Self-Assembly of Broadband White-Light Emitters. *Journal of the American Chemical Society* **2014**, *136* (5), 1718-1721.
22. Yin, J.; Li, H.; Cortecchia, D.; Soci, C.; Brédas, J.-L., Excitonic and Polaronic Properties of 2D Hybrid Organic-Inorganic Perovskites. *ACS Energy Lett.* **2017**, *2*, 417-423.
23. Cortecchia, D.; Neutzner, S.; Srimath Kandada, A. R.; Mosconi, E.; Meggiolaro, D.; De Angelis, F.; Soci, C.; Petrozza, A., Broadband Emission in Two-Dimensional Hybrid Perovskites: The Role of Structural Deformation. *J. Am. Chem. Soc.* **2017**, *139* (1), 39-42.
24. Smith, M. D.; Jaffe, A.; Dohner, E. R.; Lindenberg, A. M.; Karunadasa, H. I., Structural origins of broadband emission from layered Pb-Br hybrid perovskites. *Chemical Science* **2017**, *8* (6), 4497-4504.
25. Mao, L.; Wu, Y.; Stoumpos, C. C.; Wasielewski, M. R.; Kanatzidis, M. G., White-Light Emission and Structural Distortion in New Corrugated Two-Dimensional Lead Bromide Perovskites. *Journal of the American Chemical Society* **2017**, *139* (14), 5210-5215.

26. Tremblay, M.-H.; Thouin, F.; Leisen, J.; Bacsá, J.; Srimath Kandada, A. R.; Hoffman, J. M.; Kanatzidis, M. G.; Mohite, A. D.; Silva, C.; Barlow, S.; Marder, S. R., (4NPEA)2PbI4 (4NPEA = 4-Nitrophenylethylammonium): Structural, NMR, and Optical Properties of a 3 × 3 Corrugated 2D Hybrid Perovskite. *Journal of the American Chemical Society* **2019**, *141* (11), 4521-4525.
27. Sutherland, B. R.; Hoogland, S.; Adachi, M. M.; Wong, C. T. O.; Sargent, E. H., Conformal Organohalide Perovskites Enable Lasing on Spherical Resonators. *ACS Nano*. **2014**, *8*, 10947-10952.
28. Kim, Y.-H.; Lee, G.-H.; Kim, Y.-T.; Wolf, C.; Yun, H. J.; Kwon, W.; Park, C. G.; Lee, T. W., High efficiency perovskite light-emitting diodes of ligand-engineered colloidal formamidinium lead bromide nanoparticles. *Nano Energy* **2017**, *38* (Supplement C), 51-58.
29. Zheng, K.; Abdellah, M.; Zhu, Q.; Kong, Q.; Jennings, G.; Kurtz, C. A.; Messing, M. E.; Niu, Y.; Gosztola, D. J.; Al-Marri, M. J.; Zhang, X.; Pullerits, T.; Canton, S. E., Direct Experimental Evidence for Photoinduced Strong-Coupling Polarons in Organolead Halide Perovskite Nanoparticles. *J. Phys. Chem. Lett.* **2016**, *7*, 4535-4539.
30. Schlaus, A. P.; Spencer, M. S.; Miyata, K.; Liu, F.; Wang, X.; Datta, I.; Lipson, M.; Pan, A.; Zhu, X. Y., How lasing happens in CsPbBr3 perovskite nanowires. *Nature Communications* **2019**, *10* (1), 265.
31. Yuan, C.; Li, X.; Semin, S.; Feng, Y.; Rasing, T.; Xu, J., Chiral Lead Halide Perovskite Nanowires for Second-Order Nonlinear Optics. *Nano Letters* **2018**, *18* (9), 5411-5417.
32. Zhang, H.; Wu, Y.; Liao, Q.; Zhang, Z.; Liu, Y.; Gao, Q.; Liu, P.; Li, M.; Yao, J.; Fu, H., A Two-Dimensional Ruddlesden–Popper Perovskite Nanowire Laser Array based on Ultrafast Light-Harvesting Quantum Wells. *Angewandte Chemie International Edition* **2018**, *57* (26), 7748-7752.
33. Chen, W.; Bhaumik, S.; Veldhuis, S. A.; Xing, G.; Xu, Q.; Grätzel, M.; Mhaisalkar, S.; Mathews, N.; Sum, T. C., Giant five-photon absorption from multidimensional core-shell halide perovskite colloidal nanocrystals. *Nat. Commun.* **2017**, *8*, 15198.
34. Protesescu, L.; Yakunin, S.; Bodnarchuk, M. I.; Bertolotti, F.; Masciocchi, N.; Guagliardi, A.; Kovalenko, M. V., Monodisperse Formamidinium Lead Bromide

Nanocrystals with Bright and Stable Green Photoluminescence. *Journal of the American Chemical Society* **2016**, *138* (43), 14202-14205.

35. Zhu, H.; Fu, Y.; Meng, F.; Wu, X.; Gong, Z.; Ding, Q.; Gustafsson, M. V.; Trinh, M. T.; Jin, S.; Zhu, X. Y., Lead halide perovskite nanowire lasers with low lasing thresholds and high quality factors. *Nat. Mater.* **2015**, *14*, 636-642.
36. Sheldrick, G., SHELXT - Integrated space-group and crystal-structure determination. *Acta Crystallographica Section A* **2015**, *71* (1), 3-8.
37. Dolomanov, O. V.; Bourhis, L. J.; Gildea, R. J.; Howard, J. A. K.; Puschmann, H., OLEX2: a complete structure solution, refinement and analysis program. *Journal of Applied Crystallography* **2009**, *42* (2), 339-341.
38. Spek, A., Structure validation in chemical crystallography. *Acta Crystallographica Section D* **2009**, *65* (2), 148-155.
39. Febriansyah, B.; Giovanni, D.; Ramesh, S.; Koh, T. M.; Li, Y.; Sum, T. C.; Mathews, N.; England, J., Inducing formation of a corrugated, white-light emitting 2D lead-bromide perovskite via subtle changes in templating cation. *Journal of Materials Chemistry C* **2020**, *8* (3), 889-893.
40. Robinson, K.; Gibbs, G. V.; Ribbe, P. H., Quadratic Elongation: A Quantitative Measure of Distortion in Coordination Polyhedra. *Science* **1971**, *172* (3983), 567-570.
41. Alonso, J. A.; Martínez-Lope, M. J.; Casais, M. T.; Fernández-Díaz, M. T., Evolution of the Jahn–Teller Distortion of MnO₆ Octahedra in RMnO₃ Perovskites (R = Pr, Nd, Dy, Tb, Ho, Er, Y): A Neutron Diffraction Study. *Inorganic Chemistry* **2000**, *39* (5), 917-923.
42. Li, X.; Guo, P.; Kepenekian, M.; Hadar, I.; Katan, C.; Even, J.; Stoumpos, C. C.; Schaller, R. D.; Kanatzidis, M. G., Small Cyclic Diammonium Cation Templated (110)-Oriented 2D Halide (X = I, Br, Cl) Perovskites with White-Light Emission. *Chemistry of Materials* **2019**, *31* (9), 3582-3590.
43. Wasylishen, R. E.; Knop, O.; Macdonald, J. B., Cation rotation in methylammonium lead halides. *Solid State Communications* **1985**, *56* (7), 581-582.
44. Xu, Q.; Eguchi, T.; Nakayama, H.; Nakamura, N.; Kishita, M., Molecular Motions and Phase Transitions in Solid CH₃NH₃PbX₃ (X = Cl, Br, I) as Studied by NMR and NQR. In *Zeitschrift für Naturforschung A*, 1991; Vol. 46, p 240.
45. Baikie, T.; Barrow, N. S.; Fang, Y.; Keenan, P. J.; Slater, P. R.; Piltz, R. O.; Gutmann, M.; Mhaisalkar, S. G.; White, T. J., A combined single crystal neutron/X-ray diffraction and solid-state nuclear magnetic resonance study of the hybrid perovskites

CH₃NH₃PbX₃ (X = I, Br and Cl). *Journal of Materials Chemistry A* **2015**, 3 (17), 9298-9307.

46. Febriansyah, B.; Koh, T. M.; John, R. A.; Ganguly, R.; Li, Y.; Bruno, A.; Mhaisalkar, S. G.; England, J., Inducing Panchromatic Absorption and Photoconductivity in Polycrystalline Molecular 1D Lead-Iodide Perovskites through π -Stacked Viologens. *Chemistry of Materials* **2018**, 30 (17), 5827-5830.

47. Mosconi, E.; Amat, A.; Nazeeruddin, M. K.; Grätzel, M.; De Angelis, F., First-Principles Modeling of Mixed Halide Organometal Perovskites for Photovoltaic Applications. *The Journal of Physical Chemistry C* **2013**, 117 (27), 13902-13913.

48. Even, J.; Pedesseau, L.; Jancu, J.-M.; Katan, C., Importance of Spin–Orbit Coupling in Hybrid Organic/Inorganic Perovskites for Photovoltaic Applications. *The Journal of Physical Chemistry Letters* **2013**, 4 (17), 2999-3005.

49. Even, J.; Pedesseau, L.; Dupertuis, M. A.; Jancu, J. M.; Katan, C., Electronic model for self-assembled hybrid organic/perovskite semiconductors: Reverse band edge electronic states ordering and spin-orbit coupling. *Physical Review B* **2012**, 86 (20), 205301.

Chapter 6

Imidazolium lead bromide polymorphs: 3D polytype to 1D perovskite

Following the studies on a $\langle 110 \rangle$ oriented perovskite prepared using an alkyl substituted imidazolium cation, this chapter explores the rich polymorphism exhibited by imidazolium lead bromide. The structural connectivity of the lead halide octahedra are seen to vary considerably and the structures of each polymorph are closely examined. A new naming nomenclature of perovskite-like ‘perovskitoids’ is also proposed to help classify the growing class of ‘perovskitoids’. The structures of each polymorph are thoroughly characterized through XRD and the cation dynamics through SSNMR, The optical characterization of all three imidazolium lead bromide polymorphs hints at the presence of self-trapped states.

*Part of this chapter has been published as Wong, W.P.D., Hanna, J.V. & Grimsdale, A.C. (2021). *Acta Cryst. B* 77, <https://doi.org/10.1107/S2052520621004376>.

6.1 Introduction

Keeping an imidazole head as the charged portion of the A-site cation, this chapter further explores the role of the A-site cation in determining the structure and properties of HOIPs. Imidazole is known to exhibit chemical activity at the nitrogen sites and is can be protonated to become a symmetrical imidazolium cation. The reversible protonation of imidazole is a known source of proton conductivity in polymers¹ and thus, is often utilized to improve proton conductivities in polymeric membranes, mostly in fuel cells applications^{2, 3}. In the previous chapter, in the cations, API and IEA, this protonation activity is suppressed due to the presence of the alkyl side chain on the nitrogen. However, the importance of reversible protonation is seen directly in this chapter where three different polymorphed structures which are obtained by varying the precursor concentration of imidazole to lead as described in chapter 3.

Structurally, the three polymorphs are distinctly different. IMIPbBr₃ closely resembles a 4H perovskite polytype and shows two phase transitions; IMI₂PbBr₄ has a structure where each lead bromide octahedron exhibits sharing at one edge and two corners to form an extended chain of inorganic units along one dimension; lastly, IMI₃PbBr₅ possesses a structure where each lead bromide octahedron shares only corners, to form a 1D chain. To further differentiate these ‘perovskitoids’, a new nomenclature is proposed, as discussed in a subsequent section.

All three polymorphs were thoroughly characterized through SSNMR and XRD. DFT calculations we also performed to obtain a theoretical estimate of the NMR chemical shifts and the theoretical band structure. Optical absorption measurements showed a good agreement with theoretical estimates, and the photoluminescence emissions of all three systems are distinctly broadband, which gives a strong indication of the presence of self-trapped states.

6.2 Experimental

6.2.1 X-ray diffraction

The crystals were dispersed in Fomblin ® and were hand-picked under a polarizing microscope and mounted onto MiTeGen microloops of the appropriate size for room temperature X-ray diffraction investigations or mounted onto a glass fibre approximately 100 µm in diameter to reduce the likelihood of crystal frosting for measurements at low temperatures ($T < 200$ K). The X-ray initialization and early processing was done together using software package CrysAlisPro on the Rigaku Gemini diffractometer and Rigaku SuperNova diffractometer using Mo $K_{\alpha} = 0.71$ Å. The collection strategy and integration were as suggested through CrysAlis. The structure solution and refinement were done with SHELXT⁴, Olex2⁵. Checked with PLATON⁶, and verified with IUCr CheckCIF. Powder XRD was carried out at Diamond Light Source Beamline I11 with radiation of 0.825Å. Samples were packed into 0.1mm capillaries and referenced against SiO₂ for Rietveld refinements.

6.2.2 Nuclear Magnetic Resonance

NMR experiments were performed using a suite of different magnets. Variable temperature ¹H T_1 , ¹³C CPMAS, hCH HETCOR and ²⁰⁷Pb measurements were done on Bruker 600 MHz Advance III 1.9mm probe; ¹H – ¹H NOESY, ¹H – ¹H BABA, ¹H One Pulse (with deconvolution) were carried out on Bruker 700 MHz Advance III 1.3mm probe.

6.2.3 Calorimetric Characterization

Differential Scanning Calorimetry (DSC) was performed on TA Instruments DSC Q10 with powdered samples crimped in an aluminium pan. Thermogravimetric analysis (TGA) was done on TA Instruments Q500 with powdered samples placed in an alumina crucible. The crucible is then placed on a platinum pan.

6.2.4 Steady state absorption and photoluminescence

Variable temperature absorption was measured on a PerkinElmer Lambda 1050 with the Linkam stage purged with N₂ as the temperature controller stage. Powdered samples were placed in a BaSO₄ filled crucible and the absorption spectra are referenced against pure BaSO₄. Variable temperature photoluminescence was carried out on a Horiba

Fluorolog Spectrophotometer. Samples were mounted onto sticky carbon tape in an Oxford system cryostat evacuated to 4×10^{-4} mbar. Excitation wavelengths was set at 290 nm, while the second order effects arising from the monochromator are filtered off with a Schott WG-320nm long pass filter.

6.2.5 Theoretical analysis through Density Functional Theory

Similar to Chapter 5, Density Functional Theory calculations were performed on the experimentally determined structures to obtain the electronic structure of the imidazole-based hybrid materials using the CASTEP plane-wave pseudopotential code. The PBE parameterisation of the Generalised Gradient Approximation (GGA) and the rSCAN meta-GGA exchange-correlation functionals were implemented in this study. In these calculations, a 800 eV plane-wave cutoff was used and the Brillouin zone was sampled using Monkhorst-Pack k-point grids at a spacing of 0.03 \AA^{-1} or less. On-the-fly generated ultrasoft pseudopotentials were employed throughout, which included scalar-relativistic effects approximated by the Koelling-Harmon scheme. Band structure calculations including spin-orbit coupling were also performed employing the PBE functional and norm-conserving pseudopotentials. All dispersion interactions were approximated using the many-body dispersion scheme. Starting from the single crystal X-ray determined structures, the atomic coordinates and the lattice parameters using the PBE and rSCAN functionals were relaxed to tolerances of 0.05 eV/\AA for forces and 0.05 GPa for stresses. In the cases where the X-ray results indicated partial occupancies of the atomic sites associated with the imidazolium cations, initial structures with randomly oriented imidazolium cations were generated which were subsequently relaxed. The band structure calculations were performed on the relaxed structures, and the resulting total, partial and joint density of states were computed using the OptaDOS program. The calculation of the NMR parameters was undertaken using the gauge-including projector augmented wave (GIPAW) approach on the rSCAN relaxed structures.

6.3 Results and Discussion

6.3.1 New proposed notation for haloplumbate structures or ‘perovskitoid’

The results of the single crystal XRD and the key parameters of the three polymorphic of imidazolium lead bromides are presented in Table 6.1 and the projections of each polymorph are shown in Fig 6.1. Given the significance of polymorphism and ‘perovskitoid’ structures discussed in this chapter, their nomenclature need close examination. In the studies of oxide perovskites, a wide variety of polymorphism and polytypism has been examined. The conventions utilized naming in oxide perovskites are easily applicable to the ‘perovskitoid’ structures in 3D structures using the modified Gard notation⁷ or Ramsdell notation⁸, or in layered 2D perovskite structures by the specific names (Ruddlesden-popper, etc) or by the direction of the layers. However, in the area of 1D and 1D-like perovskites, an agreed classification system is currently sorely lacking, and the definition of ‘perovskitoids’ has expanded from materials containing only face-sharing lead halide octahedra⁹ to include structures with both face and edge sharing octahedra.¹⁰

Therefore, when considering these 1D ‘perovskitoids’ structures, three main parameters are required to describe the structural connectivity of ‘perovskitoids’. These could be used to produce a new way to describe 1D perovskite structures. However, it should be noted that while this proposed notation can also be applicable to 2D and 3D structures, it would take on a rather awkward form, and hence, where applicable, the more established Ramsdell or modified Gard notation should continue to be utilized for such materials.

Firstly, the main parameter to consider is the number of octahedra per layer. If there is more than one octahedron per layer, the intra-layer connectivity would also have to be defined in parentheses. Special considerations, for example cyclic connectivity should also include in this section if it arises from the intra-layer connectivity. The octahedra connectivity type should be specified as follow: F for face-sharing, E for edge-sharing and C for corner-sharing. It should be noted that corner sharing would typically be interlayer rather intralayer connectivity.

The second parameter would be the number of octahedral layers required for the stacking or connectivity sequence to repeat itself. If there are more than one octahedron layer for the stacking sequence to repeat, the interlayer connectivity type should be

specified: F for face-sharing, E for edge-sharing and C for corner-sharing. Although it is obvious that if there are N number of connected octahedral, there would be $(N - 1)$ connectivity, both the number and connectivity type should not be dropped because they provide a facile method for communication of the stacking sequence. The last parameter pertains to the connectivity to the repeating sequence, with again F, E, C for face, edge, and corner sharing respectively, or X, for no connectivity. Although a material having no connectivity would strictly speaking not be a 1D ‘perovskitoid’, such a framework would also help to describe similar systems for easy comparison. To narrow down the periodicity effect of the notation, the convention would be taken such that corner sharing would take a priority over edge sharing over face sharing over no connectivity, i.e. $C > E > F > X$. Thus, it is recommended that the naming first follows the connectivity pattern in the unit cell, then shift the “origin” to the type with the highest priority.

Hence, this proposed naming convention, also called the reduced notation, is separated into three parts, each defining the afore-mentioned parameters. It would take a general form of (number, intralayer connectivity if any) – (number, interlayer connectivity). A list of examples are as follows:

For $\text{API}_2\text{Pb}_3\text{Br}_{10}$, which was studied in the previous chapter and first seen in Fig 5.1 a and also in Fig 6.1 a, there is one octahedron per layer, and therefore no intra-layer connectivity. There are three octahedra which are connected in the order of face-edge-face (FEF) within the unit cell. Thus, shifting the “origin” such that E take a priority over F, we would have a repeat unit of (EFF). The three-octahedra repeating unit are then connected to the next repeating unit by an edge-sharing octahedron. Therefore, $\text{API}_2\text{Pb}_3\text{Br}_{10}$ would be called 1-3FEE.

In $\text{IMI}_2\text{PbBr}_4$, as seen in Fig 6.1 b, there are two octahedra per layer which are edge connected. It has only one stacking sequence (i.e. no change in stacking sequence) and is connected to the next layer through a corner shared octahedra. Hence, $\text{IMI}_2\text{PbBr}_4$ would be 2EE-1(CC).

For $\text{IMI}_3\text{PbBr}_5$, which is a true 1D perovskite as seen in Fig 6.1 c, there is only one octahedron per repeating unit, which are corner shared to form a 1D chain. Therefore,

IMI₃PbBr₅ would be 1-1C.

In other well-known materials, such as in 1-(ethyl)pyridin-1-ium bromide,¹¹ 1-benzylpyridin-1-ium iodide,¹¹ catena-(2-methylimidazo[1,5-a]pyridin-2-ium tris(μ -bromo)-lead)¹², and imidazolium lead iodide¹³, the structure has one octahedron per layer, and it has two octahedra per repeating unit which are connected through face sharing. Each unit is then connected to the next repeating unit through face sharing. Hence, such structure would be given the notation 1-2FF.

As mentioned above, the use of this notation should be used primarily for 1D ‘perovskitoids’ particularly because when used for a 3D structure, it would take on an awkward form. For example, a 4H polytype would take a notation of 1-4(CCC)F(CCC)F. Similarly, it is also seen that when this terminology is used in a macromolecular 1D nanotube, as in (HMTA)₃PbBr₇ which can be seen in Fig 6.1 e, f, it also becomes awkward. In (HMTA)₃PbBr₇, there are six octahedra in one layer, and the octahedron face-shared to give three face-shared dimers per layer. The repeating unit has two layers and the two layers are related by a 6₁ screw axis and connected at the edge to form a rugged ring. Since the cyclic connectivity forms only across two layers, the square parenthesis is done across the first and second section. Lastly, the repeating unit connects to the next repeating unit through a 6₁-screw axis, all of which are corner shared. Thus, (HMTA)₃PbBr₇ would have the notation Cyclo[6(2CFC)-2(6₁CCCCCCC)]- 6₁CCCCCCC.

This proposed naming nomenclature would help to improve the clarity in the field of 1D hybrid perovskites where it would be more meaningful to make comparison of connectivity types which would sometimes be cluttered by intra or inter layer connectivity, especially when a cross system comparison is done.

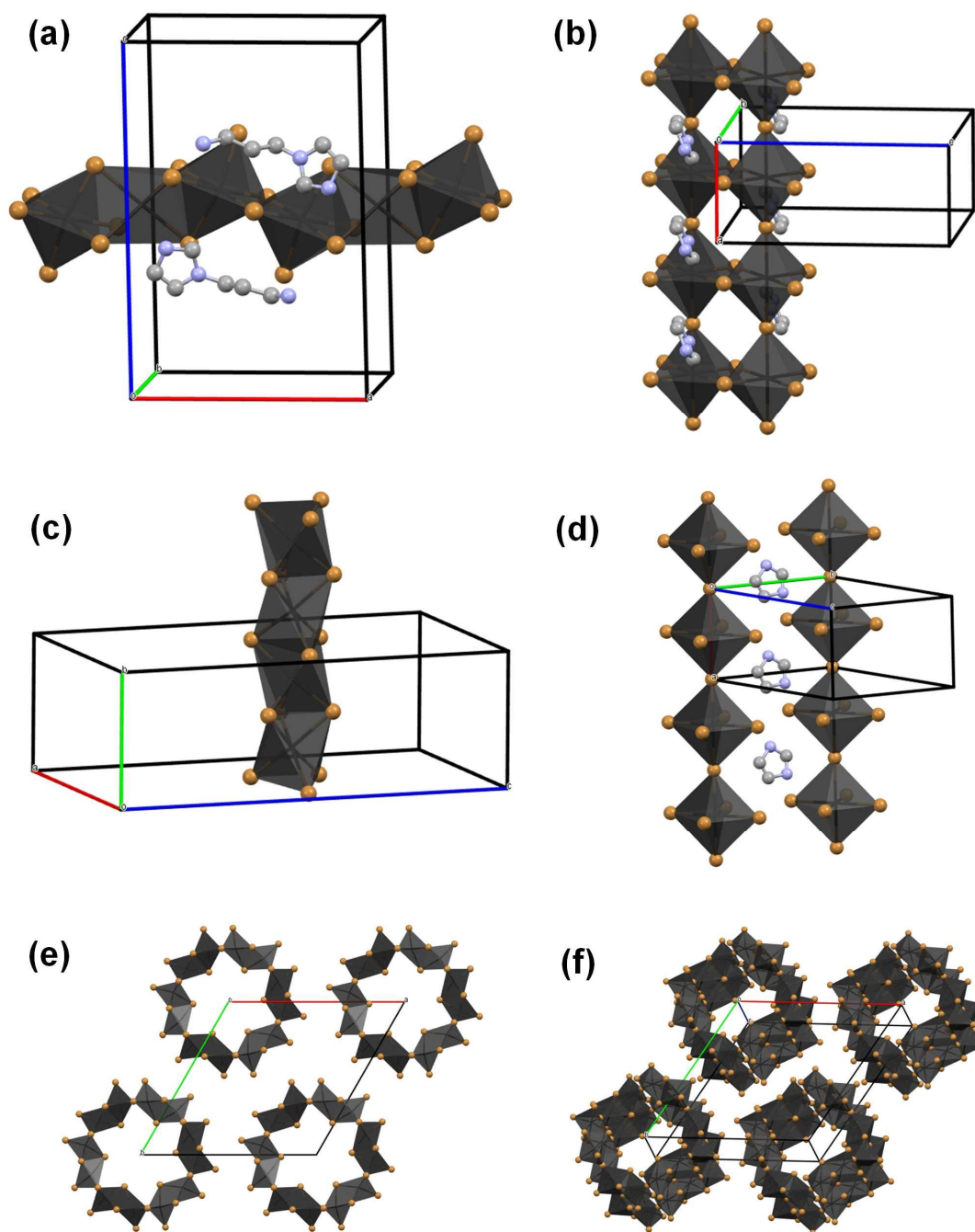


Figure 6.1 Crystal structure of (a) $\text{API}_2\text{Pb}_3\text{Br}_{10}$ which can be seen to be in the 1-3EFF configuration, (b) $\text{IMI}_2\text{PbBr}_4$ which can be seen to be in the 2EE-1(CC) configuration, (c) catena-(2-methylimidazo[1,5-a]pyridin-2-ium tris(μ -bromo)-lead)¹² which can be seen to be in the 1-2FF configuration, (d) $\text{IMI}_3\text{PbBr}_5$ which can be seen to be in the 1-1C configuration, (e-f) the configuration of 1D tubular structure of $(\text{HMTA})\text{PbBr}_4$ ¹⁴. In this case the notation breaks down into an awkward form and this proposed notation should not be used.

6.3.2 X-ray Structural Characterization of imidazolium lead bromide

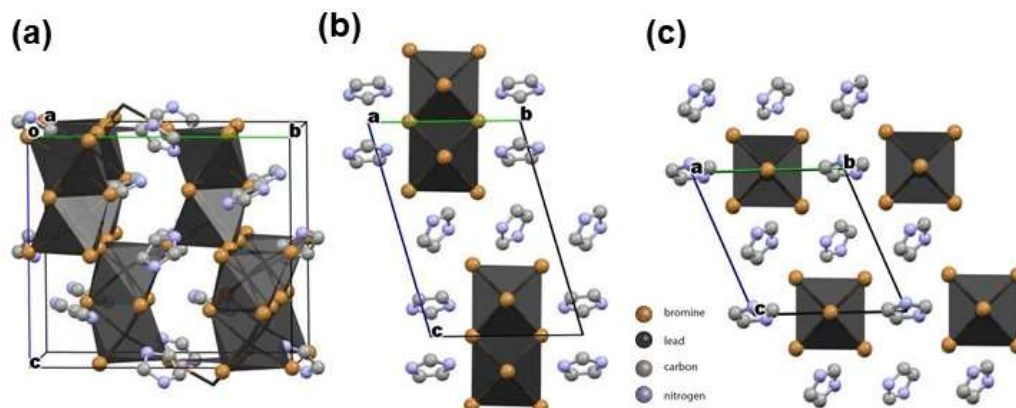


Figure 6.2 Crystal structure of the three imidazole lead bromide polymorphs, (a) IMIPbBr₃ in the room temperature *Cmc m* phase (b) IMI₂PbBr₄ in *P* $\bar{1}$, and (c) IMI₃PbBr₅ in *P* $\bar{1}$

IMIPbBr₃ exhibits a structure which closely resembles a 4H polytype, which has 4 distinct layers and appears to take on a hexagonal structure. Calorimetric studies agree with scXRD results which shows three distinct phases between room temperature and 180 K. While another phase transition cannot be ruled out, cryogenic temperatures are at the experimental limits of DSC and furthermore, IMIPbBr₃ crystals always fracture catastrophically below 150 K.

At room temperature, the structure of IMIPbBr₃ is considerably different from that of imidazole lead iodide counterpart^{15, 16} but closely resembles a hexagonal 4H polymorph. However, a detailed inspection of the powder XRD pattern, as shown in Fig 6.2, reveals that the structure is likely to be orthorhombic, instead of the hexagonal structure. Although single crystal XRD refinement shows that *P*6₃/*mmc* and *Cmc m* are both likely solutions, giving *R*₁ values of 0.0351 and 0.0273 respectively, and PLATON flags the “missing symmetry” to be considered in the *Cmc m* solution, powder XRD Rietveld refinements, seen in Fig 6.2, provide conclusive evidence that *Cmc m* is the better solution. While it is beyond the scope of this work, further experimental observations, such as by polarization microscopy, might be utilized to further confirm the symmetry point group. While at first glance, this difference may seem insignificant, there are some major implications in whether this material has a hexagonal or an orthorhombic crystal structure, such as significantly different optical and electronic properties. Particularly in the optical properties, the polarization is isotropic down the hexagonal *c*–axis but is

anisotropic when viewed down the a – and b –axes. In an orthorhombic structure, the polarization would be unique down all three a –, b – and c –axes. Hence, from a simplified, but relevant analysis, any misassignment will affect further work based on the structure, including DFT calculations.

Table 6.1: Selected parameters to the solution and refinement of scXRD results

Sample name	IMIPbBr ₃ (network)	IMIPbBr ₃ (network)	IMIPbBr ₃ (network)	IMI ₂ PbBr ₄ (ladder)	IMI ₃ PbBr ₅ (needle)
Empirical formula	C ₆ H ₁₀ N ₄ Br ₆ Pb ₂	C ₁₂ H ₂₀ N ₈ Br ₁₂ Pb ₄	C ₆ H ₁₀ N ₄ Br ₆ Pb ₂	C ₆ H ₁₀ N ₄ Br ₄ Pb	C ₉ H ₁₅ N ₆ Br ₅ Pb
Formula wt	1032.02	2064.04	1032.02	665.01	814.01
Temp (K)	298(2)	220(2)	180(2)	50(2)	200(2)
Crystal system	orthorhombic	orthorhombic	orthorhombic	triclinic	triclinic
Space group	<i>Cmcm</i>	<i>P2₁2₁2₁</i>	<i>Pnma</i>	<i>P</i> $\bar{1}$	<i>P</i> $\bar{1}$
unit cell dimension					
a (Å)	9.0938(5)	9.1272(3)	14.2082(6)	5.9868(1)	6.0272(6)
b (Å)	15.7372(10)	13.8052(5)	14.9482(6)	9.4085(3)	9.3862(9)
c (Å)	13.8445(6)	31.072(1)	8.8811(3)	13.3434(4)	9.5844(12)
α (°)	90	90	90	73.891(3)	67.468(10)
β (°)	90	90	90	86.227(2)	86.205(9)
γ (°)	90	90	90	86.828(2)	87.980(8)
Volume (Å ³)	1981.30(19)	3915.2(3)	1886.2(1)	719.98(4)	499.70(10)
Z	4	4	4	2	1
ρ_{calc} (g cm ³)	3.46	3.502	3.634	3.068	2.705
μ (mm ⁻¹)	29.062	29.414	30.527	22.793	18.437
$F(000)$	1792	3584	1792.0	592	368
Crystal size (mm ³)	0.279 × 0.203 × 0.198	0.15 × 0.106 × 0.063	0.156 × 0.105 × 0.071	0.19 × 0.071 × 0.048	0.245 × 0.215 × 0.061
2 Θ range (°)	7.84 to 54.93	4.652 to 61.014	7.346 to 65.26	6.194 to 77.002	7.74 to 51.364
Index ranges	-11 ≤ h ≤ 11 -20 ≤ k ≤ 20 -17 ≤ l ≤ 17	-13 ≤ h ≤ 8 -19 ≤ k ≤ 19 -44 ≤ l ≤ 35	-14 ≤ h ≤ 20 -19 ≤ k ≤ 22 -12 ≤ l ≤ 9	-10 ≤ h ≤ 10 -16 ≤ k ≤ 16 -22 ≤ l ≤ 22	-7 ≤ h ≤ 7 -11 ≤ k ≤ 11 -11 ≤ l ≤ 11
Refln collected	8468	23461	10531	34117	3136
Refinement mtd		<i>full-matrix least squares on F^2</i>			
Indep reflns	1223 $R_{\text{int}} = 0.0453$, $R_{\text{sigma}} = 0.0228$	11719 $R_{\text{int}} = 0.0550$, $R_{\text{sigma}} = 0.0924$	3283 $R_{\text{int}} = 0.0401$, $R_{\text{sigma}} = 0.0428$	7672 $R_{\text{int}} = 0.0496$, $R_{\text{sigma}} = 0.0414$	3136 $R_{\text{sigma}} = 0.0614$
Data/restraints/param	1223/60/99	11719/120/290	3283/79/103	7672/0/136	3135/30/113
GoF on F^2	1.159	1.004	1.084	1.094	1.000
Final R indexes [$I \geq 2\sigma(I)$]	$R_1 = 0.0273$, $wR_2 = 0.0695$	$R_1 = 0.0505$, $wR_2 = 0.0855$	$R_1 = 0.0304$, $wR_2 = 0.0590$	$R_1 = 0.0284$, $wR_2 = 0.0540$	$R_1 = 0.0410$, $wR_2 = 0.0949$
Final R indexes [all data]	$R_1 = 0.0337$, $wR_2 = 0.0723$	$R_1 = 0.0916$, $wR_2 = 0.0994$	$R_1 = 0.0443$, $wR_2 = 0.0629$	$R_1 = 0.0369$, $wR_2 = 0.0563$	$R_1 = 0.0582$, $wR_2 = 0.0999$
Fourier diff max and min (e Å ⁻³)	0.91/-0.60	1.84 and -1.57	1.58 and -1.43	2.55 and -2.20	1.44/-1.20
Flack parameter	-	Racemic mixture	-	-	-

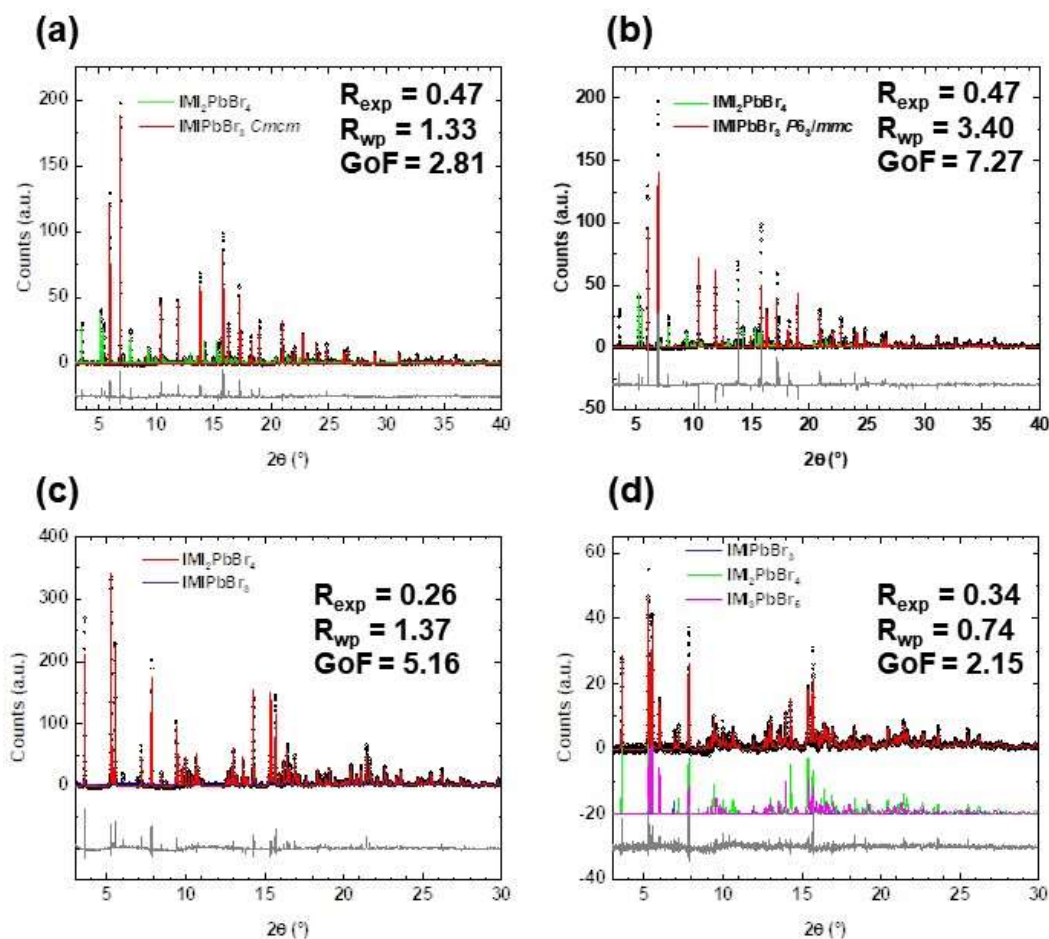


Figure 6.3 Rietveld refinements of the samples (a) IMIPbBr₃ fitted to the *Cmcm* space group, (b) IMIPbBr₃ fitted to the *P6₃/mmc* space group. The difference in the R_{wp} and overall fitting, particularly between 13° and 20° showed that IMIPbBr₃ would take on the orthorhombic *Cmcm* space group. The presence of contaminant IMIPbBr₄ phase is shown in the green curve (c) Rietveld refinement of 98% IMI₂PbBr₄ with 2% of IMIPbBr₃ contaminant, and (d) Rietveld refinement of the bulk synthesized IMI₃PbBr₅. Refinement results showed the bulk sample consist of approximately 0.2% of IMIPbBr₃, 37% IMI₂PbBr₄, and 63% IMI₃PbBr₅.

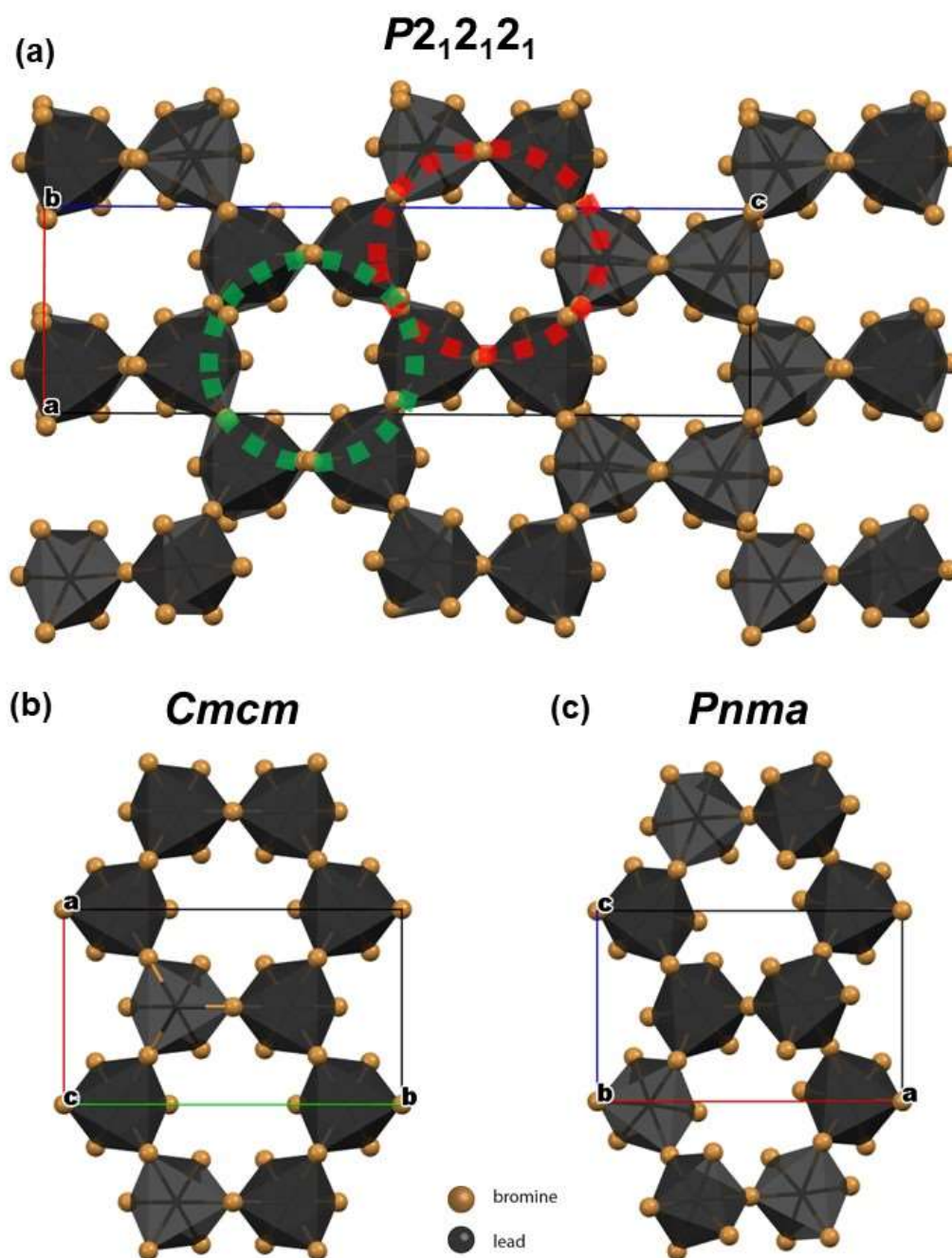


Figure 6.4 Comparison of IMIPbBr₃ phases, with the organic imidazole cation hidden for clarity. (a) shows the intermediate $P2_12_12_1$ superstructure through the doubling of the c-axis. A slight modulation of the octahedra connectivity can be seen, as highlighted by the red and green dotted circles. Such behaviour is neither seen in (b) the higher temperature $Cmcm$ phase nor in (c) the lower temperature $Pnma$ phase. Note the change in axis orientation to match crystallographic convention.

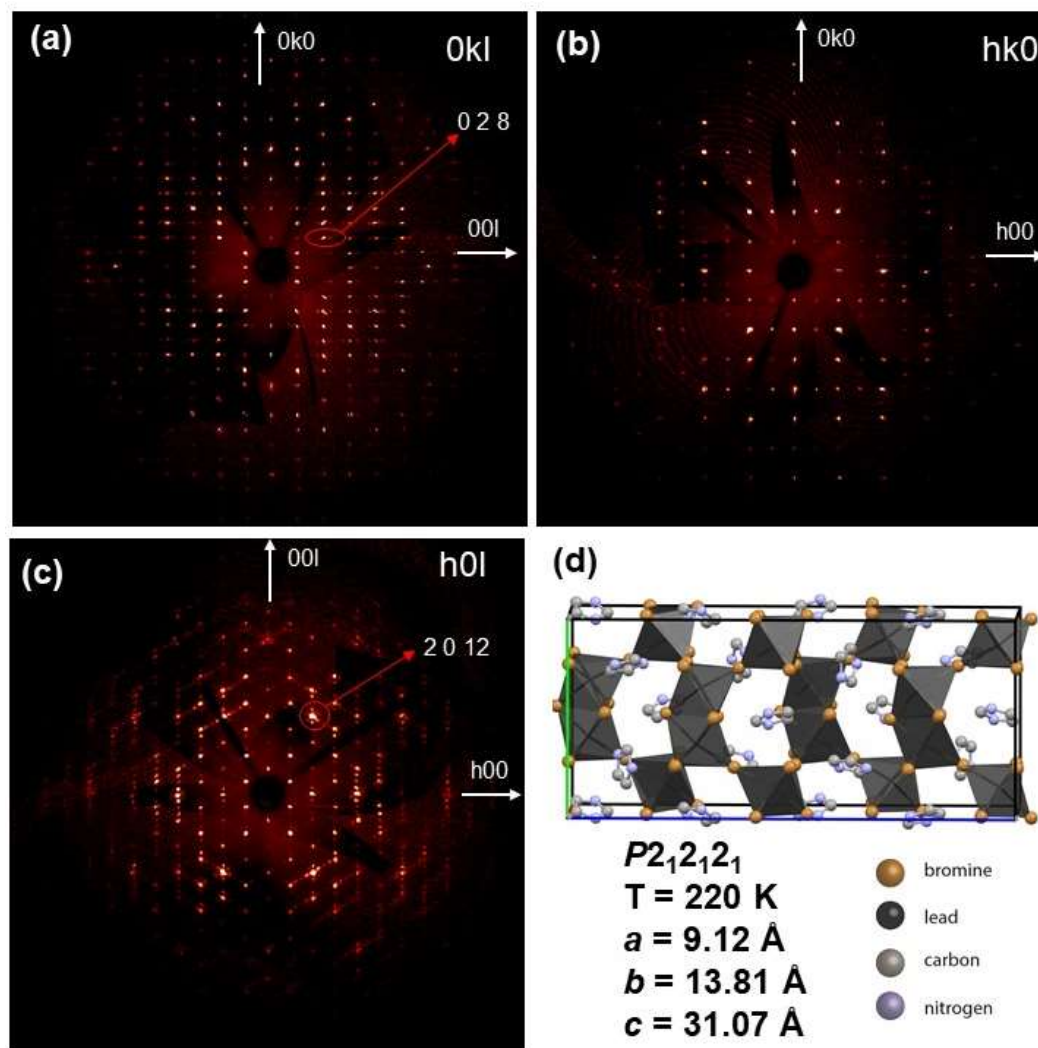


Figure 6.5 Simulated precession image of IMIPbBr₃ in the $P2_12_12_1$ phase showing (a) reflections from $0kl$. Weak satellite peaks can be observed in several $(0\ 2\ l)$ planes (b) reflections of $hk0$ showing no satellite peaks (c) reflections on the $h0l$ showing a threefold twinning and satellite peak on several reflection such as $(2\ 0\ 12)$ (d) projection of the superstructure IMIPbBr₃ down the a -axis.

As the temperature decreases, IMIPbBr₃ undergoes a phase transition which takes on a superstructure and is also typically accompanied by a three-fold twinning. The superstructure can be immediately seen by the doubling of the $Cmcm$ b -axis from 15.7 Å to 31.1 Å in the $P2_12_12_1$ phase and from the precession image of the XRD scan in Fig 6.4, which shows the presence of a main peak, accompanied by satellites. Furthermore, from Fig 6.4 (c), a threefold twinning can be observed on top of the structural modulation. Structurally, a very slight modulation on the cavity can be seen

in Fig 6.3 (a), where there are two very subtly different connectivity of the lead bromide octahedra. Further cooling of IMIPbBr₃ would cause a phase transition to the *Pnma* phase. Here, the system returns to ‘normal’ structure where the lattice parameters decrease which is consistent with decreasing temperature. When the *P2₁2₁2₁* structure is compared against the higher temperature *Cmcm* phase, as in Fig 6.3 (b), or against the lower temperature *Pnma* phase, as in Fig 6.3 (c), it can be seen that neither the *Cmcm* nor *Pnma* phase shows the unique behaviour of the modulation of octahedra connectivity.

When the phase transition is examined more closely and taking a symmetry perspective, a transition from *Cmcm* to *P2₁2₁2₁* to *Pnma* is not allowed from a group-subgroup relation. However, a transition from *Cmcm* to *P2₁2₁2₁* via *Pnma* is allowed, with an index of 4 as shown in Fig 6.5 (f). This agrees with *P2₁2₁2₁* being an intermediate phase as has also been observed with sodium-potassium niobate solid solution system by Ahtee and Glazer¹⁷. In the Na_{0.98}K_{0.2}NbO₃ system, the intermediary phase *G* only exists over a narrow 50 K range, and similarly, in IMIPbBr₃, the intermediary *P2₁2₁2₁* phase, as seen on DSC in Fig 6.5 (e), exists in a temperature range of around 40 K.

From a structural perspective, it is likely that the phase transition involves the gradual ordering of the imidazole A-site cation. In the asymmetric unit cell at room temperature (*Cmcm*), there are two imidazole rings, and is likely to be spinning in plane, like a turntable. With a decrease in temperature, one of the imidazole gains partial ordering, and hence takes on a superstructure. With even greater cooling, this partially ordered imidazole then becomes fully ordered while the other imidazole remains disordered and continues spinning in-plane. Hence, another phase transition is expected to occur, but this cannot be observed experimentally because the crystal always fractures catastrophically.

The phase transition would also be expected to be observed through powder XRD, and the diffraction results are shown in Fig 6.5 (a) for decreasing the temperature from room temperature to 100 K and (b) for warming the sample from 100 K to room temperature. Detailed analysis showed that only the transition from *Cmcm* to *P2₁2₁2₁* is observed but IMIPbBr₃ remains in the *P2₁2₁2₁* phase even when cooled to 100 K, even though the phase transition temperature as recorded and observed through DSC and single crystal

XRD is at 180 K. However, upon heating back from 100 K to room temperature, the diffraction pattern and refinement details showed that IMIPbBr_3 still remains in the $P2_12_12_1$ phase. Due to the presence of an impurity $\text{IMI}_2\text{PbBr}_4$ the unit cell volume is seen to increase gradually with increasing temperature and there was no sudden changes in either the diffractogram or refinement parameters. Similarly, Rietveld refinements of the $P2_12_12_1$ phase, as seen in Fig 6.5 (d), shows a gradual increase of R_{wp} with increasing temperature and an increasing unit cell volume with increasing temperature. This all indicates that instrumental temperature control effects or artefacts from the radiation source can be ruled out. Hence, this would therefore indicate that the sample either has degraded upon exposure to radiation or has undergone an irreversible phase transition, which showed very close resemblance to a $P2_12_12_1$ symmetry, or both. Time did not permit the study of this phenomenon in greater details.

For the second polymorph, $\text{IMI}_2\text{PbBr}_4$, each repeating unit has two lead halide octahedra connected through an edge, with only one stacking sequence, and linked between the layers through corner sharing only. It would therefore take on the notation of 2E-1-C, as discussed in the earlier section. From a structural perspective, this polymorph does not exhibit any phase transition, even when cooled to extreme temperatures or heated to degradation.

In the third polymorph $\text{IMI}_3\text{PbBr}_5$, the structural configuration is similar to that in $\text{IMI}_2\text{PbBr}_4$, but in this structure would be a true 1D perovskite, taking the notation of 1-1-C. Similar to $\text{IMI}_2\text{PbBr}_4$, it also does not exhibit any phase transition even when taken to cryogenic temperatures.

It is interesting to note that such polymorphism is only a function of the initial imidazole to lead concentration, where the highest imidazole to lead concentration (4:1 molar ratio) yields $\text{IMI}_3\text{PbBr}_5$, and the impurity $\text{IMI}_2\text{PbBr}_4$, and the lowest (1:1 molar ratio) produces IMIPbBr_3 , and the impurity $\text{IMI}_2\text{PbBr}_4$. Hence, this gives an indication that the chemistry of the A-site cation should not be overlooked. Imidazolium cations are known to take on different resonance structures¹⁶ and this might contribute greatly to the polymorphism. Furthermore, the Goldschmidt tolerance factor should also be examined closely. During the formulation of the semi-empirical Goldschmidt tolerance factor, it was largely applied to oxide perovskites where the approximation of A-site

cations being spheres is valid. However, in the field of hybrid perovskites, the versatility of the A-site cation has shown to be the origin of many structural engineering effects where the Goldschmidt tolerance factor is not directly applicable. Time did not permit the study of the origin of polymorphism, including whether it arises from chemical activity or structural geometry.

Physically, IMIPbBr₃ and IMI₂PbBr₄ were always produced from the precursor solution, with an imidazole to lead ratio of 1:1, in a ratio of approximately 60% IMIPbBr₃ and 40% IMI₂PbBr₄, as determined by powder XRD. Further attempts to isolate the systems into the individual phases through chemical means were not successful, and hence, the crystallized samples were separated under a polarizing microscope. Since IMIPbBr₃ and IMI₂PbBr₄ are in different crystal systems, orthorhombic for the former and triclinic for the latter, the crystals were first screened through their shapes and then through their response under polarized light. IMIPbBr₃ generally appears to be a triangular rod with corrugated edges while IMI₂PbBr₄ generally appear to be a flat block, but with non-perpendicular edges. The physical separation allowed further analysis to be carried out, by solid state NMR and optical characterization.

However, there are no discernible physical differences between IMI₂PbBr₄ and IMI₃PbBr₅. This is largely because these two polymorphs are both in the triclinic phase and form very similar flat blocks with non-perpendicular edges. Even their responses to polarized light are indistinguishable to the eye. The only noticeable difference is the brittleness of the crystals, wherein some (probably IMI₃PbBr₅) crystals seemed to be subtly more brittle and cleave with lesser force being applied, but even so, this is not a definitive way of differentiating the crystals and being destructive, cannot be used for their physical separation. From powder XRD analysis, the bulk sample contains approximately 37% IMI₂PbBr₄ and 63% IMI₃PbBr₅. Hence, further analysis must be carried out on a physical mixture of IMI₂PbBr₄ and IMI₃PbBr₅, and the contributions from IMI₂PbBr₄ then subtracted from the bulk sample to obtain an approximation for the spectral results from pure IMI₃PbBr₅. Although inadequate, under these conditions this is the best that can be achieved.

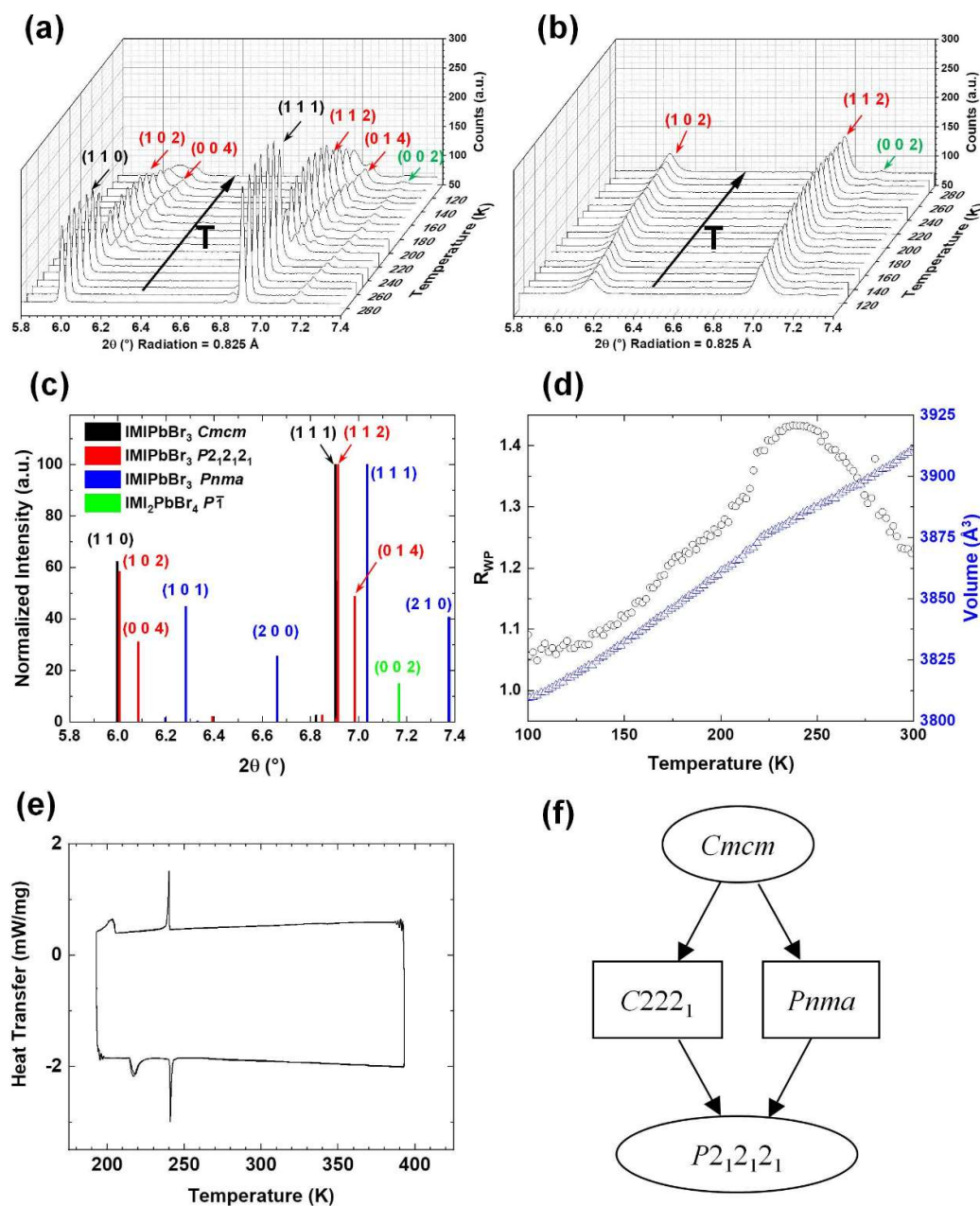


Figure 6.6 (a) powder XRD pattern of IMIPbBr₃ from 300 K to 100 K, in steps of 10 K for clarity. The pattern shows a clear transition at around 220 K. (b) powder XRD pattern from 100 K to 300 K, in steps of 10 K for clarity, but the diffractogram shows that IMIPbBr₃ does not undergo any phase transition. The hkl indices of the respective phases are labelled with black (*Cmcm* IMIPbBr₃) red (*P2₁2₁2₁* IMIPbBr₃) and green (IMI₂PbBr₄). (c) the theoretical XRD pattern of the various phases of IMIPbBr₃ as predicted from the single crystal XRD results. The inclusion of the contaminant IMI₂PbBr₄ shows the presence of a peak at 7.18° and is observed in the experimental XRD plots (d) the plot of refinement R_{wp} against temperature showing the stability of the sequential refinements. The plot of IMIPbBr₃ *P2₁2₁2₁* unit cell volume against temperature with increasing temperature shows that logical validity of the

refinement (e) differential scanning calorimetric study of IMIPbBr₃, showing a first phase transition between 236 K and 244 K and a second phase transition between 193 K and 225 K (f) Group subgroup relation, from *Cmcm* to *P2₁2₁2₁* with index 4. Since *P2₁2₁2₁* is a superstructure, it would have twice as large a *Z* value than the *Cmcm* phase. *D_{2h}*(mmm) would have order 8 while *D₂*(222) would have order 4.

6.3.3 Nuclear Magnetic Resonance Characterization

In the fully relaxed, and hence quantitative, ¹H spectra as seen in Fig 6.6, three main peaks can be observed in that of IMIPbBr₃, and four main peaks in those of IMI₂PbBr₄ and IMI₃PbBr₅. In the ¹³C spectra, it can be seen clearly that there are three peaks for IMIPbBr₃, four peaks for IMI₂PbBr₄ and three peaks for IMI₃PbBr₅. Since the MAS conditions and magnetic field are identical, the considerably narrower peak widths in ¹H spectra of IMIPbBr₃ compared to IMI₂PbBr₄ and IMI₃PbBr₅ indicates a more efficient averaging of the ¹H – ¹H dipolar interaction, and hence, indicates a more dynamic imidazolium cation. In the ²⁰⁷Pb spectra, a single peak is observed from all three polymorphs and agrees with the single Pb site seen in the asymmetric unit cell as determined from single crystal XRD.

Notably, in the spectra of IMIPbBr₃ and IMI₂PbBr₄ the peaks between 8 ppm and 10 ppm appear to be a split peak rather than two individual peaks. Concurrently, this effect is also seen in ¹³C spectra for the peaks between 130 ppm and 136 ppm of IMIPbBr₃ and IMI₂PbBr₄. Therefore, 2D heteronuclear and homonuclear correlation experiments were carried out to ascertain the identity of these peaks. Also, the integral of the ¹H peak centred around 11.5 ppm indicates that it could be a convolution of two peaks, could also be distinguished in 2D correlation experiments

In constructing the model from single crystal XRD results, an imidazole is placed in the cavity and can be seen to sit on a special positions, for example, cutting across a mirror plane for IMIPbBr₃ in *Cmcm* phase, or sitting on the inversion centre for IMI₃PbBr₅. Furthermore, the light carbon and nitrogen atoms are almost equally weak in scattering X-rays whose scattering has been dominated by the heavy atoms, lead and bromine, so in the hybrid perovskite, the accuracy of the imidazole position cannot be

ascertained. Therefore, to further provide conclusive evidence for the position of the imidazole, solid state NMR was carried out and where the NMR dynamics would provide an indication of the presence of disorder.

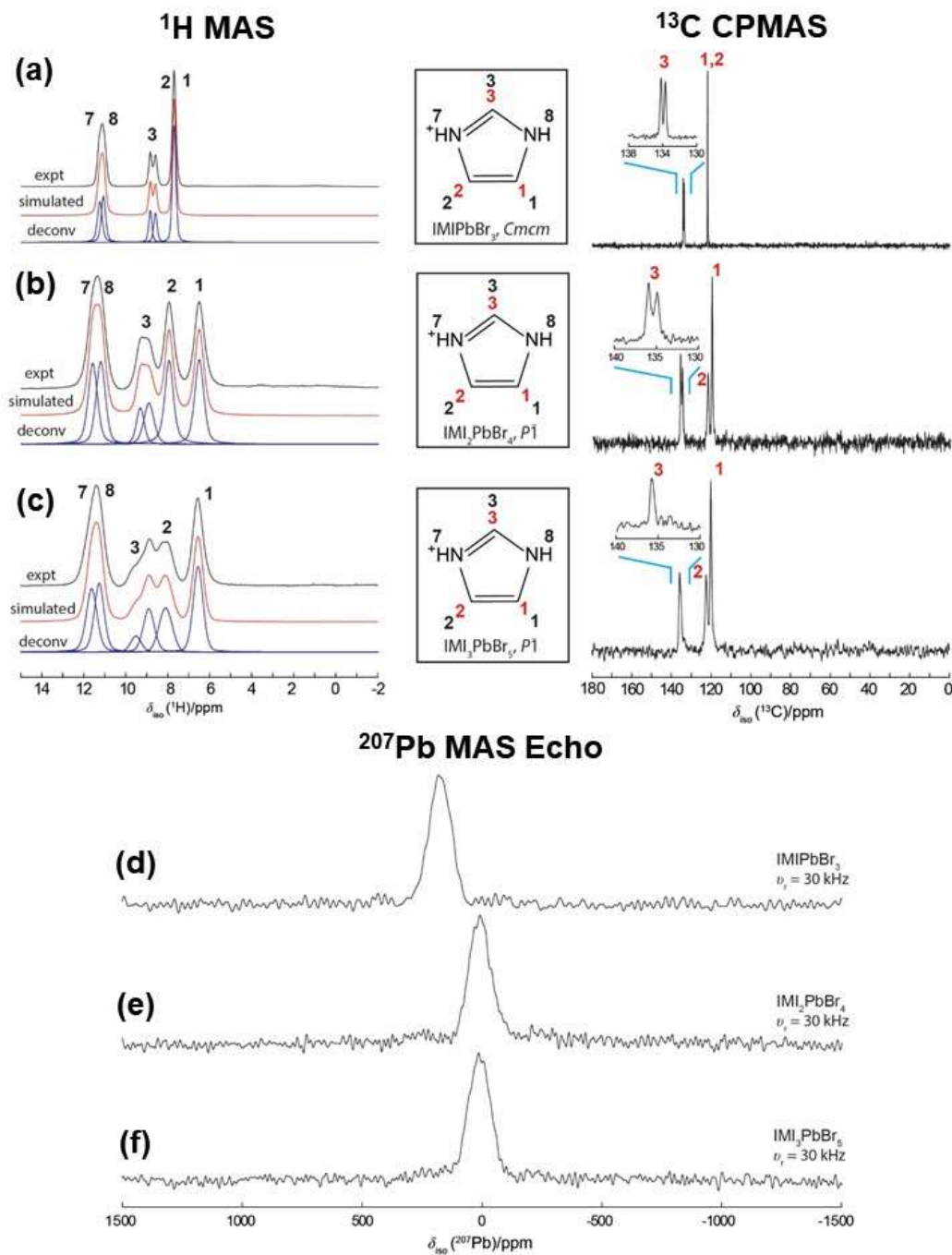


Figure 6.7 Multinuclear Solid State Nuclear Magnetic Resonance (SSNMR) studies of (a) IMIPbBr₃ (b) IMI₂PbBr₄ and (c) IMI₃PbBr₅, where ¹H spectra is shown on the left and ¹³C spectra on the right. In the ¹H spectra, the experimental spectra are fitted to the deconvolution of peaks, and the details are shown in Table 6.2. In the ¹³C spectra, the insert shows the zoomed

in section of each peak, which is split for IMIPbBr₃ and IMI₂PbBr₄. The ²⁰⁷Pb Hahn Echo spectra are seen for (d) IMIPbBr₃, (e) IMI₂PbBr₄ and (f) IMI₃PbBr₅. ¹H and ¹³C are referenced to alanine and ²⁰⁷Pb referenced to PbNO₃.

From the homonuclear NOESY experiments, as seen in Fig 6.7, the ¹H peak centred at 11.2 ppm is indeed a convolution of two peaks for all of the IMIPbBr₃, IMI₂PbBr₄ and IMI₃PbBr₅ systems. These peaks are therefore assigned to the two ¹Hs attached directly to nitrogen atom in the imidazole ring. For IMIPbBr₃, the lone peak at 7.7 ppm also has an integral corresponding to two ¹H atoms and the NOESY experiment indicated that this is a single site, indicating some form of chemical equivalence or exchange. Lastly, the integral of the double peak at 8.6 ppm and 8.7 ppm sums up to one ¹H atom and the consistent correlations of the integral for the other sites (e.g. ¹H-3 with ¹H-7 or ¹H-3 with ¹H-1,2) indicates that this is a peak splitting effect rather than from two independent sites. Similarly, the same can be said for the double peak between 9 ppm and 10 ppm in IMI₂PbBr₄, and is also consequently assigned to ¹H-3, while the double ¹³C peak between 130 ppm and 140 ppm is assigned to ¹³C-3.

The $T_{1\rho}$ relaxation dynamics of the individual ¹H are given in table 6.2 and variable field T_1 relaxation times are listed in table 6.3. The main difference between the two techniques revolves around the regime of motion of the nuclei. $T_{1\rho}$ are sensitive to motion in the kilohertz regime while T_1 are sensitive to motion in the megahertz to gigahertz regime. From table 6.2, ¹H $T_{1\rho}$ in IMIPbBr₃ is around 6 to 20 times greater than that in IMI₂PbBr₄ and is around 4 times greater than that in IMI₃PbBr₅. Looking at the variable field T_1 dynamics, a lower field would give a lower T_1 and follows a well-established trend observed by Bloembergen et al.¹⁸ and seen in Figure 2.X. Based on the interpretation of $T_{1\rho}$, it is likely that the long T_1 in IMI₂PbBr₄ and IMI₃PbBr₅ indicate that the relative motion of ¹H is much lower than IMIPbBr₃, as is the case to the right of the minimum point. Furthermore, from 2D homonuclear NOESY experiment as seen in Fig 6.7, 6.8 and 6.9, with the same contact time of 500 ms, there is a much lower correlation intensity in IMIPbBr₃ than in IMI₂PbBr₄ or IMI₃PbBr₅. Since NOE effect depends on the dipolar interaction between the ¹H atoms, the lower correlation indicates that the ¹H in IMI₂PbBr₄ and IMI₃PbBr₅ are likely to be more subdued, consistent with that observed in T_1 and $T_{1\rho}$.

Table 6.2 Table showing experimental and theoretically predicted values of the ^1H and ^{13}C chemical shifts based on XRD results, the relative intensities of each ^1H peak and the $T_{1\rho}$ results of each identity peak. Since ^{13}C CPMAS is carried out, the ^{13}C spectra do not provide any quantitation. The experimental deconvolution for ^1H is seen in Figure 6.6.

IMIPbBr ₃ (<i>Cmcm</i>)					IMI ₂ PbBr ₄ (<i>P1</i>)				IMI ₃ PbBr ₅ (<i>P1</i>)			
¹ H site	¹ H δ_{iso} Expt. /ppm	¹ H δ_{iso} Calc. DFT /ppm	Rel. Int. /% (\pm 1%)	$T_{1\rho}$ /ms	¹ H δ_{iso} Expt. /ppm	¹ H δ_{iso} Calc. DFT /ppm	Rel. Int. /% (\pm 1%)	$T_{1\rho}$ /ms	¹ H δ_{iso} Expt. /ppm	¹ H δ_{iso} Calc. DFT /ppm	Rel. Int. /% (\pm 1%)	$T_{1\rho}$ /ms
1	7.7	6.5	40.3	144	6.5	6.4	20.4	14	6.6	6.4		38
2	7.7	7.4			9.0	8.4	20.4	7.1	8.1	7.1		27
3	8.6/ 8.5 ^b 8.7/ 9.0 ^c	9.3	20.4	124	8.9/ 9.3 ^b 8.8/ 9.4 ^c	9.7	18.5	20	8.9/ 9.5 ^b 8.4/ 9.1 ^c	10.0		28
8	11.1	10.6	20.3	-	11.2	11.2	20.3	-	11.3	13.7	20.1	-
7	11.3	14.1	19.9	-	11.5	13.5	20.3	-	11.7	12.6	20.8	-
¹³ C site	¹³ C δ_{iso} Expt. /ppm	¹³ C δ_{iso} Calc. DFT /ppm			¹³ C δ_{iso} Expt. /ppm	¹³ C δ_{iso} Calc. DFT /ppm			¹³ C δ_{iso} Expt. /ppm	¹³ C δ_{iso} Calc. DFT /ppm		
1	121.9	120.1			120.0	121.5			120.0	109.8		
2	121.9	121.9			122.1	128.4			122.1	126.6		
3	133.7/ 134.2	135.1			134.9/ 135.9	130.8			134.9/ 135.9	139.2		

Table 6.3 Comparison of variable field T_1 for IMIPbBr₃, IMI₂PbBr₄ and IMI₃PbBr₅. The decreasing T_1 with decreasing magnetic field follows a well-established trend observed by Bloembergen et al.¹⁸

IMIPbBr ₃ (<i>Cmcm</i>)				IMI ₂ PbBr ₄ (<i>P1</i>)				IMI ₃ PbBr ₅ (<i>P1</i>)			
¹ H site	¹ H δ_{iso} Expt. /ppm	T_1 16.4T /s (± 2 s)	T_1 7.1T /s (± 2 s)	¹ H site	¹ H δ_{iso} Expt. /ppm	T_1 16.4T /s (± 5 s)	T_1 7.1T /s (± 3 s)	¹ H site	¹ H δ_{iso} Expt. /ppm	T_1 16.4T /s (± 5 s)	T_1 7.1T /s (± 3 s)
1,2	7.7	17.4	15.7	1	6.5	37.5	26.2	1	6.6	44.5	30
				2	9.0	37.8	26.4	2	8.1	39.3	31
	8.6/ 8.5 ^a 8.7/ 9.0 ^b	17.0	15.7	3	8.9/ 9.3 ^a 8.8/ 9.4 ^c	38.6	26.9	3	8.9/ 9.5 ^b 8.4/ 9.1 ^c	41.1	30
8	11.1	14.3	14.8	8	11.2	38.3	26.4	8	11.3	42.1	32
7	11.3	14.3	14.8	7	11.5	38.3	26.4	7	11.7	42.1	32

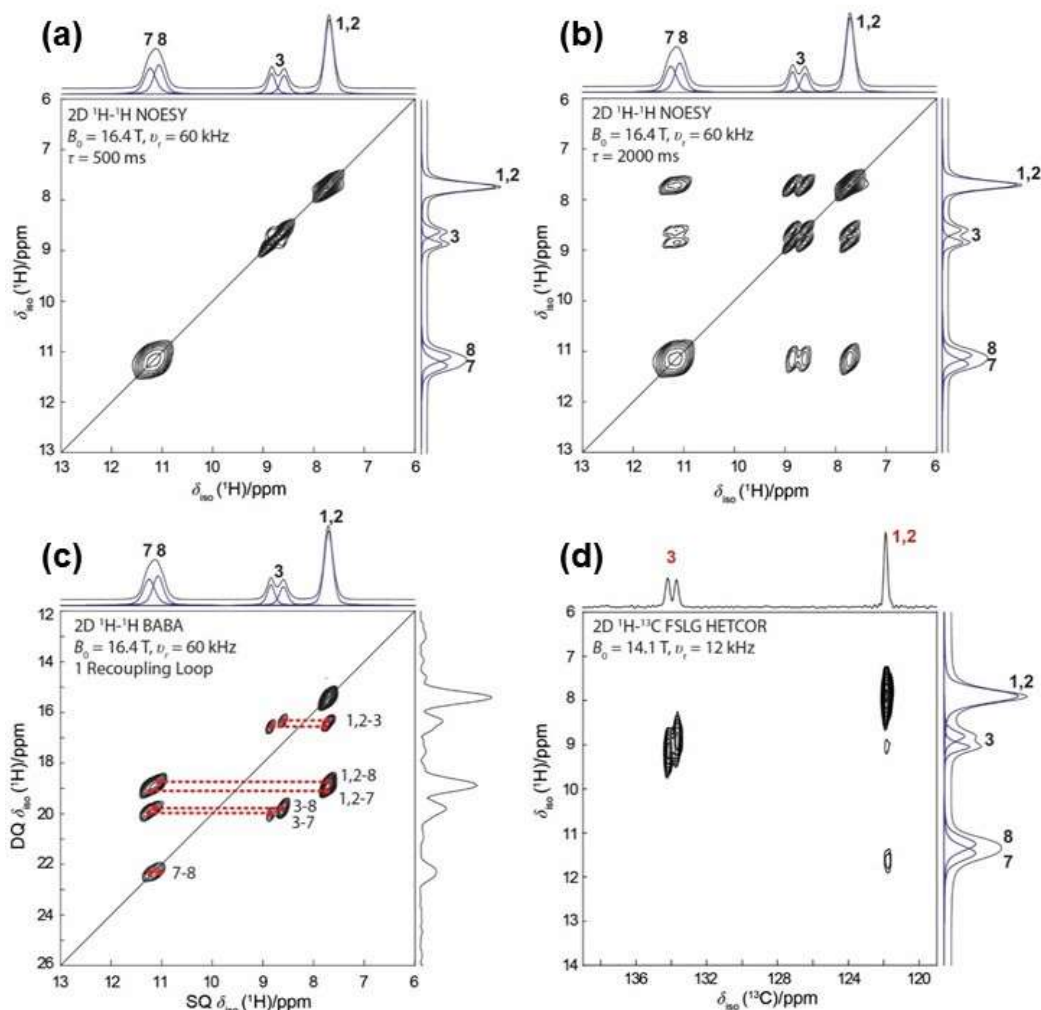


Figure 6.8 2D NMR correlation of IMIPbBr₃ (a) ¹H-¹H homonuclear NOESY, with a relatively short contact time of 500 ms, (b) NOESY with a relatively long contact time of 2000 ms. The NOESY results provide evidence for the presence of two peaks, ¹H-7 and ¹H-8, between 11 ppm and 12 ppm, while the peak, ¹H-3, is a split peak. (c) ¹H-¹H BABA homonuclear correlation boosts the confidence in peak assignment (d) The heteronuclear FSLG correlation shows a clear correlation for ¹H-1,2 with ¹³C-1,2 and ¹H-3 with ¹³C-3 and provides further evidence to support the assignments.

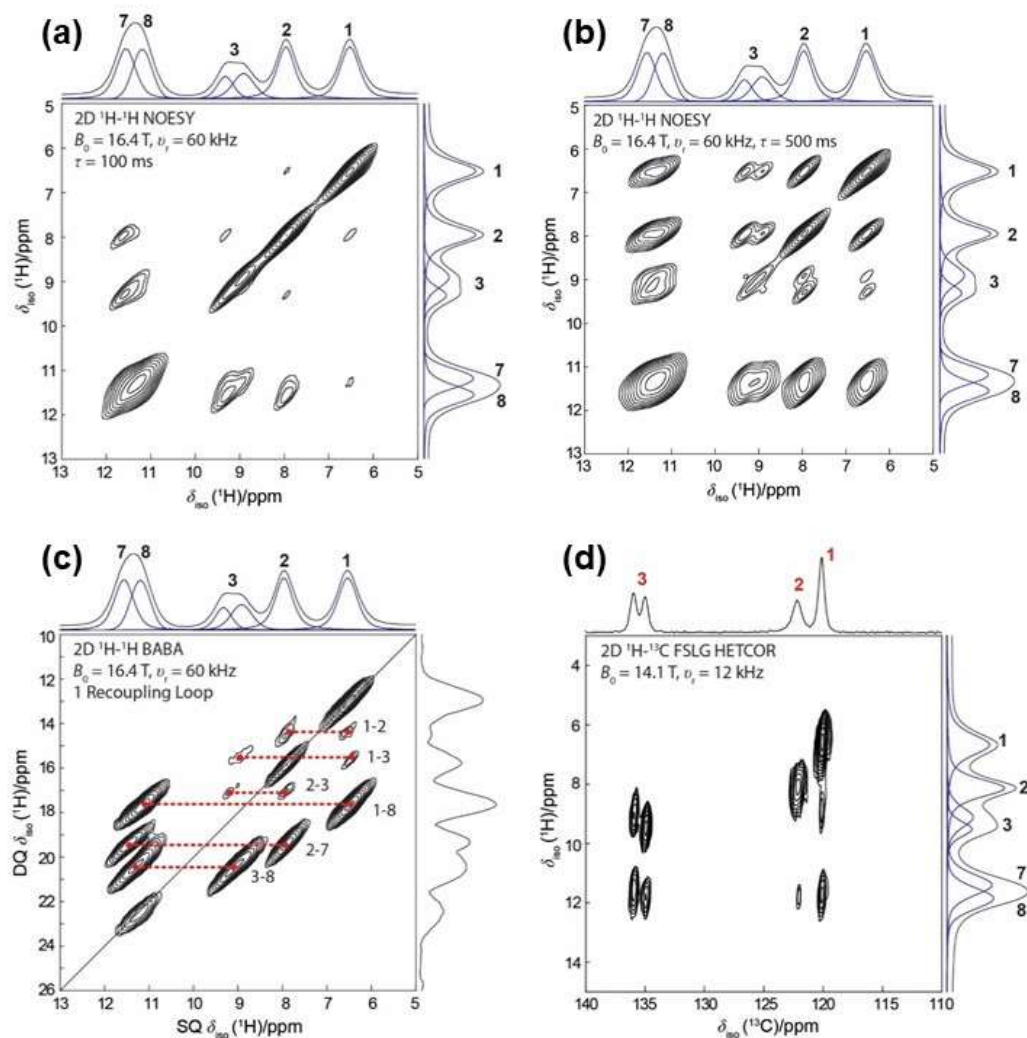


Figure 6.9 2D NMR correlation of IMI₂PbBr₄ (a) ¹H-¹H homonuclear NOESY, with a relatively short contact time of 100 ms, (b) NOESY with a relatively long contact time of 500 ms. The NOESY results provide evidence for the presence of two peaks, ¹H-7 and ¹H-8, between 11 ppm and 12 ppm, while the peak, ¹H-3, is a split peak. (c) ¹H-¹H BABA homonuclear correlation boosts the confidence in peak assignment (d) The heteronuclear FSLG correlation shows a clear correlation for ¹H-1 with ¹³C-1, ¹H-2 with ¹³C-2 and ¹H-3 with ¹³C-3. The correlation for ¹H-7 with ¹³C-3 and ¹H-8 with ¹³C-3 is not unexpected because of the close proximity of the atoms.

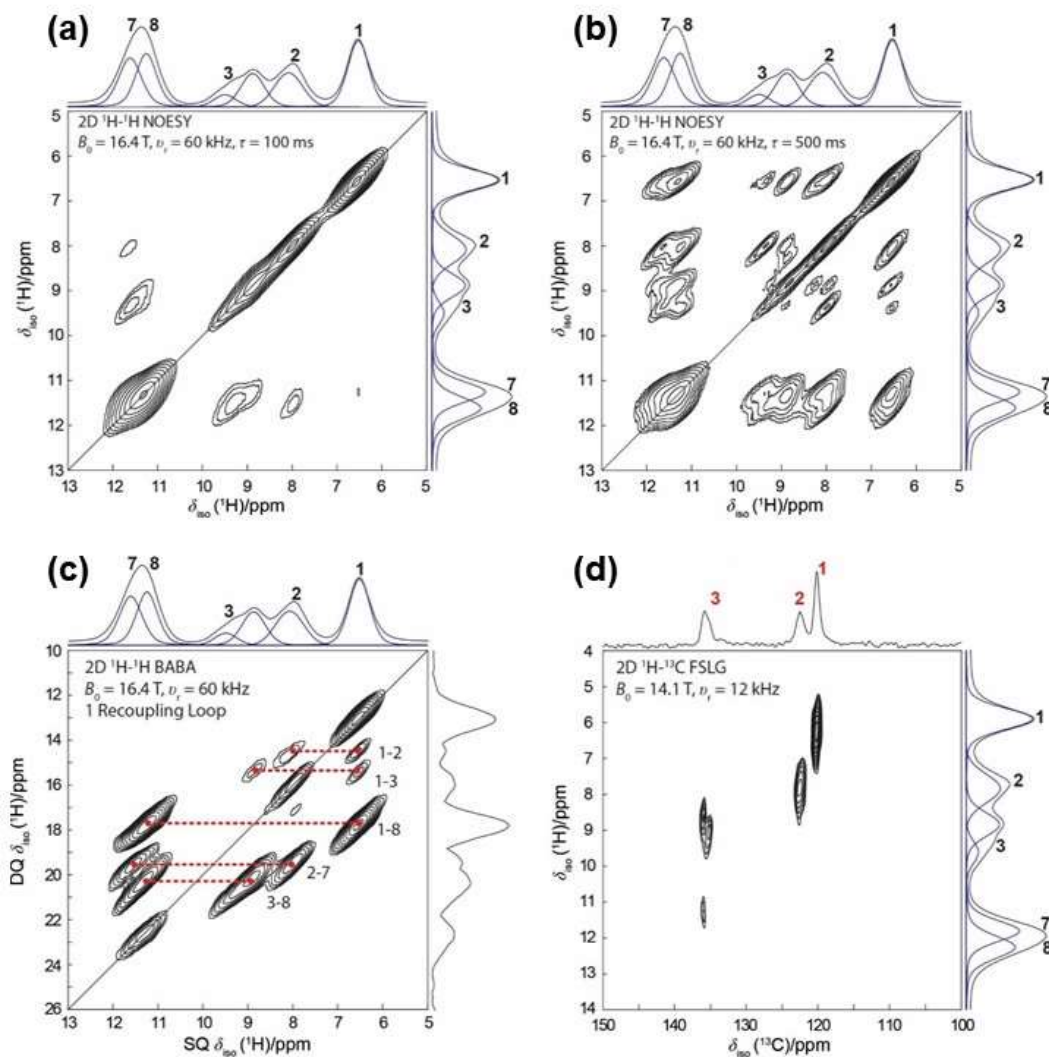


Figure 6.10 2D NMR correlation of a 63% IMI₃PbBr₅ – 37% IMI₂PbBr₄ mixture (a) ¹H-¹H homonuclear NOESY, with a relatively short contact time of 100 ms, (b) NOESY with a relatively long contact time of 500 ms. (c) ¹H-¹H BABA homonuclear correlation boosts the confidence in peak assignment (d) The heteronuclear FSLG correlation shows a clear correlation for ¹H-1 with ¹³C-1, ¹H-2 with ¹³C-2 and ¹H-3 with ¹³C-3. The correlation for ¹H-7 with ¹³C-3 and ¹H-8 with ¹³C-3 is not unexpected because of the proximity of the atoms.

Table 6.3 Comparison of variable field T_1 for IMIPbBr₃, IMI₂PbBr₄ and IMI₃PbBr₅. The decreasing T_1 with decreasing magnetic field follows a well-established trend observed by Bloembergen et al.¹⁸

IMIPbBr ₃ (<i>Cmcm</i>)				IMI ₂ PbBr ₄ (<i>P1</i>)				IMI ₃ PbBr ₅ (<i>P1</i>)			
¹ H site	¹ H δ_{iso} Expt. /ppm	T_1 16.4T /s (± 2 s)	T_1 7.1T /s (± 2 s)	¹ H site	¹ H δ_{iso} Expt. /ppm	T_1 16.4T /s (± 5 s)	T_1 7.1T /s (± 3 s)	¹ H site	¹ H δ_{iso} Expt. /ppm	T_1 16.4T /s (± 5 s)	T_1 7.1T /s (± 3 s)
1,2	7.7	17.4	15.7	1	6.5	37.5	26.2	1	6.6	44.5	30
				2	9.0	37.8	26.4	2	8.1	39.3	31
	8.6/ 8.5 ^a				8.9/ 9.3 ^a				8.9/ 9.5 ^b		
3	8.7/ 9.0 ^b	17.0	15.7	3	8.8/ 9.4 ^c	38.6	26.9	3	8.4/ 9.1 ^c	41.1	30
8	11.1	14.3	14.8	8	11.2	38.3	26.4	8	11.3	42.1	32
7	11.3	14.3	14.8	7	11.5	38.3	26.4	7	11.7	42.1	32

In Fig 6.10, the variable field dependence of the peak profiles can be seen. With the presence of two quadrupolar ¹⁴N neighbours surrounding ¹³C-3 and ¹H-3, the origin of the peak splitting can be better analysed from the variable field study of the spectra. The two main interactions to consider here would be chemical shift anisotropy (CSA), and the perturbation from the second order quadrupolar interaction. With an increasing field strength, a CSA dominated peak profile would become narrower while the second order quadrupolar dominated peak profile would become broader. From the ¹³C-3 peak profiles between 132 ppm and 138 ppm, the peaks can be observed to become narrower with increasing field strength. Furthermore, if the peak splitting were to originate from the J-coupling of ¹³C with ¹⁴N, the ¹³C peak would become split into a doublet with a 1:2 ratio. The coupling frequency would have an inverse relationship with the magnetic field strength and the peak profile would also take on an asymmetric profile as predicted theoretically¹⁹.

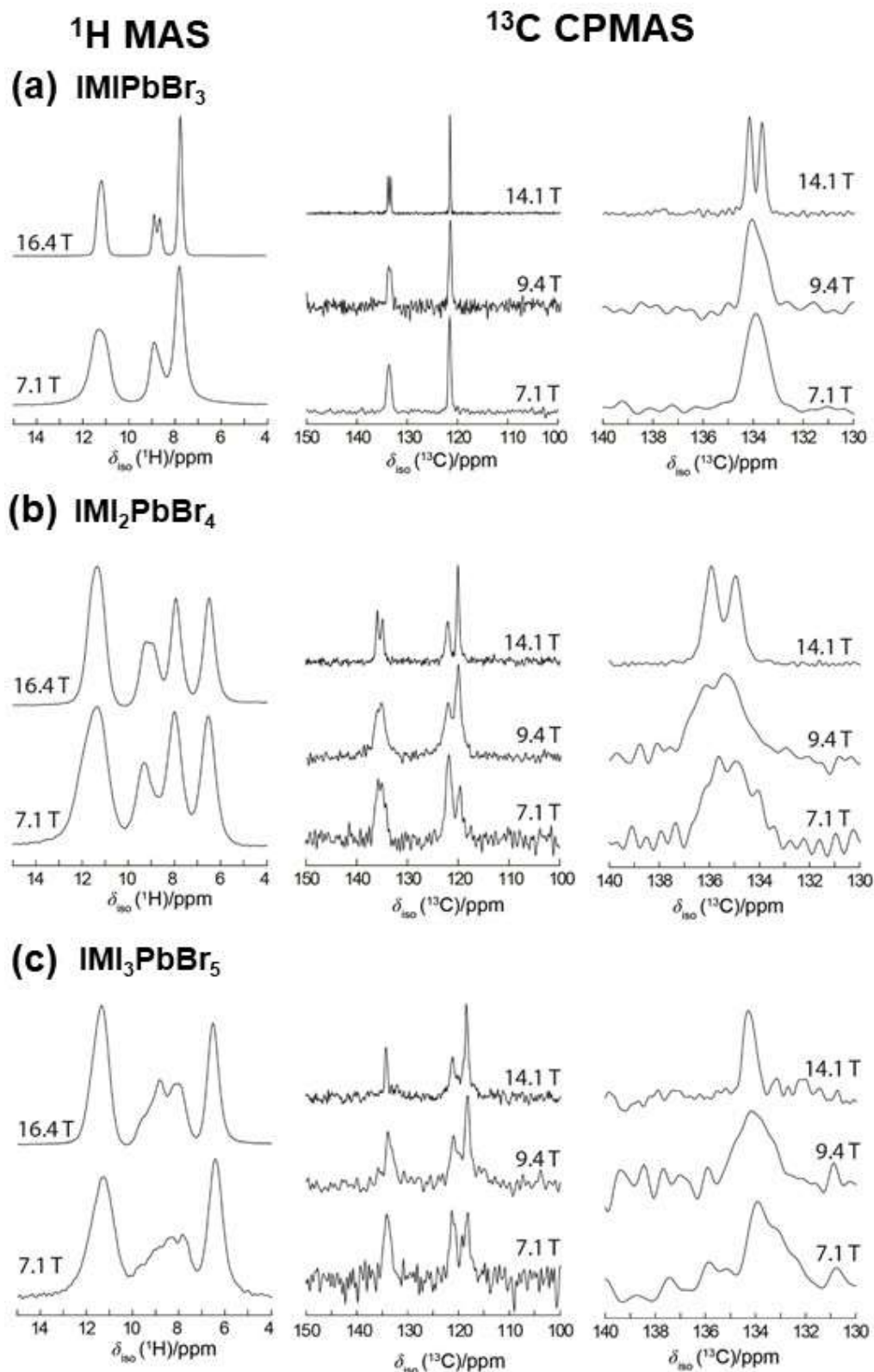


Figure 6.11 ^1H and ^{13}C spectra compared against variable field strength. Since both ^1H and ^{13}C peaks become narrower with increasing field strength, CSA is the dominant process in the NMR spectra.

Hence, from this variable field ^1H and ^{13}C spectra, it can be concluded that there are slight differences in the chemical environment of the imidazolium ions in the framework. In all three polymorphs, IMIPbBr_3 , $\text{IMI}_2\text{PbBr}_4$ and $\text{IMI}_3\text{PbBr}_5$, there are two imidazolium cations in the asymmetric unit cell. Therefore, the observed ^1H -3 and ^{13}C -3 “doublets” with 1:1 ratio in IMIPbBr_3 and $\text{IMI}_2\text{PbBr}_4$ are likely to originate from the slight differences between the chemical environment of the ^1H -3 and ^{13}C -3 of the two unique imidazolium cation. With an increasing field strength, the chemical shifts of the “doublet” remain about the same but the splitting becomes broader since CSA is being reduced. Therefore, sufficient resolution is gained, and this “doublet” can be more appropriately identified as two chemically distinct sites. Although the similar peak splitting is not experimentally observed in $\text{IMI}_3\text{PbBr}_5$, it should be considered that these are subtracted spectra, and thus, the fine features of the peak splitting would likely be lost. Should a sufficiently pure sample be obtained, it is likely that the peak splitting features would also be seen.

6.3.4 Band structure predicted by Density Functional Theory and validated experimentally through steady-state absorption and photoluminescence

Like in Chapter 5, the DFT calculations for DOS and JDOS are based on the single crystal XRD results using the obtained CIF files, and the results are shown in Fig 6.11 with a summary of the calculated band gap in Table 6.4. Notably, for IMIPbBr_3 , the room temperature *Cmcm* and intermediate $P2_12_12_1$ phase has a direct band gap. The low temperature *Pnma* phase along with $\text{IMI}_2\text{PbBr}_4$ and $\text{IMI}_3\text{PbBr}_5$ has an indirect band gap with a small momentum mismatch of around 0.01 eV and has flat dispersion relation around the valance band to conduction band transition region. The results shown here is also consistent with that seen in the chapter 5, where the inclusion of SOC effects would lower the energy levels of Pb and Br *p*-orbitals, thus, obtain a band gap closer to experimental values shown in Table 6.5. Since PBE functionals are known to underestimate the band gaps in hybrid perovskites²⁰, the different band gap values predicted by rSCAN and PBE functionals are expected. When SOC effects are accounted in the rSCAN functional, it is likely that the calculated band gap values would agree closely with experimental results. Nevertheless, the DFT calculations provides a good benchmark against the obtained experimental values.

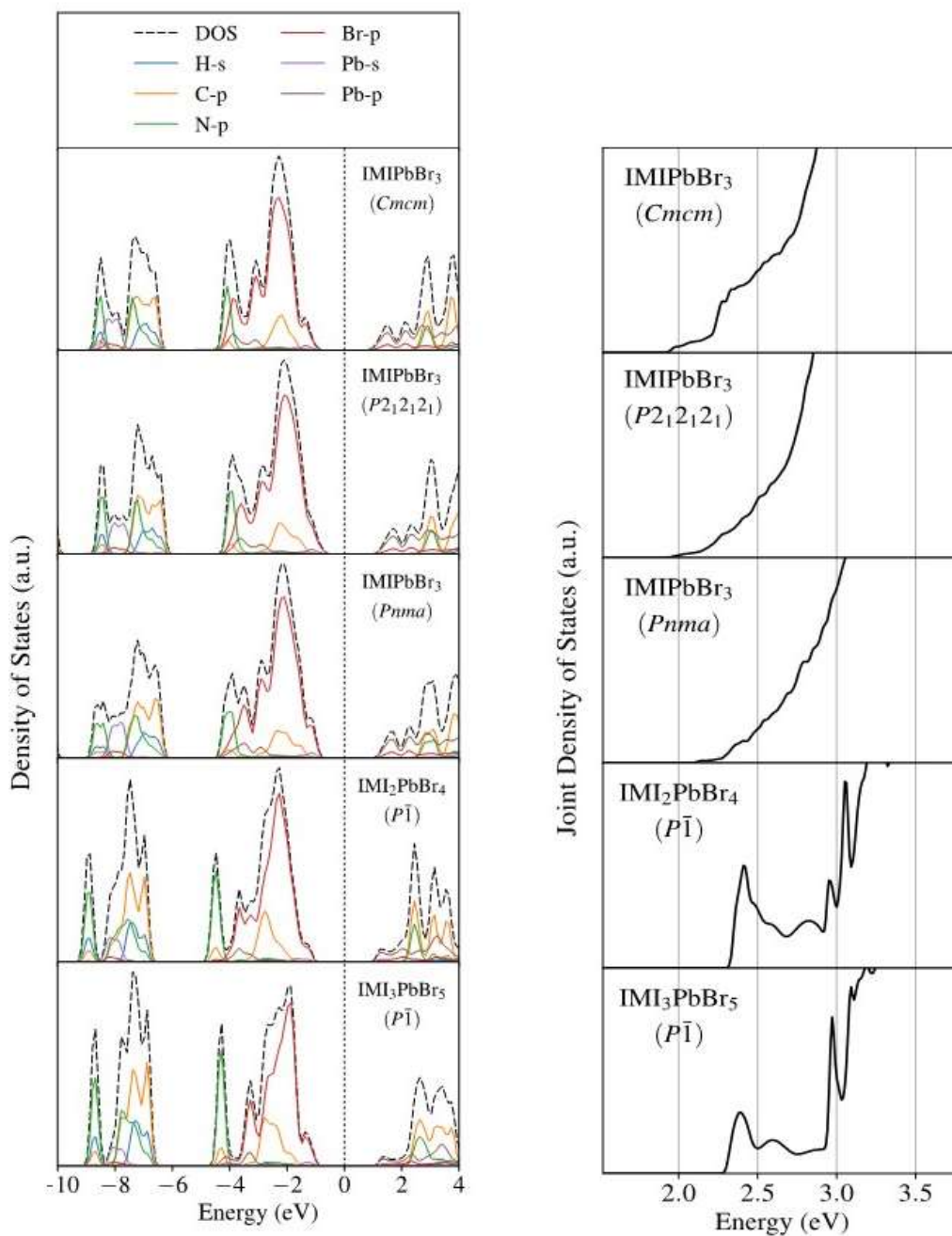


Figure 6.12 The density of states (left) and joint density of states (right) of the three phases of IMIPbBr₃, IMI₂PbBr₄ and IMI₃PbBr₅ as calculated by Density Functional Theory (DFT) using the Perdew–Burke–Ernzerhof (PBE) with Spin Orbit Coupling (SOC) functional.

Table 6.4 Band gaps of the IMIPbBr₃, IMI₂PbBr₄ and IMI₃PbBr₅ systems obtained from DFT calculations. The inclusion of SOC effects gives a more accurate estimate of the predicted band gaps.

Sample	E_g / eV (rSCAN)	E_g / eV (PBE)	E_g / eV (PBE + SOC)	E_g / eV (Experimental)
IMIPbBr ₃ (<i>Cmcm</i>)	3.22	2.88	1.98	3.03 (30 °C)
IMIPbBr ₃ (<i>P2₁2₁2₁</i>)	3.19	2.84	1.91	3.08 (-60 °C)
IMIPbBr ₃ (<i>Pnma</i>)	3.32	2.96	2.13	3.16 (-150 °C)
IMI ₂ PbBr ₄ ($\bar{P}1$)	3.16	2.92	2.33	3.00 (30 °C)
IMI ₃ PbBr ₅ ($\bar{P}1$)	3.18	2.81	2.33	3.00 (30 °C)

Linear absorption and steady state photoluminescence measurements were carried out and the results are presented in Fig 6.12. Even though the *Pnma* phase of IMIPbBr₃, IMI₂PbBr₄ and IMI₃PbBr₅ are not a direct band gap materials, the small momentum mismatch of around 0.01 eV coupled with the almost flat band dispersion near the valance band to conduction band transition, it is fair to approximate the systems as direct band gap materials. Hence, a corresponding Tauc plot is utilized to extract the band gap values, which are then plotted against the temperature and shown in the insert of Fig 6.12. Photoluminescence measurements were carried out under challenging experimental conditions using an excitation energy of 290 nm; under such high excitation energy conditions even the traditionally non-fluorescent CaF₂ windows become fluorescent thus contributing to the strong background.

In IMIPbBr₃, while increasing the temperature from -150 °C to 100 °C, it can be seen that there is an abrupt jump in the band gap value between -90 °C and -60 °C, and this corresponds well with the phase transition from *Pnma* to *P2₁2₁2₁*, at between -80 °C and -50 °C. Subsequently, it can be observed that the band gap value gradually decreases with increasing temperature. But from the absorption spectra, it can be observed that there is a slight jump in the onset of absorption edge from the curve between -30 °C to 0 °C, and this also corroborates well with the known phase transition from *P2₁2₁2₁* to *Cmcm* phase at around -30 °C. Notably, the excitonic absorption peak is only observable in the low temperature *Pnma* phase and disappears upon the transition to *P2₁2₁2₁* and *Cmcm* phase. From the photoluminescence spectra, the strong

background is seen to be on approximately the same order of magnitude as the photoluminescence signal originating from the sample, thus meddling with any definitive conclusions. Combined with the experimental absorption spectra, the peak at 410 nm is likely to be an excitonic emission the broadband emission centre estimated to be centre at 480 nm, with a full width half maximum (FWHM) of around 20 nm.

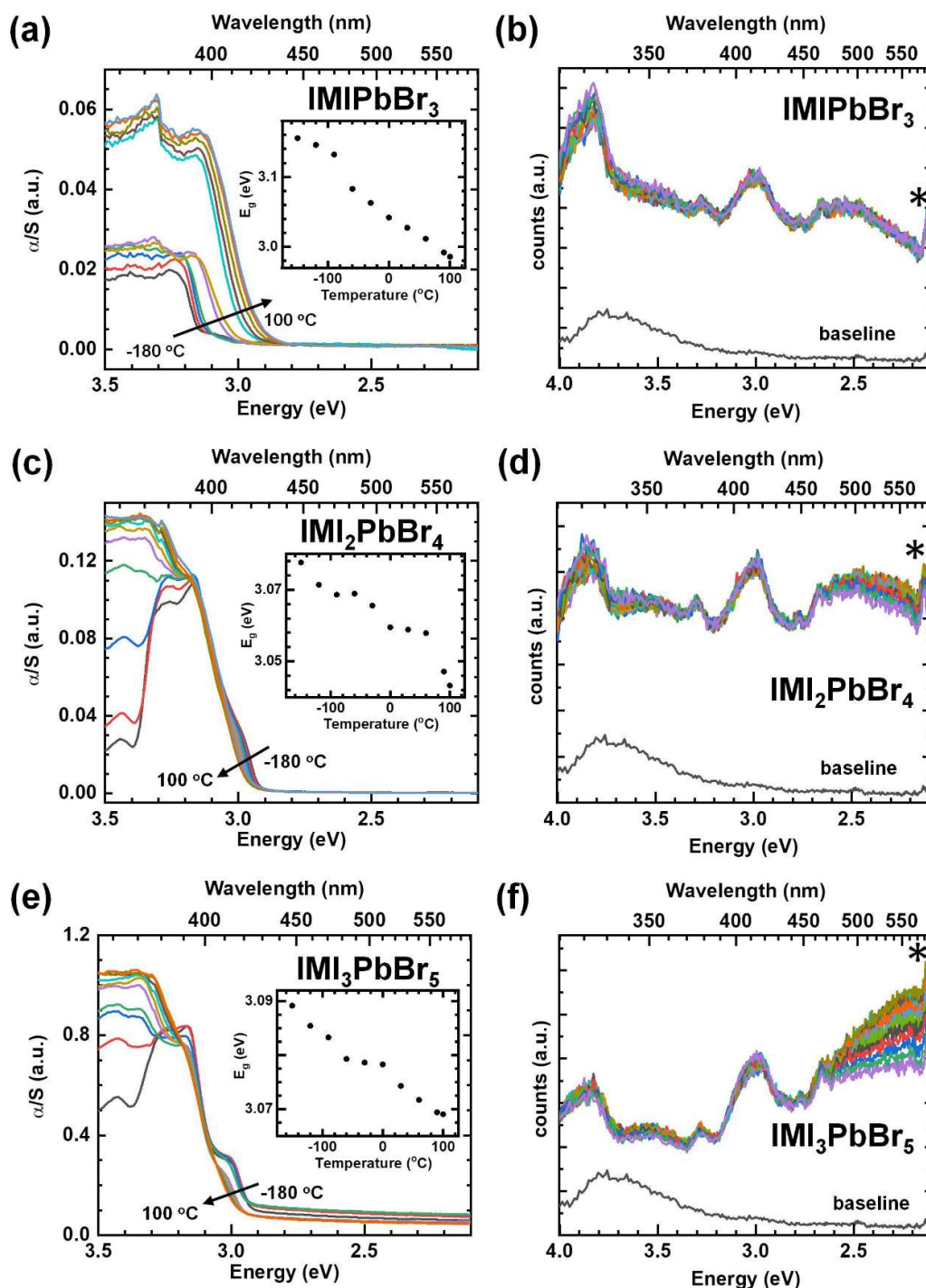


Figure 6.13 Steady state absorption of (a) IMIPbBr₃, (c) IMI₂PbBr₄, and (d) a physical mixture of 63% IMI₃PbBr₅ – 37% IMI₂PbBr₄ and photoluminescence of (b) IMIPbBr₃, (d) IMI₂PbBr₄, and (f) a physical mixture of 63% IMI₃PbBr₅ – 37% IMI₂PbBr₄. The insert on the absorption plot (a, c, d) shows the extracted band gap values taken from the Tauc plot of the absorption spectra at different temperatures. Due to experimental limitations in photoluminescence measurement, the peak at 290 nm arising from the second order effects of the monochromator cannot be completely filtered and is marked with an asterisk.

Table 6.5 Table of key optical properties extracted from photoluminescence results

IMIPbBr ₃ (<i>Cmcm</i>)		IMI ₂ PbBr ₄ (<i>P1</i>)		IMI ₃ PbBr ₅ (<i>P1</i>)	
Excitonic emission peak/nm	410	Excitonic emission peak/nm	410	Excitonic emission peak/nm	410
PL centre /nm	480	PL centre /nm	480	PL centre /nm	530
PL FWHM /nm	20±10	PL FWHM /nm	80±10	PL FWHM /nm	100±20
T/°C	E _g /eV	T/°C	E _g /eV	T/°C	E _g /eV
-180	3.16	-180	2.96	-180	2.96
-150	3.16	-150	2.97	-150	2.97
-120	3.15	-120	2.98	-120	2.98
-90	3.13	-90	2.98	-90	2.98
-60	3.08	-60	2.99	-60	2.99
-30	3.06	-30	2.99	-30	2.99
0	3.04	0	3.00	0	3.00
30	3.03	30	3.00	30	3.00
60	3.01	60	3.01	60	3.01
90	2.99	90	3.01	90	3.01
100	2.99	100	3.01	100	3.01

In IMI₂PbBr₄, there is a gradual decrease in the band gap with an increasing temperature from -150 °C to 100 °C. From the absorption spectra, an excitonic absorption peak can be seen at the onset of the absorption edge and the intensity of excitonic absorption gradually decreases with increasing temperature. Notably, a hint of excitonic absorption

persist even up to room temperature. Since $\text{IMI}_2\text{PbBr}_4$ does not undergo any phase transition across this temperature range, difference in the absorption profile below 380 nm is likely due to indirect transitions which are not favoured at lower temperatures. From the photoluminescence spectra, a profile similar to IMIPbBr_3 can be seen, with an excitonic emission peak at 410 nm and the broadband emission centre estimated at 480 nm, with a FWHM of 80 nm.

In $\text{IMI}_3\text{PbBr}_5$, the sample could not be separated into its pure form and thus, the work presented here is a physical mixture of $\text{IMI}_3\text{PbBr}_5$ and $\text{IMI}_2\text{PbBr}_4$, at a ratio of 63% to 37% respectively, as determined through pXRD. Hence, the accuracy of the experimentally determined band gap should be taken with some caution. Notably, the absorption profiles of the two samples are similar, showing a strong excitonic peak absorption at low temperatures which gradually decreases with increasing temperature. From the photoluminescence results, a strong excitonic emission peak is also seen at 415 nm but the broadband emission profile is much more sensitive to the temperature. The broadband emission centred at 530 nm increases gradually from 100 K to the maximum at 220 K then continues to decrease steadily until 380 K. This is in contrast with the photoluminescence profile in pure $\text{IMI}_2\text{PbBr}_4$ where the broadband component remains somewhat similar from 100 K to 380 K. Therefore, it is likely for the broadband component of $\text{IMI}_3\text{PbBr}_5$ to respond to the temperature effect as outlined earlier.

One common theme which runs across all three polymorphs of imidazole lead bromide is the presence of broadband photoluminescence emission. In other reduced dimensional hybrid perovskite and perovskitoid systems, broadband emission has very often been linked to the geometrical considerations, like octahedra tilting and distortion²¹⁻²⁶. From other similar $\langle 110 \rangle$ oriented perovskites, including IEAPbBr_4 which was studied in the previous chapter, evidence has been seen for the broadband emission originating from self-trapped charge carriers. Furthermore, in an earlier chapter, experimental evidence was also provided to show that the lead – halide bonds are relatively soft and prone to local distortion. Hence, it would not be surprising for the lead – bromide bonds to also follow the trend of local distortion in these three imidazole lead bromide polymorphs. Therefore, the experimentally observed broadband emission in all three imidazole lead bromide polymorphs would also be likely to originate from self-trapped charge carriers. Unlike IEAPbBr_4 , where the excitonic absorption can be

observed even at room temperature, the excitonic absorption profile in the three polymorphs shown here have varying degree of sensitivity to temperature, but the broadband emission profile persists even into high temperature. Therefore, it is likely that other charged species, like electron and holes are self-trapped giving rise to the range of recombination energy, and thus, broadband emission.

6.4 Conclusion

In conclusion, this chapter first demonstrated the need for a new naming nomenclature to give more clarity to the comparison of 1D perovskitoids. The three systems studied in this chapter are different polymorphs of imidazole lead bromide and this shows the significance of A-site chemical activity. When the side group activity is suppressed, through an alkyl group substitution as in the previous chapter, such polymorphism is not seen. Furthermore, work of this chapter also showed the limitations of the Goldschmidt tolerance factor in hybrid perovskites, where the A-site cation takes on geometries other than the ideal spherical shape.

The structural properties of each polymorph are characterized thoroughly and only IMIPbBr₃ exhibits a series of phase transformation. From a structural symmetry perspective, the phase transition from the room temperature to low temperature phases goes through an unusual superstructure intermediate route. The remaining two polymorphs, IMI₂PbBr₄ and IMI₃PbBr₅ does not show any phase transition upon extreme cooling and demonstrates the robustness of the inorganic framework up to thermal disintegration. Further analysis from NMR showed conclusively the presence of an imidazolium cation in all three polymorphs. The NMR $T_{1\rho}$ relaxation dynamics provided an indication of the presence of dynamic disorder, particularly in IMIPbBr₃.

First principles DFT calculations were also carried out by starting from the structural model as determined in XRD, where several experimental observations are in good agreement with the calculations. The chemical shifts predicted by DFT are consistent with the experimentally observed ¹H and ¹³C chemical shifts. DFT was also used to predict the optical band gap and has seen close agreement with the experimental values.

Remarkably, in the analysis of the optical properties of the three polymorphs, broadband photoluminescence emission is seen in all the samples. Such behaviour is typically seen in self-trapped states, and hints at the existence of self-trapped charge carriers. The excitonic absorption peak, has expectedly, diminishes with increasing temperature for all three samples studied in this chapter and thus, gives an indication that the self-trapping mechanism is different from the <110> oriented 2D layered perovskite examined in the previous chapter.

References

1. Fu, Y. Z.; Manthiram, A., Nafion–Imidazole–H₃PO₄ Composite Membranes for Proton Exchange Membrane Fuel Cells. *Journal of The Electrochemical Society* **2007**, *154* (1), B8.
2. Kreuer, K. D., On the development of proton conducting polymer membranes for hydrogen and methanol fuel cells. *Journal of Membrane Science* **2001**, *185* (1), 29-39.
3. Smitha, B.; Sridhar, S.; Khan, A. A., Solid polymer electrolyte membranes for fuel cell applications—a review. *Journal of Membrane Science* **2005**, *259* (1), 10-26.
4. Sheldrick, G., SHELXT - Integrated space-group and crystal-structure determination. *Acta Crystallographica Section A* **2015**, *71* (1), 3-8.
5. Dolomanov, O. V.; Bourhis, L. J.; Gildea, R. J.; Howard, J. A. K.; Puschmann, H., OLEX2: a complete structure solution, refinement and analysis program. *Journal of Applied Crystallography* **2009**, *42* (2), 339-341.
6. Spek, A., Structure validation in chemical crystallography. *Acta Crystallographica Section D* **2009**, *65* (2), 148-155.
7. Guinier, A.; Bokij, G. B.; Boll-Dornberger, K.; Cowley, J. M.; Durovic, S.; Jagodzinski, H.; Krishna, P.; de Wolff, P. M.; Zvyagin, B. B.; Cox, D. E.; Goodman, P.; Hahn, T.; Kuchitsu, K.; Abrahams, S. C., Nomenclature of polytype structures. Report of the International Union of Crystallography Ad hoc Committee on the Nomenclature of Disordered, Modulated and Polytype Structures. *Acta Crystallographica Section A* **1984**, *40* (4), 399-404.
8. Ramsdell, L. S., Studies on silicon carbide. *American Mineralogist* **1947**, *42*, 64.

9. Stoumpos, C. C.; Mao, L.; Malliakas, C. D.; Kanatzidis, M. G., Structure–Band Gap Relationships in Hexagonal Polytypes and Low-Dimensional Structures of Hybrid Tin Iodide Perovskites. *Inorganic Chemistry* **2017**, *56* (1), 56-73.
10. Li, X.; He, Y.; Kepenekian, M.; Guo, P.; Ke, W.; Even, J.; Katan, C.; Stoumpos, C. C.; Schaller, R. D.; Kanatzidis, M. G., Three-Dimensional Lead Iodide Perovskitoid Hybrids with High X-ray Photoresponse. *Journal of the American Chemical Society* **2020**, *142* (14), 6625-6637.
11. Febriansyah, B.; Neo, C. S. D.; Giovanni, D.; Srivastava, S.; Lekina, Y.; Koh, T. M.; Li, Y.; Shen, Z. X.; Asta, M.; Sum, T. C.; Mathews, N.; England, J., Targeted Synthesis of Trimeric Organic–Bromoplumbate Hybrids That Display Intrinsic, Highly Stokes-Shifted, Broadband Emission. *Chemistry of Materials* **2020**, *32* (11), 4431-4441.
12. Skelton, B. W.; Kokozay, V. N.; Vassilyeva, O. Y.; Buvaylo, E. A., Experimental Crystal Structure Determination. *CSD Communication* **2019**.
13. Arora, Y.; Seth, C.; Khushalani, D., Crafting Inorganic Materials for Use in Energy Capture and Storage. *Langmuir* **2019**, *35* (28), 9101-9114.
14. Lin, H.; Zhou, C.; Tian, Y.; Besara, T.; Neu, J.; Siegrist, T.; Zhou, Y.; Bullock, J.; Schanze, K. S.; Ming, W.; Du, M.-H.; Ma, B., Bulk assembly of organic metal halide nanotubes. *Chemical Science* **2017**, *8* (12), 8400-8404.
15. Seth, C.; Jana, D.; Jindal, V.; Khushalani, D.; Ghosh, S., One-Dimensional Behavior of Imidazolium Lead Iodide. *The Journal of Physical Chemistry C* **2019**, *123* (26), 16449-16455.
16. Seth, C.; Khushalani, D., Non-Perovskite Hybrid Material, Imidazolium Lead Iodide, with Enhanced Stability. *ChemNanoMat* **2019**, *5* (1), 85-91.
17. Ahtee, M.; Glazer, A. M., Lattice parameters and tilted octahedra in sodium-potassium niobate solid solutions. *Acta Crystallographica Section A* **1976**, *32* (3), 434-446.
18. Bloembergen, N.; Purcell, E. M.; Pound, R. V., Relaxation Effects in Nuclear Magnetic Resonance Absorption. *Physical Review* **1948**, *73* (7), 679-712.
19. Zumbulyadis, N.; Henrichs, P. M.; Young, R. H., Quadrupole effects in the magic-angle-spinning spectra of spin-1/2 nuclei. *The Journal of Chemical Physics* **1981**, *75* (4), 1603-1611.
20. Mosconi, E.; Amat, A.; Nazeeruddin, M. K.; Grätzel, M.; De Angelis, F., First-Principles Modeling of Mixed Halide Organometal Perovskites for Photovoltaic Applications. *The Journal of Physical Chemistry C* **2013**, *117* (27), 13902-13913.

21. Cortecchia, D.; Neutzner, S.; Srimath Kandada, A. R.; Mosconi, E.; Meggiolaro, D.; De Angelis, F.; Soci, C.; Petrozza, A., Broadband Emission in Two-Dimensional Hybrid Perovskites: The Role of Structural Deformation. *J. Am. Chem. Soc.* **2017**, *139* (1), 39-42.
22. Cortecchia, D.; Yin, J.; Bruno, A.; Lo, S.-Z. A.; Gurzadyan, G. G.; Mhaisalkar, S.; Bredas, J.-L.; Soci, C., Polaron self-localization in white-light emitting hybrid perovskites. *J. Mater. Chem. C* **2017**, *5* (11), 2771-2780.
23. Yin, J.; Li, H.; Cortecchia, D.; Soci, C.; Brédas, J.-L., Excitonic and Polaronic Properties of 2D Hybrid Organic–Inorganic Perovskites. *ACS Energy Lett.* **2017**, *2*, 417-423.
24. Smith, M. D.; Jaffe, A.; Dohner, E. R.; Lindenberg, A. M.; Karunadasa, H. I., Structural origins of broadband emission from layered Pb-Br hybrid perovskites. *Chemical Science* **2017**, *8* (6), 4497-4504.
25. Dohner, E. R.; Hoke, E. T.; Karunadasa, H. I., Self-Assembly of Broadband White-Light Emitters. *Journal of the American Chemical Society* **2014**, *136* (5), 1718-1721.
26. Dohner, E. R.; Jaffe, A.; Bradshaw, L. R.; Karunadasa, H. I., Intrinsic White-Light Emission from Layered Hybrid Perovskites. *Journal of the American Chemical Society* **2014**, *136* (38), 13154-13157.

Chapter 7

Conclusions and Recommendations

Hybrid organic-inorganic perovskites have proven to be an extremely rich field of underexplored chemistry and physics. In chapter 4, the physics of MAPbI₃ was studied in detail through the optical signature charge transport of polarons. 2D layered <110> oriented perovskites were studied in chapter 5, particularly the pioneering APIPbBr₄ and recently discovered IEAPbBr₄. Thorough structural characterization shows APIPbBr₄ to exist as a polymorph API₂Pb₃Br₁₀, where the cation dynamics is distinct from IEAPbBr₄. Chapter 6 explores the less studied 1D perovskite and ‘perovskitoid’, where a new naming nomenclature is proposed. The polymorphism seen in imidazole lead bromide demonstrates the importance of the perovskite A-site cation chemistry. The presence of white light emission across all the reduced dimensional perovskite systems hints at the presence of self-trapped states.

7.1 Summary of thesis

The aim of this thesis was to study the effects and implications of the local structural distortion upon the localization effect of charge carriers in hybrid perovskites, and the resultant bulk effects. This commenced with the well-studied prototypical 3D MAPbI₃, in chapter 4, through examining vibrionic features in the infrared and visible regions. The experimental observations were further substantiated through first principles DFT simulations. In chapter 5, the focus then moved onto <110> oriented 2D layered hybrid perovskites, APIPbBr₄ and IEAPbBr₄ which has only recently been reported. In an unexpected result, APIPbBr₄ was shown to exist as a previously unknown polymorph API₂Pb₃Br₁₀. In chapter 6, three different polymorphs of imidazole lead bromide were studied, of which one takes on a 3D structure closely resembling a 4H perovskite polytype while the remaining two are clearly 1D perovskites. Thus comparisons have been made of effects in 3D, 2D and 1D perovskites.

7.2 Contributions and Implications

In chapter 4, direct evidence for the existence for polarons is presented, starting from an *ab initio* DFT calculation. The accuracy of the DFT model is first checked against steady-state absorption and steady-state photocurrent measurements. Following the accurate estimations, DFT predicted the existence of an energy state within the band gap arising from the electron-phonon coupling, which would give rise to the formation of a polaron. Concurrently, DFT also predicted the modulation of several vibrionic features in the infrared regime which can be attributed to mode softening. These predictions are further validated through steady state photoinduced absorption measurements. The formation and decay dynamics of polarons are then studied through transient absorption in the visible regime and through fast transient photocurrent measurements. Since neutral species, like excitons, do not contribute to photocurrent, the two fast spectroscopic techniques showed clearly that the charge carriers are coupled with phonons to form large polarons. The formation of large polarons would thus reconcile several anomalous charge transport properties observed in MAPbI₃.

Moving to reduced dimensional perovskites, chapter 5 focuses on <110> oriented 2D

layered hybrid perovskite, APIPbBr₄ and IEAPbBr₄. The most important conclusion of this chapter is showing that the former exists as a polymorph which does not take on the <110> oriented 2D layered hybrid perovskite. The inorganic framework instead form a truncated 1D chain where the API cation spreads out the charges along the 1D chain instead of across two layers. API₂Pb₃Br₁₀ is seen to take on a phase transition at lower temperatures and always forms a twin. Such a phase transition is not observed in IEAPbBr₄ and shows the robustness of the inorganic perovskite framework. Evidences from NMR and optical characterization shows distinct differences across a variety of spectrum, from the cation dynamics to the optical band gap. Notably, the excitonic absorption and emission peak is seen in IEAPbBr₄, which matches well with other <110> 2D layered perovskites reported in literature¹⁻⁴. Notably, IEAPbBr₄ has also demonstrated the limit to the correlation of octahedra distortion with the broadness of the emission.

Chapter 6 explores 1D perovskites which can be obtained by using unsubstituted imidazolium cation and shows that three different polymorphs can be obtained, based on the starting ratio of imidazole to lead oxide. This chapter starts off by examining and proposes a new classification regime for 1D perovskitoids. During the structural analysis, the need for complementary analysis is highlighted in IMIPbBr₃, which was shown clearly to take on an orthorhombic crystal lattice. Dynamics disorder of the imidazolium ring across all three polymorphs were studied through NMR and can be elucidated that IMIPbBr₃ is likely to be spinning like a turntable in the imidazole ring plane while motion in IMI₂PbBr₄ and IMI₃PbBr₅ is likely to be restricted. The NMR spectral feature which shows an apparent split peak in both the ¹³C and ¹H spectra is likely to be of structural origin arising from two unique imidazole rings in one asymmetric unit cell.

7.3 Future work and direction

From the detailed studies carried out from the thesis, a thorough optical characterization and analysis of the new structures examined in chapter 5 and 6, like IEAPbBr₄ and IMIPbBr₃, by optical methods utilized in chapter 4, such as photoinduced absorption and transient fast spectroscopy, would shed more light on the nature of these materials.

This is because IEAPbBr₄ shows evidences of self-trapped excitons even at room temperature, which is highly unusual in many materials. The study on polymorphs of imidazole lead bromide would help to shed light on the mechanism of self-trapping and whether charge carriers or neutral species contribute more towards the broadband emission. However, moving onto such optical studies would also present itself several challenges; the greatest would be regarding the type of sample because a thin film sample might end up structurally different from the bulk and the effect of grain boundaries might dominate the observed spectroscopic effects. Conversely, pellet pressing of the samples with KBr would also be equally challenging due to the well observed phenomena of ion exchange in hybrid perovskites⁵⁻⁸.

Chapter 5 and 6 also demonstrated the significance of the perovskite A-site cation. While Goldschmidt tolerance factor has provided a good reference in predicting the perovskite crystal structure, it was developed by assuming that all the ions are spherical. While this would remain accurate in oxide perovskites, hybrid perovskites have shown instances where the tolerance factor would fail, particularly in the formation of 2D hybrid perovskites by using a long or bulky side chain. From a surfactant chemistry perspective, the micelle critical packing parameter has been utilized to predict the packing shape and micelle structure formed by considering the contributions from the head and tail group. Such an approach could possibly modify the Goldschmidt tolerance factor to also include organic cations and aid the structural engineering of perovskites.

Another area for further investigation which the results in chapter 5 and 6 has demonstrated is the significance of the perovskite A-site cation. In lead halide perovskites, the A-site cation is typically monovalent (i.e. +1) for the structure to maintain charge neutrality. From IEAPbBr₄ and all three polymorphs of imidazole lead bromide, the chemical activity in the perovskite A-site cation chemistry is demonstrated. To further probe the validity of this hypothesis, a comparison with pyrrolium based perovskite or perovskitoids to examine the importance of the chemical activity by the lone pair of electrons on imidazolium cations. Alternatively, studies can also start off from the system based on pyridinium based hybrid perovskite⁹, and then compared against pyrazine and pyrimidine-based hybrid perovskites.

References

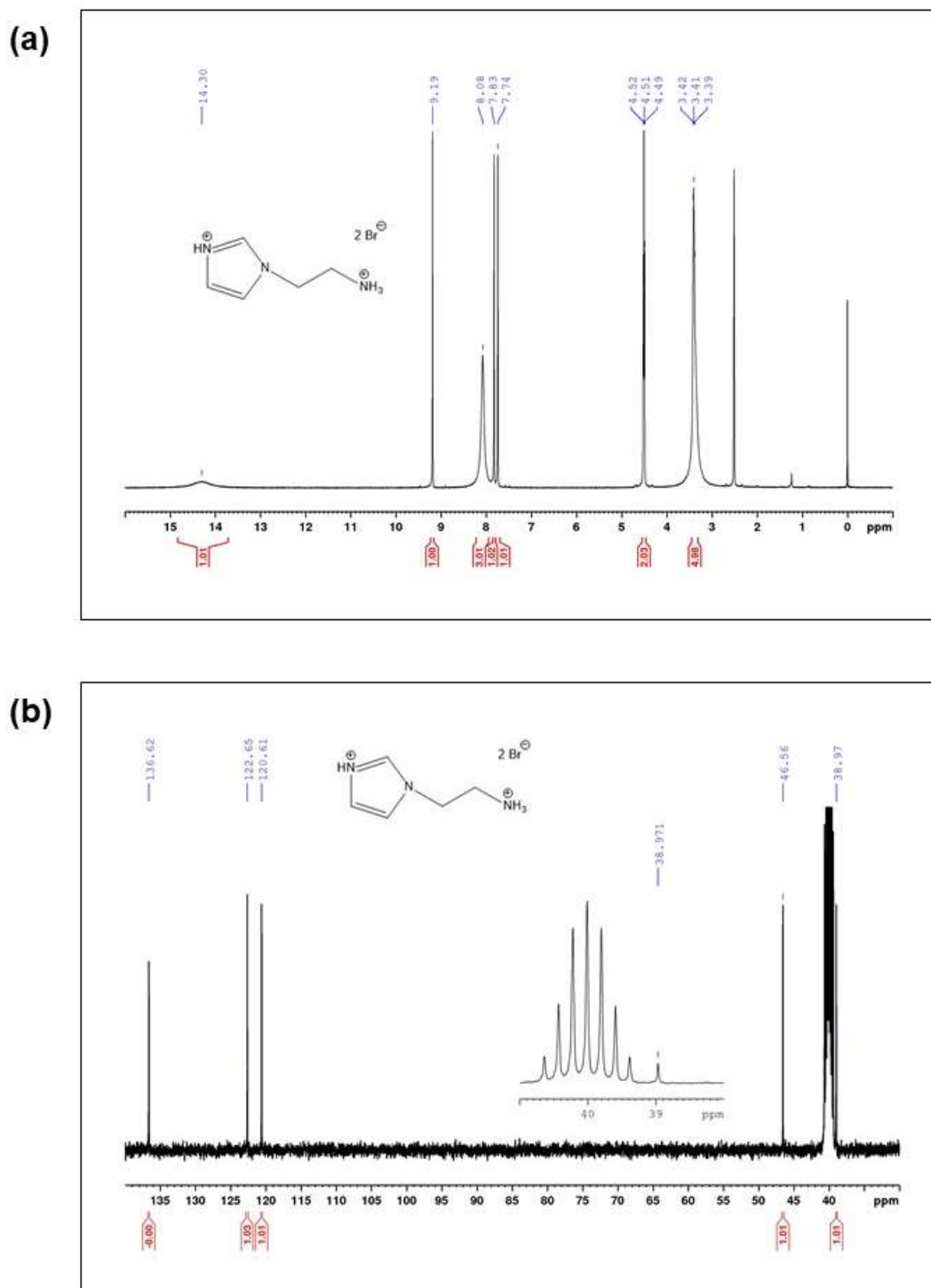
1. Dohner, E. R.; Hoke, E. T.; Karunadasa, H. I., Self-Assembly of Broadband White-Light Emitters. *Journal of the American Chemical Society* **2014**, *136* (5), 1718-1721.
2. Smith, M. D.; Jaffe, A.; Dohner, E. R.; Lindenberg, A. M.; Karunadasa, H. I., Structural origins of broadband emission from layered Pb-Br hybrid perovskites. *Chemical Science* **2017**, *8* (6), 4497-4504.
3. Tremblay, M.-H.; Thouin, F.; Leisen, J.; Bacsá, J.; Srimath Kandada, A. R.; Hoffman, J. M.; Kanatzidis, M. G.; Mohite, A. D.; Silva, C.; Barlow, S.; Marder, S. R., (4NPEA)₂PbI₄ (4NPEA = 4-Nitrophenylethylammonium): Structural, NMR, and Optical Properties of a 3 × 3 Corrugated 2D Hybrid Perovskite. *Journal of the American Chemical Society* **2019**, *141* (11), 4521-4525.
4. Cortecchia, D.; Yin, J.; Petrozza, A.; Soci, C., White light emission in low-dimensional perovskites. *Journal of Materials Chemistry C* **2019**, *7* (17), 4956-4969.
5. Jodlowski, A. D.; Yépez, A.; Luque, R.; Camacho, L.; de Miguel, G., Benign-by-Design Solventless Mechanochemical Synthesis of Three-, Two-, and One-Dimensional Hybrid Perovskites. *Angewandte Chemie International Edition* **2016**, *55* (48), 14972-14977.
6. Yang, Z.; Wei, M.; Voznyy, O.; Todorovic, P.; Liu, M.; Quintero-Bermudez, R.; Chen, P.; Fan, J. Z.; Proppe, A. H.; Quan, L. N.; Walters, G.; Tan, H.; Chang, J.-W.; Jeng, U. S.; Kelley, S. O.; Sargent, E. H., Anchored Ligands Facilitate Efficient B-Site Doping in Metal Halide Perovskites. *Journal of the American Chemical Society* **2019**, *141* (20), 8296-8305.
7. Wang, J.; Leng, J.; Liu, J.; He, S.; Wang, Y.; Wu, K.; Jin, S., Engineered Directional Charge Flow in Mixed Two-Dimensional Perovskites Enabled by Facile Cation-Exchange. *The Journal of Physical Chemistry C* **2017**, *121* (39), 21281-21289.
8. Karmakar, A.; Askar, A. M.; Bernard, G. M.; Terskikh, V. V.; Ha, M.; Patel, S.; Shankar, K.; Michaelis, V. K., Mechanochemical Synthesis of Methylammonium Lead Mixed-Halide Perovskites: Unraveling the Solid-Solution Behavior Using Solid-State NMR. *Chemistry of Materials* **2018**, *30* (7), 2309-2321.
9. Selivanov, N. I.; Murashkina, A. A.; Kevorkyants, R.; Emeline, A. V.; Bahnemann, D. W., Pyridinium lead tribromide and pyridinium lead triiodide: quasi-

one-dimensional perovskites with an optically active aromatic π -system. *Dalton Transactions* **2018**, 47 (45), 16313-16319.

List of Publications

1. **Walter P. D. Wong**, J. Yin, B. Chaudhary, X. Y. Chin, D. Cortecchia, S-Z A. Lo, A. C. Grimsdale, O. F. Mohammed, G. Lanzani, and C. Soci *ACS Materials Letters* **2020** 2 (1), 20-27
2. **Walter P.D. Wong**, J. V. Hanna, A. C. Grimsdale *Acta Cryst.* **2021**, B77, 408-415
3. I. Bargigia , E. Zucchetti, A. R. S. Kandada, M. Moreira, C. Bossio, **W. P. D. Wong**, P. B. Miranda, P. Decuzzi, C. Soci, C. D'Andrea, G. Lanzani, *ChemBioChem* **2019**, 20, 532.

Appendix A



Appendix B

Table B1 Fractional Atomic Coordinates ($\times 10^4$) and Equivalent Isotropic Displacement Parameters ($\text{\AA}^2 \times 10^3$) for $\text{API}_2\text{Pb}_3\text{Br}_{10}$ at 298 K. U_{eq} is defined as 1/3 of the trace of the orthogonalised U_{ij} tensor

Atom	<i>x</i>	<i>y</i>	<i>z</i>	<i>U</i> (eq)
Pb(2)	10000	4707.9(6)	5000	42.68(11)
Pb(1)	6721.2(2)	4975.0(3)	4596.4(2)	39.91(7)
Br(2)	5000	2401.4(14)	5000	50.1(3)
Br(6)	11339.0(8)	7398.2(11)	5817.7(5)	53.2(2)
Br(5)	8039.9(7)	4835.7(15)	6082.4(4)	60.4(2)
Br(3)	5905.0(7)	5228.7(12)	3028.1(4)	56.6(2)
Br(1)	5000	7598.6(14)	5000	56.8(3)
Br(4)	8445.5(9)	2404.1(12)	4068.5(6)	60.3(2)
N(2)	2219(5)	5592(9)	1637(3)	48.8(15)
N(1)	3482(6)	4772(13)	852(4)	65.1(19)
C(1)	4000(6)	4988(15)	1549(4)	59(2)
C(3)	2408(7)	5154(13)	923(4)	57(2)
C(2)	3194(7)	5468(12)	2013(4)	56(2)
C(4)	1131(7)	6183(11)	1945(5)	49.9(18)
C(5)	273(7)	4846(15)	1933(5)	68(2)
C(6)	-872(7)	5414(13)	2214(6)	64(2)
N(3)	-1736(7)	4200(13)	2131(7)	98(3)

Table B2 Anisotropic Displacement Parameters ($\text{\AA}^2 \times 10^3$) for $\text{API}_2\text{Pb}_3\text{Br}_{10}$ at 298 K

Atom	<i>U</i> ₁₁	<i>U</i> ₂₂	<i>U</i> ₃₃	<i>U</i> ₂₃	<i>U</i> ₁₃	<i>U</i> ₁₂
Pb(2)	36.66(16)	51.5(3)	39.87(17)	0	-1.95(13)	0
Pb(1)	37.28(11)	44.38(14)	38.07(12)	0.63(11)	-1.90(8)	-2.17(12)
Br(2)	47.7(6)	39.0(5)	63.5(7)	0	-4.3(6)	0
Br(6)	57.0(5)	50.5(5)	52.1(5)	-6.9(3)	-1.5(4)	7.1(4)
Br(5)	65.0(4)	82.5(6)	33.9(3)	0.0(4)	3.7(3)	-7.4(6)
Br(3)	55.4(4)	67.9(6)	46.3(4)	2.0(4)	-11.8(3)	-3.1(4)
Br(1)	66.5(9)	38.1(6)	65.9(8)	0	-3.3(7)	0
Br(4)	66.2(6)	51.8(5)	62.9(5)	-13.4(4)	0.7(4)	5.6(4)
N(2)	45(3)	59(4)	43(3)	6(3)	2(3)	4(3)
N(1)	58(4)	86(6)	52(3)	-13(4)	9(3)	5(5)
C(1)	37(3)	85(6)	53(4)	11(5)	-1(3)	6(5)
C(3)	51(4)	78(6)	41(3)	0(4)	-8(3)	1(5)

C(2)	43(4)	90(7)	36(3)	1(4)	-2(3)	1(4)
C(4)	44(4)	57(5)	49(4)	3(3)	5(3)	3(3)
C(5)	49(4)	80(6)	74(5)	-7(6)	11(4)	-3(6)
C(6)	42(4)	64(6)	86(6)	-9(5)	7(4)	3(4)
N(3)	62(5)	75(6)	157(9)	-28(6)	16(6)	-6(5)

Table B3 Bond Lengths for API₂Pb₃Br₁₀ at 298 K

Atom	Atom	Length/Å	Atom	Atom	Length/Å
Pb(2)	Br(6) ¹	3.0435(10)	Pb(1)	Br(4)	3.0446(9)
Pb(2)	Br(6)	3.0434(10)	N(2)	C(3)	1.336(9)
Pb(2)	Br(5)	3.0063(7)	N(2)	C(2)	1.329(9)
Pb(2)	Br(5) ¹	3.0063(7)	N(2)	C(4)	1.471(9)
Pb(2)	Br(4) ¹	3.0826(11)	N(1)	C(1)	1.390(11)
Pb(2)	Br(4)	3.0826(11)	N(1)	C(3)	1.305(10)
Pb(1)	Br(2)	2.9825(8)	C(1)	C(2)	1.314(10)
Pb(1)	Br(6) ¹	3.0892(9)	C(4)	C(5)	1.474(13)
Pb(1)	Br(5)	3.0627(8)	C(5)	C(6)	1.507(11)
Pb(1)	Br(3)	2.9546(8)	C(6)	N(3)	1.417(13)
Pb(1)	Br(1)	3.0106(8)			

¹2-X,+Y,1-Z**Table B4** Bond Angles for API₂Pb₃Br₁₀ at 298 K

Atom	Atom	Atom	Angle/°	Atom	Atom	Atom	Angle/°
Br(6)	Pb(2)	Br(6) ¹	89.39(4)	Br(3)	Pb(1)	Br(1)	87.681(19)
Br(6)	Pb(2)	Br(4) ¹	82.25(3)	Br(3)	Pb(1)	Br(4)	88.33(3)
Br(6) ¹	Pb(2)	Br(4)	82.25(3)	Br(1)	Pb(1)	Br(6) ¹	96.38(2)
Br(6) ¹	Pb(2)	Br(4) ¹	171.63(3)	Br(1)	Pb(1)	Br(5)	99.16(2)
Br(6)	Pb(2)	Br(4)	171.63(3)	Br(1)	Pb(1)	Br(4)	175.78(2)
Br(5)	Pb(2)	Br(6) ¹	83.42(3)	Br(4)	Pb(1)	Br(6) ¹	82.12(2)
Br(5)	Pb(2)	Br(6)	93.78(3)	Br(4)	Pb(1)	Br(5)	84.56(3)
Br(5) ¹	Pb(2)	Br(6)	83.42(3)	Pb(1) ²	Br(2)	Pb(1)	92.11(3)
Br(5) ¹	Pb(2)	Br(6) ¹	93.78(3)	Pb(2)	Br(6)	Pb(1) ¹	79.56(2)
Br(5) ¹	Pb(2)	Br(5)	176.08(5)	Pb(2)	Br(5)	Pb(1)	80.563(16)
Br(5)	Pb(2)	Br(4) ¹	97.50(3)	Pb(1)	Br(1)	Pb(1) ²	91.01(3)
Br(5)	Pb(2)	Br(4)	84.86(3)	Pb(1)	Br(4)	Pb(2)	79.65(2)
Br(5) ¹	Pb(2)	Br(4)	97.50(3)	C(3)	N(2)	C(4)	125.8(7)
Br(5) ¹	Pb(2)	Br(4) ¹	84.86(3)	C(2)	N(2)	C(3)	108.3(7)
Br(4) ¹	Pb(2)	Br(4)	106.11(4)	C(2)	N(2)	C(4)	125.9(6)

Br(2)	Pb(1)	Br(6) ¹	175.02(2)	C(3)	N(1)	C(1)	107.9(6)
Br(2)	Pb(1)	Br(5)	96.28(2)	C(2)	C(1)	N(1)	106.3(7)
Br(2)	Pb(1)	Br(1)	88.44(2)	N(1)	C(3)	N(2)	108.4(7)
Br(2)	Pb(1)	Br(4)	93.16(3)	C(1)	C(2)	N(2)	109.2(7)
Br(5)	Pb(1)	Br(6) ¹	81.74(3)	N(2)	C(4)	C(5)	110.7(7)
Br(3)	Pb(1)	Br(2)	93.206(19)	C(4)	C(5)	C(6)	112.7(9)
Br(3)	Pb(1)	Br(6) ¹	88.27(3)	N(3)	C(6)	C(5)	113.4(8)
Br(3)	Pb(1)	Br(5)	168.43(2)				

¹2-X,+Y,1-Z; ²1-X,+Y,1-Z

Table B5 Hydrogen Atom Coordinates ($\text{\AA}\times 10^4$) and Isotropic Displacement Parameters ($\text{\AA}^2\times 10^3$) for $\text{API}_2\text{Pb}_3\text{Br}_{10}$ at 298 K

Atom	x	y	z	U(eq)
H(1)	3811.14	4444.21	447.05	78
H(1A)	4763.97	4824.55	1664.81	70
H(3)	1866.91	5127.6	540.9	68
H(2)	3290.69	5687	2522.4	68
H(4A)	860.14	7117.55	1649.33	60
H(4B)	1243.59	6560.85	2457.35	60
H(5A)	537.06	3932.1	2243.27	81
H(5B)	191.59	4437.23	1422.51	81
H(6A)	-805.86	5707.42	2741.13	76
H(6B)	-1094.39	6407.73	1940.99	76
H(3A)	-1741.14	3826.24	1660.15	118
H(3B)	-2408.69	4651.35	2237.37	118
H(3C)	-1602.55	3358.88	2444.52	118

Appendix C

Table C1 Fractional Atomic Coordinates ($\times 10^4$) and Equivalent Isotropic Displacement Parameters ($\text{\AA}^2 \times 10^3$) for $\text{API}_2\text{Pb}_3\text{Br}_{10}$ at 240 K. U_{eq} is defined as 1/3 of the trace of the orthogonalised U_{ij} tensor

Atom	x	y	z	U(eq)
Pb(1)	6717.2(6)	6242.8(6)	2141.3(4)	29.33(15)
Pb(2)	10000	10000	5000	29.02(18)
Br(3)	6195.9(17)	7933.0(15)	4567.0(12)	34.4(3)
Br(4)	10963.0(18)	7492.4(16)	4182.5(12)	35.4(3)
Br(2)	5721.5(19)	3914.5(16)	2929.9(12)	38.3(3)
Br(5)	11926(2)	10957.1(17)	8050.7(13)	43.2(4)
Br(1)	2610.1(17)	5190.7(16)	391.6(12)	37.5(3)
N(2)	11676(14)	8763(12)	10520(9)	30(2)
N(1)	13450(16)	9133(13)	12527(10)	37(3)
C(1)	14269(18)	10226(17)	12348(12)	40(4)
C(4)	10157(18)	8043(16)	9116(12)	38(3)
C(3)	11874(18)	8213(15)	11417(12)	33(3)
N(3)	7644(16)	5196(13)	6376(10)	44(3)
C(2)	13170(17)	10047(15)	11075(12)	36(3)
C(6)	9357(19)	6434(17)	6681(12)	44(4)
C(5)	10797(19)	7191(18)	8165(12)	47(4)

Table C2 Anisotropic Displacement Parameters ($\text{\AA}^2 \times 10^3$) for $\text{API}_2\text{Pb}_3\text{Br}_{10}$ at 240 K

Atom	U ₁₁	U ₂₂	U ₃₃	U ₂₃	U ₁₃	U ₁₂
Pb(1)	25.5(2)	35.2(3)	25.2(2)	11.33(19)	10.44(18)	11.8(2)
Pb(2)	27.0(4)	32.0(5)	27.0(3)	12.2(3)	10.7(3)	11.9(3)
Br(3)	29.8(6)	42.8(9)	32.5(6)	14.9(6)	17.2(5)	14.7(6)
Br(4)	30.9(7)	46.6(9)	39.7(7)	23.9(6)	16.9(5)	22.5(7)
Br(2)	42.0(8)	38.7(9)	41.4(7)	19.7(6)	20.4(6)	20.5(7)
Br(5)	54.7(9)	54.2(10)	38.8(7)	30.5(7)	23.4(6)	30.7(8)
Br(1)	27.7(7)	46.2(9)	37.2(7)	13.6(6)	13.5(5)	18.1(6)
N(2)	36(6)	32(7)	32(5)	19(5)	16(5)	18(5)
N(1)	49(7)	43(8)	34(6)	27(5)	18(5)	25(6)
C(1)	25(7)	61(12)	29(6)	14(6)	8(5)	21(7)
C(4)	32(7)	50(10)	36(7)	20(6)	12(6)	22(7)
C(3)	37(7)	36(9)	36(7)	21(6)	23(6)	13(6)
N(3)	49(7)	43(9)	37(6)	8(5)	18(5)	23(6)
C(2)	30(7)	40(9)	39(7)	22(6)	11(6)	15(7)

C(6)	44(8)	46(10)	37(7)	16(6)	7(6)	21(8)
C(5)	36(8)	68(13)	34(7)	16(7)	17(6)	21(8)

Table C3 Bond Lengths for API₂Pb₃Br₁₀ at 240 K

Atom	Atom	Length/Å	Atom	Atom	Length/Å
Pb(1)	Br(3)	3.0084(13)	Pb(2)	Br(5)	2.9976(13)
Pb(1)	Br(4)	3.1034(14)	N(2)	C(4)	1.470(15)
Pb(1)	Br(2)	2.9486(17)	N(2)	C(3)	1.324(15)
Pb(1)	Br(5) ¹	3.0732(18)	N(2)	C(2)	1.372(17)
Pb(1)	Br(1)	2.9592(14)	N(1)	C(1)	1.305(19)
Pb(1)	Br(1) ²	3.0789(13)	N(1)	C(3)	1.324(16)
Pb(2)	Br(3)	3.0360(14)	C(1)	C(2)	1.363(16)
Pb(2)	Br(3) ¹	3.0360(14)	C(4)	C(5)	1.507(17)
Pb(2)	Br(4) ¹	3.0454(14)	N(3)	C(6)	1.494(19)
Pb(2)	Br(4)	3.0454(14)	C(6)	C(5)	1.510(16)
Pb(2)	Br(5) ¹	2.9976(13)			

¹2-X,2-Y,1-Z; ²1-X,1-Y,-Z**Table C4** Bond Angles for API₂Pb₃Br₁₀ at 240 K

Atom	Atom	Atom	Angle/°	Atom	Atom	Atom	Angle/°
Br(3)	Pb(1)	Br(4)	85.04(4)	Br(5) ¹	Pb(2)	Br(3)	83.33(4)
Br(3)	Pb(1)	Br(5) ¹	82.52(4)	Br(5)	Pb(2)	Br(3)	96.67(4)
Br(3)	Pb(1)	Br(1) ²	173.63(5)	Br(5)	Pb(2)	Br(3) ¹	83.33(4)
Br(2)	Pb(1)	Br(3)	87.38(4)	Br(5)	Pb(2)	Br(4)	96.14(4)
Br(2)	Pb(1)	Br(4)	91.73(4)	Br(5)	Pb(2)	Br(4) ¹	83.86(4)
Br(2)	Pb(1)	Br(5) ¹	168.35(4)	Br(5) ¹	Pb(2)	Br(4) ¹	96.14(4)
Br(2)	Pb(1)	Br(1)	88.07(4)	Br(5) ¹	Pb(2)	Br(4)	83.86(4)
Br(2)	Pb(1)	Br(1) ²	98.98(4)	Br(5) ¹	Pb(2)	Br(5)	180.00(6)
Br(5) ¹	Pb(1)	Br(4)	81.65(4)	Pb(1)	Br(3)	Pb(2)	79.93(3)
Br(5) ¹	Pb(1)	Br(1) ²	91.11(4)	Pb(2)	Br(4)	Pb(1)	78.31(3)
Br(1)	Pb(1)	Br(3)	90.06(4)	Pb(2)	Br(5)	Pb(1) ¹	79.51(4)
Br(1)	Pb(1)	Br(4)	175.10(4)	Pb(1)	Br(1)	Pb(1) ²	89.44(4)
Br(1) ²	Pb(1)	Br(4)	94.30(4)	C(3)	N(2)	C(4)	124.3(13)
Br(1)	Pb(1)	Br(5) ¹	97.70(5)	C(3)	N(2)	C(2)	109.3(11)
Br(1)	Pb(1)	Br(1) ²	90.56(4)	C(2)	N(2)	C(4)	126.2(11)
Br(3)	Pb(2)	Br(3) ¹	180.0	C(1)	N(1)	C(3)	110.8(10)
Br(3) ¹	Pb(2)	Br(4)	94.42(4)	N(1)	C(1)	C(2)	108.2(13)
Br(3)	Pb(2)	Br(4) ¹	94.42(4)	N(2)	C(4)	C(5)	109.0(10)

Br(3)	Pb(2)	Br(4)	85.59(4)	N(1)	C(3)	N(2)	106.7(13)
Br(3) ¹	Pb(2)	Br(4) ¹	85.58(4)	C(1)	C(2)	N(2)	105.0(13)
Br(4)	Pb(2)	Br(4) ¹	180.0	N(3)	C(6)	C(5)	115.0(12)
Br(5) ¹	Pb(2)	Br(3) ¹	96.67(4)	C(4)	C(5)	C(6)	113.4(11)

¹2-X,2-Y,1-Z; ²1-X,1-Y,-Z

Table C5 Hydrogen Atom Coordinates ($\text{\AA} \times 10^4$) and Isotropic Displacement Parameters ($\text{\AA}^2 \times 10^3$) for $\text{API}_2\text{Pb}_3\text{Br}_{10}$ at 240 K

Atom	<i>x</i>	<i>y</i>	<i>z</i>	U(eq)
H(1)	13880.41	9024.16	13273.88	44
H(1A)	15418.66	11003.11	12985.98	48
H(4A)	9887.25	8727.61	8807.04	45
H(4B)	8986.36	7431.83	9103.49	45
H(3)	11053.69	7338	11291.23	40
H(3A)	6932.14	4744.64	5460.89	53
H(3B)	6947.42	5481.86	6804.44	53
H(3C)	8022.16	4617.64	6678.91	53
H(2)	13388.02	10667.6	10667.06	43
H(6A)	8927.37	7093.58	6424	53
H(6B)	9993.09	6125.36	6099.85	53
H(5A)	11049.33	6506.25	8481.72	57
H(5B)	11997.55	7810.18	8219.03	57

Appendix D

Table D1 Fractional Atomic Coordinates ($\times 10^4$) and Equivalent Isotropic Displacement Parameters ($\text{\AA}^2 \times 10^3$) for IEAPbBr₄ at 298 K. U_{eq} is defined as 1/3 of of the trace of the orthogonalised U_{ij} tensor

Atom	x	y	z	U(eq)
Pb01	2629.6(2)	7199.9(2)	3374.9(2)	25.37(7)
Br02	4872.0(6)	6583.0(6)	4142.6(3)	38.09(16)
Br03	3160.7(9)	9721.0(5)	3355.2(3)	46.20(19)
Br04	889.1(8)	7737.6(7)	4275.3(4)	51.7(2)
Br05	-38.9(8)	7229.8(7)	2608.2(4)	54.6(2)
N006	7870(5)	4492(4)	4209(2)	34.0(12)
N007	5940(7)	4783(5)	3149(3)	48.5(16)
C008	8694(7)	5420(6)	4317(3)	41.2(17)
C009	8443(7)	5743(6)	4850(3)	42.6(16)
N00A	7470(6)	5020(6)	5052(3)	48.5(17)
C00B	7839(7)	3859(6)	3672(3)	44.3(18)
C00C	7145(7)	4269(7)	4676(3)	44.9(17)
C4	7435(7)	4551(7)	3177(4)	49(2)

Table D2 Anisotropic Displacement Parameters ($\text{\AA}^2 \times 10^3$) for IEAPbBr₄ at 298 K

Atom	U ₁₁	U ₂₂	U ₃₃	U ₂₃	U ₁₃	U ₁₂
Pb01	25.38(11)	23.52(11)	27.20(11)	-0.25(10)	0.98(9)	1.85(8)
Br02	34.5(3)	47.4(4)	32.4(3)	4.5(3)	-4.5(3)	1.1(3)
Br03	66.7(5)	20.7(3)	51.2(4)	-0.4(3)	2.1(4)	-2.3(3)
Br04	46.2(4)	54.2(4)	54.5(4)	-21.1(4)	25.6(4)	-13.3(3)
Br05	60.9(5)	48.8(5)	54.0(5)	-12.4(4)	-29.6(4)	18.6(3)
N006	35(3)	32(3)	35(3)	-3(3)	-3(3)	-1(2)
N007	63(4)	37(3)	46(4)	-1(3)	-13(3)	4(3)
C008	37(3)	43(4)	43(4)	-3(4)	3(3)	-13(3)
C009	46(4)	39(4)	43(4)	-1(4)	-2(4)	-9(3)
N00A	52(4)	61(4)	33(3)	1(3)	-1(3)	-7(3)
C00B	42(4)	36(4)	55(5)	-12(4)	-4(4)	6(3)
C00C	45(4)	46(4)	43(4)	9(4)	-1(4)	-11(3)
C4	49(4)	59(5)	40(4)	-14(4)	4(4)	-1(4)

Table D3 Bond Lengths for IEAPbBr₄ at 298 K

Atom	Atom	Length/ \AA	Atom	Atom	Length/ \AA
Pb01	Br02	2.9105(7)	N006	C00B	1.479(8)
Pb01	Br03	3.0368(7)	N006	C00C	1.334(9)

Pb01	Br03 ¹	3.0399(7)	N007	C4	1.461(8)
Pb01	Br04	2.7837(7)	C008	C009	1.344(10)
Pb01	Br05 ²	3.2296(7)	C009	N00A	1.355(9)
Pb01	Br05	3.1385(7)	N00A	C00C	1.300(10)
N006	C008	1.380(8)	C00B	C4	1.484(11)

¹1/2-X,-1/2+Y,+Z; ²1/2+X,+Y,1/2-Z

Table D4 Bond Angles for IEAPbBr₄ at 298 K.

Atom	Atom	Atom	Angle/°	Atom	Atom	Atom	Angle/°
Br02	Pb01	Br03	97.70(2)	Br04	Pb01	Br05	87.30(2)
Br02	Pb01	Br03 ¹	87.13(2)	Br05	Pb01	Br05 ²	98.393(8)
Br02	Pb01	Br05 ²	86.73(2)	Pb01	Br03	Pb01 ³	155.85(3)
Br02	Pb01	Br05	165.26(2)	Pb01	Br05	Pb01 ⁴	169.12(3)
Br03	Pb01	Br03 ¹	174.902(14)	C008	N006	C00B	125.2(6)
Br03	Pb01	Br05 ²	82.07(2)	C00C	N006	C008	107.6(6)
Br03 ¹	Pb01	Br05	78.40(2)	C00C	N006	C00B	127.1(6)
Br03 ¹	Pb01	Br05 ²	99.90(2)	C009	C008	N006	107.5(6)
Br03	Pb01	Br05	96.69(2)	C008	C009	N00A	106.0(6)
Br04	Pb01	Br02	91.20(2)	C00C	N00A	C009	110.9(7)
Br04	Pb01	Br03 ¹	94.85(2)	N006	C00B	C4	113.8(6)
Br04	Pb01	Br03	83.47(2)	N00A	C00C	N006	108.0(6)
Br04	Pb01	Br05 ²	164.97(2)	N007	C4	C00B	113.3(6)

¹1/2-X,-1/2+Y,+Z; ²1/2+X,+Y,1/2-Z; ³1/2-X,1/2+Y,+Z; ⁴-1/2+X,+Y,1/2-Z

Table D5 Hydrogen Atom Coordinates (Å×10⁴) and Isotropic Displacement Parameters (Å²×10³) for IEAPbBr₄ at 298 K.

Atom	x	y	z	U(eq)
H00A	5759.46	5207.38	2848.78	58
H00B	5676.1	5146.1	3460.07	58
H00C	5473.91	4137.1	3122.85	58
H008	9309.93	5760.15	4066.07	49
H009	8852.9	6340.89	5041.99	51
H00D	7114.81	5053.68	5385.16	58
H00E	7186.64	3238.87	3707.84	53
H00F	8756.21	3540.68	3604.19	53
H00G	6518.23	3679.18	4723.91	54
H4A	7936.71	5260.14	3191.19	59

H4B	7715.53	4162.55	2835.42	59
-----	---------	---------	---------	----

Appendix E

Table E1 Fractional Atomic Coordinates ($\times 10^4$) and Equivalent Isotropic Displacement Parameters ($\text{\AA}^2 \times 10^3$) for IMIPbBr₃ at 298 K. U_{eq} is defined as 1/3 of the trace of the orthogonalised U_{ij} tensor.

Atom	<i>x</i>	<i>y</i>	<i>z</i>	<i>U</i> (eq)
Pb(1)	5000	6666.8(2)	11062.9(2)	51.98(15)
Br(1)	5000	8111.3(8)	12500	54.1(3)
Br(2)	2832.3(9)	5944.1(6)	12500	53.9(2)
Br(3)	5000	5000	10000	90.8(5)
Br(4)	7500	7500	10000	91.1(4)
C(2AA)	6130(20)	7119(11)	7500	55(8)
C(1AA)	6083(15)	6266(13)	7831(18)	81(13)
N(1)	4610(15)	5975(11)	7750(30)	93(16)
C(0AA)	3748(16)	6650(15)	7370(30)	112(15)
N(2)	4690(30)	7357(12)	7220(20)	102(12)
C(4)	10000	5160(30)	9270(20)	120(10)
C(2)	8960(40)	4750(20)	10270(30)	80(6)
C(1)	9160(40)	4620(30)	9680(30)	92(7)
C(3)	10000	4332(19)	10230(30)	103(7)

Table E2 Anisotropic Displacement Parameters ($\text{\AA}^2 \times 10^3$) for IMIPbBr₃ at 298 K

Atom	<i>U</i> ₁₁	<i>U</i> ₂₂	<i>U</i> ₃₃	<i>U</i> ₂₃	<i>U</i> ₁₃	<i>U</i> ₁₂
Pb(1)	60.8(2)	58.3(2)	36.84(18)	0.12(13)	0	0
Br(1)	58.2(7)	42.0(6)	62.3(7)	0	0	0
Br(2)	48.2(4)	52.5(5)	61.1(5)	0	0	-5.9(3)
Br(3)	108.0(13)	88.0(12)	76.4(10)	-37.0(9)	0	0
Br(4)	96.0(8)	101.1(9)	76.3(7)	18.0(7)	32.7(6)	-8.8(7)
C(2AA)	56(17)	45(13)	70(20)	0	0	6(10)
C(1AA)	34(12)	71(14)	140(40)	28(16)	6(12)	-13(9)
N(1)	42(14)	100(14)	140(50)	7(16)	-26(14)	-24(7)
C(0AA)	48(10)	160(20)	130(40)	30(30)	10(20)	19(13)
N(2)	80(20)	108(14)	120(30)	4(14)	-14(15)	30(10)
C(4)	130(20)	150(30)	72(16)	18(16)	0	0
C(2)	73(13)	79(17)	89(14)	-27(12)	-16(11)	-41(8)
C(1)	86(15)	100(20)	85(14)	-48(12)	-31(9)	-45(11)
C(3)	126(16)	74(16)	110(19)	-5(14)	0	0

Table E3 Bond Lengths for IMIPbBr₃ at 298 K

Atom	Atom	Length/ \AA	Atom	Atom	Length/ \AA
------	------	----------------------	------	------	----------------------

Pb(1)	Br(1)	3.0209(9)	N(1)	C(0AA) ⁵	1.84(2)
Pb(1)	Br(2)	3.0229(7)	C(0AA)	C(0AA) ³	0.35(8)
Pb(1)	Br(2) ¹	3.0229(7)	C(0AA)	N(2) ³	1.51(2)
Pb(1)	Br(3)	3.0076(4)	C(0AA)	N(2) ⁵	1.89(5)
Pb(1)	Br(4)	3.0089(2)	C(0AA)	N(2)	1.4200
Pb(1)	Br(4) ²	3.0089(2)	C(0AA)	N(2) ⁴	1.82(4)
C(2AA)	C(1AA) ³	1.420(16)	N(2)	N(2) ⁴	0.57(5)
C(2AA)	C(1AA)	1.4200	N(2)	N(2) ³	0.78(6)
C(2AA)	N(1) ⁴	1.954(9)	N(2)	N(2) ⁵	0.97(5)
C(2AA)	N(1) ⁵	1.954(17)	C(4)	C(2) ⁶	1.16(4)
C(2AA)	C(0AA) ⁵	0.768(7)	C(4)	C(2) ⁷	1.80(5)
C(2AA)	C(0AA) ⁴	0.768(4)	C(4)	C(2) ⁸	1.16(4)
C(2AA)	N(2) ⁴	0.92(4)	C(4)	C(2)	1.80(5)
C(2AA)	N(2)	1.4200	C(4)	C(1) ⁶	1.67(4)
C(2AA)	N(2) ³	1.420(15)	C(4)	C(1)	1.28(5)
C(2AA)	N(2) ⁵	0.92(4)	C(4)	C(1) ⁷	1.28(5)
C(1AA)	C(1AA) ³	0.92(5)	C(4)	C(1) ⁸	1.67(4)
C(1AA)	C(1AA) ⁴	1.97(3)	C(4)	C(3)	1.87(5)
C(1AA)	N(1)	1.4200	C(4)	C(3) ⁶	1.05(5)
C(1AA)	N(1) ³	1.63(4)	C(2)	C(2) ⁸	1.09(7)
C(1AA)	N(1) ⁴	0.79(2)	C(2)	C(2) ⁷	1.90(7)
C(1AA)	N(1) ⁵	1.12(5)	C(2)	C(1) ⁶	1.98(4)
C(1AA)	C(0AA) ⁵	0.684(15)	C(2)	C(1)	0.85(5)
C(1AA)	C(0AA) ⁴	0.889(5)	C(2)	C(1) ⁷	1.90(4)
C(1AA)	N(2) ⁵	1.86(2)	C(2)	C(1) ⁸	1.02(4)
N(1)	N(1) ⁵	0.99(5)	C(2)	C(3)	1.15(4)
N(1)	N(1) ³	0.70(7)	C(2)	C(3) ⁶	1.87(4)
N(1)	N(1) ⁴	0.71(3)	C(1)	C(1) ⁷	1.53(8)
N(1)	C(0AA) ³	1.331(10)	C(1)	C(1) ⁸	1.48(7)
N(1)	C(0AA) ⁴	1.91(2)	C(1)	C(3)	1.17(5)
N(1)	C(0AA)	1.4200	C(1)	C(3) ⁶	1.82(4)

¹1-X,+Y,5/2-Z; ²-1/2+X,3/2-Y,2-Z; ³+X,+Y,3/2-Z; ⁴1-X,+Y,+Z; ⁵1-X,+Y,3/2-Z; ⁶2-X,1-Y,2-Z; ⁷2-X,+Y,+Z; ⁸+X,1-Y,2-Z

Table E4 Bond Angles for IMIPbBr₃ at 298 K

Atom	Atom	Atom	Angle/°	Atom	Atom	Atom	Angle/°
Br(1)	Pb(1)	Br(2)	81.352(19)	N(2)	C(0AA)	N(1) ⁷	90.3(5)
Br(1)	Pb(1)	Br(2) ¹	81.353(19)	N(2)	C(0AA)	N(1) ⁸	87.1(7)
Br(2) ¹	Pb(1)	Br(2)	81.40(3)	N(2)	C(0AA)	N(2) ⁷	14.4(9)

Br(3)	Pb(1)	Br(1)	168.099(19)	N(2) ⁶	C(0AA) N(2) ⁸	14.3(12)
Br(3)	Pb(1)	Br(2)	89.650(17)	N(2) ⁶	C(0AA) N(2) ⁷	32.1(17)
Br(3)	Pb(1)	Br(2) ¹	89.649(17)	N(2)	C(0AA) N(2) ⁶	30.8(19)
Br(3)	Pb(1)	Br(4) ²	98.093(7)	N(2)	C(0AA) N(2) ⁸	29.8(10)
Br(3)	Pb(1)	Br(4)	98.093(7)	N(2) ⁷	C(0AA) N(2) ⁸	24.3(10)
Br(4) ²	Pb(1)	Br(1)	89.666(13)	C(2AA) ⁸ N(2)	C(2AA)	121.6(16)
Br(4)	Pb(1)	Br(1)	89.666(13)	C(2AA) N(2)	C(1AA) ⁸	96.7(8)
Br(4)	Pb(1)	Br(2)	168.118(14)	C(2AA) ⁸ N(2)	C(1AA) ⁸	48.3(14)
Br(4) ²	Pb(1)	Br(2)	89.606(15)	C(2AA) N(2)	C(0AA) ⁸	21.3(5)
Br(4)	Pb(1)	Br(2) ¹	89.607(15)	C(2AA) ⁸ N(2)	C(0AA)	29.6(18)
Br(4) ²	Pb(1)	Br(2) ¹	168.118(14)	C(2AA) N(2)	C(0AA) ⁶	103.0(11)
Br(4) ²	Pb(1)	Br(4)	98.152(10)	C(2AA) ⁸ N(2)	C(0AA) ⁸	104.0(8)
Pb(1) ³	Br(1)	Pb(1)	82.39(3)	C(2AA) ⁸ N(2)	C(0AA) ⁷	109.6(8)
Pb(1) ³	Br(2)	Pb(1)	82.32(2)	C(2AA) N(2)	C(0AA) ⁷	23.6(5)
Pb(1)	Br(3)	Pb(1) ⁴	180.0	C(2AA) ⁸ N(2)	C(0AA) ⁶	23.9(9)
Pb(1)	Br(4)	Pb(1) ⁵	180.0	C(2AA) ⁸ N(2)	N(2) ⁸	97(2)
C(1AA) ⁶	C(2AA)	C(1AA)	37.6(19)	C(1AA) ⁸ N(2)	C(0AA) ⁸	75.6(5)
C(1AA) ⁶	C(2AA)	N(1) ⁷	34.4(16)	C(0AA) N(2)	C(2AA)	108.0
C(1AA)	C(2AA)	N(1) ⁷	19.9(7)	C(0AA) N(2)	C(1AA) ⁸	18.7(19)
C(1AA) ⁶	C(2AA)	N(1) ⁸	19.9(11)	C(0AA) ⁶ N(2)	C(1AA) ⁸	28.3(6)
C(1AA)	C(2AA)	N(1) ⁸	34.4(17)	C(0AA) ⁷ N(2)	C(1AA) ⁸	74.6(5)
C(1AA) ⁶	C(2AA)	N(2) ⁶	108.0(8)	C(0AA) N(2)	C(0AA) ⁶	13(3)
C(1AA) ⁶	C(2AA)	N(2)	97.5(7)	C(0AA) ⁷ N(2)	C(0AA) ⁸	10.7(9)
C(1AA)	C(2AA)	N(2) ⁶	97.5(8)	C(0AA) ⁶ N(2)	C(0AA) ⁸	83.1(9)
N(1) ⁷	C(2AA)	N(1) ⁸	20.6(19)	C(0AA) N(2)	C(0AA) ⁷	88.5(6)
C(0AA) ⁷	C(2AA)	C(1AA) ⁶	11(2)	C(0AA) ⁶ N(2)	C(0AA) ⁷	87.0(7)
C(0AA) ⁸	C(2AA)	C(1AA) ⁶	33.7(6)	C(0AA) N(2)	C(0AA) ⁸	86.9(6)
C(0AA) ⁸	C(2AA)	C(1AA)	11(2)	N(2) ⁶ N(2)	C(2AA) ⁸	65(3)
C(0AA) ⁷	C(2AA)	C(1AA)	33.7(6)	N(2) ⁶ N(2)	C(2AA)	74.0
C(0AA) ⁸	C(2AA)	N(1) ⁷	28.5(18)	N(2) ⁷ N(2)	C(2AA)	22.4
C(0AA) ⁷	C(2AA)	N(1) ⁸	28.5(18)	N(2) ⁷ N(2)	C(2AA) ⁸	144.0(16)
C(0AA) ⁸	C(2AA)	N(1) ⁸	37.2(14)	N(2) ⁸ N(2)	C(2AA)	40(2)
C(0AA) ⁷	C(2AA)	N(1) ⁷	37.2(14)	N(2) ⁷ N(2)	C(1AA) ⁸	112.2(10)
C(0AA) ⁸	C(2AA)	C(0AA) ⁷	27(2)	N(2) ⁶ N(2)	C(1AA) ⁸	92(2)
C(0AA) ⁸	C(2AA)	N(2) ⁸	114(2)	N(2) ⁸ N(2)	C(1AA) ⁸	104.5(18)
C(0AA) ⁸	C(2AA)	N(2)	117(2)	N(2) ⁶ N(2)	C(0AA) ⁷	83.20(9)
C(0AA) ⁸	C(2AA)	N(2) ⁶	109(2)	N(2) ⁷ N(2)	C(0AA)	127.1
C(0AA) ⁷	C(2AA)	N(2) ⁸	127(3)	N(2) ⁸ N(2)	C(0AA) ⁸	46.9(17)
C(0AA) ⁷	C(2AA)	N(2) ⁶	117(2)	N(2) ⁸ N(2)	C(0AA)	103.3(14)
C(0AA) ⁷	C(2AA)	N(2)	109(2)	N(2) ⁶ N(2)	C(0AA)	81.3
C(0AA) ⁸	C(2AA)	N(2) ⁷	127(3)	N(2) ⁷ N(2)	C(0AA) ⁷	38.6(6)

C(0AA) ⁷	C(2AA)	N(2) ⁷	114(2)	N(2) ⁸	N(2)	C(0AA) ⁶	92(3)
N(2) ⁸	C(2AA)	C(1AA)	102.8(9)	N(2) ⁸	N(2)	C(0AA) ⁷	56.4(17)
N(2) ⁸	C(2AA)	C(1AA) ⁶	120(2)	N(2) ⁷	N(2)	C(0AA) ⁸	41.3(7)
N(2) ⁷	C(2AA)	C(1AA)	119.7(15)	N(2) ⁶	N(2)	C(0AA) ⁶	68(3)
N(2) ⁷	C(2AA)	C(1AA) ⁶	102.8(12)	N(2) ⁶	N(2)	C(0AA) ⁸	72.5(9)
N(2)	C(2AA)	C(1AA)	108.0	N(2) ⁷	N(2)	C(0AA) ⁶	124.4(8)
N(2)	C(2AA)	N(1) ⁷	88.4(7)	N(2) ⁶	N(2)	N(2) ⁸	36(2)
N(2)	C(2AA)	N(1) ⁸	82.8(11)	N(2) ⁷	N(2)	N(2) ⁸	54(2)
N(2) ⁶	C(2AA)	N(1) ⁸	88.4(10)	N(2) ⁷	N(2)	N(2) ⁶	90.0
N(2) ⁶	C(2AA)	N(1) ⁷	82.8(8)	C(2) ⁹	C(4)	C(2) ¹⁰	110(5)
N(2) ⁸	C(2AA)	N(1) ⁷	91.0(13)	C(2) ⁹	C(4)	C(2)	93(3)
N(2) ⁷	C(2AA)	N(1) ⁷	99.8(17)	C(2) ¹⁰	C(4)	C(2) ¹¹	93(3)
N(2) ⁷	C(2AA)	N(1) ⁸	91.0(16)	C(2) ¹⁰	C(4)	C(2)	35(3)
N(2) ⁸	C(2AA)	N(1) ⁸	99.8(19)	C(2) ⁹	C(4)	C(2) ¹¹	35(3)
N(2) ⁷	C(2AA)	N(2) ⁶	42(2)	C(2) ¹¹	C(4)	C(2)	64(2)
N(2) ⁸	C(2AA)	N(2) ⁷	50(3)	C(2) ⁹	C(4)	C(1)	109(4)
N(2)	C(2AA)	N(2) ⁶	32(2)	C(2) ⁹	C(4)	C(1) ¹¹	49(2)
N(2) ⁸	C(2AA)	N(2)	42(3)	C(2) ¹⁰	C(4)	C(1)	49(2)
N(2) ⁷	C(2AA)	N(2)	13.5(17)	C(2) ¹⁰	C(4)	C(1) ¹¹	109(4)
N(2) ⁸	C(2AA)	N(2) ⁶	13.5(19)	C(2) ¹⁰	C(4)	C(1) ⁹	82(3)
C(2AA)	C(1AA)	C(1AA) ⁷	91.8	C(2) ⁹	C(4)	C(1) ¹⁰	82(3)
C(2AA)	C(1AA)	N(1) ⁶	97.5(10)	C(2) ¹⁰	C(4)	C(1) ¹⁰	28(3)
C(2AA)	C(1AA)	N(2) ⁸	29.0(11)	C(2) ⁹	C(4)	C(1) ⁹	28(3)
C(1AA) ⁶	C(1AA)	C(2AA)	71.2	C(2)	C(4)	C(3)	36.5(14)
C(1AA) ⁶	C(1AA)	C(1AA) ⁷	90.0	C(2) ¹⁰	C(4)	C(3)	72(2)
C(1AA) ⁶	C(1AA)	N(1) ⁸	44(3)	C(2) ¹¹	C(4)	C(3)	36.5(14)
C(1AA) ⁶	C(1AA)	N(1)	85.6	C(2) ⁹	C(4)	C(3)	72(2)
C(1AA) ⁶	C(1AA)	N(1) ⁶	60(2)	C(1) ⁹	C(4)	C(2)	69.5(19)
C(1AA) ⁶	C(1AA)	N(2) ⁸	88.0(11)	C(1)	C(4)	C(2)	25.7(17)
N(1)	C(1AA)	C(2AA)	108.0	C(1)	C(4)	C(2) ¹¹	74(2)
N(1) ⁷	C(1AA)	C(2AA)	122.0(9)	C(1) ¹¹	C(4)	C(2) ¹¹	25.6(17)
N(1) ⁸	C(1AA)	C(2AA)	99.9(15)	C(1) ¹⁰	C(4)	C(2)	33.8(16)
N(1) ⁷	C(1AA)	C(1AA) ⁷	36.7(12)	C(1) ⁹	C(4)	C(2) ¹¹	33.8(16)
N(1) ⁸	C(1AA)	C(1AA) ⁷	56(2)	C(1) ¹⁰	C(4)	C(2) ¹¹	69.5(19)
N(1)	C(1AA)	C(1AA) ⁷	19.3	C(1) ¹¹	C(4)	C(2)	74(2)
N(1) ⁷	C(1AA)	C(1AA) ⁶	82.0(2)	C(1) ⁹	C(4)	C(1) ¹⁰	54(3)
N(1) ⁶	C(1AA)	C(1AA) ⁷	34.7(18)	C(1)	C(4)	C(1) ¹⁰	58(3)
N(1) ⁷	C(1AA)	N(1)	17.4(12)	C(1) ¹¹	C(4)	C(1) ¹⁰	91(2)
N(1) ⁸	C(1AA)	N(1)	44(3)	C(1) ¹¹	C(4)	C(1) ⁹	58(3)
N(1)	C(1AA)	N(1) ⁶	25(2)	C(1)	C(4)	C(1) ¹¹	73(5)
N(1) ⁷	C(1AA)	N(1) ⁸	38(3)	C(1)	C(4)	C(1) ⁹	91(2)

N(1) ⁷	C(1AA)	N(1) ⁶	27.0(17)	C(1) ⁹	C(4)	C(3)	62(2)
N(1) ⁸	C(1AA)	N(1) ⁶	21.1(12)	C(1) ¹¹	C(4)	C(3)	38(2)
N(1) ⁷	C(1AA)	C(0AA) ⁷	115.7(17)	C(1)	C(4)	C(3)	38(2)
N(1) ⁷	C(1AA)	N(2) ⁸	103(2)	C(1) ¹⁰	C(4)	C(3)	62(2)
N(1) ⁶	C(1AA)	N(2) ⁸	86.0(16)	C(3) ⁹	C(4)	C(2)	77(3)
N(1) ⁸	C(1AA)	N(2) ⁸	98.0(13)	C(3) ⁹	C(4)	C(2) ¹¹	77(3)
N(1)	C(1AA)	N(2) ⁸	86.4(16)	C(3) ⁹	C(4)	C(2) ¹⁰	63(3)
C(0AA) ⁸	C(1AA)	C(2AA)	13(2)	C(3) ⁹	C(4)	C(2) ⁹	63(3)
C(0AA) ⁷	C(1AA)	C(2AA)	28.6(5)	C(3) ⁹	C(4)	C(1) ¹⁰	44(2)
C(0AA) ⁷	C(1AA)	C(1AA) ⁶	44.5(3)	C(3) ⁹	C(4)	C(1) ⁹	44(2)
C(0AA) ⁷	C(1AA)	C(1AA) ⁷	99.9(18)	C(3) ⁹	C(4)	C(1)	102(3)
C(0AA) ⁸	C(1AA)	C(1AA) ⁶	66(2)	C(3) ⁹	C(4)	C(1) ¹¹	102(3)
C(0AA) ⁸	C(1AA)	C(1AA) ⁷	103(2)	C(3) ⁹	C(4)	C(3)	93(3)
C(0AA) ⁸	C(1AA)	N(1)	118(2)	C(4) ⁹	C(2)	C(4)	87(3)
C(0AA) ⁸	C(1AA)	N(1) ⁶	103(3)	C(4) ⁹	C(2)	C(2) ¹¹	35(3)
C(0AA) ⁷	C(1AA)	N(1) ⁸	82(2)	C(4)	C(2)	C(2) ¹¹	58.2(12)
C(0AA) ⁸	C(1AA)	N(1) ⁸	101(4)	C(4) ⁹	C(2)	C(1) ⁹	38(2)
C(0AA) ⁸	C(1AA)	N(1) ⁷	130(3)	C(4)	C(2)	C(1) ¹¹	40.4(16)
C(0AA) ⁷	C(1AA)	N(1)	109.1(17)	C(4) ⁹	C(2)	C(1) ¹¹	61(2)
C(0AA) ⁷	C(1AA)	N(1) ⁶	89(2)	C(4)	C(2)	C(1) ⁹	52.3(16)
C(0AA) ⁸	C(1AA)	C(0AA) ⁷	21(2)	C(4)	C(2)	C(3) ⁹	33.4(16)
C(0AA) ⁸	C(1AA)	N(2) ⁸	41.7(18)	C(4) ⁹	C(2)	C(3) ⁹	72(2)
C(0AA) ⁷	C(1AA)	N(2) ⁸	53.9(7)	C(2) ¹⁰	C(2)	C(4)	38.0(19)
N(2) ⁸	C(1AA)	C(1AA) ⁷	67.8(15)	C(2) ¹⁰	C(2)	C(4) ⁹	107(3)
C(1AA) ⁶	N(1)	C(2AA) ⁸	86.4(12)	C(2) ¹⁰	C(2)	C(2) ¹¹	90.00(3)
C(1AA) ⁸	N(1)	C(2AA) ⁸	45.7(14)	C(2) ¹⁰	C(2)	C(1) ⁹	69.7(18)
C(1AA)	N(1)	C(2AA) ⁸	92.5(14)	C(2) ¹¹	C(2)	C(1) ⁹	30.3(13)
C(1AA) ⁷	N(1)	C(2AA) ⁸	38.0(12)	C(2) ¹⁰	C(2)	C(1) ¹¹	78(2)
C(1AA)	N(1)	C(1AA) ⁶	34.1(15)	C(2) ¹¹	C(2)	C(1) ¹¹	25.9(12)
C(1AA) ⁸	N(1)	C(1AA) ⁶	90(3)	C(2) ¹⁰	C(2)	C(3) ⁹	35(2)
C(1AA) ⁷	N(1)	C(1AA) ⁸	54(3)	C(2) ¹⁰	C(2)	C(3)	113(4)
C(1AA) ⁸	N(1)	C(1AA)	117(2)	C(1)	C(2)	C(4) ⁹	112(5)
C(1AA) ⁷	N(1)	C(1AA) ⁶	124.4(10)	C(1) ¹⁰	C(2)	C(4)	66(3)
C(1AA) ⁷	N(1)	C(1AA)	124.0(12)	C(1) ¹⁰	C(2)	C(4) ⁹	72(4)
C(1AA) ⁷	N(1)	N(1) ⁸	132.0(18)	C(1)	C(2)	C(4)	41(3)
C(1AA) ⁷	N(1)	C(0AA) ⁶	23(3)	C(1)	C(2)	C(2) ¹¹	77(4)
C(1AA)	N(1)	C(0AA) ⁸	19.2(6)	C(1) ¹⁰	C(2)	C(2) ¹¹	79(3)
C(1AA) ⁷	N(1)	C(0AA) ⁷	110.1(8)	C(1) ¹⁰	C(2)	C(2) ¹⁰	47(3)
C(1AA) ⁸	N(1)	C(0AA) ⁶	41.4(9)	C(1)	C(2)	C(2) ¹⁰	62(4)
C(1AA) ⁷	N(1)	C(0AA)	34.3(4)	C(1)	C(2)	C(1) ⁹	88(3)
C(1AA) ⁶	N(1)	C(0AA) ⁸	28.9(5)	C(1)	C(2)	C(1) ¹¹	52(4)

C(1AA)	N(1)	C(0AA) ⁷	26.2(5)	C(1)	C(2)	C(1) ¹⁰	105(5)
C(1AA) ⁸	N(1)	C(0AA) ⁷	90.9(19)	C(1) ¹¹	C(2)	C(1) ⁹	45(2)
C(1AA) ⁷	N(1)	C(0AA) ⁸	109.2(8)	C(1) ¹⁰	C(2)	C(1) ¹¹	88(3)
C(1AA) ⁸	N(1)	C(0AA)	28(2)	C(1) ¹⁰	C(2)	C(1) ⁹	49(4)
C(1AA) ⁸	N(1)	C(0AA) ⁸	98.9(18)	C(1) ¹⁰	C(2)	C(3)	114(4)
C(1AA) ⁶	N(1)	C(0AA) ⁷	20.4(10)	C(1)	C(2)	C(3) ⁹	74(4)
N(1) ⁷	N(1)	C(2AA) ⁸	110.2(13)	C(1)	C(2)	C(3)	69(5)
N(1) ⁸	N(1)	C(2AA) ⁸	97.0(15)	C(1) ¹⁰	C(2)	C(3) ⁹	34(3)
N(1) ⁶	N(1)	C(2AA) ⁸	79.7(12)	C(3)	C(2)	C(4)	75(3)
N(1) ⁷	N(1)	C(1AA) ⁸	124(3)	C(3)	C(2)	C(4) ⁹	54(3)
N(1) ⁶	N(1)	C(1AA) ⁷	98.0(2)	C(3) ⁹	C(2)	C(2) ¹¹	59.4(14)
N(1) ⁶	N(1)	C(1AA) ⁶	60.3(15)	C(3)	C(2)	C(2) ¹¹	34.5(19)
N(1) ⁸	N(1)	C(1AA)	52(3)	C(3) ⁹	C(2)	C(1) ⁹	35.1(15)
N(1) ⁷	N(1)	C(1AA) ⁶	34.7(13)	C(3)	C(2)	C(1) ⁹	65(2)
N(1) ⁷	N(1)	C(1AA)	19.3	C(3) ⁹	C(2)	C(1) ¹¹	57.8(17)
N(1) ⁷	N(1)	C(1AA) ⁷	143.3(12)	C(3)	C(2)	C(1) ¹¹	35(3)
N(1) ⁶	N(1)	C(1AA) ⁸	44(3)	C(3)	C(2)	C(3) ⁹	90(3)
N(1) ⁸	N(1)	C(1AA) ⁶	21.0(9)	C(4)	C(1)	C(4) ⁹	89(2)
N(1) ⁸	N(1)	C(1AA) ⁸	84(5)	C(4)	C(1)	C(2) ¹¹	66(2)
N(1) ⁶	N(1)	C(1AA)	94.4	C(4) ⁹	C(1)	C(2) ¹¹	37.0(13)
N(1) ⁶	N(1)	N(1) ⁸	45(3)	C(4)	C(1)	C(2) ⁹	33.5(18)
N(1) ⁷	N(1)	N(1) ⁸	45(3)	C(4) ⁹	C(1)	C(2) ⁹	58.2(17)
N(1) ⁶	N(1)	N(1) ⁷	90.0	C(4)	C(1)	C(1) ¹⁰	74(3)
N(1) ⁷	N(1)	C(0AA) ⁸	35.7(5)	C(4)	C(1)	C(1) ¹¹	53(2)
N(1) ⁷	N(1)	C(0AA) ⁷	38.4(5)	C(4) ⁹	C(1)	C(3) ⁹	64.4(18)
N(1) ⁸	N(1)	C(0AA) ⁷	41.2(17)	C(4)	C(1)	C(3) ⁹	35(2)
N(1) ⁷	N(1)	C(0AA)	123.5	C(2) ¹⁰	C(1)	C(4)	59(3)
N(1) ⁸	N(1)	C(0AA)	98(2)	C(2) ¹⁰	C(1)	C(4) ⁹	80(3)
N(1) ⁸	N(1)	C(0AA) ⁶	109(3)	C(2)	C(1)	C(4)	114(4)
N(1) ⁸	N(1)	C(0AA) ⁸	49.9(14)	C(2)	C(1)	C(4) ⁹	40(3)
N(1) ⁷	N(1)	C(0AA) ⁶	126.1(3)	C(2)	C(1)	C(2) ¹¹	77(4)
N(1) ⁶	N(1)	C(0AA) ⁶	83(3)	C(2) ¹⁰	C(1)	C(2) ⁹	70(4)
N(1) ⁶	N(1)	C(0AA)	68.3	C(2)	C(1)	C(2) ⁹	92(3)
N(1) ⁶	N(1)	C(0AA) ⁸	84.6(9)	C(2) ¹⁰	C(1)	C(2) ¹¹	92(3)
N(1) ⁶	N(1)	C(0AA) ⁷	74.0(2)	C(2) ¹¹	C(1)	C(2) ⁹	32(2)
C(0AA)	N(1)	C(2AA) ⁸	19.1(14)	C(2)	C(1)	C(2) ¹⁰	71(5)
C(0AA) ⁷	N(1)	C(2AA) ⁸	73.1(9)	C(2) ¹⁰	C(1)	C(1) ¹⁰	34(3)
C(0AA) ⁸	N(1)	C(2AA) ⁸	74.5(9)	C(2) ¹⁰	C(1)	C(1) ¹¹	101(3)
C(0AA) ⁶	N(1)	C(2AA) ⁸	16.0(15)	C(2)	C(1)	C(1) ¹⁰	42(3)
C(0AA) ⁶	N(1)	C(1AA) ⁶	101.4(19)	C(2)	C(1)	C(1) ¹¹	103(4)
C(0AA)	N(1)	C(1AA)	108.0	C(2) ¹⁰	C(1)	C(3)	117(4)

C(0AA) ⁶ N(1)	C(1AA)	108.03(14)	C(2)	C(1)	C(3)	67(4)
C(0AA) N(1)	C(1AA) ⁶	93.5(7)	C(2)	C(1)	C(3) ⁹	80(3)
C(0AA) ⁸ N(1)	C(0AA) ⁷	10.6(9)	C(2) ¹⁰	C(1)	C(3) ⁹	35(3)
C(0AA) N(1)	C(0AA) ⁸	89.0(6)	C(1) ¹⁰	C(1)	C(4) ⁹	47(2)
C(0AA) ⁶ N(1)	C(0AA) ⁸	90.4(7)	C(1) ¹¹	C(1)	C(4) ⁹	62.9(15)
C(0AA) ⁶ N(1)	C(0AA)	14(3)	C(1) ¹¹	C(1)	C(2) ⁹	30.3(13)
C(0AA) N(1)	C(0AA) ⁷	85.1(5)	C(1) ¹⁰	C(1)	C(2) ¹¹	70.5(15)
C(0AA) ⁶ N(1)	C(0AA) ⁷	89.0(9)	C(1) ¹¹	C(1)	C(2) ¹¹	25.9(12)
C(2AA) ⁸ C(0AA)	C(1AA) ⁷	118(3)	C(1) ¹⁰	C(1)	C(2) ⁹	64.7(16)
C(2AA) ⁸ C(0AA) N(1)		124(3)	C(1) ¹⁰	C(1)	C(1) ¹¹	89.999(19)
C(2AA) ⁸ C(0AA) N(1) ⁸		117(3)	C(1) ¹⁰	C(1)	C(3) ⁹	40(2)
C(2AA) ⁸ C(0AA) N(1) ⁶		136(3)	C(1) ¹¹	C(1)	C(3) ⁹	65.2(14)
C(2AA) ⁸ C(0AA) N(1) ⁷		111(3)	C(3)	C(1)	C(4) ⁹	39(2)
C(2AA) ⁸ C(0AA) N(2)		36(3)	C(3)	C(1)	C(4)	99(3)
C(2AA) ⁸ C(0AA) N(2) ⁷		48(2)	C(3) ⁹	C(1)	C(2) ¹¹	60.1(15)
C(2AA) ⁸ C(0AA) N(2) ⁶		29(3)	C(3)	C(1)	C(2) ¹¹	34.6(19)
C(2AA) ⁸ C(0AA) N(2) ⁸		42.1(18)	C(3)	C(1)	C(2) ⁹	67(2)
C(1AA) ⁸ C(0AA) C(2AA) ⁸		156(6)	C(3) ⁹	C(1)	C(2) ⁹	34.9(14)
C(1AA) ⁸ C(0AA) C(1AA) ⁷		70(6)	C(3)	C(1)	C(1) ¹⁰	86(3)
C(1AA) ⁸ C(0AA) N(1) ⁶		27.1(18)	C(3)	C(1)	C(1) ¹¹	49(2)
C(1AA) ⁸ C(0AA) N(1)		51(5)	C(3)	C(1)	C(3) ⁹	92(2)
C(1AA) ⁷ C(0AA) N(1) ⁸		62(2)	C(4) ⁹	C(3)	C(4)	87(3)
C(1AA) ⁸ C(0AA) N(1) ⁸		43.1(15)	C(4) ⁹	C(3)	C(2) ⁹	70(3)
C(1AA) ⁷ C(0AA) N(1) ⁶		57(3)	C(4) ⁹	C(3)	C(2)	63(2)
C(1AA) ⁷ C(0AA) N(1)		29.9(14)	C(4) ⁹	C(3)	C(2) ¹¹	63(2)
C(1AA) ⁷ C(0AA) N(1) ⁷		44.8(13)	C(4) ⁹	C(3)	C(2) ¹⁰	70(3)
C(1AA) ⁸ C(0AA) N(1) ⁷		56(3)	C(4) ⁹	C(3)	C(1)	98(3)
C(1AA) ⁷ C(0AA) N(2) ⁷		111(2)	C(4) ⁹	C(3)	C(1) ¹⁰	44(2)
C(1AA) ⁸ C(0AA) N(2)		120(4)	C(4) ⁹	C(3)	C(1) ⁹	44(2)
C(1AA) ⁷ C(0AA) N(2)		122.5(14)	C(4) ⁹	C(3)	C(1) ¹¹	98(3)
C(1AA) ⁸ C(0AA) N(2) ⁶		133(3)	C(2) ⁹	C(3)	C(4)	36.1(13)
C(1AA) ⁷ C(0AA) N(2) ⁸		93(2)	C(2) ¹¹	C(3)	C(4)	69(3)
C(1AA) ⁷ C(0AA) N(2) ⁶		98(2)	C(2)	C(3)	C(4)	69(3)
C(1AA) ⁸ C(0AA) N(2) ⁷		108(4)	C(2) ¹⁰	C(3)	C(4)	36.1(13)
C(1AA) ⁸ C(0AA) N(2) ⁸		118(3)	C(2) ¹¹	C(3)	C(2)	111(4)
N(1) ⁶ C(0AA) N(1) ⁸		18.2(7)	C(2)	C(3)	C(2) ⁹	90(3)
N(1) C(0AA) N(1) ⁷		18.1(5)	C(2) ⁹	C(3)	C(2) ¹⁰	61(3)
N(1) ⁶ C(0AA) N(1) ⁷		30(2)	C(2) ¹¹	C(3)	C(2) ¹⁰	90(3)
N(1) C(0AA) N(1) ⁸		32.4(17)	C(2)	C(3)	C(2) ¹⁰	33(3)
N(1) ⁶ C(0AA) N(1)		29(3)	C(2) ¹¹	C(3)	C(2) ⁹	33(3)
N(1) ⁸ C(0AA) N(1) ⁷		21(2)	C(2) ¹¹	C(3)	C(1) ¹¹	43(2)

N(1) ⁶	C(0AA)	N(2) ⁷	90.7(10)	C(2) ¹¹	C(3)	C(1)	110(4)
N(1) ⁶	C(0AA)	N(2) ⁸	93.7(14)	C(2) ¹¹	C(3)	C(1) ⁹	31(2)
N(1) ⁸	C(0AA)	N(2) ⁸	76.0(13)	C(2) ¹¹	C(3)	C(1) ¹⁰	80(3)
N(1) ⁶	C(0AA)	N(2) ⁶	107.6(11)	C(2)	C(3)	C(1)	43(2)
N(1) ⁶	C(0AA)	N(2)	104.5(6)	C(2)	C(3)	C(1) ¹⁰	31(2)
N(1)	C(0AA)	N(2) ⁷	94.0(9)	C(2)	C(3)	C(1) ¹¹	110(4)
N(1)	C(0AA)	N(2) ⁶	95.6(9)	C(2)	C(3)	C(1) ⁹	80(3)
N(1)	C(0AA)	N(2) ⁸	85.0(10)	C(1)	C(3)	C(4)	43(2)
C(0AA) ⁶	C(0AA)	C(2AA) ⁸	77(3)	C(1) ⁹	C(3)	C(4)	54.0(18)
C(0AA) ⁶	C(0AA)	C(1AA) ⁸	114(6)	C(1) ¹¹	C(3)	C(4)	43(2)
C(0AA) ⁶	C(0AA)	C(1AA) ⁷	44.5(3)	C(1) ¹⁰	C(3)	C(4)	54.0(18)
C(0AA) ⁶	C(0AA)	N(1) ⁶	97(3)	C(1) ¹¹	C(3)	C(2) ¹⁰	78(3)
C(0AA) ⁶	C(0AA)	N(1)	68.3	C(1) ⁹	C(3)	C(2) ¹⁰	62.1(18)
C(0AA) ⁶	C(0AA)	N(1) ⁷	74.0(2)	C(1)	C(3)	C(2) ⁹	78(3)
C(0AA) ⁶	C(0AA)	N(1) ⁸	95(2)	C(1) ¹⁰	C(3)	C(2) ⁹	62.1(18)
C(0AA) ⁶	C(0AA)	N(2) ⁸	72.5(9)	C(1) ¹¹	C(3)	C(2) ⁹	29(2)
C(0AA) ⁶	C(0AA)	N(2) ⁷	96.81(15)	C(1)	C(3)	C(2) ¹⁰	29(2)
C(0AA) ⁶	C(0AA)	N(2) ⁶	68(2)	C(1) ⁹	C(3)	C(2) ⁹	26.7(15)
C(0AA) ⁶	C(0AA)	N(2)	98.74(7)	C(1) ¹⁰	C(3)	C(2) ¹⁰	26.7(15)
N(2) ⁸	C(0AA)	N(1) ⁷	69.9(11)	C(1) ⁹	C(3)	C(1) ¹⁰	50(3)
N(2) ⁷	C(0AA)	N(1) ⁷	76.1(11)	C(1)	C(3)	C(1) ⁹	88(2)
N(2) ⁶	C(0AA)	N(1) ⁷	82.1(6)	C(1)	C(3)	C(1) ¹⁰	54(3)
N(2) ⁶	C(0AA)	N(1) ⁸	90.0(11)	C(1) ¹¹	C(3)	C(1) ¹⁰	88(2)
N(2) ⁷	C(0AA)	N(1) ⁸	73.0(12)	C(1) ¹¹	C(3)	C(1)	82(5)
N(2)	C(0AA)	N(1)	108.0	C(1) ¹¹	C(3)	C(1) ⁹	54(3)

¹1-X,+Y,5/2-Z; ²-1/2+X,3/2-Y,2-Z; ³+X,+Y,5/2-Z; ⁴1-X,1-Y,2-Z; ⁵3/2-X,3/2-Y,2-Z;
⁶+X,+Y,3/2-Z; ⁷1-X,+Y,+Z; ⁸1-X,+Y,3/2-Z; ⁹2-X,1-Y,2-Z; ¹⁰+X,1-Y,2-Z; ¹¹2-X,+Y,+Z

Table E5 Atomic Occupancy for IMIPbBr₃ at 298 K

Atom	Occupancy	Atom	Occupancy	Atom	Occupancy
C(2AA)	0.25	C(1AA)	0.25	N(1)	0.25
C(0AA)	0.25	N(2)	0.25	C(4)	0.5
C(2)	0.25	C(1)	0.25	C(3)	0.5

Appendix F

Table F1 Fractional Atomic Coordinates ($\times 10^4$) and Equivalent Isotropic Displacement Parameters ($\text{\AA}^2 \times 10^3$) for IMIPbBr₃ at 220 K. U_{eq} is defined as 1/3 of of the trace of the orthogonalised U_{ij} tensor

Atom	<i>x</i>	<i>y</i>	<i>z</i>	<i>U</i> (eq)
Pb(1)	2238.0(7)	11440.3(5)	4573.4(2)	31.53(14)
Pb(2)	1983.8(6)	8564.1(5)	4620.7(2)	30.38(14)
Pb(3)	2667.4(6)	6413.2(5)	2958.2(2)	31.75(15)
Pb(4)	2369.4(6)	3567.3(5)	2852.4(2)	31.83(15)
Br(8)	285.3(16)	5026.7(15)	3261.8(5)	34.3(4)
Br(4)	4325.4(17)	9900.7(14)	4227.2(5)	34.6(4)
Br(2)	11.8(17)	10088.6(16)	4200.3(5)	36.2(4)
Br(9)	2574.6(17)	5120.7(13)	2177.6(6)	37.7(4)
Br(10)	4603.0(18)	4823.3(14)	3298.6(6)	37.9(4)
Br(3)	2093.6(18)	10096.4(12)	5320.7(5)	37.7(4)
Br(7)	259(2)	7655.5(16)	2592.4(7)	53.3(6)
Br(6)	2294(3)	7438.6(16)	3804.6(6)	53.1(5)
Br(11)	2267(3)	2442.7(16)	3690.2(7)	55.5(5)
Br(1)	-137(2)	12613.9(18)	4969.4(8)	57.4(6)
Br(12)	4729(2)	2480.9(18)	2392.1(8)	61.1(7)
Br(5)	4357(3)	7449.5(19)	5036.8(9)	68.4(7)
C(7)	2010(20)	4782(13)	4197(5)	81(8)
N(6)	3255(15)	4528(13)	4445(7)	142(11)
C(9)	3000(20)	4824(14)	4876(6)	137(14)
C(8)	1590(30)	5262(12)	4895(6)	119(12)
N(5)	980(14)	5237(13)	4475(7)	140(11)
C(11)	6330(20)	6923(14)	3908(6)	96(9)
C(12)	7640(30)	6595(13)	3713(7)	120(10)
N(8)	8454(17)	7420(20)	3580(7)	194(17)
C(10)	7640(20)	8259(13)	3693(7)	112(10)
N(7)	6326(19)	7951(14)	3896(5)	94(7)
C(2)	2110(20)	9893(12)	3279(5)	70(6)
C(3)	3444(16)	9646(12)	3070(6)	85(8)
N(2)	3350(20)	9963(14)	2636(5)	123(9)
C(1)	1960(30)	10407(13)	2577(6)	133(13)
N(1)	1197(14)	10364(12)	2975(9)	140(11)
C(5)	4062(17)	7163(15)	1316(8)	151(15)
N(3)	3220(20)	7570(14)	1655(5)	109(8)
C(4)	1840(20)	7842(13)	1483(6)	103(10)
N(4)	1830(20)	7602(15)	1039(6)	141(10)

C(6) 3200(30) 7182(16) 936(6) 138(14)

Table F2 Anisotropic Displacement Parameters ($\text{\AA}^2 \times 10^3$) for IMIPbBr₃ at 220 K

Atom	U ₁₁	U ₂₂	U ₃₃	U ₂₃	U ₁₃	U ₁₂
Pb(1)	33.2(3)	23.3(3)	38.2(3)	-0.4(3)	2.4(3)	-0.6(3)
Pb(2)	32.3(3)	24.7(3)	34.2(3)	0.1(3)	1.0(3)	-0.6(3)
Pb(3)	32.9(3)	25.7(3)	36.7(3)	-2.4(3)	3.0(3)	-1.0(3)
Pb(4)	33.1(3)	24.7(3)	37.7(3)	-2.2(3)	4.1(3)	-0.2(3)
Br(8)	30.9(8)	35.8(10)	36.2(10)	0.6(8)	3.9(7)	0.6(8)
Br(4)	31.8(8)	34.9(10)	37.2(10)	-1.6(8)	4.1(7)	0.1(8)
Br(2)	32.2(8)	39.8(11)	36.6(10)	-0.8(9)	-4.0(7)	-1.5(8)
Br(9)	43.3(9)	39.6(11)	30.2(9)	-1.1(7)	3.4(7)	0.1(9)
Br(10)	33.9(9)	36.9(12)	43.0(11)	-0.9(9)	-5.1(7)	-0.3(8)
Br(3)	42.7(9)	39.8(11)	30.5(9)	1.2(7)	0.7(7)	-0.2(9)
Br(7)	52.2(12)	49.4(14)	58.5(14)	10.4(10)	-9.6(10)	12.6(10)
Br(6)	60.9(12)	49.9(12)	48.5(11)	-19.5(9)	2.4(10)	-4.8(10)
Br(11)	69.8(13)	43.2(11)	53.6(12)	17.7(10)	-0.4(11)	-3.6(10)
Br(1)	56.4(13)	49.2(14)	66.6(14)	-11.8(11)	6.1(11)	19.5(11)
Br(12)	53.8(13)	47.7(13)	81.7(18)	-11.5(12)	16.8(12)	14.0(11)
Br(5)	57.0(14)	54.2(14)	94.0(18)	15.7(12)	-26.2(13)	15.0(12)
C(7)	80(15)	110(20)	50(13)	-2(13)	-9(11)	25(16)
N(6)	68(14)	180(30)	180(20)	0(20)	10(15)	23(17)
C(9)	200(30)	100(30)	110(20)	-20(20)	-90(20)	30(20)
C(8)	190(30)	80(20)	84(18)	14(17)	78(18)	40(20)
N(5)	64(14)	160(30)	190(30)	10(20)	25(16)	44(16)
C(11)	100(20)	80(16)	110(20)	28(17)	0(16)	2(15)
C(12)	150(30)	130(20)	90(20)	-21(18)	-28(18)	50(20)
N(8)	160(30)	190(30)	230(40)	30(30)	120(30)	50(20)
C(10)	140(20)	81(18)	120(20)	3(17)	-35(18)	-51(16)
N(7)	88(15)	103(15)	89(16)	-9(14)	18(13)	41(13)
C(2)	112(17)	49(14)	50(13)	6(10)	38(12)	7(14)
C(3)	76(16)	66(17)	114(19)	26(16)	7(14)	18(14)
N(2)	190(20)	100(20)	73(16)	12(13)	45(16)	-30(20)
C(1)	200(30)	80(20)	120(20)	40(20)	-90(20)	-40(20)
N(1)	77(15)	80(20)	260(30)	-10(20)	-32(17)	14(14)
C(5)	150(30)	140(30)	170(30)	20(30)	20(20)	80(30)
N(3)	140(20)	102(19)	88(16)	24(13)	-29(14)	-11(16)
C(4)	78(17)	120(20)	107(19)	-17(19)	46(15)	36(17)
N(4)	120(20)	200(30)	106(18)	10(20)	-25(17)	30(20)
C(6)	100(20)	170(40)	150(30)	-60(30)	45(19)	-10(20)

Table F3 Bond Lengths for IMIPbBr₃ at 220 K

Atom	Atom	Length/Å	Atom	Atom	Length/Å
Pb(1)	Br(4)	3.0504(19)	Pb(4)	Br(11)	3.032(2)
Pb(1)	Br(2)	2.9925(19)	Pb(4)	Br(12)	2.989(2)
Pb(1)	Br(3)	2.9752(18)	C(7)	N(6)	1.4200
Pb(1)	Br(11) ¹	3.074(2)	C(7)	N(5)	1.4200
Pb(1)	Br(1)	2.973(2)	N(6)	C(9)	1.4200
Pb(1)	Br(1) ²	3.076(2)	C(9)	C(8)	1.4200
Pb(2)	Br(4)	3.0769(18)	C(8)	N(5)	1.4200
Pb(2)	Br(2)	3.062(2)	C(11)	C(12)	1.4200
Pb(2)	Br(3)	3.0358(18)	C(11)	N(7)	1.4200
Pb(2)	Br(6)	2.987(2)	C(12)	N(8)	1.4200
Pb(2)	Br(5)	2.955(2)	N(8)	C(10)	1.4200
Pb(2)	Br(5) ³	2.973(2)	C(10)	N(7)	1.4200
Pb(3)	Br(8)	3.0463(18)	C(2)	C(3)	1.4200
Pb(3)	Br(9)	3.0123(18)	C(2)	N(1)	1.4200
Pb(3)	Br(10)	3.009(2)	C(3)	N(2)	1.4200
Pb(3)	Br(7)	3.011(2)	N(2)	C(1)	1.4200
Pb(3)	Br(6)	3.006(2)	C(1)	N(1)	1.4200
Pb(3)	Br(12) ⁴	3.000(2)	C(5)	N(3)	1.4200
Pb(4)	Br(8)	3.0489(19)	C(5)	C(6)	1.4200
Pb(4)	Br(9)	3.005(2)	N(3)	C(4)	1.4200
Pb(4)	Br(10)	3.0141(19)	C(4)	N(4)	1.4200
Pb(4)	Br(7) ⁵	3.041(2)	N(4)	C(6)	1.4200

¹+X,1+Y,+Z; ²1/2+X,5/2-Y,1-Z; ³-1/2+X,3/2-Y,1-Z; ⁴1-X,1/2+Y,1/2-Z; ⁵-X,-1/2+Y,1/2-Z

Table F4 Bond Angles for IMIPbBr₃ at 220 K

Atom	Atom	Atom	Angle/°	Atom	Atom	Atom	Angle/°
Br(4)	Pb(1)	Br(11) ¹	89.62(6)	Br(9)	Pb(4)	Br(10)	82.43(5)
Br(4)	Pb(1)	Br(1) ²	88.41(6)	Br(9)	Pb(4)	Br(7) ⁵	91.57(6)
Br(2)	Pb(1)	Br(4)	81.54(5)	Br(9)	Pb(4)	Br(11)	165.07(6)
Br(2)	Pb(1)	Br(11) ¹	86.60(6)	Br(10)	Pb(4)	Br(8)	81.37(5)
Br(2)	Pb(1)	Br(1) ²	166.51(6)	Br(10)	Pb(4)	Br(7) ⁵	168.70(6)
Br(3)	Pb(1)	Br(4)	82.44(5)	Br(10)	Pb(4)	Br(11)	85.44(6)
Br(3)	Pb(1)	Br(2)	83.30(5)	Br(7) ⁵	Pb(4)	Br(8)	88.34(5)
Br(3)	Pb(1)	Br(11) ¹	167.96(6)	Br(11)	Pb(4)	Br(8)	87.76(6)
Br(3)	Pb(1)	Br(1) ²	86.49(6)	Br(11)	Pb(4)	Br(7) ⁵	98.86(7)
Br(11) ¹	Pb(1)	Br(1) ²	102.39(7)	Br(12)	Pb(4)	Br(8)	168.75(7)

Br(1)	Pb(1)	Br(4)	168.85(6)	Br(12)	Pb(4)	Br(9)	88.81(6)
Br(1)	Pb(1)	Br(2)	90.29(6)	Br(12)	Pb(4)	Br(10)	91.22(6)
Br(1)	Pb(1)	Br(3)	89.11(6)	Br(12)	Pb(4)	Br(7) ⁵	98.24(6)
Br(1)	Pb(1)	Br(11) ¹	97.50(7)	Br(12)	Pb(4)	Br(11)	100.14(7)
Br(1)	Pb(1)	Br(1) ²	98.363(19)	Pb(3)	Br(8)	Pb(4)	80.84(4)
Br(2)	Pb(2)	Br(4)	80.02(5)	Pb(1)	Br(4)	Pb(2)	81.02(4)
Br(3)	Pb(2)	Br(4)	81.02(5)	Pb(1)	Br(2)	Pb(2)	82.20(4)
Br(3)	Pb(2)	Br(2)	81.15(5)	Pb(4)	Br(9)	Pb(3)	82.11(5)
Br(6)	Pb(2)	Br(4)	84.77(6)	Pb(3)	Br(10)	Pb(4)	82.00(5)
Br(6)	Pb(2)	Br(2)	92.93(6)	Pb(1)	Br(3)	Pb(2)	82.92(5)
Br(6)	Pb(2)	Br(3)	165.35(6)	Pb(3)	Br(7)	Pb(4) ⁶	169.48(9)
Br(5) ³	Pb(2)	Br(4)	169.95(7)	Pb(2)	Br(6)	Pb(3)	176.64(9)
Br(5)	Pb(2)	Br(4)	88.68(6)	Pb(4)	Br(11)	Pb(1) ⁷	175.76(9)
Br(5) ³	Pb(2)	Br(2)	90.13(6)	Pb(1)	Br(1)	Pb(1) ⁸	172.04(10)
Br(5)	Pb(2)	Br(2)	167.30(7)	Pb(4)	Br(12)	Pb(3) ⁹	172.18(9)
Br(5) ³	Pb(2)	Br(3)	95.63(7)	Pb(2)	Br(5)	Pb(2) ¹⁰	173.16(11)
Br(5)	Pb(2)	Br(3)	91.44(7)	N(5)	C(7)	N(6)	108.0
Br(5)	Pb(2)	Br(6)	91.78(8)	C(7)	N(6)	C(9)	108.0
Br(5) ³	Pb(2)	Br(6)	97.79(7)	C(8)	C(9)	N(6)	108.0
Br(5)	Pb(2)	Br(5) ³	100.916(19)	C(9)	C(8)	N(5)	108.0
Br(9)	Pb(3)	Br(8)	81.79(5)	C(7)	N(5)	C(8)	108.0
Br(10)	Pb(3)	Br(8)	81.49(5)	N(7)	C(11)	C(12)	108.0
Br(10)	Pb(3)	Br(9)	82.38(5)	C(11)	C(12)	N(8)	108.0
Br(10)	Pb(3)	Br(7)	167.60(6)	C(10)	N(8)	C(12)	108.0
Br(7)	Pb(3)	Br(8)	87.35(6)	N(8)	C(10)	N(7)	108.0
Br(7)	Pb(3)	Br(9)	90.74(6)	C(11)	N(7)	C(10)	108.0
Br(6)	Pb(3)	Br(8)	86.80(6)	N(1)	C(2)	C(3)	108.0
Br(6)	Pb(3)	Br(9)	168.58(6)	C(2)	C(3)	N(2)	108.0
Br(6)	Pb(3)	Br(10)	95.88(6)	C(1)	N(2)	C(3)	108.0
Br(6)	Pb(3)	Br(7)	88.82(7)	N(2)	C(1)	N(1)	108.0
Br(12) ⁴	Pb(3)	Br(8)	170.45(7)	C(2)	N(1)	C(1)	108.0
Br(12) ⁴	Pb(3)	Br(9)	91.21(6)	C(6)	C(5)	N(3)	108.0
Br(12) ⁴	Pb(3)	Br(10)	91.20(6)	C(4)	N(3)	C(5)	108.0
Br(12) ⁴	Pb(3)	Br(7)	99.28(6)	N(4)	C(4)	N(3)	108.0
Br(12) ⁴	Pb(3)	Br(6)	100.12(7)	C(4)	N(4)	C(6)	108.0
Br(9)	Pb(4)	Br(8)	81.86(5)	C(5)	C(6)	N(4)	108.0

¹+X,1+Y,+Z; ²1/2+X,5/2-Y,1-Z; ³-1/2+X,3/2-Y,1-Z; ⁴1-X,1/2+Y,1/2-Z; ⁵-X,-1/2+Y,1/2-Z; ⁶-X,1/2+Y,1/2-Z; ⁷+X,-1+Y,+Z; ⁸-1/2+X,5/2-Y,1-Z; ⁹1-X,-1/2+Y,1/2-Z; ¹⁰1/2+X,3/2-Y,1-Z

Table F5 Hydrogen Atom Coordinates ($\text{\AA} \times 10^4$) and Isotropic Displacement Parameters ($\text{\AA}^2 \times 10^3$) for IMIPbBr₃ at 220 K

Atom	<i>x</i>	<i>y</i>	<i>z</i>	U(eq)
H(7)	1879.69	4670.34	3900.93	97
H(6)	4038.09	4240.13	4349.1	171
H(9)	3649.86	4744.26	5108.17	165
H(8)	1149.55	5523.44	5141.58	142
H(5)	124.34	5459.79	4401.4	168
H(11)	5589.64	6528.59	4025.22	115
H(12)	7929.19	5945.7	3677.33	144
H(8A)	9301.43	7414.4	3451.31	232
H(10)	7920.24	8904.14	3642.79	134
H(7A)	5639.33	8326.79	3995.86	112
H(2)	1878.16	9767.54	3568.61	84
H(3)	4246.22	9327.24	3196.8	103
H(2A)	4027.29	9897.63	2441.15	147
H(1)	1611.89	10681.89	2320.53	160
H(1A)	320.56	10586.84	3023.16	168
H(5A)	5022.63	6922.49	1340.1	181
H(3A)	3497.49	7641.23	1920.35	131
H(4)	1062.02	8129.33	1636.56	123
H(4A)	1103.61	7695.48	860.64	169
H(6A)	3493.29	6957.15	663.11	166

Appendix G

Table G1 Fractional Atomic Coordinates ($\times 10^4$) and Equivalent Isotropic Displacement Parameters ($\text{\AA}^2 \times 10^3$) for IMIPbBr₃ at 180 K. U_{eq} is defined as 1/3 of of the trace of the orthogonalised U_{ij} tensor

Atom	<i>x</i>	<i>y</i>	<i>z</i>	<i>U</i> (eq)
Pb(1)	6711.0(2)	6196.1(2)	5148.7(2)	18.14(6)
Br(1)	5000	5000	5000	30.28(17)
Br(4)	5676.9(5)	7500	7044.3(7)	28.88(17)
Br(5)	8292.7(5)	7500	5561.3(8)	31.10(18)
Br(2)	7381.1(4)	5105.5(4)	7851.7(5)	29.76(13)
Br(3)	6195.8(5)	7500	2671.0(7)	33.5(2)
N(2)	6817(4)	3212(4)	5229(6)	48.0(14)
C(3)	6291(4)	2940(4)	6409(6)	40.7(15)
C(1)	7145(7)	2500	4504(9)	49(2)
N(3)	4577(7)	5284(11)	8921(8)	57(4)
C(5)	4627(8)	4396(8)	9483(16)	46(3)
C(6)	5221(8)	4399(5)	10768(14)	34(3)
N(4)	5539(6)	5289(8)	11000(7)	39(3)
C(4)	5141(8)	5836(4)	9859(12)	29(2)

Table G2 Anisotropic Displacement Parameters ($\text{\AA}^2 \times 10^3$) for IMIPbBr₃ at 180 K

Atom	<i>U</i> ₁₁	<i>U</i> ₂₂	<i>U</i> ₃₃	<i>U</i> ₂₃	<i>U</i> ₁₃	<i>U</i> ₁₂
Pb(1)	22.25(10)	13.59(10)	18.57(9)	-2.26(6)	-1.06(6)	-0.36(7)
Br(1)	28.8(4)	29.1(4)	33.0(4)	-2.6(3)	-4.2(3)	-1.2(3)
Br(4)	32.2(4)	28.9(4)	25.6(3)	0	12.7(3)	0
Br(5)	17.3(3)	46.4(5)	29.7(3)	0	-3.9(3)	0
Br(2)	33.8(3)	24.6(3)	30.9(3)	-0.1(2)	-5.1(2)	2.4(2)
Br(3)	25.7(4)	56.3(6)	18.5(3)	0	-4.6(3)	0
N(2)	62(4)	21(3)	61(3)	14(2)	-6(2)	-8(3)
C(3)	34(3)	44(4)	44(3)	-14(3)	6(2)	5(3)
C(1)	65(7)	59(6)	23(4)	0	7(4)	0
N(3)	70(9)	62(8)	40(6)	-21(6)	-29(6)	1(7)
C(5)	42(8)	58(7)	38(8)	-25(6)	-14(6)	-4(7)
C(6)	30(7)	46(6)	27(6)	-3(5)	-6(4)	13(5)
N(4)	53(7)	42(6)	24(5)	14(5)	-20(4)	11(5)
C(4)	36(7)	32(5)	18(5)	7(4)	-11(4)	9(5)

Table G3 Bond Lengths for IMIPbBr₃ at 180 K

Atom	Atom	Length/ \AA	Atom	Atom	Length/ \AA
------	------	----------------------	------	------	----------------------

Pb(1)	Br(1)	3.0206(2)	N(2)	C(1)	1.328(8)
Pb(1)	Br(4)	2.9651(5)	C(3)	C(3) ²	1.317(12)
Pb(1)	Br(5)	2.9974(6)	N(3)	C(5)	1.4200
Pb(1)	Br(2)	3.0540(5)	N(3)	C(4)	1.4200
Pb(1)	Br(2) ¹	3.1001(5)	C(5)	C(6)	1.4200
Pb(1)	Br(3)	3.0293(5)	C(6)	N(4)	1.4200
N(2)	C(3)	1.350(7)	N(4)	C(4)	1.4200

¹3/2-X,1-Y,-1/2+Z; ²+X,1/2-Y,+Z

Table G4 Bond Angles for IMIPbBr₃ at 180 K

Atom	Atom	Atom	Angle/°	Atom	Atom	Atom	Angle/°
Br(1)	Pb(1)	Br(2) ¹	86.252(11)	Br(3)	Pb(1)	Br(2) ¹	91.511(15)
Br(1)	Pb(1)	Br(2)	88.240(12)	Pb(1) ²	Br(1)	Pb(1)	180.0
Br(1)	Pb(1)	Br(3)	98.896(13)	Pb(1) ³	Br(4)	Pb(1)	82.194(18)
Br(4)	Pb(1)	Br(1)	90.866(13)	Pb(1)	Br(5)	Pb(1) ³	81.123(19)
Br(4)	Pb(1)	Br(5)	82.801(18)	Pb(1)	Br(2)	Pb(1) ⁴	169.10(2)
Br(4)	Pb(1)	Br(2) ¹	172.899(18)	Pb(1) ³	Br(3)	Pb(1)	80.094(17)
Br(4)	Pb(1)	Br(2)	93.388(16)	C(1)	N(2)	C(3)	109.3(6)
Br(4)	Pb(1)	Br(3)	82.516(16)	C(3) ⁵	C(3)	N(2)	107.5(4)
Br(5)	Pb(1)	Br(1)	173.566(14)	N(2) ⁵	C(1)	N(2)	106.5(8)
Br(5)	Pb(1)	Br(2)	90.990(16)	C(5)	N(3)	C(4)	108.0
Br(5)	Pb(1)	Br(2) ¹	100.169(17)	N(3)	C(5)	C(6)	108.0
Br(5)	Pb(1)	Br(3)	81.463(17)	N(4)	C(6)	C(5)	108.0
Br(2)	Pb(1)	Br(2) ¹	93.009(6)	C(6)	N(4)	C(4)	108.0
Br(3)	Pb(1)	Br(2)	171.791(15)	N(3)	C(4)	N(4)	108.0

¹3/2-X,1-Y,-1/2+Z; ²1-X,1-Y,1-Z; ³+X,3/2-Y,+Z; ⁴3/2-X,1-Y,1/2+Z; ⁵+X,1/2-Y,+Z

Table G5 Hydrogen Atom Coordinates (Å×10⁴) and Isotropic Displacement Parameters (Å²×10³) for IMIPbBr₃ at 180 K

Atom	x	y	z	U(eq)
H(2)	6925.74	3772.26	4979.27	58
H(3A)	5978.06	3316.25	7111.16	49
H(1)	7537.61	2499.99	3637.61	59
H(3)	4253.19	5461.11	8130.3	68
H(5)	4316.75	3888.62	9071.02	55
H(6)	5379.09	3894.3	11366.76	41
H(4)	5916.32	5470.01	11724.4	47

H(4A)	5234.6	6461.45	9742.9	34
-------	--------	---------	--------	----

Table G6 Atomic occupancy for IMIPbBr₃ at 180 K

Atom	<i>Occupancy</i>	Atom	<i>Occupancy</i>	Atom	<i>Occupancy</i>
N(3)	0.5	H(3)	0.5	C(5)	0.5
H(5)	0.5	C(6)	0.5	H(6)	0.5
N(4)	0.5	H(4)	0.5	C(4)	0.5
H(4A)	0.5				

Appendix H

Table H1 Fractional Atomic Coordinates ($\times 10^4$) and Equivalent Isotropic Displacement Parameters ($\text{\AA}^2 \times 10^3$) for $\text{IMl}_2\text{PbBr}_4$ at 50 K. U_{eq} is defined as 1/3 of of the trace of the orthogonalised U_{ij} tensor

Atom	x	y	z	U(eq)
Pb01	4792.4(2)	4288.5(2)	1698.8(2)	5.64(2)
Br02	9693.6(4)	4077.3(3)	1643.0(2)	7.97(5)
Br03	5080.7(4)	2738.3(3)	21.8(2)	7.05(5)
Br04	4595.1(5)	5960.6(3)	3365.4(2)	8.14(5)
Br05	4896.5(4)	1440.4(3)	3297.5(2)	8.20(5)
N006	1433(4)	8619(3)	1826(2)	10.4(4)
N007	-622(4)	10593(3)	1317(2)	10.9(4)
N008	11669(4)	3234(3)	5081(2)	10.3(4)
N009	8803(4)	2357(3)	4613(2)	12.7(5)
C00A	-1720(5)	9466(3)	1107(2)	11.9(5)
C00B	10178(5)	3473(4)	4360(2)	12.4(5)
C00C	9447(5)	1372(4)	5532(2)	12.3(5)
C00D	1275(5)	10056(3)	1755(2)	11.5(5)
C00E	-419(5)	8223(3)	1433(2)	11.1(5)
C00F	11258(5)	1915(3)	5823(2)	11.5(5)

Table H2 Anisotropic Displacement Parameters ($\text{\AA}^2 \times 10^3$) for $\text{IMl}_2\text{PbBr}_4$ at 50 K

Atom	U ₁₁	U ₂₂	U ₃₃	U ₂₃	U ₁₃	U ₁₂
Pb01	4.81(4)	5.90(5)	5.70(4)	-0.60(3)	-0.42(3)	-0.73(3)
Br02	5.40(10)	8.40(12)	9.87(12)	-1.99(10)	-0.61(8)	-0.66(8)
Br03	8.31(11)	6.14(12)	6.45(11)	-1.15(9)	-0.97(8)	-0.46(9)
Br04	9.54(11)	7.71(12)	7.09(11)	-1.41(9)	-1.93(9)	-1.05(9)
Br05	8.52(11)	7.29(12)	7.83(11)	0.32(9)	-2.14(9)	-2.36(9)
N006	10.4(10)	9.9(11)	10.1(11)	-1.4(9)	-1.1(8)	-0.2(8)
N007	13.0(11)	7.5(11)	12.3(11)	-3.0(9)	-0.4(9)	-0.7(8)
N008	9.2(10)	11.0(12)	11.3(11)	-3.7(9)	-0.9(8)	-1.2(8)
N009	9.5(10)	19.1(14)	11.4(11)	-6.6(10)	-3.6(9)	-1.3(9)
C00A	12.4(12)	12.5(14)	11.4(13)	-3.4(11)	-2.5(10)	-2.0(10)
C00B	15.5(13)	11.8(14)	9.1(12)	-1.3(10)	-1.6(10)	-1.1(10)
C00C	13.1(12)	12.1(14)	10.7(13)	-1.6(11)	3.4(10)	-3.5(10)
C00D	10.6(12)	13.3(14)	9.9(12)	-1.7(11)	-0.2(9)	-3.9(10)
C00E	12.1(12)	7.8(13)	12.8(13)	-2.0(10)	0.5(10)	-2.2(10)
C00F	12.4(12)	12.2(14)	8.9(12)	-1.3(10)	-2.0(10)	0.5(10)

Table H3 Bond Lengths for IMI₂PbBr₄ at 50 K

Atom	Atom	Length/Å	Atom	Atom	Length/Å
Pb01	Br02	2.9275(3)	N007	C00A	1.379(4)
Pb01	Br02 ¹	3.0771(3)	N007	C00D	1.321(4)
Pb01	Br03	2.9828(3)	N008	C00B	1.321(4)
Pb01	Br03 ²	3.0884(3)	N008	C00F	1.378(4)
Pb01	Br04	3.0528(3)	N009	C00B	1.325(4)
Pb01	Br05	2.9260(3)	N009	C00C	1.380(4)
N006	C00D	1.328(4)	C00A	C00E	1.351(4)
N006	C00E	1.370(4)	C00C	C00F	1.347(4)

¹-1+X,+Y,+Z; ²1-X,1-Y,-Z
Table H4 Bond Angles for IMI₂PbBr₄ at 50 K

Atom	Atom	Atom	Angle/°	Atom	Atom	Atom	Angle/°
Br02	Pb01	Br02 ¹	171.198(12)	Br05	Pb01	Br04	91.194(8)
Br02	Pb01	Br03 ²	90.530(8)	Pb01	Br02	Pb01 ³	171.199(12)
Br02 ¹	Pb01	Br03 ²	93.381(8)	Pb01	Br03	Pb01 ²	91.532(8)
Br02	Pb01	Br03	87.080(8)	C00D	N006	C00E	109.5(2)
Br02	Pb01	Br04	91.880(8)	C00D	N007	C00A	109.3(3)
Br03	Pb01	Br02 ¹	85.148(8)	C00B	N008	C00F	109.4(3)
Br03	Pb01	Br03 ²	88.466(8)	C00B	N009	C00C	108.8(2)
Br03	Pb01	Br04	177.999(8)	C00E	C00A	N007	106.6(3)
Br04	Pb01	Br02 ¹	96.010(8)	N008	C00B	N009	108.3(3)
Br04	Pb01	Br03 ²	89.835(8)	C00F	C00C	N009	107.1(3)
Br05	Pb01	Br02	86.854(8)	N007	C00D	N006	107.8(3)
Br05	Pb01	Br02 ¹	89.082(8)	C00A	C00E	N006	106.8(3)
Br05	Pb01	Br03	90.456(8)	C00C	C00F	N008	106.5(3)
Br05	Pb01	Br03 ²	177.218(8)				

¹-1+X,+Y,+Z; ²1-X,1-Y,-Z; ³1+X,+Y,+Z
Table H5 Hydrogen Atom Coordinates (Å×10⁴) and Isotropic Displacement Parameters (Å²×10³) for IMI₂PbBr₄ at 50 K

Atom	x	y	z	U(eq)
H006	2555.4	8013.86	2086.44	12
H007	-1107.53	11523.24	1180.47	13
H008	12755.04	3824.16	5087.02	12

H009	7666.8	2261	4253.66	15
H00A	-3118.49	9547.67	794.37	14
H00B	10104.73	4302.57	3762	15
H00C	8745.57	477.88	5891.96	15
H00D	2335.87	10602.01	1978.53	14
H00E	-729.49	7259.95	1395.51	13
H00F	12088.28	1476.24	6421.44	14

Appendix I

Table I1 Fractional Atomic Coordinates ($\times 10^4$) and Equivalent Isotropic Displacement Parameters ($\text{\AA}^2 \times 10^3$) for $\text{IMI}_3\text{PbBr}_5$ at 200 K. U_{eq} is defined as 1/3 of the trace of the orthogonalised U_{ij} tensor

Atom	<i>x</i>	<i>y</i>	<i>z</i>	<i>U</i> (eq)
Pb01	5000	5000	10000	20.93(19)
Br02	0	5000	10000	38.7(4)
Br03	5206.7(18)	3795.4(13)	7477.2(14)	35.5(3)
Br04	5059.9(18)	8215.7(12)	7636.1(14)	34.2(3)
N5	-1630(17)	6758(12)	5004(13)	44(3)
N3	1294(18)	7490(15)	5628(15)	56(3)
C2	700(20)	8635(15)	4337(18)	54(4)
C4	-170(20)	6410(16)	5976(16)	53(4)
C1	-1210(20)	8180(16)	3954(16)	53(4)
C0AA	8480(30)	10840(20)	9590(20)	29(5)
C2AA	10460(40)	11194(15)	10110(20)	25(4)
N1AA	11858(17)	9870(30)	10532(19)	43(6)
C3AA	10750(40)	8690(12)	10270(20)	27(5)
N4AA	8660(30)	9290(30)	9690(20)	33(5)

Table I2 Anisotropic Displacement Parameters ($\text{\AA}^2 \times 10^3$) for $\text{IMI}_3\text{PbBr}_5$ at 200 K

Atom	U_{11}	U_{22}	U_{33}	U_{23}	U_{13}	U_{12}
Pb01	15.7(3)	22.5(3)	25.7(4)	-10.1(3)	-2.4(2)	-1.5(2)
Br02	15.7(7)	60.1(11)	37.8(10)	-16.1(9)	-2.9(7)	0.5(7)
Br03	39.5(6)	38.3(7)	33.3(7)	-18.0(6)	-4.6(5)	-5.7(5)
Br04	36.7(6)	27.9(6)	34.8(8)	-7.1(5)	-8.1(5)	-4.5(5)
N5	44(6)	47(6)	45(7)	-21(6)	4(5)	-8(5)
N3	45(6)	89(9)	50(8)	-41(8)	-12(6)	-6(7)
C2	60(9)	43(8)	64(11)	-26(8)	21(8)	-25(7)
C4	71(10)	54(9)	26(8)	-6(7)	8(7)	0(8)
C1	65(9)	56(9)	36(9)	-13(7)	-18(7)	11(7)
C0AA	38(8)	20(7)	33(14)	-15(8)	-2(8)	6(6)
C2AA	34(8)	19(7)	23(12)	-9(8)	3(7)	5(6)
N1AA	44(7)	23(7)	68(15)	-23(8)	-13(9)	11(6)
C3AA	35(8)	21(7)	25(12)	-11(7)	8(8)	3(6)
N4AA	40(8)	21(7)	44(13)	-18(8)	-1(8)	6(6)

Table I3 Bond Lengths for $\text{IMI}_3\text{PbBr}_5$ at 200 K

Atom	Atom	Length/ \AA	Atom	Atom	Length/ \AA
------	------	----------------------	------	------	----------------------

Pb01	Br02 ¹	3.0136(3)	N3	C2	1.352(18)
Pb01	Br02	3.0136(3)	N3	C4	1.295(17)
Pb01	Br03 ²	3.0309(12)	C2	C1	1.358(18)
Pb01	Br03	3.0308(12)	C0AA	C2AA	1.4200
Pb01	Br04 ²	3.0001(12)	C0AA	N4AA	1.4200
Pb01	Br04	3.0001(12)	C2AA	N1AA	1.4200
N5	C4	1.268(15)	N1AA	C3AA	1.4200
N5	C1	1.349(17)	C3AA	N4AA	1.4200

¹1+X,+Y,+Z; ²1-X,1-Y,2-Z

Table I4 Bond Angles for IMI₃PbBr₅ at 200 K

Atom	Atom	Atom	Angle/°	Atom	Atom	Atom	Angle/°
Br02 ¹	Pb01	Br02	180.0	Br04	Pb01	Br03 ²	91.53(3)
Br02	Pb01	Br03 ²	91.42(2)	Br04	Pb01	Br04 ²	180.0
Br02	Pb01	Br03	88.58(2)	Pb01 ³	Br02	Pb01	180.0
Br02 ¹	Pb01	Br03 ²	88.58(2)	C4	N5	C1	108.7(12)
Br02 ¹	Pb01	Br03	91.42(2)	C4	N3	C2	107.4(11)
Br03	Pb01	Br03 ²	180.000(17)	N3	C2	C1	106.5(12)
Br04 ²	Pb01	Br02	90.14(2)	N5	C4	N3	111.2(13)
Br04	Pb01	Br02 ¹	90.14(2)	N5	C1	C2	106.0(12)
Br04	Pb01	Br02	89.86(2)	N4AA	C0AA	C2AA	108.0
Br04 ²	Pb01	Br02 ¹	89.86(2)	N1AA	C2AA	C0AA	108.0
Br04 ²	Pb01	Br03	91.53(3)	C2AA	N1AA	C3AA	108.0
Br04 ²	Pb01	Br03 ²	88.47(3)	N1AA	C3AA	N4AA	108.0
Br04	Pb01	Br03	88.47(3)	C0AA	N4AA	C3AA	108.0

¹1+X,+Y,+Z; ²1-X,1-Y,2-Z; ³-1+X,+Y,+Z

Table I5 Hydrogen Atom Coordinates (Å×10⁴) and Isotropic Displacement Parameters (Å²×10³) for IMI₃PbBr₅ at 200 K

Atom	x	y	z	U(eq)
H5	-2740.76	6169.96	5014.03	53
H3	2458.72	7480.67	6138.71	68
H2	1460.83	9574.76	3802.95	65
H4	-141.19	5477.38	6845.42	64
H1	-2062.5	8746.52	3116.93	64
H0AA	7249.05	11517.37	9239.69	35

H2AA	10783.7	12152.31	10169.28	30
H1AA	13183.25	9786.1	10890.85	51
H3AA	11302.19	7678.46	10453.41	32
H4AA	7649.59	8792.07	9435.53	40

Table I6 Atomic occupancy for IMI₃PbBr₅ at 200 K

Atom	<i>Occupancy</i>	Atom	<i>Occupancy</i>	Atom	<i>Occupancy</i>
C(0AA)	0.5	H(0AA)	0.5	C(2AA)	0.5
H(2AA)	0.5	N(1AA)	0.5	H(1AA)	0.5
C(3AA)	0.5	H(3AA)	0.5	N(4AA)	0.5
H(4AA)	0.5				

Annex J

This section provides the supplementary discussion on the classification of 1D ‘perovskites’ notation and is heavily referenced from Wong, W.P.D., Hanna, J.V. & Grimsdale, A.C. (2021). *Acta Cryst.* B77, <https://doi.org/10.1107/S2052520621004376>.

The notation presented in Chapter 6 of this thesis is also known as the reduced notation. The main aim of the reduced notation is to keep it simple and easy to use for non-crystallographers. However, the limitation of the form is exposed in structures like 1-2EE where more than one structure can take on the same notation. Hence, to overcome this limitation, all six corners of an octahedron are labelled with the italicized number *l* to 6 as seen in Figure J1. When any corner, edge or face is defined, the lowest number combination should be taken as the reference point.

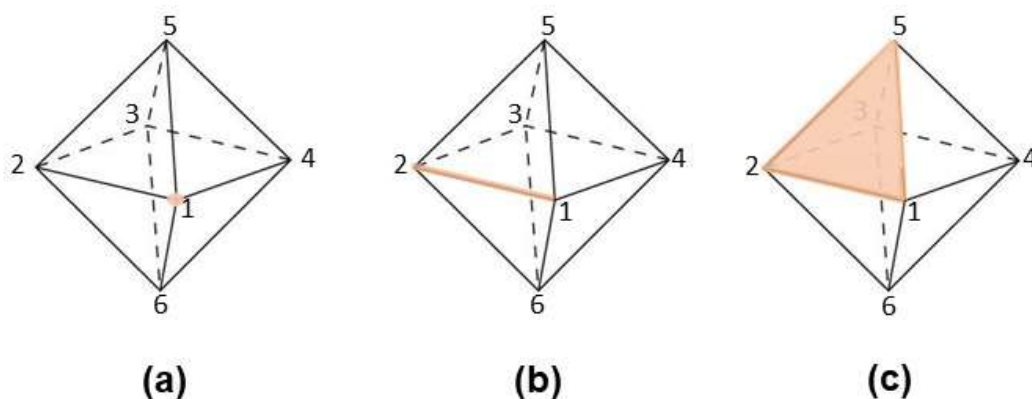


Figure J1 A schematic showing the naming convention for labelling all 6 corners, with highlighting on (a) corner *l*, (b) edge *l2* and (c) face *l25* of an octahedron.

With all vertices of an octahedron defined, the connectivity and repeat unit of such 1D structures can now be looked in detail. For the completeness of this discussion, the reduced notation would be re-introduced here followed by the natural development into the extended notation due to the said weakness, namely the non-uniqueness of the reduced notation.

In a 1D chain of connected octahedra, each layer would be perpendicular to the direction the chain’s propagation. First, the main parameter to consider is the number of octahedra per layer. If there is more than one octahedron per layer, the intra-layer

connectivity would also have to be defined in parentheses. Special considerations, for example cyclic connectivity should also include in this section if it arises from the intra-layer connectivity. In the examples analysed, however, no such special considerations are seen.

The second parameter would be the number of octahedral layers required for the stacking or connectivity sequence to repeat itself. If there are more than one octahedron per repeat of the stacking sequence, the connectivity type should be specified: F for face-sharing, E for edge-sharing and C for corner-sharing. The last parameter pertains to the connectivity to the repeating sequence, with again F, E, C for face, edge, and corner sharing respectively, or X, for no connectivity. Although materials having no connectivity would strictly speaking not be a 1D ‘perovskitoid’, such a naming framework would also help to describe similar systems for easy comparison. At this point it should be obvious that if there is one octahedron per layer, and n octahedra making up the repeating unit, there would be a connectivity of n . In instances where the connectivity involves only corner sharing, corner 5 should point in an arbitrary upwards direction, and corner 6 in an arbitrary downwards direction perpendicular to the propagation of the 1D chain. This condition is imposed to restrict any ambiguity arising from the rotational freedom.

Thereafter, one should identify the repeating pattern in the unit cell first, then shift the “origin” such that the naming priority would be given for corner sharing over edge sharing over face sharing over no connectivity, i.e. $C > E > F > X$. Subsequently, the notation would be reduced to the simplest repeating pattern without including the effects of crystallographic inequivalent B – site cations (see 1-2FF, Figure J2). Hence, this proposed naming convention, also called the reduced notation, is separated into two parts, each defining the afore-mentioned parameters. It would take a general form of (number, intralayer connectivity if any) – (number, interlayer connectivity).

It should be emphasized here that it is the objective of this notation to be kept simple for even non-crystallographers to utilize with ease. However, the limitation of this notation can be seen with certain configurations such as 1-2EE (Figure J6 and J7) which can exhibit “isomerism” through different edge connectivity. Therefore, a full notation which can be simplified to an extended notation is designed to address this limitation.

A small difference between the full and extended notation will be discussed here. The full notation would show the preceding referenced octahedra corner or edge or face superscripted on the left of the connectivity label and following connectivity of the referenced octahedra corner or edge or face subscripted to the right and would take the general form of $^{XYZ}A_{X'Y'Z'}$. By the earlier definition where the referenced corner, edge or face would have the lowest number combination, the second octahedron in the first repeating unit would always be referenced on corner 1 or edge 12 or face 125. By virtue of repeating this naming convention to the first octahedron in the second repeating unit, the first octahedron would therefore also be referenced on corner 1 or edge 12 or face 125. Therefore, the preceding reference in superscript (i.e. XYZ) can be dropped since it can only be 1, 12 or 125 for a corner edge or face shared octahedral. In doing so, we would obtain the extended notation which has a general form of $A_{X'Y'Z'}$. Consequently, the order of the numbering would also be meaningful where 1-2 $^{X1Y1Z1}F_{X1'Y1'Z1'}$, $^{X2Y2Z2}F_{X2'Y2'Z2'}$ and 1-2 $^{X3Y3Z3}F_{X3'Y3'Z3'}$, $^{X4Y4Z4}F_{X4'Y4'Z4'}$ convey different meanings; the former would mean the face connectivity between the first and second octahedra is oriented such that corner $X1'$ matches with $X2$, corner $Y1'$ matches with $Y2$ and corner $Z1'$ matches with $Z2$ while the latter would mean the face connectivity happens where corner $X3'$ matches with $X4$, corner $Z3'$ matches with $Y4$ and corner $Y3'$ matches with $Z4$. Such specificity would remove any potential room for ambiguity. During instances where the preceding connectivity would not be 1, 12, 125 or if the structure is connected in a highly novel way, it is recommended to utilize the full notation instead. It should be noted that in an X connectivity, the syntax would be slightly different for the reduced and extended notation. Taking the example of a system which has an extended notation of 1-3 $^XF_{435} F_{346} F_X$, the reduced notation is written as 1-3FFX instead of 1-3FFF or 1-3FFF_X. This is necessary because the X-connectivity must be present in the reduced notation to convey the meaning of no connectivity beyond the third octahedron, and it is the nature of the reduced notation to only show the connectivity style. 1-3FFF would convey the meaning of a full continuous 1D chain of face sharing octahedra, and 1-3FFF_X would have gone beyond the very definition of the reduced notation. At the same time, the extended notation 1-3 $^XF_{435} F_{346} F_X$ can be read as, “there is one octahedron in one layer, three layers form the repeating unit (and hence three octahedra form each repeating unit), where the reference corner 1, edge 12 and face 125 of the first octahedron is not connected to anything; face 435 of the first octahedron is connected

to face *125* of the second octahedron; face *346* of the second octahedron is connected to face *125* of the third octahedron. There is no further connectivity beyond the third octahedron”. When there is more than one way of writing the connectivity, the sum of the numbers with the smallest combination should be used (1 -1C, Figure J5). If the sum of the numbers is equal, then the combination with the most instance of smallest number would be used (see 1-2EE, Figure J7). In another unusual instance of more than one connectivity from the same layer, the use of underline would be used to specify which corner or edges are being referenced to for the subsequent connectivity (see Figure J10). Furthermore, the use of an arbitrary “+” and “-” is also introduced in section 2.2 (see Figure J10), but if the structure is also connected perpendicular to the direction of the 1D structure’s propagation, the result is not likely to be a 1-D structure and this proposed notation should not be used to describe the structure if another chemical naming convention exists.

With the naming convention and rules being outlined as mentioned, the subsequent section would look at several notable examples.

The most commonly observed configuration is the 1-2FF. Ignoring the crystallographic distinct sites for Pb and octahedral distortion effects, structures like 1-6FFFFFF and 1-4FFFF can be represented as 1-2FF. In the full notation, this structure is written as 1-2 ¹²⁵F₃₄₆ ¹²⁵F₃₄₆ but it can be seen that the superscripted *125* is redundant and thus, the full notation can be simplified into the extended notation as 1-2 F₃₄₆ F₃₄₆.

1-2 F_{346} F_{346} , (1-2FF)

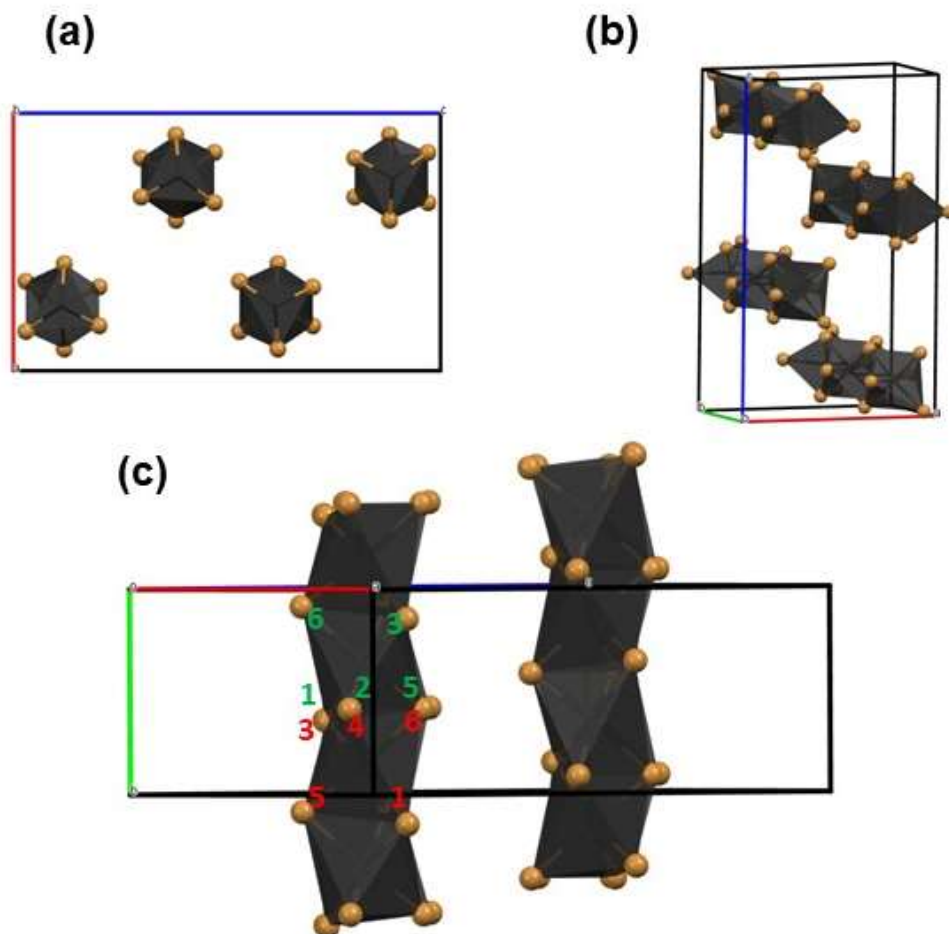


Figure J2 The structure shown here has one octahedron per layer, and the repeating unit has two layers where the octahedra are connected through face sharing. The repeating unit are connected to the next unit through a face sharing. The structure illustrated here is taken from catena-(2-methylimidazo[1,5-a]pyridin-2-ium tris(μ -bromo)-lead)¹, with the organic ligands not shown for clarity. Notably, other structures like 1-4FFFF and 1-6FFFFFF are isostructural and can be simplified to 1-2FF when the octahedra are idealized. The extended notation of this structure would be 1-2 F_{346} F_{346} .

The second most commonly observed connectivity is 1-3EFF. This structure has one octahedron per layer, and it can be seen from the unit cell that there are 3 octahedra which form the repeating unit. From Figure J3, within the unit cell, the octahedron are

connected through face, edge, face, which would give us the reduced notation of 1-3FEF. However, the priority is given for $C > E > F > X$. Thus, the sequence would be rewritten as 1-3EFF. In the full notation, it will be written as $1-3\ ^{12}E_{435}\ ^{125}F_{346}\ ^{125}F_{34}$, which can be reduced to $1-3\ E_{435}\ F_{346}\ F_{34}$. From the full notation, it can be read as, the first octahedron has a preceding connectivity from edge 12 , connected to the second octahedron through face 345 . The second octahedron is connected to the first octahedron through face 125 and with the third octahedron through face 346 . The third octahedron is connected to the second octahedron through face 125 and the fourth octahedron (i.e. the first octahedron in the next repeating unit) through the edge 34 . It should also be noted that the order of the numbering for the edges and especially for the faces does matter. In this example, it would mean the second octahedron's face 346 is shared with the third octahedron's face 125 , where the second octahedron's corner 3 matches with corner 1 of the third octahedron, second octahedron's corner 4 matches with corner 2 of the third octahedron and second octahedron's corner 6 matches with corner 5 of the third octahedron. Again, it can be seen that in a 1D chain, by definition, the preceding connectivity will always be ^{12}E or ^{125}F or 1C , thus, the extended notation of 1-3EFF would be $1-3\ E_{435}\ F_{346}\ F_{34}$.

1-3 E_{435} F_{346} F_{34} , (1-3EFF)

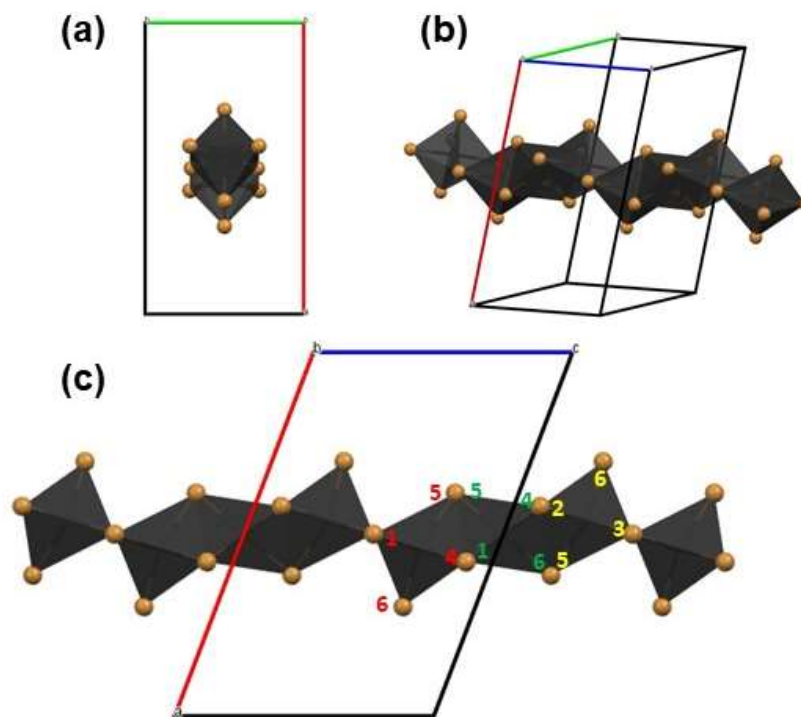


Figure J3 The structure shown here has one octahedron per layer, and the repeating unit has three layers within the unit cell with the octahedra sharing in the order of face, edge, face sharing. With the order of priority of edge sharing over face sharing, this sequence is rewritten as edge, face, face sharing and thus takes on the reduced notation of 1-3EFF, or the extended notation of 1-3 E_{435} F_{346} F_{34} . The structure illustrated here is taken from $(C_{12}N_2H_{14})_2Pb_7Br_{18}^2$, with the organic ligands not shown for clarity.

This next example seen in Figure J4 demonstrates the relevance of the notation when the connectivity does not form a continuous chain. In this configuration, there is one octahedron per layer and the repeat unit consists of three layers. Within the repeating unit, the octahedra are all connected through face sharing, similar to that in 1-2FF. However, each repeating unit, which consist of 3 octahedra, does not connect to the next and thus form mini-rods of three face connected octahedra. Hence, such connectivity would be written as 1-3FFX in the reduced notation, or with the extended notation of 1-3 $^X F_{435}$ F_{346} F_X .

1-3 ${}^X\text{F}_{346}$ F_{346} F_X , (1-3FFX)

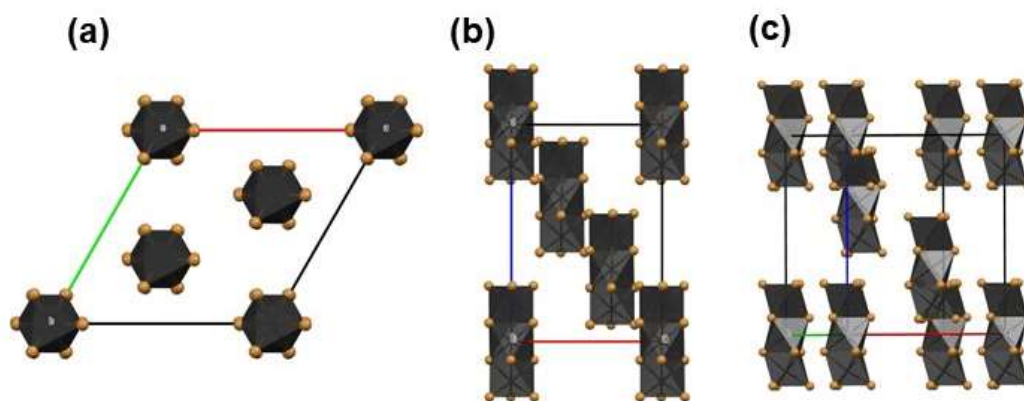


Figure J4 The structure shown here has one octahedron per layer, and the repeating unit has three layers where the octahedra are connected through face sharing. The repeating unit are not connected to the next unit, hence takes the notation 1-3FFX or in the extended notation 1-3 ${}^X\text{F}_{346}$ F_{346} F_X . The structure illustrated here is taken from $[\text{Me}_3\text{TPT}]_2[\text{Pb}_3\text{Br}_{12}] \cdot 6\text{H}_2\text{O}$ ³, with the organic ligands not shown for clarity.

The next example seen in Figure J5 would be the only true 1D perovskite structure examined in this thesis. In a perovskite structure, all lead halide octahedra are corner shared to form a large 3D network. In a 1D perovskite structure, the connectivity is now restricted to connectivity along one direction. For such connectivity, there is one octahedra per layer and one repeating unit which are all corner connected. As such, this would take the notation of 1-1C or with the extended notation of 1-1 C_3 . Corner 5 is, by convention, pointing towards an arbitrary upwards direction out of the paper since connectivity through only the corner gives an additional degree of rotation freedom.

1-1 C_3 , (1-1C)

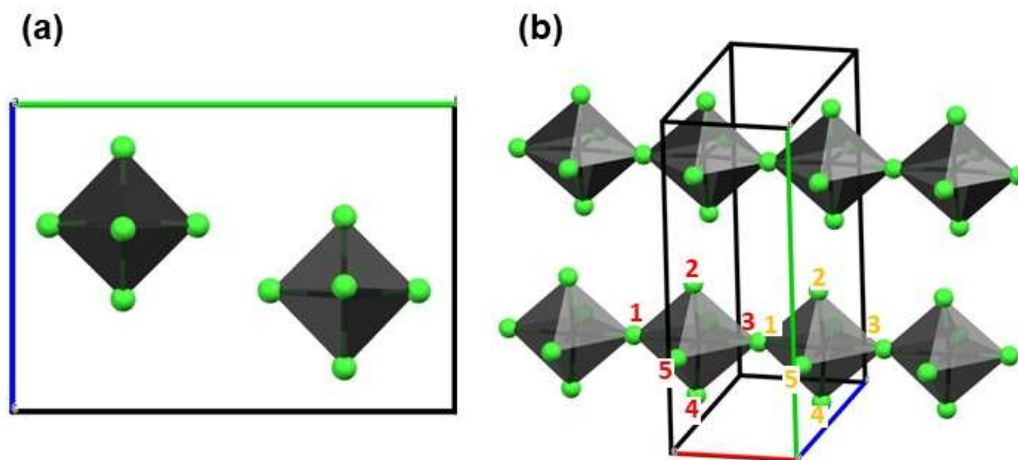


Figure J5 The structure shown here has one octahedron per layer, and the repeating unit only has one layer. The repeating unit are connected to the next unit through a corner shared halide, hence takes the notation 1-1C or the extended notation of 1-1 C_3 . The structure illustrated here is taken from $[C_3N_6H_8]_2PbCl_5.Cl$ ⁴

The following example on 1-2EE, as seen in Figure J6 and J7, would show the main limitation of the reduced notation where the same notation can give rise to more than one unique structure, which is similar to isomerism. Hence, the extended notation or even full notation is necessary here to give a clear definition. In Figure J6 and J7, there is one octahedron per layer, and it takes two octahedra for the pattern to repeat into a 1D chain. However, the connectivity is distinct in the two structures. By the earlier defined edges of an octahedron, the extended notation for the structure shown in Figure J6 is written as 1-2E₃₂ E₁₄ whereas the structure in Figure J7 is written as 1-2E₅₃ E₆₃. It should be noted that the structure in Figure J7 can also be written in several different forms, such as 1-2E₃₅ E₅₆ and 1-2E₅₃ E₅₄ but these form are less preferred. 1-2E₃₅ E₅₆ is not preferred because the sum of the numbers is larger (i.e. $5 + 3 + 6 + 3 < 3 + 5 + 5 + 6$) while 1-2E₅₃ E₅₄ is less preferred because the smallest number (i.e. 3) is more highly used in 1-2E₅₃ E₆₃. Notably, the difference between 1-2E₅₃ E₅₄ and 1-2E₅₃ E₆₃ arises from which octahedron the series starts from and it is shown in Figure J8 that by shifting the reference octahedron by one unit, both structures can be superimposed on each other.

$$1-2 E_{14} E_{32}, (1-2EE)$$

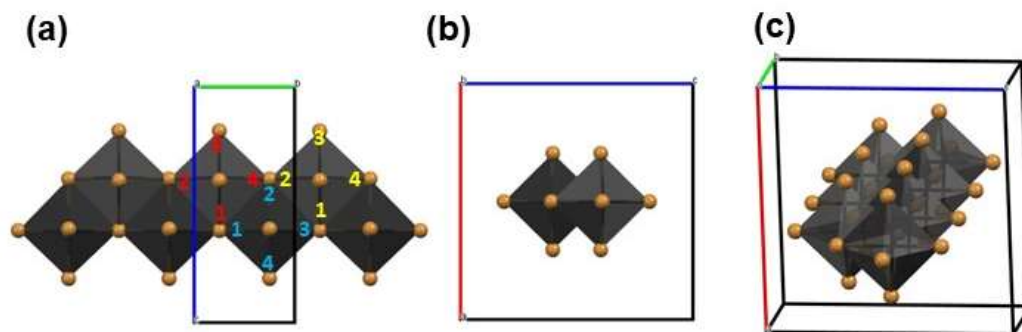


Figure J6 The structure shown here has one octahedron per layer, and the repeating unit has two layers, where the octahedra are connected through an edge sharing. The repeating unit are connected to the next repeating unit through an equivalent edge and hence takes the reduced notation of 1-2EE, or the extended notation of 1-2 $E_{14} E_{32}$. The structure illustrated here is taken from $C_4N_2H_{14}PbBr_4$ ⁵.

1-2 E_{53} E_{63} , (1-2EE)

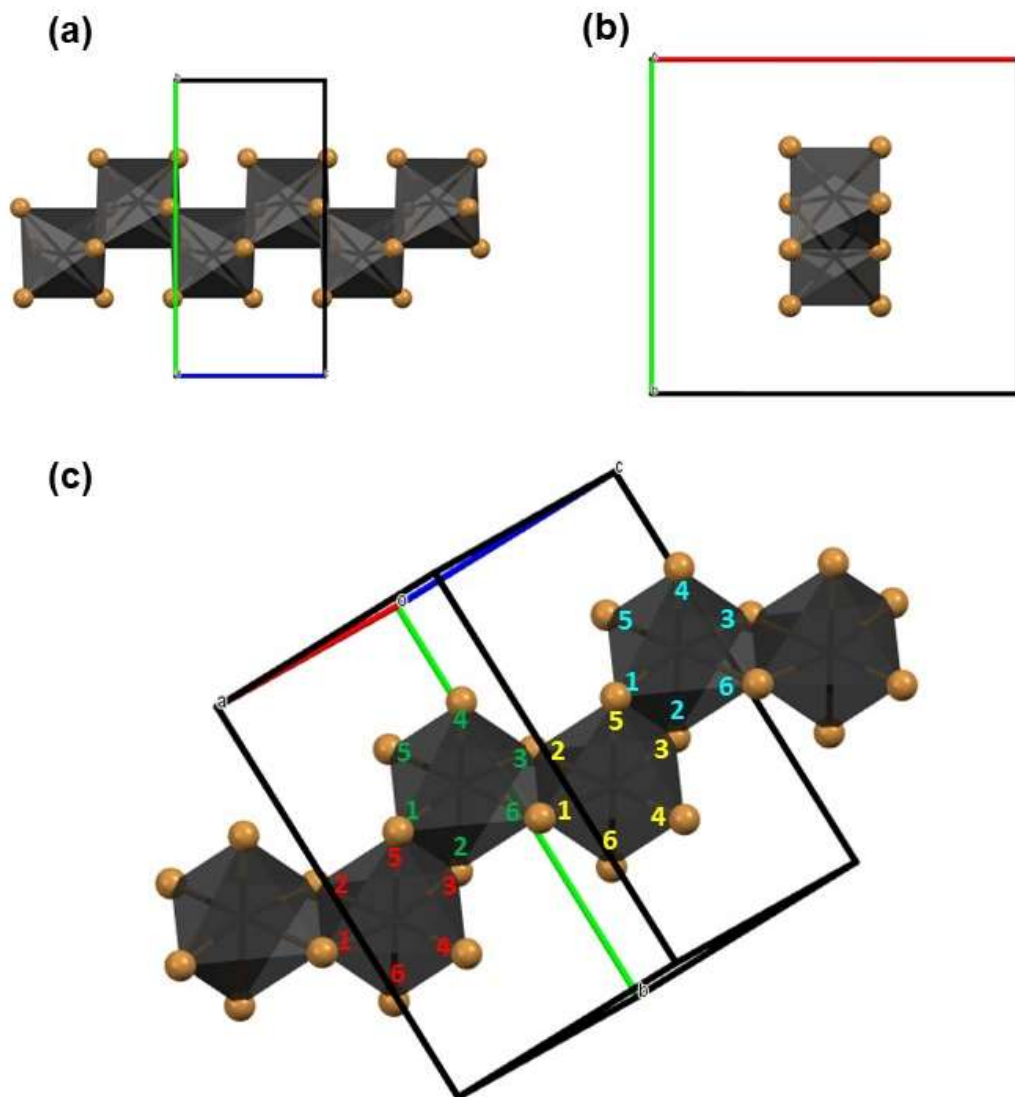


Figure J7 The structure shown here has one octahedron per layer, and it has two octahedra per repeating unit which are connected through an edge. The octahedral connectivity here is distinct from that in Figure 6, even though this structure also has a reduced notation of 1-2EE. The extended notation of this structure is written as 1-2 E_{53} E_{63} which shows the difference in the edges through which the octahedra are connected. The structure illustrated here is taken from $(\text{H}_2\text{Bpy})\text{PbBr}_4$.⁶

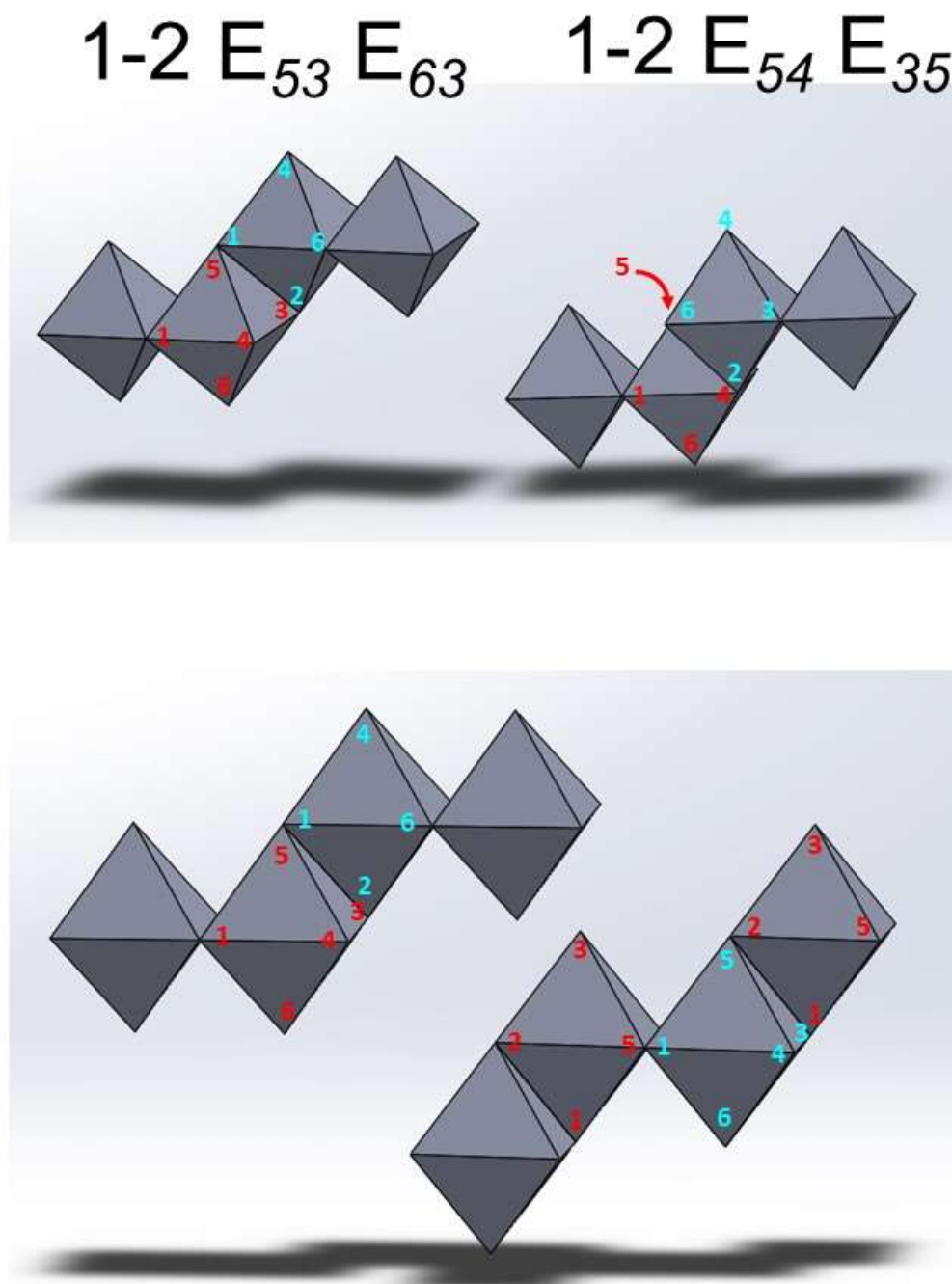


Figure J8 Using idealized octahedra, the two structures, $1-2 E_{53} E_{63}$ and $1-2 E_{54} E_{35}$, initially appear to be different. However, it can be shown that the structures are the same by shifting the “origin” by one octahedron. $1-2 E_{53} E_{63}$, will therefore, be the more preferred notation because even though the sum of the numbers for both notations are the same, the smallest number 3 appears more frequently (i.e. two times, as compared to just one time).

The example shown next in Figure J9 is the only configuration which has more than one octahedron per layer. In each layer, there are two lead halide octahedra connected through an edge and there is only one repeating layer. The terminal octahedra are connected with the next unit through corner sharing. Hence, such connectivity would be labelled 2E-1(CC). Since C has a higher priority over E, the reference corner *l* would be based on the corner which is connected to the preceding layer. Hence, this structure will take on a full notation of $2\ ^X\text{E}_{52}\ ^{25}\text{E}_X - 1(^l\text{C}_3\ ^l\text{C}_3)$ which can be simplified into the extended notation of $2\ ^X\text{E}_{52}\ ^{25}\text{E}_X - 1(\text{C}_3\ \text{C}_3)$ by dropping the reference corner *l*.

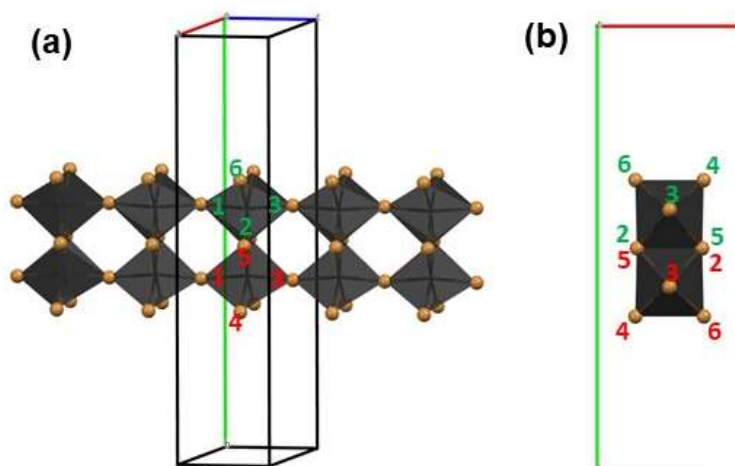
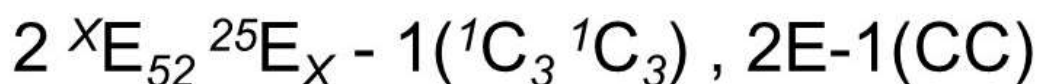


Figure J9 The structure shown here has two octahedra per layer which are connected through an edge sharing and the repeating unit only has one layer. Each repeating unit is connected to the next repeating unit through corner sharing, and hence this takes the reduced notation 2E-1(CC) or $2\ ^X\text{E}_{52}\ ^{25}\text{E}_X - 1(^l\text{C}_3\ ^l\text{C}_3)$ in the extended notation. The structure illustrated here is taken from $(\text{C}_{10}\text{H}_{12}\text{N}_2)_2[\text{Pb}_2\text{Br}_8]$ ⁷

While it would be tempting to extend this notation to include other larger 2D networks, the notation would take on an awkward form, exposing the main limitation of this notation. Based on the unit cell, the structure shown in Figure J10 can be seen as 1-6F(CC)FF(CC)F and based on the octahedral sharing priority rule, would be rewritten as 1-6(CC)FF(CC)FF. In the full notation, taking the c-axis as pointing “up” (i.e. octahedral corner 5), it will be written as $1-6(^l\text{C}_{435}\ ^l\text{C}_{325})^{125}\text{F}_{346}\ ^{125}\text{F}_{3,4} (^l\text{C}_{346},\ ^l\text{C}_{236})$

$^{125}\text{F}_{346}$ $^{125}\text{F}_{3,4}$. It can be seen here that the notation is on the verge of breaking down because the two-corner shared octahedron is accompanied by a displacement in the \pm b-axis. Even with a slight modification, by including + for displacement in the positive b-axis, and – for a displacement in the negative b-axis, as well as underlining the octahedron to specify that the subsequent connection are based on the underlined octahedron, the full notation would be 1-6 ($\underline{{}^1\text{C}_{435}}$ ${}^1\text{C}_{325}$) $^{125}\text{F}_{346}$ $^{125}\text{F}_{3-,4+}$ ($\underline{{}^1\text{C}_{346}}$, ${}^1\text{C}_{236}$) $^{125}\text{F}_{346}$ $^{125}\text{F}_{3-,4+}$.

1-6 (CC)FF(CC)FF

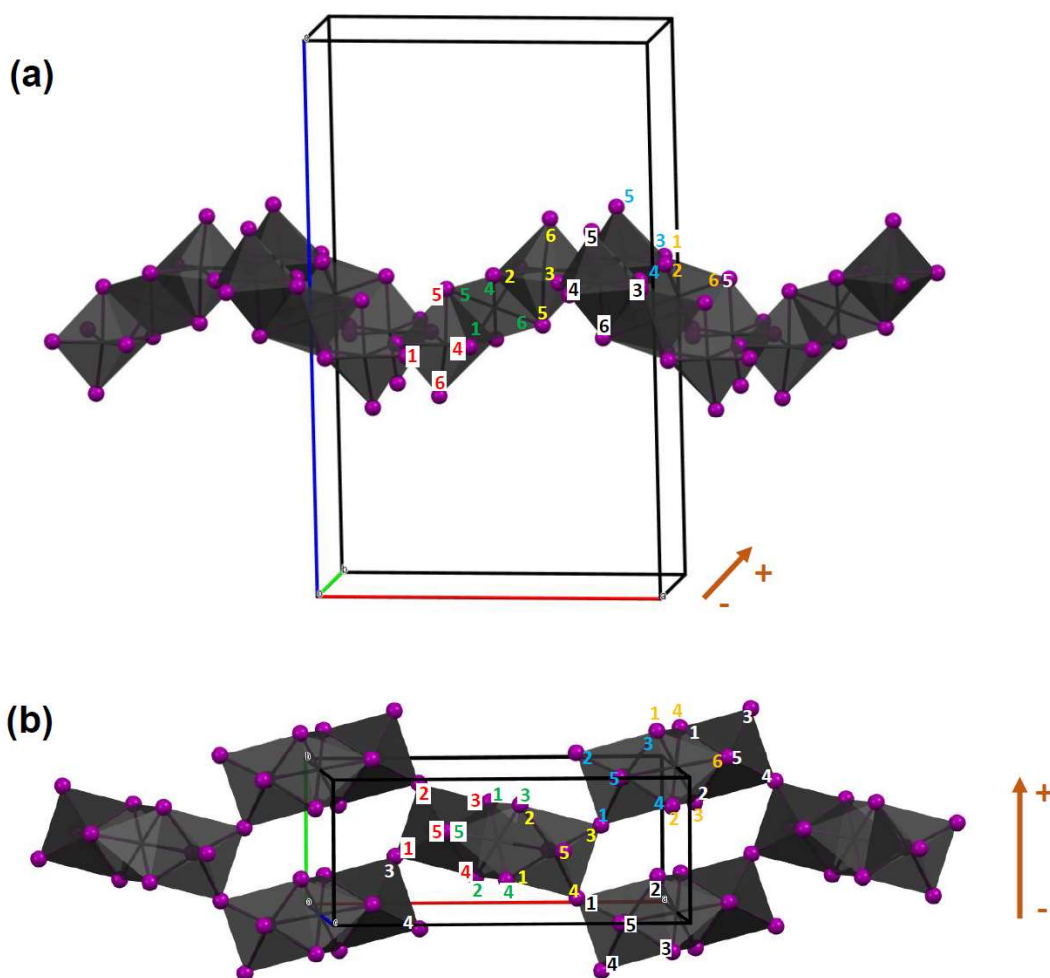


Figure J10 The structure of an 3-dimensional network of 1-6F(CC)FF(CC)F, which is rewritten as 1-6(CC)FF(CC)FF. In the full notation, the structure will be written in a

highly awkward form, 1-6 ($\underline{^1C_{435}}$ $^1C_{325}$) $^{125}F_{346}$ $^{125}F_{3,4+}$ ($\underline{^1C_{346}}$, $^1C_{236}$) $^{125}F_{346}$ $^{125}F_{3,4+}$. The “+” and “-” sign specifies the arbitrary positive direction, and the underlining would specify which octahedron the subsequent connection would be based on. The structure here is taken from $\{(C_9H_{14}N)_4[Pb_3I_{10}]\}_n$ ⁸.

Lastly, as discussed in chapter 6, this notation would take on a highly awkward form when extended to frameworks like the 4H polytype and 1D tubular structure (Fig 6.1 e,f). The 4H polytype would be written as 1-4 ($\underline{^1C_{346}}$ $^1C_{346}$ $^1C_{346}$) $^{125}F_{3,4,6}$ ($\underline{^1C_{346}}$ $^1C_{346}$ $^1C_{346}$) $^{125}F_{3,4,6}$ in the full notation, which is reduced to 1-4(CCC)F(CCC)F while the 1D tubular structure would be written as cyclo[3(2 $^X F_{346}$ $^{125}F_X$)-2(6₁ $^{6+}C_I$ $^{3-}C_5$ $^{6+}C_I$ $^{3-}C_5$ $^{6+}C_I$ $^{3-}C_5$)] (6₁ $^{6+}C_I$ $^{3-}C_5$ $^{6+}C_I$ $^{3-}C_5$ $^{6+}C_I$ $^{3-}C_5$) in the full notation which is reduced to cyclo[3(2F)-2(6₁CCCCC)] 6₁CCCCC. In those cases, the more established Gard or Ramsdell notation should be utilized in the polytypes. Or in the 1D tubular structure, this notation should be avoided altogether.

References

1. Skelton, B. W.; Kokozay, V. N.; Vassilyeva, O. Y.; Buvaylo, E. A., Experimental Crystal Structure Determination. *CSD Communication* **2019**.
2. Liu, G.; Liu, J.; Tao, X.; Li, D.-s.; Zhang, Q., Surfactants as additives make the structures of organic–inorganic hybrid bromoplumbates diverse. *Inorganic Chemistry Frontiers* **2016**, 3 (11), 1388-1392.
3. Pan, J.; Sun, A.-H.; Han, S.-D.; Wei, L.; Li, J.-H.; Wang, G.-M., Low-Dimensional Lead(II) Halides with In Situ Generated Tripyridine-Derivatives as Counteranions: Synthesis, Structures and Properties. *Journal of Cluster Science* **2017**, 28 (5), 2669-2679.
4. Hamdi, B.; Zouari, R.; Ben Salah, A., Synthesis, crystal structure, hirshfeld surface analyses and physical properties of a new hybrid compound: [C₃N₆H₈]₂PbCl₅.Cl. *Superlattices and Microstructures* **2018**, 123, 97-110.
5. Yuan, Z.; Zhou, C.; Tian, Y.; Shu, Y.; Messier, J.; Wang, J. C.; van de Burgt, L. J.; Kountouriotis, K.; Xin, Y.; Holt, E.; Schanze, K.; Clark, R.; Siegrist, T.; Ma, B.,

One-dimensional organic lead halide perovskites with efficient bluish white-light emission. *Nature Communications* **2017**, 8, 14051.

6. Liu, Y.; Liu, D.; Wu, T., Pervoskite-like hybrid lead bromides with bipyridine as structure-directing agent. *Journal of Solid State Chemistry* **2019**, 269, 220-224.

7. Ali, B. F.; Al-Far, R.; Haddad, S., A lead-halide ladder complex: catena-poly[bis(2,3-dimethylquinoxalinium) [[di-[mu]2-bromido-bis[dibromoplumbate(II)]]-di-[mu]2-bromido]]. *Acta Crystallographica Section E* **2007**, 63 (6), m1569.

8. Billing, D. G.; Lemmerer, A., catena-Poly[tetrakis(3-phenylpropylammonium) [iodoplumbate(II)-tri-[mu]-iodo-plumbate(II)-tri-[mu]-iodo-iodoplumbate(II)-di-[mu]-iodo]]. *Acta Crystallographica Section C* **2006**, 62 (5), m174-m176.